Emission and Transport of Light in Photonic Crystals

Femius Koenderink

Emission and Transport of Light in Photonic Crystals

Emission and Transport of Light in Photonic Crystals

ACADEMISCH PROEFSCHRIFT

ter verkrijging van de graad van doctor
aan de Universiteit van Amsterdam
op gezag van de Rector Magnificus
prof. mr. P. F. van der Heijden
ten overstaan van een door het college voor promoties
ingestelde commissie, in het openbaar te verdedigen
in de Aula der Universiteit
op vrijdag 27 juni 2003, te 10.00 uur

door

Albert Femius Koenderink

geboren te Utrecht

Promotiecommissie:

Promotores	Prof. Dr. W. L. Vos Prof. Dr. A. Lagendijk
Overige leden	Prof. Dr. M. S. Golden Prof. Dr. L. Kuipers Prof. Dr. H. De Raedt Prof. Dr. P. St. J. Russell Dr. R. Sprik Prof. Dr. D. A. M. Vanmaekelbergh

Faculteit der Natuurwetenschappen, Wiskunde en Informatica

The work described in this thesis is part of the research program of the "Stichting Fundamenteel Onderzoek der Materie (FOM)", which is financially supported by the "Nederlandse Organisatie voor Wetenschappelijk Onderzoek (NWO)".

It was carried out at the
Van der Waals-Zeeman Instituut, Universiteit van Amsterdam, Valckenierstraat 65, 1018 XE Amsterdam, The Netherlands,

and in the group
Complex Photonic Systems, Faculty of Science & Technology and MESA$^+$ Research Institute, University of Twente, P.O. Box 217, 7500 AE Enschede, The Netherlands,
where a limited number of copies of this thesis is available.

Druk: PrintPartners Ipskamp, Enschede, The Netherlands.
Omslag: face centered cubic marbles 180-49a.
ISBN: 90-9016903-2

Contents

Chapter 1

Photonic Crystals as a Cage for Light

1.1 Complex photonic systems

Complex photonic systems are composite optical materials in which the refractive index varies on length scales comparable to the wavelength of light. The adjective 'complex' indicates that propagation of light is most difficult to understand in such composites; the propagation strongly deviates from the rectilinear plane wave propagation in homogeneous media. The complexity resides in the fact that the optical properties of the composite are vastly dissimilar to those of the separate constituents. As two possible realizations of complex photonic systems, one may consider random media on the one hand, and ordered dielectric composites on the other hand. Wave propagation in random media is a research area with a rich history [1–3]. In contrast, ordered complex photonic systems, or *photonic crystals*, have only become subject of intense research since the last decade [4, 5].

The propagation of light in ordered complex photonic systems bears a strong similarity to the wave propagation of a conduction electron in a crystalline solid [6, 7]. Interference of waves diffracted by different lattice planes determines the optical modes and dispersion. The periodicity gives rise to Bragg diffractions, that are associated with frequency windows that are forbidden for propagation in a certain direction. Such *stop gaps* have long been known to arise for light in one-dimensionally periodic structures, known as dielectric mirrors [8]. A stop gap is associated with propagation along a specific direction. In three-dimensionally periodic dielectrics a stop gap for all directions simultaneously can be achieved, a so-called *photonic band gap*.

The total absence of optical modes for frequencies in a photonic band gap has implications beyond classical optics. Photonic crystals are expected to play an important role in cavity quantum electrodynamics, as first put forward in 1987 by Yablonovitch and John [9, 10]. Probably the most eagerly awaited phenomenon is complete inhibition of spontaneous emission: excited atoms inside a crystal with their transition frequencies tuned to the band gap cannot emit photons. The inhibition of spontaneous emission in periodic structures was first predicted by Bykov in 1972 [11]. Any

interaction mediated by vacuum fluctuations is affected by their suppression in the band gap [4, 5, 12]. In addition to spontaneous emission processes, a photonic band gap also modifies van der Waals and Casimir forces, the spectrum of black body radiation, as well as, *e.g.*, resonant dipole-dipole interactions [4, 12, 13].

Contrary to the localized suppression of spontaneous emission that can be achieved in microcavities, photonic crystals provide inhibition anywhere, in a volume only limited by the extent of the crystal. Such suppression of electromagnetic modes in the band gap is unique to photonic crystals, and can not be found in other optical materials that appear to exclude all light in a given frequency range. A photonic crystal reflects all light in the band gap not because light can't couple through the surface, as would be the case for, *e.g.*, a metal box. In a metal box a light source can still emit light, though it cannot be seen from outside the box. In a photonic band gap there are simply no electromagnetic states available and a light source can't emit at all. Once a band gap is created, the physics can be further enriched by creating isolated defects. Such defects are predicted to introduce single electromagnetic modes with frequency in the band gap, localized to within a wavelength [14–16]. Such 'cages for light' provide a route to solid state cavity quantum electrodynamics [12]. In addition, it is expected that such cavities combined with optical gain promise thresholdless lasers [9]. The threshold of a laser is reached when the gain overcomes the losses. As only one mode exists for a point defect in a band gap material, there is no loss into modes other than the lasing mode.

The field of photonic band gap crystals is intimately linked to that of random media by the role of interference in modifying the transport of light. In everyday life disordered dielectric media, such as paint, milk, fog, clouds, or biological tissue, light transport can be well described by a diffusion process, as if light consisted of particles instead of waves [1]. When the average distance between scattering events becomes comparable to the wavelength of light, interference cannot be neglected anymore. Instead, interference causes a complete halt of transport [17–20]. This phenomenon is known as Anderson localization of light. Initially, some of the interest in photonic band gaps was sparked by a proposal by John that Anderson localization would be more easily reached in photonic band gap materials with controlled disorder [10]. Both the field of Anderson localization, and of photonic band gaps are born from analogies between light and electrons. The property that binds photonic crystals with semiconductors, and optical with electron localization, is the wave nature of light and electron. The analogies carry over to many wave phenomena. Examples range from electromagnetism, electron physics, elastic and acoustic waves, to oceanography or seismology. Acoustic band gap materials, for instance, were introduced shortly after photonic band gap materials. These materials, also known as phononic crystals, are periodic composites of materials with different sound velocities and densities, that may provide a band gap for sound, instead of light [4, 5, 21, 22].

1.2 Photonic crystals and Bragg diffraction

The fundamental mechanism determining the properties of photonic crystals is due to interference, and is called Bragg diffraction. Bragg reflection of electromagnetic radiation was first studied for X-rays that are diffracted by atomic crystals [23], and later for optical waves in layered media and gratings [8, 24–27]. A set of crystal planes acts like a mirror if the Bragg condition

$$m\lambda = 2d\cos\theta \tag{1.1}$$

is met, where d is the distance between the lattice planes. Figure 1.1(a) illustrates the diffraction geometry. Reflection occurs due to constructive interference whenever the angle θ is such that the path length difference $2d\cos\theta$ between reflections off successive layers equals an integer number m of wavelengths λ. The wavelength-specific reflection causes the distinct optical appearance of photonic crystals, which is often referred to as iridescent or opalescent. By eye, periodic photonic media look strongly colored depending on illumination and orientation circumstances. In contrast, many materials derive their colored appearance by wavelength selective absorption of light. Ideally, photonic crystals do not absorb light at all, as absorption is detrimental to the formation of a photonic band gap. Natural examples of colors due to interference occur in minerals, insects, birds, reptiles and plants. Well known are, *e.g.*, gemstone opal, mother of pearl, butterfly wings, feathers of peacocks and hummingbirds [28–30]. Even the spines and hairs of a marine worm known as 'sea mouse', have recently caused a stir as natural photonic crystal fibers [31, 32].

The Bragg reflection efficiency can reach 100% for sufficiently ordered photonic crystals, when reflections from many lattice planes interfere constructively. Propagation of light into the direction of a Bragg diffraction is forbidden. Bragg diffraction is therefore associated with a stop gap: a forbidden frequency window in the dispersion relation. The dispersion relation that relates frequency ω to the wave vector is shown in Fig. 1.1(b) for propagation along the normal to the crystal planes. When the wave vector $k = 2\pi/\lambda$ reaches π/d, the Bragg condition (1.1) is met. Here, the dispersion relation splits into two branches separated by the stop gap. Throughout this thesis, the term 'stop gap' is used to identify the forbidden frequency windows in between branches of the dispersion relation along a certain direction. Experimentally observed frequency ranges of Bragg reflections, or attenuation bands in emission or transmission spectra, will be differentiated from stop gaps by the term 'stop band'.

The magnitude of the relative frequency width $\Delta\omega/\omega$ of the stop gap may be understood by considering the electromagnetic modes for $\lambda = 2d$ and $\theta = 0°$. At this wavelength, the electromagnetic modes resemble standing waves. These are due to the interference of the counterpropagating plane waves with wave vector $k = \pi/d$ and $k = -\pi/d$, that are Bragg reflected counterparts. One such standing wave is primarily concentrated in the high index material. The other linear combination of plane waves resides mainly in the low index material. As these two waves have the same wavelength at different refractive indices, they must have different frequencies. The

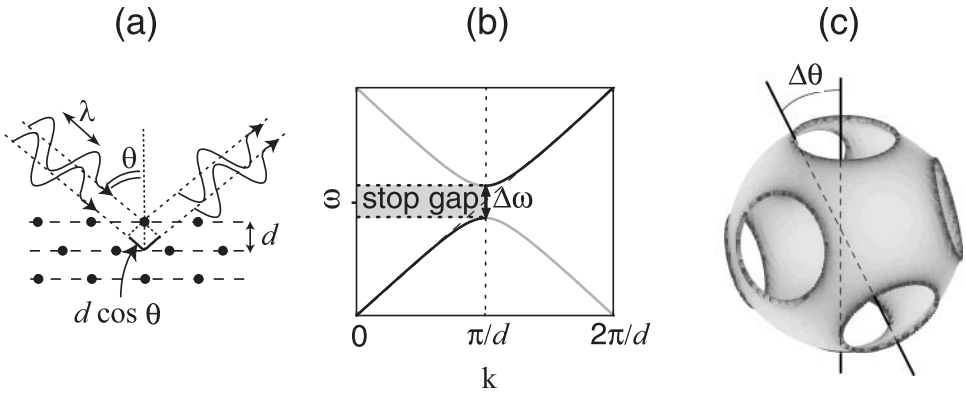

FIGURE 1.1: *(a) A family of lattice planes (spacing d) constructively reflects a wave incident at an angle* θ *if the path length difference* $2d\cos\theta$ *between reflections from successive planes equals an integer number of wavelengths* λ*. (c) Dispersion relation along the normal to the lattice planes in (a). At the Bragg condition* $k = \pi/d$*, the dispersion relation splits and folds back. The splitting* $\Delta\omega/\omega$ *relative to the center frequency* ω *is the photonic strength* Ψ*. (c) Allowed k-points at fixed frequency (high frequency edge of the stop band in (b)). A crystal has been assumed with four differently oriented sets of lattice planes with the same spacing. Correspondingly, the nearly spherical dispersion surface has eight holes, corresponding to simultaneously Bragg diffracted directions. The angular width* Δθ *of the Bragg diffraction is set by* Ψ*.*

mode residing in high index material, known as 'dielectric mode', has the lowest frequency. The 'air mode' delimits the upper edge of the stop gap [33]. The stop gap width increases with the refractive index contrast. In essence, nonzero index contrast relaxes the Bragg condition (1.1) to include reflection over a range of frequencies simultaneously. As explained in Chapter 2, the relative frequency width $\Delta\omega/\omega$ can be directly identified with a *photonic interaction strength* Ψ, defined as the polarizability per volume of a unit cell [34, 35]. This interaction strength involves both the refractive index contrast, and the geometry of the crystal. The number of lattice planes needed to build up a Bragg reflection is reduced in proportion to the increase in stop band width. Indeed, the Bragg attenuation length that measures the exponential decay of incident light at the stop gap center frequency satisfies

$$L_B = \frac{2d}{\pi\Psi} = \frac{\lambda}{\pi\Psi}. \tag{1.2}$$

Atoms in a crystal lattice scatter X-rays only very weakly, causing stop gaps to occur only in very narrow frequency intervals ($\Psi \sim 10^{-4}$ for X-rays). For visible light however, the interaction between light and matter is strong enough to cause very wide stop gaps ($\Psi \sim 0.1$). Correspondingly, light with frequencies in the stop gap penetrates only a few lattice plane spacings into the crystal.

A diagram as displayed in Fig. 1.1(b) specifies the optical frequencies for wave vectors along a specific direction. For monochromatic experiments, it is more useful to specify all allowed wave vectors at a particular frequency [25–27]. An example of such a dispersion surface is displayed in Fig. 1.1(c). In Chapter 2, the first calculations of dispersion surfaces for realistic three-dimensional photonic crystals are presented. Stop gaps as in Fig. 1.1(b) correspond to 'holes' in the dispersion surfaces. The maximum surface area of these holes, *i.e.*, the maximum number of simultaneously forbidden propagation directions, increases with the photonic interaction strength Ψ. To first approximation, the maximum solid angle of forbidden propagation directions is attained for a frequency ω at the top of the normal-incidence stop gap, and is $\Omega = p\Psi \times 4\pi$ sr. Here, p is the number of equivalent sets of lattice planes with spacing d (*e.g.*, $p = 4$ in Fig. 1.1(c)). For sufficiently large photonic interaction ($\Psi \gtrsim 0.2$), stop gaps in all directions due to various sets of lattice planes will overlap, and create a photonic band gap. Confusingly, many authors refer to stop gaps as 'band gaps', and to photonic band gaps as 'complete photonic band gaps'. In this thesis, we reserve the term 'photonic band gap', or simply 'band gap', to mean a frequency window in which all propagating modes are forbidden. A band gap can only be achieved for specific crystal symmetries and requires a high refractive index contrast, above ~ 2. Most optical materials, with the exception of semiconductors, have refractive indices between ~ 1.3 and 1.6; one therefore needs to create optimally scattering arrangements of semiconductor materials.

Many efforts are currently devoted to creating structures with periodicity in only two dimensions. Slabs with two-dimensional periodicity are certainly more amenable to fabrication using current semiconductor technology than three-dimensional structures [5]. In this respect, it is imperative to separate the useful properties of photonic crystals in two distinct classes. Many applications rely only on Bragg diffraction along specific crystal directions or the strong dispersion in photonic crystals. Such properties only depend on the electromagnetic modes with wave vectors in certain directions, and can be realized in 2D photonic crystals. Examples include, *e.g.*, narrow band filters, dispersion compensators and diffractive components. Photonic crystal fibers, with periodicity normal to, instead of coplanar with the direction of propagation, are pursued for similar purposes that depend on manipulating the propagation of light [32, 36, 37]. The second class of properties of photonic crystals relies on the suppression or enhancement of the electromagnetic density of states (DOS). The DOS at a specific frequency depends on all the modes, and not just those with specific wave vectors. Only three-dimensional photonic crystals hold the promise of a strongly modulated DOS, a photonic band gap, and the concomitant new quantum optics. This thesis is solely concerned with optical properties of three-dimensional photonic crystals.

1.3 Fabrication of three-dimensional photonic crystals

The fabrication of photonic band gap crystals continues to be a rich problem, even after over a decade of work. This may come as a surprise since the first photonic band gap material was created in 1991, just a few years after the founding papers on photonic crystals [38]. However this photonic crystal functioned in the microwave range [38]. A main goal of the field is the fabrication of photonic band gap materials at optical frequencies, which will allow both fundamental studies and applications to go forward. Knowledge from many different fields can be brought into play, ranging from semiconductor processing techniques, to approaches based on colloid science, sol-gel chemistry, electrochemistry, chemical vapor deposition and polymer science. Two popular fabrication methods adapted to achieving photonic crystals are layer-by-layer fabrication and self-assembly using colloidal particles. Other schemes based on etching, lithographic or holographic techniques have not been as widely pursued yet. In some cases, the power and flexibility of these methods may be increased by casting the high index photonic crystal from a low index template. While photonic band gaps have recently been claimed at near-infrared wavelengths [39–42], the challenges of disorder and finite size effects, as well as the inherent difficulty of proving the existence of a photonic band gap leave the field of fabrication open for new ideas.

The layer-by-layer micromachining approach allows fabrication of photonic crystals for near-infrared frequencies from high-index semiconductors. Considerable control over the crystal symmetry is possible. Following a proposal by Ho and coworkers [43], efforts focus on the so-called 'woodpile' structures with diamond symmetry. These structures were first created for microwaves, and have since been scaled down to near-infrared wavelengths [39, 40, 44]. As the name 'layer-by-layer fabrication' suggests, these photonic crystals are created by an elaborate sequence of carefully aligning, stacking, and fusing separate 2D layers. The fabrication profits from known semiconductor processing techniques to pattern each 2D layer on a wafer. If infinitely extended, the woodpiles are expected to have a photonic band gap. However, only quasi 2D structures can be achieved due to accumulation of alignment faults with increasing number of layers. Progress is further impeded by the extraordinarily long time-frame for fabrication, on the order of ~ 6 months for thicknesses < 2 unit cells.

Self-assembly of colloidal spheres into crystals results in truly 3D periodic arrays, easily reaching hundreds of microns of thickness, thus solving the thickness issue mentioned above. Colloidal particles are particles with a size between 1 and 1000 nm. Colloidal spheres of polystyrene or silica can be made routinely with a very controlled size. It has long been known that colloidal spheres self-assemble into colloidal crystals, or opals [28]. An example of such an opal is demonstrated by the scanning electron micrograph in Fig. 1.2(a). The use of such structures as photonic crystals *per se* is limited by the small photonic interaction strength. A major step forward has been the recent use of self-assembled structures as templates for high index materials [45–51]. In this thesis, highly ordered 'inverse opals' are studied, that have been created by infiltration of liquid precursor of high index material into opal, and subsequent removal of the template [47, 52]. This method results in ordered arrays of

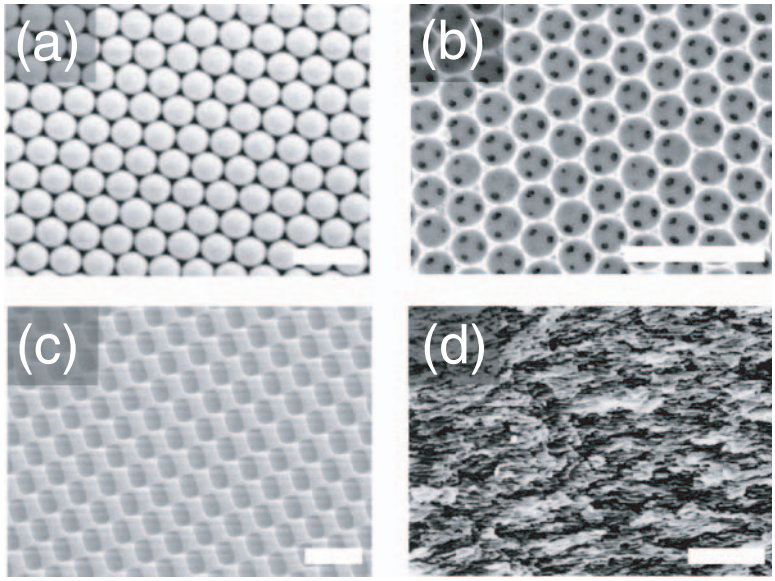

FIGURE 1.2: *Scanning Electron Micrographs (SEMs) of various complex dielectrics. (a) 111 plane of an fcc close-packed crystal of polystyrene spheres (opal). (b) 111 plane of air holes in a titania matrix (titania inverse opal). (c) hexagonal array of holes in a 2D layer of photoresist, created by laser interference lithography. (d) random anisotropic air pores in a GaP wafer ('photonic sponge'). Scalebars represent* 2 μm. *Images courtesy of Lydia Bechger ((a) and (b)), Tijmen Euser (c) and Boris Bret (d).*

close-packed air spheres in a solid matrix (see Fig. 1.2(b)). Inverse opals for infrared wavelengths of very high index materials such as silicon have recently been fabricated by chemical vapor deposition onto silica opals [41, 42]. Other inversion methods are being developed, including electrochemical deposition and nanoparticle infiltration [53, 54]. While inverse opals offer an elegant solution to the problem of size, they are accompanied by their own challenges. The main drawback of inverse opals is the lack of control over the crystal symmetry. Using charged spheres, well-ordered crystals with a face centered cubic (*fcc*) arrangement [52] can be made. Such a crystal structure is less favorable for creating a band gap than the diamond symmetry of layer-by-layer structures. The diamond symmetry so far appears unattainable using self-assembly methods.

Various etching and other lithographic techniques may be used to create a periodic structure by removing material from a solid block. These techniques have the potential to combine the size of the colloidal crystal with the controllable symmetry of layer-by-layer assembly. As these techniques are designed for creating two-dimensional patterns, progress in creating three-dimensional crystals has been limited [55–57]. An elegant approach, recently described in Ref. [58–61], uses a laser interference lithography method to create a periodic interference pattern in a block

of photoresist. A 3D periodic exposure can be realized by simultaneously combining four laser beams. Theoretically, a variety of crystal structures can be created by varying the orientation and polarization of the four laser beams. Alternatively, the photoresist can be exposed to several two-beam interference patterns in succession, giving rise to patterns as shown in Fig. 1.2(c). After development, one may increase the refractive index contrast by using the developed photoresist as a low-index template for inversion, similar to the fabrication of inverse opals. Although such holographic means to create 3D periodic structures appear powerful, the fabrication of high index photonic crystals from holographic templates remains unexplored.

1.4 External optical probes of photonic crystals

Since stop gaps are the precursors to a photonic band gap, the study of their optical properties is essential. Stop gaps in the photonic dispersion are conveniently probed by continuous-wave measurements of Bragg reflections. The center frequency of the first order stop band is commonly used to determine the lattice spacing of photonic crystals according to Bragg's law (1.1) [34, 62, 63]. The dependence of stop bands on crystal orientation, and bands at higher diffraction orders are not commonly studied, however. Recently, reflectivity experiments on inverse opals have been extended to higher frequencies and studied depending on the crystal orientation [64, 65]. The reflectivity reveals intriguing properties of the photonic dispersion that can not be explained by the simple Bragg law (1.1). Such phenomena are caused by the simultaneous coupling of diffractions by several families of lattice planes. This coupling can cause flat dispersion over a considerable wave vector range and is the mechanism that ultimately creates the photonic band gap.

Time-resolved reflection and transmission experiments can provide additional information about the photonic dispersion relation. At the edges of stop gaps, the photon bands become highly dispersive. Using ultrashort pulses, the theoretically expected reduction of the group velocity at the stop band edges has been observed in colloidal crystals [66, 67]. In a phase-sensitive ultrashort-pulse interferometric experiment, it was observed that the group velocity dispersion diverges near stop band edges, with branches of both normal and anomalous dispersion [67]. In analogy with electrons, the group velocity dispersion may be interpreted as an 'effective photon mass', that also diverges near gaps [7]. Such experiments still need to be extended to more strongly photonic crystals, and to propagation along other than high symmetry directions. Interesting dispersive phenomena are expected, since the magnitude and orientation of the group velocity depend sensitively on the wave vector.

Both the continuous-wave and the time-resolved reflection and transmission experiments probe the coupling of propagating waves into photonic crystal structures. Additional information may be gathered from near-field measurements. Using an optical scanning probe, local information is retrieved on how light couples into evanescent modes. In such experiments, one may either illuminate from the far field, and detect in the near field, or vice versa [68]. The latter experiment appears strongly

related to how spontaneous emission of atoms or molecules is modified near the interface of a photonic crystal. Recent experiments on opals have shown that the local coupling efficiency is spatially nonuniform in a strongly frequency-dependent manner [69]. Currently, a theoretical framework to interpret these interesting phenomena is lacking.

1.5 Probing inside photonic crystals

Structural and optical characterization of photonic crystals is usually based on scanning electron microscope images and reflectivity measurements. These probes only provide information about crystal planes close to external interfaces of photonic crystals. However, the interest in photonic crystals stems from properties expected to originate in the bulk. It is therefore of prime interest to develop both structural and optical probes of the inside of photonic crystals.

The most obvious method to probe the inside of photonic crystals optically, is to embed sources of spontaneous emission. Since 3D photonic crystals fundamentally modify the electromagnetic density of states, it is natural to study their influence on spontaneous emission. To this end, light sources such as excited atoms, quantum dots, fluorescent molecules or thermal radiation sources should be placed inside photonic crystals. In essence, such a light source will experience two effects: *(i)* an angular redistribution of intensity due to stop gaps for propagation in certain directions, and *(ii)* a change of the local radiative density of states at its spatial position [70], resulting in a change of radiative lifetime or radiated power spectrum.

Angular redistribution of spontaneous emission by photonic crystals is commonly observed, both in weakly and in strongly photonic crystals. An attenuation band appears when a stop gap overlaps the emission spectrum [71–78]. Stop bands in emission thereby represent a route to study the photonic dispersion relation without reverting to reflectivity measurements. A photonic effect on the spontaneous emission lifetime has yet to be clearly observed. An increase of the spontaneous emission lifetime would be a clear step towards full inhibition of emission, the 'holy grail' of photonic band gap materials. Several time resolved emission experiments in search of lifetime changes in colloidal photonic crystals showed no modified emission rate due to insufficient dielectric contrast of the crystals [79–82]. The study of a modified radiative rate not only revolves around fabricating a strongly photonic crystal, but also depends on issues like quantum efficiency, and finding a suitable reference host for comparison. Ultimately, inhibition of emission is expected to be one of the few proofs for the occurrence of a photonic band gap. Omnidirectional reflectivity is certainly not sufficient evidence, as it does not imply the absence of electromagnetic modes [83].

A logical next step would be to study stimulated emission in photonic crystals. Lacking a photonic band gap, however, the thresholdless laser remains currently out of reach. Recent experiments have shown photonic effects on stimulated emission due to distributed feedback by Bragg diffraction [84]. Other groups have reported

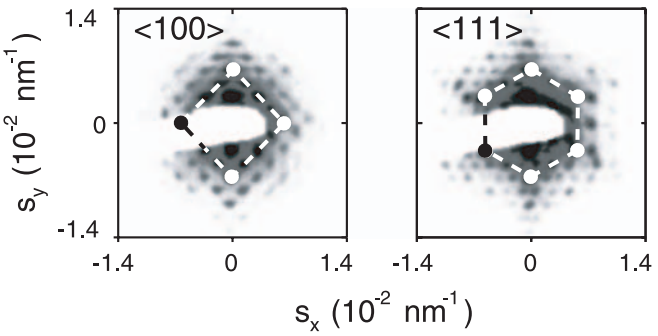

FIGURE 1.3: *Scattered intensity versus scattering vector in a small angle X-ray scattering experiment on a titania inverse opal. Count rate increases with darkening gray-scale. The patterns are partly obscured due to a beam stop for the transmitted beam. The left panel shows diffraction spots due to the cubic 100 planes, the right panel corresponds to hexagonal 111 planes. Excellent* fcc *arrangement is confirmed by the observation of high order diffraction spots (dots connected by lines correspond to 4th order). Graphs courtesy of Judith Wijnhoven, Lydia Bechger, and Willem Vos.*

data that may be interpreted in the framework of random lasers, *i.e.*, media with gain and feedback due to scattering by disordered scatterers [85–87].

1.6 Disorder in photonic crystals

Detailed analysis of reflection and transmission spectra, as well as of angle-dependent spontaneous emission, shows features that are not expected for perfect photonic crystals. It appears that scattering by defects is crucial for the understanding of light transport in all real photonic crystals. The length scale which characterizes the effect of disorder on light transport is the transport mean free path ℓ, which is the distance over which light propagates before its propagation direction is randomized by scattering [1]. Regarding applications, the disorder in photonic crystals must be controlled to the extent that ℓ remains larger than the length scale necessary to build up a Bragg diffraction or band gap. It is therefore essential to quantify the mean free path, and to determine which forms of structural disorder determine the magnitude of ℓ. As randomly scattered light traverses long light paths through the crystal, the diffuse light can truly be considered as a probe that explores the bulk of photonic crystals.

Since the structure of photonic crystals is defined on the scale of hundreds of nanometers, scanning electron microscopy (SEM) is ideal for characterizing surfaces and cross-sections of samples (Fig. 1.2a-c). Understanding the 3D degree of order, however, is essential for the interpretation of optical experiments and of the transport mean free path. Recently, small angle X-ray diffraction experiments have been initiated to identify the crystal structure of colloidal crystals, opals, and inverse opals and to determine the content of the unit cell (Fig. 1.3)[52, 88, 89]. Essential parameters

that gauge bulk structural disorder can be quantified by small angle X-ray scattering. Small angle X-ray scattering is complementary to microscopy since it yields volume-averaged structural parameters that are otherwise difficult to access. Polydispersity and small displacements of building blocks in opals and inverse opals cause mean free paths comparable to those in, *e.g.*, milk. Scattering is ~ 100 times less effective than in the most strongly scattering random media created to date, such as the macroporous semiconductor sponge shown in Fig. 1.2(d) [90–92]. Still, diffusion of light due to inevitable structural disorder is essential to understand the transport of light in three-dimensional photonic crystals. On length scales exceeding the mean free path, photonic crystals will not allow to 'mold' or 'guide' the 'flow of light' [33], putting a limit on applications. It may appear that the interest in diffusion is solely dictated by the presence of unwanted but inevitable fabrication artifacts and their impact on photonic applications. The diffusion of light in photonic crystals is of broader interest, however. The fundamental link between disorder in photonic crystals and Anderson localization provides motivation for detailed studies. Photonic crystals provide a platform to test diffusion theory for otherwise inaccessible parameters and boundary conditions.

1.7 This thesis

This thesis describes experimental studies of optical probes inside strongly photonic crystals. Experiments are presented that are concerned with spontaneous emission, and experiments designed to quantify the stationary diffuse transport of light in photonic crystals. For the most part, titania inverse opals were used in the experiments. These crystals are among the most strongly photonic materials to operate at visible wavelengths. In order to quantitatively interpret the data, we rely both on theoretical concepts from the field of photonic crystals, and on the theory of light transport in random media. This thesis is organized as follows.

- Chapter 2 lays down a theoretical framework to describe the propagation of light in perfect photonic crystals. The purpose of this chapter is twofold; firstly, we explain how results of the plane wave method were calculated that are used to interpret experiments. Secondly, the chapter serves to introduce several important optical properties of photonic crystals to the reader, as illustrated by numerical examples. Though this chapter mainly discusses basic concepts and methods well known in the literature, several new aspects are introduced. We present the first calculations of dispersion surfaces in three-dimensional photonic crystals, and discuss their use in solving diffraction problems.

- In Chapter 3 spontaneous emission spectra of laser dyes in strongly photonic titania inverse opals are discussed. The experiment describes the angular redirection of spontaneous emission spectra due to diffraction by the photonic crystal. We identify two stop bands that attenuate the emission spectra. The angle-dependent stop band frequencies display an avoided crossing that differs from

simple Bragg diffraction. The avoided crossing is identified as the result of coupling of simultaneous Bragg diffraction by multiple families of lattice planes. The strongly reduced dispersion of the Bloch modes in the wide range of the avoided crossing illustrates how coupling of many diffractions cooperate to ultimately form a photonic band gap.

- In Chapter 4 we present the first experimental proof of strong angle-independent modification of spontaneous emission spectra from laser dyes in photonic crystals. The data reveal inhibition of emission up to a factor ~ 5 over a large bandwidth. The center frequency and bandwidth of the inhibition agree with the calculated reduction of the density of states, but the measured inhibition of the vacuum fluctuations is much larger. We discuss the key role of fluorescence quantum efficiency, weak disorder, and choice of reference host in interpreting the experimental data.
- Chapter 5 contains a theoretical proposal to switch the photonic band gap of semiconductor photonic crystals on a femtosecond time scale. A method by which photonic crystal properties can be controlled in time will greatly enhance the potential of photonic crystals, both for applications and cavity QED experiments. The proposal is based on two-photon excitation of free carriers to optically switch the refractive index of the semiconductor backbone of inverse opals. Using realistic parameters for GaAs, we show that ultrafast control of spontaneous emission and microcavities is feasible.
- Chapter 6 describes the first experimental study of enhanced backscattering in photonic crystals. Enhanced backscattering is an interference effect in random multiple scattering that allows to quantify the mean free path ℓ. Enhanced backscattering measurements are presented, both for polystyrene opals and for strongly photonic crystals of air spheres in TiO_2 in the wavelength range of first and higher order stop bands. The shape of the enhanced backscattering cones is well described by diffusion theory, and corresponds to mean free paths ℓ of about 40 lattice plane spacings both for opals and air spheres. We present a model that incorporates photonic effects on the cone width and successfully explains the data. Furthermore, we propose that sphere polydispersity and displacements play a dominant role in determining the mean free path.
- Chapter 7 describes an experiment that quantifies the spectral and angular properties of the diffuse intensity transmitted by photonic crystals. The diffusely transmitted intensity is distributed over angle in a strikingly non-Lambertian manner, depending strongly on frequency. The remarkable frequency- and angle dependence is quantitatively explained by a model incorporating diffusion theory and band structure on equal footing. The model also applies to the angle-dependent modification observed in emission spectra of internal sources in photonic crystals (Chapter 3). The total transmission shows a scaling of the transport mean free path with frequency and lattice spacing that is consistent with findings in Chapter 6.

The work described in this thesis is among the first efforts to gather physical understanding of the optical properties of state of the art strongly photonic crystals. In an attempt to catch up with the theory of quantum optics in photonic band gap materials, the majority of the work in the field of photonic crystals is concerned with fabricating structures meeting the requirements for a band gap. Due to the extraordinary material constraints, it remains unclear if the desired band gap regime will ever be realized for optical wavelengths. Even then, questions remain on how large, and how fault-free a photonic crystal should be to obtain a significant (though local) control over spontaneous emission. Our experiments show that even without a band gap, a rich variety of diffraction, dispersion, emission and scattering phenomena occurs. Ultimately, experiments designed to probe photonic crystals at frequencies near the photonic band gap will be difficult to interpret due to the complex transport of light in photonic crystals. If anything, this thesis illustrates the dire need for theory and experiments to harness these aspects of strongly photonic crystals.

References

[1] A. Ishimaru, *Wave Propagation and Scattering in Random Media* (Academic Press, New York, 1978).

[2] H. C. van de Hulst, *Multiple Light Scattering and Radiative Transfer* (Academic Press, New York, 1980).

[3] P. Sheng, *Introduction to Wave Scattering, Localization, and Mesoscopic Phenomena* (Academic Press, New York, 1995).

[4] *Photonic Band Gap Materials*, edited by C. M. Soukoulis (Kluwer, Dordrecht, 1996).

[5] *Photonic Crystals and Light Localization in the* 21st *Century*, edited by C. M. Soukoulis (Kluwer, Dordrecht, 2001).

[6] F. Bloch, *Über die Quantenmechanik der Elektronen in Kristallgittern*, Z. f. Physik **52**, 555 (1928).

[7] N. W. Ashcroft and N. D. Mermin, *Solid State Physics* (Holt, Rinehard and Winston, New York, 1976).

[8] A. Yariv and P. Yeh, *Optical Waves in Crystals: Propagation and Control of Laser Radiation* (John Wiley & Sons, New York, 1983).

[9] E. Yablonovitch, *Inhibited Spontaneous Emission in Solid-State Physics and Electronics*, Phys. Rev. Lett. **58**, 2059 (1987).

[10] S. John, *Strong Localization of Photons in Certain Disordered Dielectric Superlattices*, Phys. Rev. Lett. **58**, 2486 (1987).

[11] V. P. Bykov, *Spontaneous Emission in a Periodic Structure*, Sov. Phys.–JETP **35**, 269 (1972).

[12] S. Haroche, in *Systèmes Fondamentaux en Optique Quantique / Fundamental Systems in Quantum Optics*, edited by J. Dalibard, J. M. Raimond, and J. Zinn-Justin (North-Holland, Amsterdam, 1992), Chap. 13, pp. 767–940.

[13] R. Loudon, *The Quantum Theory of Light, 2nd ed.* (Oxford University Press, Oxford, England, 1983).

[14] E. Yablonovitch, T. J. Gmitter, R. D. Meade, A. M. Rappe, K. D. Brommer, and J. D. Joannopoulos, *Donor and Acceptor Modes in Photonic Band-Structure*, Phys. Rev. Lett. **67**, 3380 (1991).

[15] P. R. Villeneuve, S. H. Fan, and J. D. Joannopoulos, *Microcavities in Photonic Crystals: Mode Symmetry, Tunability, and Coupling Efficiency*, Phys. Rev. B **54**, 7837 (1996).
[16] K. Sakoda, *Optical Properties of Photonic Crystals* (Springer Verlag, Berlin, 2001).
[17] P. W. Anderson, *Absence of Diffusion in Certain Random Lattices*, Phys. Rev. **109**, 1492 (1958).
[18] D. S. Wiersma, P. Bartolini, A. Lagendijk, and R. Righini, *Anderson Localization of Light*, Nature **390**, 671 (1997).
[19] F. J. P. Schuurmans, *Light in Complex Dielectrics*, Ph.D. thesis, University of Amsterdam, 1999.
[20] J. Gómez Rivas, R. Sprik, A. Lagendijk, L. D. Noordam, and C. W. Rella, *Static and Dynamic Transport of Light Close to the Anderson Localization Transition*, Phys. Rev. E **63**, 046613 (2001).
[21] M. S. Kushwaha, P. Halevi, L. Dobrzynski, and B. Djafari-Rouhani, *Acoustic Band Structure of Periodic Elastic Composites*, Phys. Rev. Lett. **71**, 2022 (1993).
[22] R. Sprik and G. H. Wegdam, *Acoustic Band Gaps in Composites of Solids and Viscous Liquids*, Solid. State Commun. **106**, 77 (1998).
[23] R. W. James, *The Optical Principles of the Diffraction of X-Rays* (G. Bell & Sons, London, 1954).
[24] K. Ohtaka, *Energy Band of Photons and Low-Energy Photon Diffraction*, Phys. Rev. B **19**, 5057 (1979).
[25] P. St. J. Russell, *Optics of Floquet-Bloch Waves in Dielectric Gratings*, Appl. Phys. B **39**, 231 (1986).
[26] P. St. J. Russell, *Photonic Band Gaps*, Physics World **5**, 37 (1992).
[27] P. St. J. Russell, T. A. Birks, and F. D. Lloyd-Lucas, in *Confined Electrons and Photons*, edited by E. Burstein and C. Weisbuch (Plenum, New York, 1995), pp. 585–633.
[28] J. V. Sanders, *Colour of precious opal*, Nature **204**, 1151 (1964).
[29] H. Ghiradella, *Light and Color on the Wing: Structural Colors in Butterflies and Moths*, Appl. Optics **30**, 3492 (1991).
[30] D. Osorio and A. D. Ham, *Spectral Reflectance and Directional Properties of Structural Coloration in Bird Plumage*, J. Exp. Biol. **205**, 2017 (2002).
[31] A. R. Parker, R. C. McPhedran, D. R. McKenzie, L. C. Botten, and N. A. Nicorovici, *Photonic Engineering: Aphrodite's iridescence*, Nature **409**, 36 (2001).
[32] P. St. J. Russell, *Photonic Crystal Fibers*, Science **299**, 358 (2003).
[33] J. D. Joannopoulos, R. D. Meade, and J. N. Winn, *Photonic Crystals: Molding the Flow of Light* (Princeton University Press, Princeton, 1995).
[34] W. L. Vos, R. Sprik, A. van Blaaderen, A. Imhof, A. Lagendijk, and G. H. Wegdam, *Strong Effects of Photonic Band Structures on the Diffraction of Colloidal Crystals*, Phys. Rev. B **53**, 16231 (1996).
[35] W. L. Vos, M. Megens, C. M. van Kats, and P. Bösecke, *Transmission and Diffraction by Photonic Colloidal Crystals*, J. Phys.-Condens. Matter **8**, 9503 (1996).
[36] J. C. Knight, T. A. Birks, and P. St. J. Russell, *All-Silica Single-Mode Optical Fiber with Photonic Crystal Cladding*, Opt. Lett. **21**, 1547 (1996).
[37] R. F. Cregan, B. J. Mangan, J. C. Knight, T. A. Birks, P. St. J. Russell, P. J. Roberts, and D. C. Allan, *Single-mode Photonic Band Gap Guidance of Light in Air*, Science **285**, 1537 (1999).
[38] E. Yablonovitch, T. J. Gmitter, and K. M. Leung, *Photonic Band Structure: The Face-Centered-Cubic Case Employing Nonspherical Atoms*, Phys. Rev. Lett. **67**, 2295 (1991).
[39] S.-Y. Lin, J. G. Fleming, D. L. Hetherington, B. K. Smith, R. Biswas, K.-M.. Ho, M. M.

Sigalas, W. Zubrzycki, S. R. Kurtz, and J. Bur, *A Three-Dimensional Photonic Crystal Operating at Infrared Wavelengths*, Nature **394**, 251 (1998).

[40] S. Noda, K. Tomoda, N. Yamamoto, and A. Chutinan, *Full Three-Dimensional Photonic Bandgap Crystals at Near-Infrared Wavelengths*, Science **289**, 604 (2000).

[41] A. Blanco, E. Chomski, S. Grabtchak, M. Ibisate, S. John, S. W. Leonard, C. López, F. Meseguer, H. Míguez, J. P. Mondia, G. A. Ozin, O. Toader, and H. M. van Driel, *Large-Scale Synthesis of a Silicon Photonic Crystal with a Complete Three-Dimensional Bandgap Near 1. 5 Micrometres*, Nature **405**, 437 (2000).

[42] Y. A. Vlasov, X. Z. Bo, J. C. Sturm, and D. J. Norris, *On-Chip Natural Assembly of Silicon Photonic Bandgap Crystals*, Nature **414**, 289 (2001).

[43] K.-M. Ho, C. T. Chan, C. M. Soukoulis, R. Biswas, and M. Sigalas, *Photonic Band-Gaps in 3-Dimensions - New Layer-by-Layer Periodic Structures*, Solid State Commun. **89**, 413 (1994).

[44] E. Özbay, E. Michel, G. Tuttle, R. Biswas, K.-M. Ho, J. Bostak, and D. M. Bloom, *Double-etch Geometry for Millimeter-Wave Photonic Band-Gap Crystals*, Appl. Phys. Lett. **65**, 1617 (1994).

[45] A. Imhof and D. J. Pine, *Ordered Macroporous Materials by Emulsion Templating*, Nature **389**, 948 (1997).

[46] B. T. Holland, C. F. Blanford, and A. Stein, *Synthesis of Macroporous Minerals with Highly Ordered Three-Dimensional Arrays of Spherical Voids*, Science **281**, 538 (1998).

[47] J. E. G. J. Wijnhoven and W. L. Vos, *Preparation of Photonic Crystals Made of Air Spheres in Titania*, Science **281**, 802 (1998).

[48] A. A. Zakhidov, R. H. Baughman, Z. Iqbal, C. X. Cui, I. Khayrullin, S. O. Dantas, I. Marti, and V. G. Ralchenko, *Carbon Structures with Three-Dimensional Periodicity at Optical Wavelengths*, Science **282**, 897 (1998).

[49] O. D. Velev and E. W. Kaler, *Structured Porous Materials Via Colloidal Crystal Templating: From Inorganic Oxides to Metals*, Adv. Mater. **12**, 531 (2000).

[50] Y. N. Xia, B. Gates, and Z. Y. Li, *Self-Assembly Approaches to Three-Dimensional Photonic Crystals*, Adv. Mater. **13**, 409 (2001).

[51] D. J. Norris and Y. A. Vlasov, *Chemical Approaches to Three-Dimensional Semiconductor Photonic Crystals*, Adv. Mater. **13**, 371 (2001).

[52] J. E. G. J. Wijnhoven, L. Bechger, and W. L. Vos, *Fabrication and Characterization of Large Macroporous Photonic Crystals in Titania*, Chem. Mater. **13**, 4486 (2001).

[53] L. K. Van Vught, A. F. Van Driel, R. W. Tjerkstra, L. Bechger, W. L. Vos, D. Vanmaekelbergh, and J. J. Kelly, *Macroporous Germanium by Electrochemical Deposition*, Chem. Comm. 2054 (2002).

[54] G. Subramania, R. Biswas, K. Constant, M. M. Sigalas, and K.-M. Ho, *Structural Characterization of Thin Film Photonic Crystals*, Phys. Rev. B **63**, 235111 (2001).

[55] C. Cuisin, A. Chelnokov, J. M. Lourtioz, D. Decanini, and Y. Chen, *Fabrication of Three-Dimensional Photonic Structures with Submicrometer Resolution by X-Ray Lithography*, J. Vac. Sci. Technol. B **18**, 3505 (2000).

[56] A. Chelnokov, K. Wang, S. Rowson, P. Garoche, and J. M. Lourtioz, *Near-Infrared Yablonovite-Like Photonic Crystals by Focused-Ion-Beam Etching of Macroporous Silicon*, Appl. Phys. Lett. **77**, 2943 (2000).

[57] J. Schilling, F. Müller, S. Matthias, R. B. Wehrspohn, U. Gösele, and K. Busch, *Three-Dimensional Photonic Crystals Based on Macroporous Silicon with Modulated Pore Diameter*, Appl. Phys. Lett. **78**, 1180 (2001).

[58] M. Campbell, D. N. Sharp, M. T. Harrison, R. G. Denning, and A. J. Turberfield, *Fabrication of Photonic Crystals for the Visible Spectrum by Holographic Lithography*, Nature **404**, 53 (2000).

[59] S. Yang, M. Megens, J. Aizenberg, P. Wiltzius, P. M. Chaikin, and W. B. Russel, *Creating Periodic Three-Dimensional Structures by Multibeam Interference of Visible Laser*, Chem. Mat. **14**, 2831 (2002).

[60] L. Vogelaar, W. Nijdam, H. A. G. M. van Wolferen, R. M. de Ridder, F. B. Segerink, E. Flück, L. Kuipers, and N. F. van Hulst, *Large Area Photonic Crystal Slabs for Visible Light with Waveguiding Defect Structures: Fabrication with Focused Ion Beam Assisted Laser Interference Lithography*, Adv. Mater. **13**, 1551 (2001).

[61] T. G. Euser, *A Game of μ-Golf: Growth and Analysis of Colloidal Crystals on 2D Structures Fabricated with Laser Interference Lithography*, Master's thesis, University of Twente, 2002.

[62] H. Míguez, A. Blanco, F. Meseguer, C. López, H. M. Yates, M. E. Pemble, V. Fornes, and A. Mifsud, *Bragg Diffraction from Indium Phosphide Infilled Fcc Silica Colloidal Crystals*, Phys. Rev. B **59**, 1563 (1999).

[63] V. N. Astratov, A. M. Adawi, M. S. Skolnick, V. K. Tikhomirov, V. Lyubin, D. G. Lidzey, M. Ariu, and A. L. Reynolds, *Opal Photonic Crystals Infiltrated with Chalcogenide Glasses*, Appl. Phys. Lett. **78**, 4094 (2001).

[64] H. M. van Driel and W. L. Vos, *Multiple Bragg Wave Coupling in Photonic Band-Gap Crystals*, Phys. Rev. B **62**, 9872 (2000).

[65] W. L. Vos and H. M. van Driel, *Higher Order Bragg Diffraction by Strongly Photonic Fcc Crystals: Onset of a Photonic Bandgap*, Phys. Lett. A **272**, 101 (2000).

[66] Y. A. Vlasov, S. Petit, G. Klein, B. Hönerlage, and C. Hirlimann, *Femtosecond Measurements of the Time of Flight of Photons in a Three-Dimensional Photonic Crystal*, Phys. Rev. E **60**, 1030 (1999).

[67] A. Imhof, W. L. Vos, R. Sprik, and A. Lagendijk, *Large Dispersive Effects Near the Band Edges of Photonic Crystals*, Phys. Rev. Lett. **83**, 2942 (1999).

[68] A. Dereux, G. Christian, and J. B. Weeber, *Theoretical Principles of Near-field Optical Microscopies and Spectroscopies*, J. Chem. Phys. **112**, 7775 (2000).

[69] E. Flück, N. F. van Hulst, W. L. Vos, and L. Kuipers, *Near-Field Optical Investigation of Three-Dimensional Photonic Crystals*, Phys. Rev. E (2003), submitted.

[70] R. Sprik, B. A. van Tiggelen, and A. Lagendijk, *Optical Emission in Periodic Dielectrics*, Europhys. Lett. **35**, 265 (1996).

[71] V. N. Bogomolov, S. V. Gaponenko, I. N. Germanenko, A. M. Kapitonov, E. P. Petrov, N. V. Gaponenko, A. V. Prokofiev, A. N. Ponyavina, N. I. Silvanovich, and S. M. Samoilovich, *Photonic Band Gap Phenomenon and Optical Properties of Artificial Opals*, Phys. Rev. E **55**, 7619 (1997).

[72] S. G. Romanov, A. V. Fokin, V. Alperovich, N. P. Johnson, and R. M. De La Rue, *The Effect of the Photonic Stop-Band Upon the Photoluminescence of CdS in Opal*, Phys. Status Solidi A **164**, 169 (1997).

[73] T. Yamasaki and T. Tsutsui, *Spontaneous Emission from Fluorescent Molecules Embedded in Photonic Crystals Consisting of Polystyrene Microspheres*, Appl. Phys. Lett. **72**, 1957 (1998).

[74] K. Yoshino, S. B. Lee, S. Tatsuhara, Y. Kawagishi, M. Ozaki, and A. A. Zakhidov, *Observation of Inhibited Spontaneous Emission and Stimulated Emission of Rhodamine 6G in Polymer Replica of Synthetic Opal*, Appl. Phys. Lett. **73**, 3506 (1998).

[75] A. Blanco, C. López, R. Mayoral, H. Míguez, F. Meseguer, A. Mifsud, and J. Herrero, *CdS Photoluminescence Inhibition by a Photonic Structure*, Appl. Phys. Lett. **73**, 1781 (1998).

[76] M. Megens, J. E. G. J. Wijnhoven, A. Lagendijk, and W. L. Vos, *Light Sources Inside Photonic Crystals*, J. Opt. Soc. Am. B **16**, 1403 (1999).

[77] S. Y. Lin, J. G. Fleming, E. Chow, J. Bur, K. K. Choi, and A. Goldberg, *Enhancement and Suppression of Thermal Emission by a Three-Dimensional Photonic Crystal*, Phys. Rev. B **62**, R2243 (2000).

[78] H. P. Schriemer, H. M. van Driel, A. F. Koenderink, and W. L. Vos, *Modified Spontaneous Emission Spectra of Laser Dye in Inverse Opal Photonic Crystals*, Phys. Rev. A **63**, 011801 (2001).

[79] J. Martorell and N. M. Lawandy, *Observation of Inhibited Spontaneous Emission in a Periodic Dielectric Structure*, Phys. Rev. Lett. **65**, 1877 (1990).

[80] E. P. Petrov, V. N. Bogomolov, I. I. Kalosha, and S. V. Gaponenko, *Modification of the Spontaneous Emission of Dye Molecules in Photonic Crystals*, Acta Phys. Pol. A **94**, 761 (1998).

[81] M. Megens, J. E. G. J. Wijnhoven, A. Lagendijk, and W. L. Vos, *Fluorescence Lifetimes and Linewidths of Dye in Photonic Crystals*, Phys. Rev. A **59**, 4727 (1999).

[82] M. Megens, H. P. Schriemer, A. Lagendijk, and W. L. Vos, *Comment on "Spontaneous Emission of Organic Molecules Embedded in a Photonic Crystal"*, Phys. Rev. Lett. **83**, 5401 (1999).

[83] C. Hooijer, D. Lenstra, and A. Lagendijk, *Mode Density Inside an Omnidirectional Reflector is Heavily Directional But Not Small*, Opt. Lett. **25**, 1666 (2000).

[84] Y. A. Vlasov, K. Luterova, I. Pelant, B. Hönerlage, and V. N. Astratov, *Enhancement of Optical Gain of Semiconductors Embedded in Three-Dimensional Photonic Crystals*, Appl. Phys. Lett. **71**, 1616 (1997).

[85] K. Yoshino, Y. Tatsuhara, S. ad Kawagishi, M. Ozaki, A. A. Zakhidov, and Z. V. Vardeny, *Amplified Spontaneous Emission and Lasing in Conducting Polymers and Fluorescent Dyes in Opals As Photonic Crystals*, Appl. Phys. Lett. **74**, 2590 (1999).

[86] S. V. Frolov, S. V. Vardeny, A. A. Zakhidov, and R. H. Baughman, *Laser-like Emission in Opal Photonic Crystals*, Opt. Comm. **162**, 241 (1999).

[87] G. van Soest, *Experiments on Random Lasers*, Ph.D. thesis, University of Amsterdam, 2001.

[88] W. L. Vos, M. Megens, C. M. van Kats, and P. Bösecke, *X-Ray Diffraction of Photonic Colloidal Single Crystals*, Langmuir **13**, 6004 (1997).

[89] M. Megens and W. L. Vos, *Particle Excursions in Colloidal Crystals*, Phys. Rev. Lett. **86**, 4855 (2001).

[90] F. J. P. Schuurmans, D. Vanmaekelbergh, J. van de Lagemaat, and A. Lagendijk, *Strongly Photonic Macroporous Gallium Phosphide Networks*, Science **284**, 141 (1999).

[91] F. J. P. Schuurmans, M. Megens, D. Vanmaekelbergh, and A. Lagendijk, *Light Scattering Near the Localization Transition in Macroporous GaP Networks*, Phys. Rev. Lett. **83**, 2183 (1999).

[92] P. M. Johnson, B. P. J. Bret, J. Gómez Rivas, J. Kelly, and A. Lagendijk, *Anisotropic Diffusion of Light in a Strongly Scattering Material*, Phys. Rev. Lett. **89**, 243901 (2002).

Chapter 2

Dispersion, Density of States and Refraction

We review the most widely used theoretical approach to calculate properties of three-dimensional periodic composites, known as the plane-wave method. This chapter aims at explaining how the results of the plane-wave method were calculated that are used to interpret experiments presented in subsequent chapters, and to develop the switching schemes discussed in Chapter 5. Several important optical properties of photonic crystals are discussed and illustrated by numerical examples, concerning optical dispersion and the relation between the density of states and spontaneous emission. Finally, we present the first calculations of dispersion surfaces of inverse opals, and discuss their use in solving diffraction problems.

2.1 Introduction

In two founding papers, published simultaneously in 1987, photonic crystals were put forward as ideal materials to realize complete inhibition of spontaneous emission [1] and Anderson localization of light [2–4]. At the heart of these ideas is the concept of a photonic band gap, *i.e.*, the absence of photon modes in a specific frequency window. The quantum electrodynamical implications of such a frequency window of zero density of states (DOS) have been discussed in a large body of theory [5–20], partly based on unphysical assumptions concerning the DOS chosen for analytic ease of use, rather than physical relevance. The relevance of original proposals has recently started to be reassessed [15, 17–20]. On the other hand many calculational efforts [21–27] after the original proposal were devoted to settle the debate whether it is possible for a periodic dielectric composite to have a photonic band gap at all [27]. To tackle this problem, plane-wave expansion methods [28, 29] from electronic band structure theory were extended to determine the eigenfrequencies and the density of states of Bloch modes in infinitely extended perfectly periodic photonic crystals. Photonic band structures are presently the most commonly used tool for the interpretation of experiments on photonic crystal structures. Nonetheless it is important to realize that band structures

only hold any meaning for infinite and perfectly periodic structures. Band structure calculations as such strictly do not apply to experiments, since real fabricated structures are finite and contain random deviations from perfect periodicity. Widespread use of the plane-wave method is based on the ease of calculation, and the well established correspondence of photonic band structures with reflection, transmission and diffraction experiments. Results from plane-wave calculations will be used profusely throughout this thesis to interpret diffraction and emission data in terms of the photonic dispersion and density of states. Therefore the method is discussed in this chapter.

Theoretical approaches to photonic crystals not based on plane-wave expansions appear more amenable to solve two important classes of problems, *i.e.*, scattering problems and defect problems. Scattering problems are concerned with reflection, transmission and diffraction of continuous or pulsed beams incident on *finite* photonic crystal blocks or slabs. For slab geometries transfer matrix methods are often employed [30], in which real space discretized, time harmonic Maxwell equations are solved slice by slice throughout a slab (which is still infinite in 2 out of 3 dimensions). This method appears easy to use even for thick photonic crystals, as the transfer matrix of a single crystal layer can be used to generate the transfer matrix of a thick ($\sim 2^N$ layers) structure in only $\sim N$ matrix multiplications. The main challenge is to maintain a correct energy balance as the number of layers is increased. This issue is also relevant for a different method designed to solve the same diffraction problems for infinitely extended slabs, the layer KKR method [31]. This method is limited to crystals built from non-overlapping spherical scatterers. Such a structure is generally not favorable for achieving a photonic band gap, and not applicable to strongly photonic crystals fabricated to date.

A separate class of methods is formed by finite difference time domain (FDTD) simulations, in which Maxwell's equations are discretized in real space and time [32, 33]. As this technique does not use crystal symmetry properties, the method appears versatile, but at the price of heavy computational burden. Calculations are therefore limited to small structures (order 10×10×10 unit cells) and limited time spans. FDTD calculations are often used to study 'defect problems'. Both point defects, which may serve as high Q cavities, and line defects, proposed to act as waveguides, are of interest. FDTD simulations are most suitable for transient problems. Simulations of stationary reflection and transmission are hampered by the long time scales needed to reach a stationary state. This problem is aggravated by the small group velocities of photonic Bloch modes. A unique niche of FDTD calculations is to shed light on how large truly finite photonic crystal clusters must be to exhibit a photonic band gap (locally). Surprisingly, clusters of a few lattice parameters in radius appear sufficient to provide over a hundredfold spontaneous emission inhibition relative to vacuum [34]. This important result shows that photonic band gap effects predicted by plane-wave calculations are experimentally feasible.

2.2 Bloch modes, dispersion and the plane-wave method

The plane-wave method is a direct adaptation of electronic band structure methods, and allows optimal account of the crystal lattice symmetry in determining the electromagnetic properties of a photonic crystal. We start from Maxwell's equations for an inhomogeneous dielectric medium without charges or currents [35]

$$\begin{aligned} \nabla \times \mathbf{E} &= -\frac{\partial \mathbf{B}}{\partial t}, & \nabla \cdot \mathbf{D} &= 0, \\ \nabla \times \mathbf{H} &= \frac{\partial \mathbf{D}}{\partial t}, & \nabla \cdot \mathbf{B} &= 0, \end{aligned} \tag{2.1}$$

together with the constitutive relations for a non-magnetic dielectric composite

$$\begin{aligned} \mathbf{D} &= \varepsilon_0 \varepsilon(\mathbf{r}) \mathbf{E}, \\ \mathbf{B} &= \mu_0 \mathbf{H}. \end{aligned} \tag{2.2}$$

It is well known that Eq. (2.1) can be combined with Eq. (2.2) into a wave equation for, *e.g.*, the electric field $\mathbf{E}$

$$\nabla \times (\nabla \times \mathbf{E}(\mathbf{r})) + [1 - \varepsilon(\mathbf{r})] \frac{\omega^2}{c^2} \mathbf{E}(\mathbf{r}) = \frac{\omega^2}{c^2} \mathbf{E}(\mathbf{r}), \tag{2.3}$$

assuming harmonic time dependence with frequency ω, and with c the speed of light in vacuum. Throughout this thesis, the dielectric constant ε is understood to be the square of the refractive index n at frequency ω. For photonic crystals the dielectric constant $\varepsilon(\mathbf{r})$ is by definition a periodic function, which is often piecewise constant for fabricated composites. We will discuss the adverse effect of the step discontinuities of $\varepsilon(\mathbf{r})$ on the convergence of the plane-wave method at the end of this section. The borrowing of electronic band structure methods to solve (2.3) is inspired by the similarity of this wave equation (2.3) with the time-independent Schrödinger equation for an electron in a periodic potential [36]. Indeed, the physics appears simpler for photons, as they do not interact with each other. However, several differences are readily apparent. Firstly, the vectorial nature of electromagnetic waves plays an important role. Secondly the 'potential' $-[1 - \varepsilon(\mathbf{r})]\omega^2/c^2$ in the E-field wave equation depends on the eigenvalue ω^2/c^2. Also, its sign indicates that the potential is nowhere 'attractive'; the modes are determined by the delicate interference of spatially oscillatory terms.

Since we assume the dielectric constituents to be nonmagnetic it is more advantageous to solve the H-field wave equation [28, 29]

$$\nabla \times \left(\frac{1}{\varepsilon(\mathbf{r})} \nabla \times \mathbf{H}(\mathbf{r}) \right) = \frac{\omega^2}{c^2} \mathbf{H}(\mathbf{r}). \tag{2.4}$$

The benefit of using the H-field wave equation solely rests on the fact that the operator

$$\nabla \times \frac{1}{\varepsilon(\mathbf{r})} \nabla \times \tag{2.5}$$

is hermitian[1]. As a result it is immediately clear that its eigenvalues ω^2/c^2 are real. Furthermore it follows that nondegenerate H-field eigenmodes are orthogonal and can be classified according to symmetry properties [37]. In addition, the hermitian nature of the H-field operator facilitates variational and perturbational calculations [38]. In contrast the electric field eigenvalue equation (2.3) is not a hermitian eigenvalue problem, causing inferior convergence of E-field plane-wave methods. This asymmetry between E-field and H-field methods disappears for more general problems where the magnetic permeability is also spatially dependent. A spatial dependence of the magnetic permeability is taken into account by generalizing Eq.(2.2) to $\mathbf{B} = \mu_0\mu(\mathbf{r})\mathbf{H}$.

Due to the periodicity of the dielectric constant $\varepsilon(\mathbf{r})$, Bloch's theorem is applicable to the eigenmodes of the eigenvalue problem Eq. (2.4) and asserts that eigenmodes can be decomposed as

$$\mathbf{H}_{n,\mathbf{k}}(\mathbf{r}) = e^{i\mathbf{k}\cdot\mathbf{r}}\mathbf{u}_{n,\mathbf{k}}(\mathbf{r}), \tag{2.6}$$

where $\mathbf{u}_{n,\mathbf{k}}(\mathbf{r})$ has the periodicity of the crystal lattice [36, 39, 40]. Such a Bloch mode is periodic up to a phase factor $e^{i\mathbf{k}\cdot\mathbf{r}}$. At the edge of the Brillouin zone the dispersion relation $\omega_n(\mathbf{k})$ folds back, and thus organizes into bands, labelled by n. All the modes can be uniquely labelled with a Bloch wave vector $\mathbf{k}$ within the first Brillouin zone, and the integer index n.

For explicit solution of Eq. (2.4) one expands both the known inverse dielectric constant, and the unknown Bloch-modes in a Fourier series over the reciprocal lattice vectors $\mathbf{G}$

$$\eta(\mathbf{r}) = \frac{1}{\varepsilon(\mathbf{r})} = \sum_{\mathbf{G}} \eta_{\mathbf{G}} e^{i\mathbf{G}\cdot\mathbf{r}} \quad \text{and} \quad \mathbf{H}_{n,\mathbf{k}}(\mathbf{r}) = \sum_{\mathbf{G}} \mathbf{u}_{\mathbf{G}}^{n,\mathbf{k}} e^{i(\mathbf{k}+\mathbf{G})\cdot\mathbf{r}}. \tag{2.7}$$

An infinite set of linear eigenvalue equations

$$\sum_{\mathbf{G}} \eta_{\mathbf{G}-\mathbf{G}'}(\mathbf{k}+\mathbf{G}') \times [(\mathbf{k}+\mathbf{G}) \times \mathbf{u}_{\mathbf{G}}^{n,\mathbf{k}}] = \frac{\omega_n(\mathbf{k})^2}{c^2}\mathbf{u}_{\mathbf{G}'}^{n,\mathbf{k}} \qquad \forall\, \mathbf{G}' \tag{2.8}$$

results from substitution of the Fourier series Eqs. (2.7,2.8) in the H-field wave equation. The linear eigenvalue problem is the starting point for numerical approximations to the photonic dispersion relation and electromagnetic eigenmodes, known as the H-field plane-wave method [27, 28]. For a numerical approximation to the eigenvalues $\omega_n(\mathbf{k})^2/c^2$ the infinite matrix problem is reduced to a finite system by truncating the set of reciprocal lattice vectors. As the resulting eigenmatrix is real and symmetric[2] the H-field formulation is particularly suited for standard diagonalization techniques and especially desirable if eigenvectors need to be calculated [41]. The matrix dimension of the problem may be further reduced by eliminating one vector component of the H-field, using $\nabla \cdot \mathbf{H} = 0$, as described in Ref. [29].

[1] Assuming the standard inner product $\langle \mathbf{f}|\mathbf{g}\rangle = \int \mathbf{f}(\mathbf{r}) \cdot \mathbf{g}(\mathbf{r}) \mathrm{d}^3\mathbf{r}$, where $\cdot$ denotes the standard complex vector inner product.

[2] The eigenmatrix is only real and symmetric if the origin of the unit cell is chosen at a point of inversion symmetry of $\varepsilon(\mathbf{r})$. For real $\varepsilon(\mathbf{r})$ the complex eigenmatrix is still hermitian.

Several problems of plane-wave methods have been described in a seminal paper by Sözüer and Haus [28]. It is well known that the plane-wave method converges only slowly with increasing number of reciprocal lattice vectors. For realistic photonic band gap structures discussed in Section 2.5, even ~ 1400 plane waves do not suffice for an accuracy of 10% for the lowest 10 eigenvalues. The origin of the slow convergence has been attributed to the step discontinuities of the dielectric constant $\varepsilon(\mathbf{r})$. Discontinuities in $\varepsilon(\mathbf{r})$ and in electromagnetic fields cause Gibbs oscillations in the truncated Fourier expansions. Physically this implies that many oscillatory terms need to be summed to establish the balanced effect of interference of many Bragg diffracted waves.

As first demonstrated by Ho, Chan and Soukoulis [27] the convergence of the H-field method is not optimal if the matrix of Fourier components $\eta_{\mathbf{G}-\mathbf{G}'}$ of the inverse dielectric constant is used in Eq. (2.8). The convergence may be drastically improved by using the inverse of the truncated matrix of Fourier components of $\varepsilon(\mathbf{r})$ ('inverted matrix method'). The actual calculation of $\eta_{\mathbf{G}}$ or $\varepsilon_{\mathbf{G}}$ for a two-component system presents the same computational burden. For a two-component system, the dielectric constant can be written as $\varepsilon(\mathbf{r}) = \varepsilon_1 + (\varepsilon_2 - \varepsilon_1) f(\mathbf{r})$, where the indicator function $f(\mathbf{r})$ is unity or zero, depending on whether $\mathbf{r}$ is inside a region of dielectric constant ε_1 or ε_2 respectively. The Fourier components are defined by

$$\begin{aligned} \varepsilon_{\mathbf{G}} &:= \frac{1}{V}\int_V \varepsilon(\mathbf{r}) e^{-i\mathbf{G}\cdot\mathbf{r}} \mathrm{d}^3\mathbf{r} \\ &= \varepsilon_1 \delta_{\mathbf{G},0} + (\varepsilon_2 - \varepsilon_1)\frac{1}{V}\int_V f(\mathbf{r}) e^{-i\mathbf{G}\cdot\mathbf{r}} \mathrm{d}^3\mathbf{r} \\ &= \varepsilon_1 \delta_{\mathbf{G},0} + \Delta\varepsilon f_{\mathbf{G}}. \end{aligned} \tag{2.9}$$

In this equation the integration runs over the volume V of the unit cell, and $\delta_{\mathbf{k},\mathbf{k}'}$ is the Kronecker delta. The Fourier components of $\eta(\mathbf{r})$ can be expressed in complete analogy as $\eta_{\mathbf{G}} = \eta_1 \delta_{\mathbf{G},0} + \Delta\eta f_{\mathbf{G}}$ (with $\eta_i = \varepsilon_i^{-1}$ and $\Delta\eta = \eta_2 - \eta_1$). The computation of $\eta_{\mathbf{G}}$ and $\varepsilon_{\mathbf{G}}$ involves exactly the same integration. For infinite expansions the matrix of Fourier coefficients $\eta_{\mathbf{G}-\mathbf{G}'}$ coincides with the coefficients of the inverse of the matrix $\varepsilon_{\mathbf{G}-\mathbf{G}'}$. For the truncated case, however, these matrices are different. A mathematical explanation of the numerical superiority of the inverted matrix method is presented in Ref. [42], based on the realization that the product $1/\varepsilon(\mathbf{r})\boldsymbol{\nabla} \times \mathbf{H}$ consists of terms with complementary jump discontinuities that cancel in the product.

The magnitudes of the coefficients $\varepsilon_{\mathbf{G}}$ relative to the geometrically averaged dielectric constant $\bar{\varepsilon} = \varepsilon_{000} = \varepsilon_1 + \Delta\varepsilon f_{000}$ represent the strength of the periodic 'potential' for light. From Equation (2.9) it can be inferred that Bloch waves are more strongly coupled by Bragg diffraction in a crystal with a specified geometry $f(\mathbf{r})$ if the ratio $\Delta\varepsilon/\bar{\varepsilon}$ of the fluctuating part $\Delta\varepsilon = \varepsilon_2 - \varepsilon_1$ to the geometrically averaged dielectric constant $\bar{\varepsilon}$ is larger. Indeed, many efforts are currently devoted to fabricate composites that provide a maximum difference in dielectric constant. Section 2.3 illustrates the role of $\Delta\varepsilon/\bar{\varepsilon}$ in achieving the fervently pursued photonic band gap.

In summary, all plane-wave calculations presented in this thesis have been performed using the H-field 'inverted matrix' method, further taking advantage of the

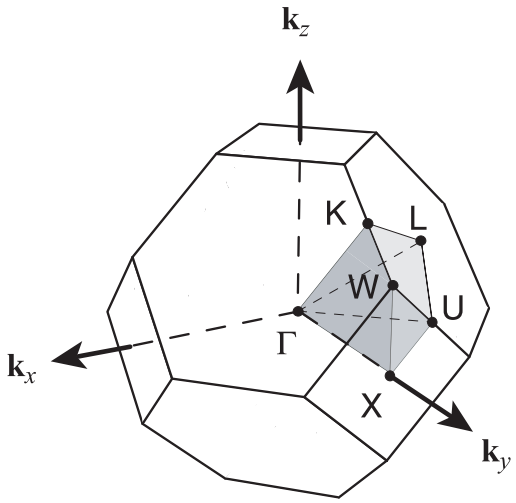

FIGURE 2.1: *The Brillouin zone of the* fcc *lattice is a truncated octahedron (also see page 175). Special symmetry points are traditionally labelled* Γ, L, X, U, K, W *corresponding to* $(0,0,0)$, $(\frac{1}{2},\frac{1}{2},\frac{1}{2})$, $(1,0,0)$, $(1,\frac{1}{4},\frac{1}{4})$, $(\frac{3}{4},\frac{3}{4},0)$, $(1,\frac{1}{2},0)$ *(and symmetry related) in units* $2\pi/a$. *The irreducible part of the Brillouin zone in which eigenfrequencies on a* $\mathbf{k}$*-point grid were determined for DOS calculations is the convex hull of the set of special points as shown.*

transversality of the H-field to reduce the dimension of the eigenvalue problem (2.8) from $3N_{\mathbf{G}}$ to $2N_{\mathbf{G}}$. The number $N_{\mathbf{G}}$ of reciprocal lattice vectors was typically 725 in order to obtain convergence of the lowest 10 eigenvalues to within 0.5%. The convergence of eigenvalues for a specific photonic crystal structure will be discussed in Section 2.5. Fourier components of $\varepsilon(\mathbf{r})$ were calculated using a three-dimensional adaptive Legendre-Gauss integration routine. The integration accuracy (better than 0.1% of ε_{000}) was tested for analytically solvable models for $\varepsilon(\mathbf{r})$ in which $f(\mathbf{r})$ was unity only on thin non-overlapping spherical shells. Matrix diagonalization was done using a standard QL algorithm after Householder reduction to tridiagonal form [43].

2.3 Photonic dispersion and photonic strength

Due to the discrete lattice symmetry, all Bloch modes can be labelled with a band index n and a momentum $\mathbf{k}$ restricted to the first Brillouin zone. All crystals investigated in this thesis have *fcc* symmetry. The Brillouin zone of the *fcc* crystal lattice is shown in Figure 2.1; points of special symmetry are labelled. The dispersion relation is usually only plotted on a piecewise linear trajectory through the special points on the Brillouin zone, as bands can be shown to attain their extrema along this trajectory [40]. Frequency ω is plotted in scaled units $\omega a/2\pi c$ which equals the ratio a/λ of lattice spacing a to vacuum wavelength λ. This scaling reflects the lack of fundamental length scale in Maxwell's equations. Indeed, a photonic band gap has already been

demonstrated in the microwave regime [44], and can occur in any wavelength range where a sufficient dielectric contrast can be generated. To demonstrate the concepts of stop gaps and band gaps, band structures for several types of *fcc* photonic crystals will be discussed, based on Figure 2.2.

Independently of the refractive index contrast or geometrical structure, the dispersion is linear in the long wavelength limit (small ω). In this regime, photonic crystals behave as homogeneous dielectric media[3] with effective dielectric constant equal to the volume-averaged dielectric constant $\bar{\varepsilon}$ [45]. With increasing frequency, the wave vector at some point crosses the boundary of the first Brillouin zone. For *fcc* crystals the wave vector first meets the Brillouin zone boundary at the L-point, associated with the 111 crystal planes. Bragg diffraction causes the dispersion relation to fold back into the Brillouin zone. At the L-point the dispersion relation splits; a frequency range known as *stop gap* occurs within which no k-vectors along Γ*L* are allowed. For higher frequencies stop gaps associated with different lattice planes occur. In general, splitting of the dispersion relation occurs whenever the wave vector crosses from the *n*th into the $(n+1)$th Brillouin zone [36]. These are the wave vectors for which two or more eigenfrequencies are degenerate for $\Delta\varepsilon = 0$. Nonzero periodic perturbation lifts these degeneracies, causing the bands to avoid each other and split. Bloch modes near the edge of a stop gap resemble standing waves, while modes resemble plane waves for frequencies well within a band. If a wave with frequency in a stop gap is launched onto a photonic crystal, it is Bragg reflected, due to constructive interference of reflections from subsequent lattice planes. Inside the crystal the amplitude of the wave is exponentially damped. However, caution should be exercised in identifying reflection bands with stop gaps in the dispersion relation. The reflectivity is not determined by the photonic dispersion relation alone, but also by symmetry properties of the Bloch modes (see Section 2.8).

The width of a stop gap is determined by the strength of the interaction between incident and Bragg reflected waves. For the lowest order stop gap only two reciprocal lattice vectors are involved, *i.e.*, $\mathbf{G} = 000$ and *hkl*. Here, *hkl* represent the Miller indices of the crystal planes with the largest separation d_{hkl}. For *fcc* crystals the 111 planes correspond to this lowest order diffraction, which occurs at a center frequency well approximated using Bragg's law (Eq. (1.1))

$$\omega_c = \frac{\pi}{n_{\text{eff}}\, d_{111}}. \tag{2.10}$$

The shift of the lowest order stop band to lower frequency with increasing effective refractive index $n_{\text{eff}} = \sqrt{\bar{\varepsilon}}$ is evident in Figure 2.2(a) and (b). In a two-band E-field model (a plane-wave model truncated to the two relevant G-vectors), the relative band width of the stop gap equals

$$\Psi = \frac{\Delta\omega}{\omega_c} = \left|\frac{\varepsilon_{\mathbf{G}_{hkl}}}{\varepsilon_{000}}\right| \approx \frac{|\Delta\varepsilon|}{\bar{\varepsilon}}|f_{\mathbf{G}_{hkl}}|. \tag{2.11}$$

[3] Noncubic photonic crystals may be uniaxial or biaxial in the long wavelength limit

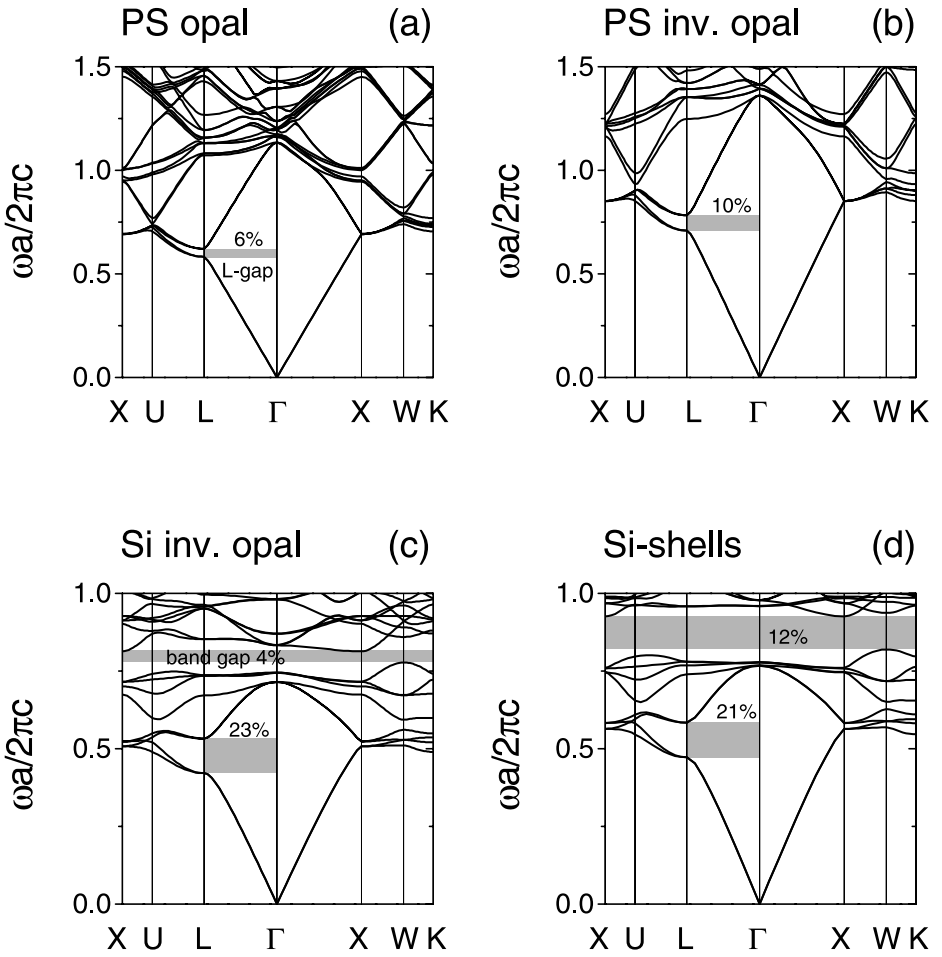

FIGURE 2.2: *The photonic dispersion relation organized into a band structure for* fcc *'opal' like structures, plotted along a Brillouin zone trajectory along special points (see Fig. 2.1). The lowest order stop gap (grey bars), or L-gap is associated with the* ΓL *direction and shifts to lower frequency with increasing* $\bar{\varepsilon}$*. The relative L-gap width is enhanced from* 6% *for synthetic polystyrene (PS) opal (a) (close-packed spheres (74 vol%) of refractive index* 1.59, $\bar{\varepsilon} = 2.13$*) to* 10% *by inverting the role of high and low dielectric material (*$\bar{\varepsilon} = 1.39$*, panel (b)). Increasing the refractive index contrast from* 1.59 *to* 3.45 *((c), corresponding to silicon) enlarges the L-gap to 23% and opens a photonic band gap of* 4% *relative bandwidth between bands 8 and 9. By making interstitial air pockets and cylindrical windows (d) connecting adjacent air spheres, the photonic band gap is enlarged to* 12% *relative bandwidth. We have used a model of closed packed air spheres (radius* $r = a/\sqrt{8}$*) surrounded by spherical shells (radius* $1.25r$*) connected by cylindrical windows (radius* $0.4r$*). The volume fraction of solid material is about* 20.7%*. Windows and interstitial voids occur in most fabricated inverse opal structures.*

The Fourier coefficient $f_{\mathbf{G}_{hkl}}$ is specific for the spatial distribution of high (ε_2) and low (ε_1) index material over the unit cell, but independent of the values ε_1 and ε_2 (see Eq. (2.9)). The relative stop band width Ψ is a convenient single parameter that is an experimentally accessible gauge of the photonic interaction strength between light and a photonic crystal. The photonic strength Ψ has a general interpretation as a polarizability per unit cell volume [46–48]. The polarizability provides a gauge for the interaction between light and any photonic structure. For periodic arrangements of, *e.g.*, atoms, a piecewise constant dielectric constant can not be defined, in contrast to the polarizability per unit cell. For instance, in the X-ray regime photonic stop gaps are very narrow-band ($\Psi \sim 10^{-4}$) due to the small polarizability of atoms at short wavelengths. If the atoms have a high polarizability, as is the case for frequencies near an atomic resonance, they can give rise to a wide stop gap in the dispersion relation [49].

For dielectric structures, the photonic strength can be increased in three ways according to Eq. (2.11): *(i)* increasing the difference in dielectric contrast $\Delta\varepsilon$, *(ii)* decreasing the volume-averaged dielectric contrast $\bar{\varepsilon}$, and *(iii)* optimizing the geometrical factor $f_{\mathbf{G}_{hkl}}$. These optimization mechanisms are demonstrated for the L-gap of *fcc* crystals in Figure 2.2. In Figure 2.2 band structures are presented for structures known as opals, and inverted opals. An opal is a structure consisting of *fcc* close-packed spheres in air. An inverted opal consists of close-packed air spheres in a solid backbone. Opals and inverse opals are among the most commonly studied three-dimensional photonic crystals [50].

The effect of changing the volume-averaged $\bar{\varepsilon}$ is illustrated by panels (a) and (b) in Figure 2.2. If a polystyrene synthetic opal is inverted by reversing the role of air and polystyrene, the volume-averaged dielectric contrast is reduced, but the index difference $\Delta\varepsilon$ and geometry $f_{\mathbf{G}_{111}}$ are the same. For the synthetic opal the L-gap width is about 6%. The inverted opal has an increased L-gap width of $\sim 10\%$, in proportion to the decrease of $\bar{\varepsilon}$. This result explains in part why strongly photonic crystals ($\Psi \gtrsim 0.10$) often mainly consist of air.

Comparison of Figure 2.2(b) and (c) reveals the influence of increasing the difference $\Delta\varepsilon$ on the photonic strength. By changing the polystyrene backbone of the inverted opal to silicon ($\varepsilon = 11.9$) the L-gap width is strongly increased to $\sim 23\%$ concomitant with the large increase of the difference in dielectric constants, which easily overcomes the small increase in $\bar{\varepsilon}$. However, indefinitely increasing the dielectric constant of one of the constituents does not provide a means to increase the photonic strength to arbitrary values. For large dielectric contrast, the increase in $\Delta\varepsilon$ is balanced by the increase in $\bar{\varepsilon}$. The photonic strength saturates at a value $\Psi_{\max} = f_{\mathbf{G}_{hkl}}/\varphi$, where φ is the volume fraction of high index material. As Fig. 2.3 shows, this limit is easily reached if high index material fills the majority of the unit cell. For inverted structures saturation of $\Delta\varepsilon/\bar{\varepsilon}$ does not occur for physically relevant refractive indices in the optical regime.

The role of the unit cell geometry is more subtle, and is best appreciated by considering the photonic band gaps in Figure 2.2(c) and (d). If the photonic strength

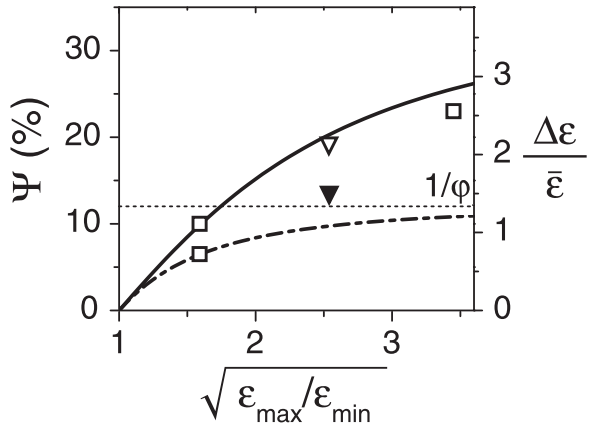

FIGURE 2.3: *Photonic strength versus index contrast* $\sqrt{\varepsilon_{max}/\varepsilon_{min}}$ *according to the two band model for opals (dashed line,* $\varphi = 74$ *vol% of material with high dielectric constant* ε_{max}*) and inverse opals (solid line). The right axis shows* $\Delta\varepsilon/\bar{\varepsilon}$*. The photonic strength saturates at* $f_{G_{111}}/\varphi$ *(horizontal dotted line) for opals, and* $f_{G_{111}}/(1-\varphi)$ *for inverse opals. The saturation value is not reached for physically relevant refractive indices (*≤ 4*) for inverse opals. Open squares indicate L-gap widths from Fig. 2.2. The solid triangle is the photonic strength of titania inverse opals studied in this thesis. Our fabricated crystals differ structurally from completely infiltrated titania inverted opal (open triangle at* $\sqrt{\varepsilon_{max}/\varepsilon_{min}} = 2.5$*).*

becomes very large, stop gaps become very wide. In such cases simultaneous diffractions by different sets of lattice planes (which occur at different center frequencies) may culminate in an omnidirectional stop gap. Such a *photonic band gap* is characterized as a frequency window in which no optical modes exist at all. Naively, this may be interpreted as the coalescing of stop gaps associated with different lattice planes as stop gaps get wider. It is important to realize, however, that simultaneous coupling of many diffractions with different $\mathbf{G}$ is at work [51]. A description as a cumulative effect of two-band models is not adequate. The band structure diagram of the silicon inverted opal in Figure 2.2(c) predicts a band gap at a frequency of around 0.77 with a relative frequency width of $\sim 4\%$. The unit cell geometry can be optimized to increase the frequency width of the photonic band gap. Compared to Fig. 2.2(c) the frequency width is strongly increased from 4% to $\sim$ 12% by connecting the air spheres in the silicon inverted opal with cylindrical windows, and creating interstitial voids where spheres are far apart (Fig. 2.2(d)). Such windows and voids are indeed observed in fabricated inverse opals [52–54].

Generally, for a given periodic geometrical arrangement of dielectric material, a photonic band gap may not appear for any refractive index contrast. For those geometries which allow a band gap, it only appears if the refractive index contrast surpasses a structure-dependent threshold. The most widely pursued crystal structures have either diamond or *fcc* symmetry. The diamond symmetry appears hard to fabricate, but promises to have a wide band gap between bands 2 and 3, for refrac-

tive contrasts above a threshold of $n = 2.0$ [55]. For crystals of spherical building blocks arranged on a *fcc* lattice the refractive index threshold is higher (2.8) and the band gap is predicted to occur only at a higher diffraction order, between bands 8 and 9 [29]. Many papers are devoted to optimizing the width of the photonic band gap at fixed dielectric contrast $\varepsilon_2/\varepsilon_1$ and crystal symmetry, by optimizing the spatial distribution of material over the unit cell. Figure 2.2(d) is but one example of the optimization of the different coefficients $f_{\mathbf{G}}$ to obtain optimum interplay of multiple Bragg diffractions [50, 56].

In this section we have demonstrated that photonic crystals can be made strongly photonic by increasing the contrast of the dielectric components, by minimizing the average dielectric constant, and by optimizing the unit cell geometry. The photonic strength Ψ can be used to classify the interaction strength of photonic crystals. As coupling of multiple Bragg diffractions becomes important for $\Psi \gtrsim 10\%$ (see Chapter 3), we will refer to crystals with $\Psi \geq 10\%$ as strongly photonic. Crystals with a photonic band gap usually have $\Psi \sim 20\%$. State-of-the art preparation techniques do not yet allow the level of control over geometrical details necessary to construct the optimized structures with the largest predicted photonic band gaps. In spite of recent reports [53, 54], it appears currently impossible to achieve the minimum necessary volume fraction of solid material $\sim$ 20% to obtain a photonic band gap in inverse opals. To date, measured volume fractions of solid material in inverted opals remain below $\sim$ 12% [57].

2.4 Spontaneous emission

It has long been realized that the spontaneous emission rate of an atom or molecule is not an immutable property of the atom or molecule alone, but also depends on the electromagnetic mode structure around the emitter [58]. An emitter can only radiatively decay from an excited state if a nonzero mode-density is available for the radiated photon. If an excited atom has a transition frequency in a photonic band gap, no modes are available for the photon it needs to radiate in order to decay. Hence, the atom will remain trapped in the excited state. One may expect that the spontaneous emission rate of an emitter is proportional to the density of states (DOS) $N(\omega)$, which counts the number of modes $N(\omega)\mathrm{d}\omega$ in the frequency window from ω to $\omega + \mathrm{d}\omega$. The DOS can be obtained from the eigenvalue problem Eq. (2.8) through:

$$N(\omega) = 2\omega \sum_{n,\mathbf{k}} \delta(\omega^2 - \omega_{n,\mathbf{k}}^2) \tag{2.12}$$

where the sum runs over all modes, *i.e.*, over all band indices n, and Bloch vectors $\mathbf{k}$ in the first Brillouin zone. Fermi's Golden Rule [59, 60] states that the fluorescence decay rate $\Gamma(\mathbf{r})$ for a dipole transition

$$\Gamma(\mathbf{r}) = \frac{2\pi}{\hbar^2} \sum_{|f\rangle} |\langle f|\hat{\mu}(\mathbf{r}) \cdot \hat{\mathbf{E}}(\mathbf{r})|i\rangle|^2 \delta(E_f - E_i) \tag{2.13}$$

of an initial atom-field state $|i\rangle$ with energy E_i is determined by summing over all available final atom-field states $|f\rangle$, with energy E_f such that energy is conserved. The transition rate

$$\Gamma(\mathbf{r}) = \frac{\pi\omega_{ab}}{3\hbar\varepsilon_0}|\langle a|\hat{\mu}|b\rangle|^2 N_{\mathrm{rad}}(\mathbf{r}, \mathbf{d}, \omega_{ab}) \tag{2.14}$$

factorizes in an 'atom part' and a position dependent 'field' part. The atom part consists of the transition dipole moment $\langle a|\hat{\mu}|b\rangle$, where $|a\rangle$, and $|b\rangle$ denote the excited, resp. ground state of the atom. The classical 'field' part is not the DOS $N(\omega)$, but a *local* radiative density of states N_{rad} that depends on the position $\mathbf{r}$, dipole orientation $\mathbf{d}$ and transition frequency ω_{ab} of the emitter. The relevance of the local radiative density of states (LDOS) for spontaneous emission in photonic systems, was first pointed out by Sprik, van Tiggelen and Lagendijk [61]. The local radiative density of states

$$N_{\mathrm{rad}}(\mathbf{r}, \mathbf{d}, \omega) = \frac{1}{\varepsilon(\mathbf{r})}\sum_{n,\mathbf{k}} 2\omega\delta(\omega^2 - \omega_{n,\mathbf{k}}^2)|\mathbf{d}\cdot\mathbf{\Lambda}_{n,\mathbf{k}}(\mathbf{r})|^2. \tag{2.15}$$

not only entails counting the eigenfrequencies $\omega_{n,\mathbf{k}}$, but also involves the complete set of electromagnetic mode functions $\mathbf{\Lambda}_{n,\mathbf{k}}(\mathbf{r})$. These are the orthonormal eigenfunctions of the symmetrized Maxwell wave equation

$$\varepsilon^{-1/2}\nabla\times\nabla\times\varepsilon^{-1/2}\mathbf{\Lambda} = \omega^2/c^2\mathbf{\Lambda}. \tag{2.16}$$

Electric and magnetic field eigenmodes $\mathbf{E}_{n,\mathbf{k}}$ and $\mathbf{H}_{n,\mathbf{k}}$ relate to $\mathbf{\Lambda}_{n,\mathbf{k}}$ according to

$$\sqrt{\varepsilon(\mathbf{r})}\mathbf{E}_{n,\mathbf{k}}(\mathbf{r}) = \mathbf{\Lambda}_{n,\mathbf{k}}(\mathbf{r}) \qquad \text{and} \qquad \mathbf{\Lambda}_{n,\mathbf{k}}(\mathbf{r}) = \frac{\nabla\times\mathbf{H}_{n,\mathbf{k}}(\mathbf{r})}{\sqrt{\varepsilon(\mathbf{r})}i\omega_{n,\mathbf{k}}}. \tag{2.17}$$

The eigenvectors of the H-field plane-wave method can be converted to $\mathbf{\Lambda}_{n,\mathbf{k}}$ using Eq. (2.6) and (2.17).

Intricacies of the local radiative density of states have been dealt with elsewhere; here we summarize some important points concerning spontaneous emission [62]. It is important to realize that the total density of states in Eq. (2.12) is *the unit cell average* of the local density of states $\varepsilon(\mathbf{r})N_{\mathrm{rad}}(\mathbf{r}, \mathbf{d}, \omega)$, (averaged over dipole orientation). Hence, a gap in the total DOS implies a gap in the LDOS, independent of the position of the emitter in the unit cell. Furthermore, the emission rate of an emitter in a photonic crystal may depend strongly on the position of the emitter in the unit cell. In the absence of a gap in the total DOS, there may still exist positions in the unit cell for which the local radiative density of states has a gap, indicating that spontaneous emission can be completely inhibited for carefully placed emitters.

Enhancement and reductions of spontaneous emission rates depending on position have been demonstrated for emitters near a metallic interface [63], near a dielectric interface [64, 65], and have been studied in the framework of cavity quantum-electrodynamics (QED) [66, 67]. In a cavity system like a confocal resonator, the spontaneous emission in a specific resonator mode can be strongly enhanced or inhibited, depending on the detuning of the cavity relative to the transition frequency.

In such a system the total reduction of spontaneous emission is limited by the total solid angle subtended by the cavity mirrors [66]. Pioneering calculations by Suzuki and Yu have demonstrated explicitly the strong position dependence of dipole emission rates in photonic crystals, both for frequencies in the range of the pseudogap of *fcc* crystals, and near the photonic band gap [41]. These calculation were confirmed by several later studies [19, 29].

The (local) DOS and the concept of a photonic band gap have a much wider relevance than for spontaneous emission alone. For instance, point defects inside a photonic band gap have been theoretically demonstrated to act as microcavities with ultrasmall mode volume (λ^3) and extremely high Q [1, 68]. Photonic band gaps may therefore allow solid state cavity QED experiments in the strong coupling limit. In this limit, the Rabi oscillation frequency is much larger than the atom decay rate, which in turn should exceed the cavity decay rate [67]. Such microcavities may also allow for applications such as highly efficient miniature light sources. The density of states is also relevant in determining the spectrum of black body radiation, and modifies interactions mediated by vacuum fluctuations such as van der Waals and Casimir forces [67].

2.5 Calculation of the DOS

To determine the total density of states one needs to sum over all modes, *i.e.*, sum over all bands n and integrate over all $\mathbf{k}$ in the first Brillouin zone. We have constructed numerical approximations by calculating histograms of eigenfrequencies calculated on an equidistant $\mathbf{k}$-vector grid using the H-field inverted matrix method. The grid can be limited to the irreducible part of the Brillouin zone, *i.e.*, the convex hull of the set of special points Γ, X, U, L, K, W indicated in Figure 2.1. Care should be taken to use a grid which avoids degenerate points in the Brillouin zone and to correct for double-counting when extending the integral over the irreducible part to the full Brillouin zone [69]. We have used a cubic grid with equal grid point spacing in all three dimensions, set as an integer fraction of the ΓX length, and with basepoint shifted from Γ by half a grid point spacing in all three directions.

The frequency resolution $\Delta\omega$ of a histogram of the density of states, is limited by the resolution Δk of the grid in $\mathbf{k}$ space to be

$$\Delta\omega \propto \Delta k |\nabla_{\mathbf{k}}\omega|, \tag{2.18}$$

as detailed in Ref. [70] for calculations of the electronic DOS. In essence, this criterion relates the separation between adjoining $\mathbf{k}$-grid points to their approximate frequency spacing. If histogram bins are chosen too narrow compared to (2.18) unphysical spikes appear in the approximation, especially in the limit of small ω, where the group velocity $|\nabla_{\mathbf{k}}\omega|$ is usually largest. To improve the resolution without adding time-consuming diagonalizations, several interpolation schemes have been suggested [70]. For calculations presented in this thesis, eigenfrequencies were linearly interpolated before histogramming, starting from a grid of 2480 points in the

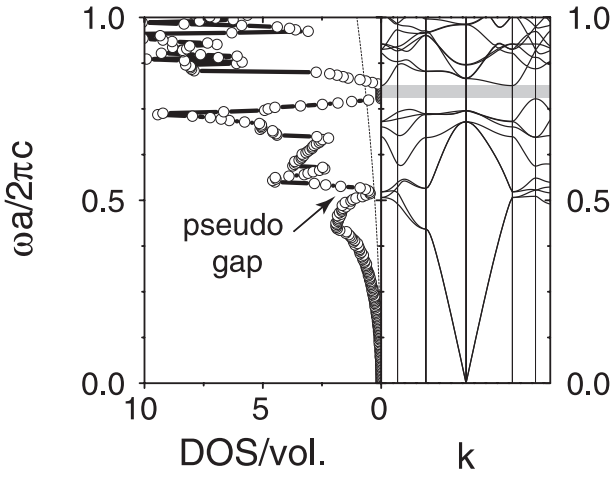

FIGURE 2.4: *Left panel: density of states per volume in units* $\omega_a^2/(\pi^2 c^3)$ *for an inverse opal of silicon* ($\varepsilon = 11.9$)*. On this scale the vacuum DOS is a parabola passing through the points* $(0,0)$ *and* $(1,1)$*, as indicated by the dotted line. Close to the L-gap the DOS is strongly depleted in a frequency range known as the pseudogap . A real band gap (grey bar) occurs between bands 8 and 9, as also evident in the band structure (right hand panel).*

irreducible part of the Brillouin zone, to a grid with doubled resolution. An increased number of grid points does not significantly affect the densities of states reported in this thesis, within the frequency resolution indicated by the frequency spacing in the graphs. A good benchmark of the accuracy of the **k**-space integration for the DOS, independent of the convergence of the plane-wave method, is to calculate the DOS of an 'empty' crystal, with uniform dielectric constant equal to unity. The 'empty' crystal presents the maximum possible $|\nabla_{\mathbf{k}}\omega|$.

As an example, the density of states for an inverse opal of close-packed air spheres in silicon $\varepsilon = 11.9$ is shown in Figure 2.4. In the long wavelength limit, the DOS exhibits the quadratic frequency dependence also encountered for homogeneous dielectrics. For a homogeneous medium of refractive index n, *i.e.*, an 'empty' crystal, the DOS per unit volume equals $\omega^2 n^3/(\pi^2 c^3)$ (with units $[\mathrm{s/m^3}]$), which may be rewritten in terms of normalized frequency $\hat{\omega} = \omega/\omega_a = \omega a/2\pi c$ as $n^3\hat{\omega}^2 \cdot [\omega_a^2/(\pi^2 c^3)]$. It is convenient to specify the DOS per unit volume in units $\omega_a^2/(\pi^2 c^3)$, as used in this thesis. In Figure 2.4 we observe that the DOS of a silicon inverted opal is strongly reduced for frequencies near the L-gap, in a frequency interval known as the 'pseudogap'. Strong deviations compared to the parabolic frequency dependence, including both enhancements and reductions occur with increasing frequency. The photonic band gap is the range of zero density of states between bands 8 and 9.

Figure 2.5 demonstrates the convergence of the Bloch mode eigenfrequencies, and of the density of states. In Fig. 2.5(a), results are shown for the eigenfrequencies of the silicon inverse opal to which Fig. 2.4 corresponds. We have calculated the low-

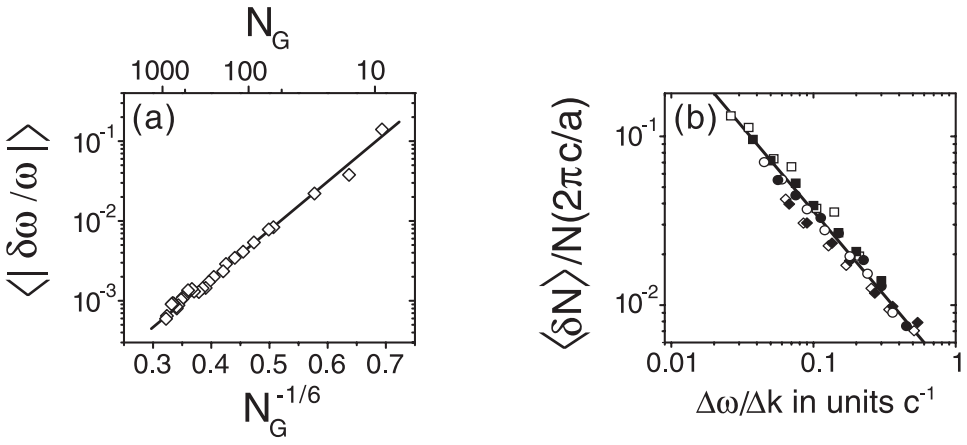

FIGURE 2.5: *(a) Average relative deviation of the lowest 10 eigenvalues for the structure corresponding to Fig. 2.4 as a function of* $N_G^{-1/6}$. N_G *is the number of plane waves (top axis). Deviations were taken relative to the eigenvalues for* $N_G = 1459$. *These results were obtained by averaging over the L and X point. (b) Average absolute deviation from the exact DOS* $N(\omega)$ *over the frequency range* $0 < \omega < 2\pi c/a$ *for an 'empty' crystal, normalized to* $N(\omega)$ *at* $\omega a/2\pi c = 1$. *In accordance with Eq. (2.18), the error is inversely proportional to the* ratio $\Delta\omega/\Delta k$ *of the histogram bin width* $\Delta\omega$, *to the integration grid spacing* Δk. *Symbols correspond to integration using 280, 770, 1300, 2480, 2992 resp. 3570 (□, ■, ○, ●, ◊, ♦) k-points, with various* $\Delta\omega$.

est ten eigenfrequencies at the L and X point for different numbers of plane waves, ranging from $N_G = 9$ to 1459. It appears that the logarithm of the average relative deviation of the eigenfrequencies compared to the eigenfrequencies for $N_G = 1459$ decreases linearly as a function of $N_G^{-1/6}$. Results converged to within 0.5% are obtained for $N_G = 725$. One can not conclude that the scaling $|\log \delta\omega/\omega| \propto N_G^{-1/6}$ holds for the convergence to the exact eigenfrequencies ($N_G = \infty$). To obtain the true convergence behavior, one should compare to the exact, or to accurately extrapolated eigenfrequencies. In general, the rate of convergence depends on the crystal structure and is adversely affected by increasing the refractive index contrast.

In Fig. 2.5(b), the error in the calculated DOS for a vacuum 'empty' crystal is shown, averaged over the frequency range $0 < \omega a/2\pi c < 1$. As predicted by Eq. (2.18), the deviation of the approximation from the analytic result is inversely proportional to the ratio $\Delta\omega/\Delta k$. In most cases, one would want to calculate the DOS with a given frequency resolution $\Delta\omega$ to within a predetermined accuracy. The vacuum DOS, for instance, can be obtained with a frequency resolution $0.01(2\pi c/a)$ to within better than 1% using $\Delta k \sim \Delta\omega/0.3c$. Taking into account the grid doubling technique, this corresponds to 2480 k-points in the irreducible wedge of the Brillouin zone. Photonic crystals with nonzero index contrast cause a pronounced frequency structure of the DOS (see Fig. 2.4). In such cases, the k-space integration should still be as accurate [4],

[4] Each dispersion band is a continuous function of $\mathbf{k}$ (see [36]).

assuming that the eigenfrequencies are known with infinite accuracy. In practice, one needs to adjust the number of plane waves to obtain all eigenfrequencies to within the desired frequency resolution $\Delta\omega$.

2.6 Transmission, reflection and refraction

In an experimental situation one can not realize an infinite photonic crystal. Properties of the photonic dispersion relation can therefore only be studied on truncated blocks of crystal. Available probes are limited to reflection and transmission of externally incident light, or using internally generated emission detected outside the sample. The result of such experiments can only be interpreted if the effect of the boundary between the crystal and the background medium is taken into account. A rigorous evaluation of reflection and transmission coefficients necessitates matching of E-field and H-field boundary conditions at the interface. To this end all the electromagnetic mode functions at the relevant frequency should be known, including mode functions of non-propagating modes with imaginary **k**-vector components. Therefore, the calculation of reflection and transmission properties, which can even depend on the precise termination plane delimiting the crystal, remains a demanding task [71]. Considerable insight may be gained from just the first step in such a computation, which consists of determining which propagating modes participate in a diffraction problem according to momentum conservation laws. Such an analysis is based on the consideration of dispersion surfaces of the infinite crystal. Dispersion surfaces allow to map out the relation between internal and external wave vectors of propagating modes at a given frequency [72].

The dispersion surface $S_{n,\omega}$ for frequency ω and band n is defined as the locus of **k** vectors for which the eigenfrequency in band n equals ω [72]. These constant frequency surfaces in 3D wave vector space may be compared with the Fermi-surface for an electron [36] and can be calculated without determining the mode functions. The dispersion surfaces for free photons in a homogeneous dielectric are two coincident spheres, one per polarization, of radius $\omega\sqrt{\varepsilon}/c$. In the repeated zone scheme [36], the dispersion surface of such a crystal (with zero index contrast) is a collection of spheres of equal radius centered at the lattice points of the reciprocal lattice. As the frequency is increased, intersections between different spheres occur. The intersections occur on the boundaries between successive Brillouin zones and indicate that a Bragg condition is met. For nonzero periodic modulation of the dielectric constant, distortions of the free photon spheres occur at the intersections, *i.e.*, near the Brillouin zone boundaries. A two-dimensional scalar example for a square lattice in Figure 2.6(a) shows how the circular dispersion surface (dashed line) is perturbed near the Brillouin zone boundary. Two bands with a large splitting evolve from the two free-photon intersections. For Fermi-surfaces this perturbational approach is known as Harrison's construction [73]. In analogy with the two-dimensional sketch in Figure 2.6(a), the three-dimensional dispersion surface for a frequency within the first order stop gap will be close to a sphere, with necks forming where the surface comes

close to touching the Brillouin zone boundary. The surface is pulled towards the Brillouin zone boundary, and can not touch the boundary, except for intersections at right angles. For strongly photonic crystals, the dispersion relation strongly deviates from the nearly free photon case, and can not be constructed anymore by perturbing the periodic free photon dispersion relation, especially when multiple intersections between different spheres come close.

The use of dispersion surfaces in diffraction problems when going from medium 1 (homogeneous) to medium 2 (photonic crystal) is based on three observations [72, 74, 75]. Firstly, at a given frequency ω the only allowed $\mathbf{k}$-vectors in medium i are on dispersion surfaces $S^{(i)}_{n,\omega}$ (by definition), where several bands n can be involved. Secondly, discrete translational symmetry along the crystal surface[5] imposes parallel momentum conservation up to a reciprocal lattice vector, *i.e.*, $\mathbf{k}_{1\|} = (\mathbf{k}_2 + \mathbf{G})_\|$ for some reciprocal lattice vector $\mathbf{G}$. Equivalently, one may use $\mathbf{k}_{1\|} = \mathbf{k}_{2\|}$ if the dispersion surfaces are considered in a repeated zone scheme. The third observation is based on causality, and requires that all waves apart from the incident wave carry energy away from the interface, *i.e.*, that the outgoing modes have time-averaged Poynting vector directed away from the interface. For a given Bloch mode, the vector components of the time averaged Poynting vector oscillate as a function of position in the unit cell [76]. One should therefore consider the unit-cell averaged Poynting vector. A convenient property of Bloch modes is that the unit-cell and time averaged Poynting vector is parallel to the group velocity $\mathbf{v}_g = \nabla_\mathbf{k}\omega(\mathbf{k})$. The proof in Ref. [74] involves the same perturbational approach used in solid state electron theory to relate the velocity of a Bloch electron to the gradient of its iso-energy surface [36]. The causality requirement therefore reduces to the condition that all waves apart from the incident wave have group velocity pointing away from the interface. To demonstrate the three steps outlined above, a diffraction problem is considered in Fig. 2.6(b) for a hypothetical two-dimensional photonic crystal at a frequency just above the lowest order stop gap and disregarding polarization. In Fig. 2.6(b) we have extended Harrison's construction in Fig. 2.6(a) to all relevant cubic reciprocal lattice vectors. The lowest band is limited to small lobes at the corners of the square Brillouin zone, and folding of the dispersion relation has resulted in a second band, with a group velocity pointing backwards relative to the wave vector ($\mathbf{k}\cdot\mathbf{v}_g < 0$). A negative sign of $\mathbf{k}\cdot\mathbf{v}_g$ does not forbid coupling from the homogeneous medium 1 into the crystal, as long as the group velocity points into the crystal. In Fig. 2.6(b) a specific incident wave vector $\mathbf{k}_{1,\mathrm{in}}$ is considered. Matching of parallel momentum, and selecting waves with group velocity pointing away from the photonic crystal interface, shows that in this case two Bloch waves can be excited. One excited Bloch mode has wave vector refracted towards the normal and $\mathbf{k}'_2\cdot\mathbf{v}'_g > 0$ in the lowest band, and one has wave vector in the higher band, is refracted away from the normal and has $\mathbf{k}''_2\cdot\mathbf{v}''_g < 0$. Small variations in the parallel component of the incident wave vector towards the edge of the Brillouin zone, cause the group velocity of the excited Bloch mode $\mathbf{k}''_2$ to sweep all the way from parallel to perpendicular to the crystal interface. Such a sensitive dependence of the internal

[5] The crystal is assumed to be cleaved along some crystal plane.

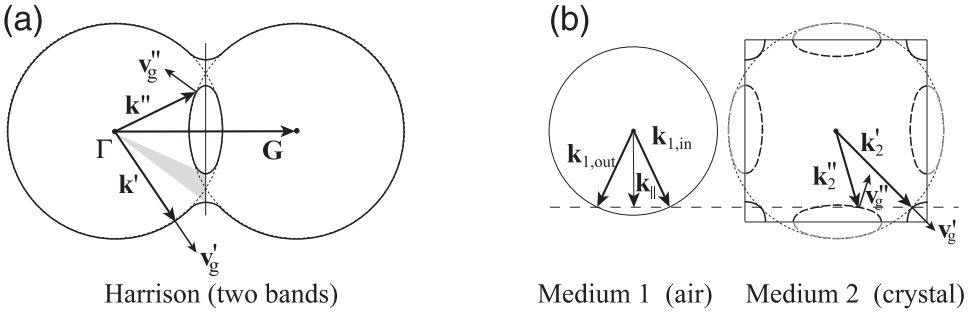

FIGURE 2.6: *(a). Sketch of the dispersion surface construction in the nearly free photon approximation. Free photon dispersion surfaces (spheres) are drawn in the repeated zone scheme (centered at the reciprocal lattice points; only shown here for two lattice points). At intersection points the dispersion splits, yielding two bands and a stop gap. The stop gap (grey) is a set of angles for which no* **k***-vectors are available. (b). Refraction construction, assuming a wave (wave vector* $\mathbf{k}_{1,in}$*) from air (medium 1) incident on a crystal with dispersion as constructed on the left. Intersection points with the dashed line, representing* $\mathbf{k}_\parallel$ *conservation, yield two internal wave vectors* $\mathbf{k}_2'$ *and* $\mathbf{k}_2''$ *with group velocity* $\mathbf{v}_g'$ *resp.* $\mathbf{v}_g''$ *pointing into the sample, and one reflected wave* $\mathbf{k}_{1,out}$*.*

propagation angle θ_g of the energy flow on the choice of frequency or wave vector has been coined the superprism phenomenon, and was first experimentally demonstrated in 2D photonic crystals by Kosaka *et al.* [77]. More generally, an incident wave from an external beam can excite many Bloch waves. Furthermore, the excited internal modes can correspond to negative refraction of waves, *i.e.*, with θ_g opposite in sign to the incident angle (see Fig. 2.6). In such a situation, both $\mathbf{k} \cdot \mathbf{v}_g > 0$ and $\mathbf{k} \cdot \mathbf{v}_g < 0$ may occur. The latter case is defined as left-handed behavior, since **E**, **H** and **k** now form a left-handed set. Left-handed materials (with effective ε and μ both negative) have recently attracted a lot of attention, and have been proposed as building blocks to make a perfect lens [78]. Unfortunately, the strong angular dependence of the dispersion in photonic crystals hampers their use as superlenses, which require isotropic dispersion. For frequencies near a photonic band gap edge, typically only one band is relevant. For two-dimensional crystals, the dispersion surface in this band can be close to circular and concentric with the origin, thus allowing an in-plane superlens. Three-dimensional photonic band gaps, however, are usually limited at the L and X point (diamond structures) or X and W point (*fcc* inverse opals). For a frequency just above the photonic band gap of a silicon inverse opal for instance (see Fig. 2.2(b)), the only allowed modes are confined to ellipsoidal dispersion surfaces concentric with the X-point, and belonging to band 9. Although this results in interesting phenomena, such as large directionality of light exiting such a crystal, isotropic left-handed behavior does not occur. In a recent paper [79] a simple cubic photonic crystal without a photonic band gap was predicted to allow nearly isotropic left-handedness in three dimensions.

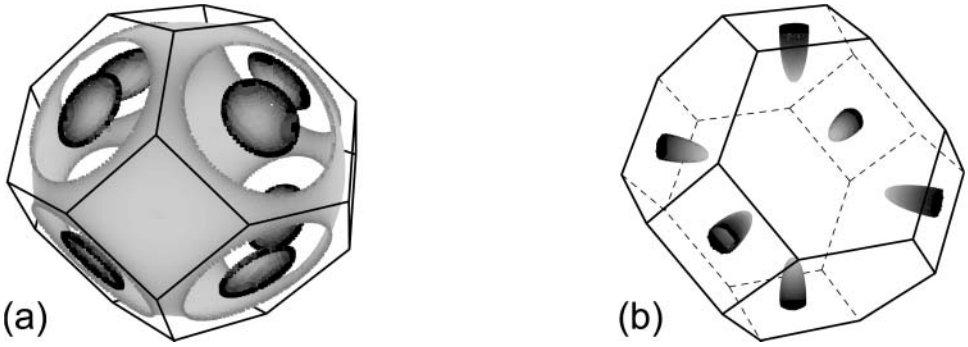

FIGURE 2.7: *(a) Dispersion surface at a normalized frequency $\omega a/2\pi c = 0.776$ for a titania inverse opal, as relevant for the experiments in this thesis. For this frequency just above the blue edge of the L-gap, the dispersion surface resembles a sphere (bands 1 (light gray), and 2 (not shown)), with large empty patches close to the Brillouin zone surface. Band 3 (dark gray) and 4 (not shown) penetrate in lobes centered at the L-points, and grow inwards with increasing frequency. (b) Just above the photonic band gap of a silicon inverse opal ($\omega a/2\pi c = 0.819$, band structure Fig. 2.4), the only allowed modes reside on ellipsoid dispersion surfaces, located close to the X-points. Darkening of the colors within a band indicates a larger distance to the Γ-point.*

2.7 Dispersion surfaces

Several studies have focused on refraction problems, superprismatic phenomena, negative refraction and dispersion surfaces for two dimensional photonic crystals in two spatial dimensions [75, 77]. Still, no calculations for three-dimensional systems have been published, apart from a pioneering paper by Ward, Pendry and Stewart [80]. Their approach is based on the transfer matrix method, in which allowed $\mathbf{k}_\perp$ at fixed ω and given $\mathbf{k}_\parallel$ are calculated. Such a method is cumbersome if dispersion surfaces for many frequencies are needed, and if group velocities need to be calculated. Dispersion surfaces can also be determined by the plane-wave method, either by using a targeted eigensolver for the matrix problem Eq. (2.8) [81], or by simply building a database of eigenfrequencies on a dense grid in $\mathbf{k}$-space. We have used the latter approach, building on the equidistant $\mathbf{k}$-grid used to calculate the DOS, augmented with planar grids covering the facets of the Brillouin zone. For sufficiently small grid spacings, a linear approximation to the dispersion in between grid points is accurate, and allows to determine $\mathbf{k}$-points with a given target frequency within a specific band. The group velocity vector field on the dispersion surface can be approximated by differences using the eigenfrequencies on the same wave vector grid, *i.e.*, without calculating the mode functions. As an example, the dispersion surfaces of bands 1 and 3 for a strongly photonic inverse opal of titania ($\varepsilon = 6.5$) relevant for the experiments reported in this thesis are shown in Fig. 2.7(a), for a frequency just above the L-gap. At this frequency the dispersion surface can still be interpreted in terms of the free photon dispersion relation, although the large rings of forbidden wave vectors

indicate a large photonic strength. The rings cover up to 55% of all solid angle, for a frequency at the blue edge of the L-gap. For somewhat higher frequency band 1 grows closer to the X-points. As the forbidden rings approach each other, a regime of strongly coupled Bragg diffraction sets in, and the nearly free photon picture breaks down. As an extraordinary example the case of a frequency just above the photonic band gap edge of an inverse opal with $\varepsilon = 11.9$ is considered in Fig. 2.7(b). Characteristically, the dispersion surfaces are limited to small pockets near the X-point, which shrink and ultimately disappear as the photonic band gap is approached.

2.8 Refraction problem in three dimensions

The refraction construction using dispersion surfaces does not give quantitative reflection and transmission coefficients of a photonic crystal. Conclusions based on the wave vector matching construction must always be scrutinized with extreme care, as illustrated by the basic example of a crystal with zero index modulation. Following Harrison's construction and solving the refraction problem, one can find conditions for which many Bloch waves can be excited simultaneously. Spurious predictions of many diffracted beams result, that can only hold for nonzero index modulation. However, one needs to invoke an amplitude argument, beyond the scope of the refraction construction, to conclude that the Bragg diffracted waves vanish for zero index contrast. Conversely, one should bear in mind that unit reflectivity does not imply the absence of modes with matching $\mathbf{k}$-vector. Coupling can also be forbidden by specific (symmetry) properties of the associated mode functions [82]. As a prime example, one may consider the case of omnidirectional reflectivity. Although the total absence of propagating modes in a material with a photonic band gap results in omnidirectional reflectivity, an omnidirectional reflector [83] does not need to have a gap in the density of states [84] at all, and can even consist of a simple dielectric multilayer stack. Still, dispersion surfaces have already proven to be useful in understanding, *e.g.*, superprismatic diffraction phenomena in two-dimensional structures. Here we discuss the solution to a different problem. We study which external plane waves can be excited by a source inside the photonic crystal, assuming that the internal source emits into all Bloch modes at the frequency of the source. This question is obviously relevant for luminescence experiments that use light sources embedded inside photonic crystals (see Chapters 3 and 4). Furthermore, inevitable weak disorder present in real structures provides a random multiple scattering mechanism that generates diffuse light which probes all internal modes (Chapters 6 and 7). To set up the calculation, one needs to (*i*) construct the dispersion surfaces in the repeated zone scheme, (*ii*) discard all Bloch modes with $\mathbf{k}_{\parallel} > \omega/c$ (assuming an external medium with $\varepsilon = 1$), and (*iii*) retain only those modes with group velocity $\mathbf{v}_g$ pointing towards the crystal-air interface. Figure 2.8(a) shows the locus of wave vectors of Bloch modes that couple to air, for a frequency $\omega a/2\pi c = 0.80$ in the pseudogap of a titania inverse opal ($\varepsilon = 6.5$). We have assumed that the outward crystal normal points upward, parallel to the 111 reciprocal lattice vector, as is the case in our experiments. As bands

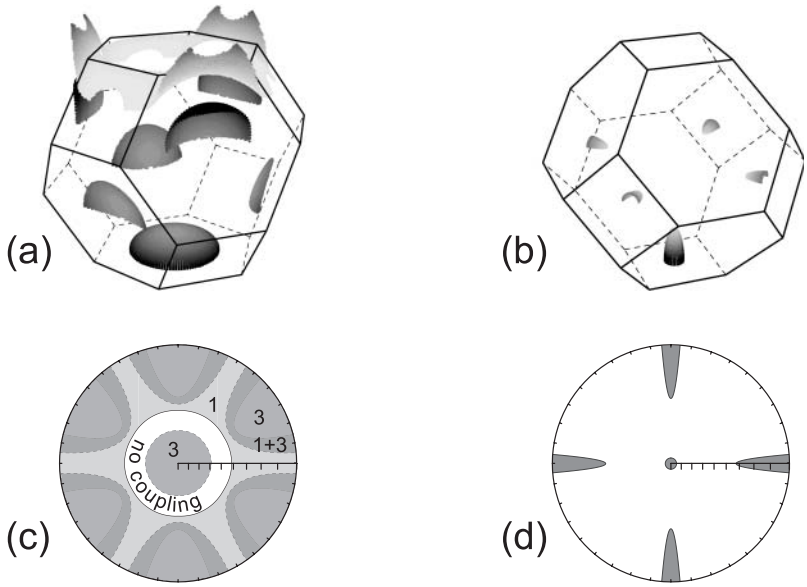

FIGURE 2.8: *Maps of those internal wave vectors that can couple from the crystal into air in the repeated zone scheme, for a 111-cleaved TiO_2 inverse opal (a) at a frequency* 0.80 *above the L-gap, and for a 100 cleaved Si* ($\varepsilon = 11.9$) *inverse opal (b) at a frequency* 0.819 *above the band gap, with color coding of the bands as in Fig. 2.7. Stereographic plots (c) and (d) show which external propagation angles may couple to which dispersion band. For the TiO_2 inverse opal (c) a ring shaped stop band occurs, inside of which coupling to band 3 is allowed, and outside of which coupling to band 1, band 3 or both simultaneously is allowed (as indicated). Just above the band gap of the Si inverse opal (d), all light inside the crystal must couple out along well defined beams.*

1 and 2, resp. 3 and 4 are nearly polarization degenerate, only bands 1 and 3 are indicated. The stereographic plot in Figure 2.8(c) shows which *external* propagation angles couple to which band. Concentric with the normal direction, a ring occurs to which no internal Bloch modes couple. This ring corresponds to the stop gap in the dispersion surface (Fig. 2.7). The large difference between inner and outer radius ($\sim 30°$ resp. $50°$) is indicative of a large photonic interaction strength. The ring of internal reflection encloses a range of angles for which only coupling to band 3 and 4 is allowed, with $\mathbf{k}_\perp$ antiparallel to $\mathbf{v}_{g,\perp}$. Outside the internal reflection ring, coupling to bands 1 and 2 is allowed, except for 6 (nearly) parabolically shaped lobes associated with X-gaps. Within, and partly also outside these lobes, coupling of 6 different band 3 and 4 pockets to air is allowed. One can not conclude that transmission is enhanced in the angular ranges in which coupling to all four bands is allowed without a complete calculation of (internal) reflection and transmission coefficients. The inner and outer radius of the ring in Figure 2.8(c) to which no Bloch modes couple, increase with increasing frequencies. At low frequencies within the L-gap, the ring is replaced by a disk of internal reflection angles (*i.e.* inner radius equal to zero). For larger

frequencies the inner and outer boundaries are increasingly noncircular (though 6-fold symmetric), due to coupling of multiple diffractions from different sets of lattice planes.

This complicated geometrical construction clearly shows how very wide internal reflection bands in emission spectra or diffusely transmitted light may come about. For a frequency just above the photonic band gap of an inverse opal with $\varepsilon = 11.9$ (see also Fig. 2.7), the light inside the photonic crystal can only exit into a few well defined directions. For a 100 cleaved crystal for instance (see Figure 2.8(b) and (d)), light would exit in a narrow beam along the crystal normal, with an angular spread proportional to the square root of the detuning from the band gap edge. The four beams at close to grazing exit angles do not appear within a small frequency window just above the band gap edge. For these frequencies all light inside the sample, be it from internal sources or multiply scattered from an external beam, can only exit along a single narrow, directional beam.

2.9 Conclusions

We have reviewed the theoretical framework that is most commonly used to describe the optical properties of photonic crystals. On the one hand, we have discussed basic concepts and methods that are well known in the literature. These include the formulation of the plane-wave method, the description of photonic dispersion in terms of a band structure, and the concept of photonic density of states. On the other hand, we have presented several new aspects of these concepts. For instance, we have included a quantitative discussion of the convergence of the plane-wave method and of the density of states calculation. It is unfortunate that many authors do not quote figures of merit for the accuracy of their results. Such reports are particularly sparse for DOS calculations. For the density of states, accurate results are of particular importance to assess the veracity of apparent narrow frequency features. We have demonstrated how to quantify the frequency resolution and accuracy of the calculated DOS.

Another novel addition to the theory of 3D photonic crystals that we have presented, is the quantitative study of dispersion surfaces. Sofar, most literature has been concerned with band structure diagrams, firstly as a tool to find band gaps, and secondly to interpret optical experiments. For the latter purpose, band structure diagrams are insufficient. Instead, one needs to calculate photonic dispersion surfaces to interpret refraction and diffraction in photonic crystals. Due to the complicated dispersion, even the incoupling, dispersion and propagation of control beams in optical experiments at frequencies near the photonic band gap will be nontrivial to control. Dispersion surfaces may prove crucial to interpret and design such experiments on photonic crystals.

References

[1] E. Yablonovitch, *Inhibited Spontaneous Emission in Solid-State Physics and Electronics*, Phys. Rev. Lett. **58**, 2059 (1987).

[2] P. W. Anderson, *Absence of Diffusion in Certain Random Lattices*, Phys. Rev. **109**, 1492 (1958).

[3] S. John, *Strong Localization of Photons in Certain Disordered Dielectric Superlattices*, Phys. Rev. Lett. **58**, 2486 (1987).

[4] D. S. Wiersma, P. Bartolini, A. Lagendijk, and R. Righini, *Anderson Localization of Light*, Nature **390**, 671 (1997).

[5] S. John and J. Wang, *Quantum Electrodynamics Near a Photonic Band Gap: Photon Bound States and Dressed Atoms*, Phys. Rev. Lett. **64**, 2418 (1990).

[6] S. John and J. Wang, *Quantum Optics of Localized Light in a Photonic Bandgap*, Phys. Rev. B **43**, 12772 (1991).

[7] S. John and T. Quang, *Spontaneous Emission near the Edge of a Photonic Band Gap*, Phys. Rev. A **50**, 1764 (1994).

[8] N. Vats and S. John, *Non-Markovian Quantum Fluctuations and Superradiance Near a Photonic Band Edge*, Phys. Rev. A **58**, 4168 (1998).

[9] S. John and T. Quang, *Optical Bistability and Phase Transitions in a Doped Photonic Band-Gap Material*, Phys. Rev. A **54**, 4479 (1996).

[10] S. John and V. I. Rupasov, *Multiphoton Localization and Propagating Quantum Gap Solitons in a Frequency Gap Medium*, Phys. Rev. Lett. **79**, 821 (1997).

[11] T. Quang, M. Woldeyohannes, S. John, and G. S. Agarwal, *Coherent Control of Spontaneous Emission Near a Photonic Band Edge: A Single-Atom Optical Memory Device*, Phys. Rev. Lett. **79**, 5238 (1997).

[12] N. Akozbek and S. John, *Optical Solitary Waves in Two- and Three-Dimensional Nonlinear Photonic Band-Gap Structures*, Phys. Rev. E **57**, 2287 (1998).

[13] S. John and V. I. Rupasov, *Quantum Self-Induced Transparency in Frequency Gap Media*, Europhys. Lett. **46**, 326 (1999).

[14] M. Woldeyohannes and S. John, *Coherent Control of Spontaneous Emission Near a Photonic Band Edge: A Qubit for Quantum Computation*, Phys. Rev. A **60**, 5046 (1999).

[15] G. M. Nikolopoulos and P. Lambropoulos, *Beyond Single-Photon Localization at the Edge of a Photonic Band Gap*, Phys. Rev. A **61**, 053812 (2000).

[16] M. Florescu and S. John, *Single-Atom Switching in Photonic Crystals*, Phys. Rev. A **64**, 033801 (2001).

[17] Y. P. Yang and S. Y. Zhu, *Spontaneous Emission from a Two-Level Atom in a Three-dimensional Photonic Crystal*, Phys. Rev. A **62**, 013805 (2000).

[18] S. Y. Zhu, Y. P. Yang, H. Chen, H. Zheng, and M. S. Zubairy, *Spontaneous Radiation and Lamb Shift in Three-Dimensional Photonic Crystals*, Phys. Rev. Lett. **84**, 2136 (2000).

[19] Z.-Y. Li and Y. N. Xia, *Full Vectorial Model for Quantum Optics in Three-Dimensional Photonic Crystals*, Phys. Rev. A **63**, 043817 (2001).

[20] Z.-Y. Li and Y. N. Xia, *Optical Photonic Band Gaps and the Lamb Shift*, Phys. Rev. B **63**, 121305(R) (2001).

[21] E. N. Economou and A. Zdetsis, *Classical Wave Propagation in Periodic Structures*, Phys. Rev. B **40**, 1334 (1989).

[22] E. Yablonovitch and T. J. Gmitter, *Photonic Band Structure: the Face-Centered-Cubic Case*, Phys. Rev. Lett. **63**, 1950 (1989).

[23] K. M. Leung and Y. F. Liu, *Photon Band Structures: The Plane-Wave Method*, Phys. Rev. B

41, 10188 (1990).
[24] S. Satpathy, Z. Zhang, and M. R. Salehpour, *Theory of Photon Bands in Three-Dimensional Periodic Dielectric Structures*, Phys. Rev. Lett. **64**, 1239 (1990).
[25] K. M. Leung and Y. F. Liu, *Full Vector Wave Calculation of Photonic Band Structures in Face-Centered-Cubic Dielectric Media*, Phys. Rev. Lett. **65**, 2646 (1990).
[26] Z. Zhang and S. Satpathy, *Electromagnetic Wave Propagation in Periodic Structures: Bloch Wave Solution of Maxwell's Equations*, Phys. Rev. Lett. **65**, 2650 (1990).
[27] K.-M. Ho, C. T. Chan, and C. M. Soukoulis, *Existence of a Photonic Gap in Periodic Dielectric Structures*, Phys. Rev. Lett. **65**, 3152 (1990).
[28] H. S. Sözüer, J. W. Haus, and R. Inguva, *Photonic Bands: Convergence Problems with the Plane-Wave Method*, Phys. Rev. B **45**, 13962 (1992).
[29] K. Busch and S. John, *Photonic Band Gap Formation in Certain Self-Organizing Systems*, Phys. Rev. E **58**, 3896 (1998).
[30] P. M. Bell, J. B. Pendry, L. M. Moreno, and A. J. Ward, *A Program for Calculating Photonic Band Structures and Transmission Coefficients of Complex Structures*, Comp. Phys. Comm. **85**, 306 (1995).
[31] A. Modinos, N. Stefanou, and V. Yannopapas, *Applications of the Layer-KKR Method to Photonic Crystals*, Optics Express **8**, 197 (2001).
[32] C. T. Chan, Q. L. Yu, and K.-M. Ho, *Order-N Spectral Method for Electromagnetic Waves*, Phys. Rev. B **51**, 16635 (1995).
[33] K. Sakoda and H. Shiroma, *Numerical Method for Localized Defect Modes in Photonic Lattices*, Phys. Rev. B **56**, 4830 (1997).
[34] J. S. Kole, *New Methods for the Numerical Solution of Maxwell's Equations*, Ph.D. thesis, Rijksuniversiteit Groningen, 2003.
[35] J. D. Jackson, *Classical Electrodynamics* (John Wiley & Sons, New York, 1975).
[36] N. W. Ashcroft and N. D. Mermin, *Solid State Physics* (Holt, Rinehard and Winston, New York, 1976).
[37] E. Zeidler, *Applied Functional Analysis* (Springer Verlag, Berlin, 1995).
[38] Z.-Y. Li, X. D. Zhang, and Z. Q. Zhang, *Disordered Photonic Crystals Understood by a Perturbation Formalism*, Phys. Rev. B **61**, 15738 (2000).
[39] F. Bloch, *Über die Quantenmechanik der Elektronen in Kristallgittern*, Z. f. Physik **52**, 555 (1928).
[40] L. P. Bouckaert, R. Smoluchowski, and E. Wigner, *Theory of Brillouin Zones and Symmetry Properties of Wave Functions in Crystals*, Phys. Rev. **50**, 58 (1936).
[41] T. Suzuki and P. K. L. Yu, *Emission Power of an Electric-Dipole in the Photonic Band-Structure of the Fcc Lattice*, J. Opt. Soc. Am. B **12**, 570 (1995).
[42] L. Li, *Use of Fourier Series in the Analysis of Discontinuous Periodic Structures*, J. Opt. Soc. Am. A **13**, 1870 (1996).
[43] G. H. Golub and C. F. Van Loan, *Matrix Computations (2nd ed.)* (The Johns Hopkins University Press, Baltimore, 1989).
[44] E. Yablonovitch, T. J. Gmitter, and K. M. Leung, *Photonic Band Structure: The Face-Centered-Cubic Case Employing Nonspherical Atoms*, Phys. Rev. Lett. **67**, 2295 (1991).
[45] S. Datta, C. T. Chan, K.-M. Ho, and C. M. Soukoulis, *Effective Dielectric Constant of Periodic Composite Structures*, Phys. Rev. B **48**, 14936 (1993).
[46] W. L. Vos, R. Sprik, A. van Blaaderen, A. Imhof, A. Lagendijk, and G. H. Wegdam, *Strong Effects of Photonic Band Structures on the Diffraction of Colloidal Crystals*, Phys. Rev. B **53**, 16231 (1996).

[47] W. L. Vos, M. Megens, C. M. van Kats, and P. Bösecke, *Transmission and Diffraction by Photonic Colloidal Crystals*, J. Phys.-Condens. Matter **8**, 9503 (1996).
[48] W. L. Vos, H. M. van Driel, M. Megens, A. F. Koenderink, and A. Imhof, *Experimental Probes of the Optical Properties of Photonic Crystals*, (2001), in [50].
[49] D. V. van Coevorden, R. Sprik, A. Tip, and A. Lagendijk, *Photonic Band Structure of Atomic Lattices*, Phys. Rev. Lett. **77**, 2412 (1996).
[50] *Photonic Crystals and Light Localization in the* 21st *Century*, edited by C. M. Soukoulis (Kluwer, Dordrecht, 2001).
[51] H. M. van Driel and W. L. Vos, *Multiple Bragg Wave Coupling in Photonic Band-Gap Crystals*, Phys. Rev. B **62**, 9872 (2000).
[52] J. E. G. J. Wijnhoven and W. L. Vos, *Preparation of Photonic Crystals Made of Air Spheres in Titania*, Science **281**, 802 (1998).
[53] A. Blanco, E. Chomski, S. Grabtchak, M. Ibisate, S. John, S. W. Leonard, C. López, F. Meseguer, H. Míguez, J. P. Mondia, G. A. Ozin, O. Toader, and H. M. van Driel, *Large-Scale Synthesis of a Silicon Photonic Crystal with a Complete Three-Dimensional Bandgap Near 1. 5 Micrometres*, Nature **405**, 437 (2000).
[54] Y. A. Vlasov, X. Z. Bo, J. C. Sturm, and D. J. Norris, *On-Chip Natural Assembly of Silicon Photonic Bandgap Crystals*, Nature **414**, 289 (2001).
[55] K.-M. Ho, C. T. Chan, C. M. Soukoulis, R. Biswas, and M. Sigalas, *Photonic Band-Gaps in 3-Dimensions - New Layer-by-Layer Periodic Structures*, Solid State Commun. **89**, 413 (1994).
[56] *Photonic Band Gap Materials*, edited by C. M. Soukoulis (Kluwer, Dordrecht, 1996).
[57] J. E. G. J. Wijnhoven, L. Bechger, and W. L. Vos, *Fabrication and Characterization of Large Macroporous Photonic Crystals in Titania*, Chem. Mater. **13**, 4486 (2001).
[58] E. M. Purcell, *Spontaneous Emission Probabilities at Radio Frequencies*, Phys. Rev. **69**, 681 (1946).
[59] E. Fermi, *Quantum Theory of Radiation*, Rev. Mod. Phys. **4**, 87 (1932).
[60] R. Loudon, *The Quantum Theory of Light, 2nd ed.* (Oxford University Press, Oxford, England, 1983).
[61] R. Sprik, B. A. van Tiggelen, and A. Lagendijk, *Optical Emission in Periodic Dielectrics*, Europhys. Lett. **35**, 265 (1996).
[62] D. V. van Coevorden, *Light Propagation in Ordered and Disordered Media*, Ph.D. thesis, University of Amsterdam, 1997.
[63] K. H. Drexhage, H. Kuhn, and F. P. Schäfer, *Variation of the Fluorescence Decay Time of a Molecule in Front of a Mirror*, Ber. Bunsenges. Phys. Chem. **72**, 329 (1968).
[64] K. H. Drexhage, *Influence of a Dielectric Interface on Fluorescence Decay Time*, J. Lumin. **1**, 693 (1970).
[65] E. Snoeks, A. Lagendijk, and A. Polman, *Measuring and Modifying the Spontaneous Emission Rate of Erbium Near an Interface*, Phys. Rev. Lett. **74**, 2459 (1995).
[66] D. J. Heinzen, J. J. Childs, J. E. Thomas, and M. S. Feld, *Enhanced and Inhibited Visible Spontaneous Emission by Atoms in a Confocal Resonator*, Phys. Rev. Lett. **58**, 1320 (1987).
[67] S. Haroche, in *Systèmes Fondamentaux en Optique Quantique / Fundamental Systems in Quantum Optics*, edited by J. Dalibard, J. M. Raimond, and J. Zinn-Justin (North-Holland, Amsterdam, 1992), Chap. 13, pp. 767–940.
[68] P. R. Villeneuve, S. H. Fan, and J. D. Joannopoulos, *Microcavities in Photonic Crystals: Mode Symmetry, Tunability, and Coupling Efficiency*, Phys. Rev. B **54**, 7837 (1996).
[69] H. J. Monkhorst and J. D. Pack, *Special Points for Brillouin-Zone Integrations*, Phys. Rev. B

13, 5188 (1976).
[70] G. Gilat, *Analysis of Methods for Calculating Spectral Properties in Solids*, J. Comput. Phys. **10**, 432 (1972).
[71] M. Doosje, B. Hoenders, and J. Knoester, *Scattering of Light on the Surfaces of Photonic Crystals*, Opt. Commun. **206**, 253 (2002).
[72] P. St. J. Russell, T. A. Birks, and F. D. Lloyd-Lucas, in *Confined Electrons and Photons*, edited by E. Burstein and C. Weisbuch (Plenum, New York, 1995), pp. 585–633.
[73] J. M. Ziman, *Principles of the Theory of Solids* (Cambridge University Press, Cambridge, 1972).
[74] K. Sakoda, *Optical Properties of Photonic Crystals* (Springer Verlag, Berlin, 2001).
[75] M. Notomi, *Theory of Light Propagation in Strongly Modulated Photonic Crystals: Refractionlike Behavior in the Vicinity of the Photonic Band Gap*, Phys. Rev. B **62**, 10696 (2000).
[76] P. St. J. Russell, *Interference of Integrated Floquet-Bloch Waves*, Phys. Rev. A **33**, 3232 (1986).
[77] H. Kosaka, T. Kawashima, A. Tomita, M. Notomi, T. Tamamura, T. Sato, and S. Kawakami, *Superprism Phenomena in Photonic Crystals*, Phys. Rev. B **58**, R10096 (1998).
[78] J. B. Pendry, *Negative Refraction Makes a Perfect Lens*, Phys. Rev. Lett. **85**, 3966 (2000).
[79] C. Luo, S. G. Johnson, and J. D. Joannopoulos, *All-Angle Negative Refraction in a Three-Dimensionally Periodic Photonic Crystal*, Appl. Phys. Lett. **81**, 2352 (2002).
[80] A. J. Ward, J. B. Pendry, and W. J. Stewart, *Photonic Dispersion Surfaces*, J. Phys.: Cond. Mat. **7**, 2217 (1995).
[81] S. G. Johnson and J. D. Joannopoulos, *Block-Iterative Frequency-Domain Methods for Maxwell's Equations in a Planewave Basis*, Opt. Express **8**, 173 (2001).
[82] K. W. K. Shung and Y. C. Tsai, *Surface Effects and Band Measurements in Photonic Crystals*, Phys. Rev. B **48**, 11265 (1993).
[83] Y. Fink, J. N. Winn, S. H. Fan, C. Chen, J. Michel, J. D. Joannopoulos, and E. L. Thomas, *A Dielectric Omnidirectional Reflector*, Science **282**, 1679 (1998).
[84] C. Hooijer, D. Lenstra, and A. Lagendijk, *Mode Density Inside an Omnidirectional Reflector is Heavily Directional But Not Small*, Opt. Lett. **25**, 1666 (2000).

Chapter 3

Angular Redistribution of Spontaneous Emission

We have measured spontaneous emission spectra of laser dyes in strongly photonic crystals, made of inverse opals in titania (TiO_2). We have observed that spontaneous emission spectra are strongly modified, and depend on the emission direction relative to the crystal lattice planes. We identify stop bands with large relative widths comparable to the dyes' emission spectra, that strongly attenuate the emission strength. For a wide range of angles, two stop bands appear simultaneously; their angle-dependent frequencies display an avoided crossing that is corroborated by reflectivity experiments. The stop band frequencies agree well with band structure calculations, but differ from simple Bragg diffraction as a result of multiple wave coupling. Strongly reduced dispersion of Bloch modes and multiple wave coupling illustrate mechanisms ultimately responsible for significant changes in the density of states.

3.1 Introduction

As control over spontaneous emission is a primary aim of photonic band gap materials, it is highly relevant to study the radiative properties of light sources inside strongly photonic crystals. Ultimately photonic band gap crystals will not only influence emission spectra, but also emission rates, as the density of states vanishes or changes rapidly. In this regime intricate spontaneous emission dynamics [1–3] are predicted. Even photonic crystals without photonic band gaps, however, can lead to important advances in the control of emission. Recent examples include, *e.g.*, miniature lasers in two-dimensional photonic crystals [4, 5]. Furthermore, it is of prime interest to study the influence of the photonic band structure on emission spectra in the relatively simple frequency range of the lowest order stop gap, before endeavoring to interpret emission spectra for frequencies near a photonic band gap.

Previous studies of organic dyes [6–9] and semiconductor quantum dots [10–12] embedded inside three-dimensional weakly photonic crystals have revealed modified emission spectra. The luminescence appeared inhibited in particular directions and frequency bands, forming stop bands whose frequencies depend on angle in accordance with Bragg diffraction from a single set of lattice planes. The crystal planes form a Bragg mirror for the luminescence, preventing part of the emission from leaving the crystal along specific directions. No major changes of spontaneous emission lifetimes have been observed, however, because these weakly photonic crystals hardly modified the density of states [13]. These experiments were limited by the low dielectric contrast involved and the concomitant weak interaction with light. The empirically demonstrated [14] minor changes in emission lifetime agree well with the few percent reduction in total solid angle for light propagation due to Bragg diffraction.

Recently developed photonic crystals with high dielectric contrast, known as inverse opals, interact so strongly with light that propagation is inhibited for more than 55% of all directions [15]. Hence, these crystals promise to bring emission experiments in the regime of strong photonic interaction, though insufficient to open a photonic band gap. In this chapter, we study spontaneous emission of laser dyes inside such photonic crystals. We identify a mechanism by which the directional properties of the spectrum are modified. For emission nearly normal to the 111 lattice planes, we observe a single stop band. Over a large angular range, however, we find dual stop bands in the emission spectra, with very large band width. The angular dependencies of the center frequencies of the two stop bands display an avoided crossing. The large angular extent and frequency band width of the avoided crossing demonstrate a multiple Bloch wave coupling phenomenon, which is characteristic for the regime of strong photonicity, and the fundamental ingredient for suppressing the density of states.

3.2 Experiment

The photonic crystals studied here are fcc crystals of close-packed air spheres in a solid matrix of anatase TiO_2, prepared by template-assisted assembly [16, 17]. The preparation and structural characterization of these crystals has been reported in Ref. [16, 18], and was performed by L. Bechger and J.E.G.J. Wijnhoven. In brief, *fcc* opal templates are prepared by drying colloidal crystals that consist of polystyrene latex spheres (Duke Scientific, polydispersity $\lesssim 2\%$) in water. Such colloidal crystals are formed by sedimentation in a capillary. The artificial opals are infiltrated up to 8 times with a mixture of ethanol and the precursor titanium-(IV) propoxide. After each infiltration step, the precursor is allowed to react with water from the air for one day. After the infiltration steps, the samples are heated up to 450°C in an oven in air. This heat treatment serves the dual purpose of calcining the latex template spheres, and of completing the alkoxides reaction to crystalline anatase TiO_2 as confirmed by X-ray powder diffraction. The volume fraction of solid material comprising these so-called 'inverse opals' or 'air-sphere crystals' ranges from 6 to 12%, depending on the

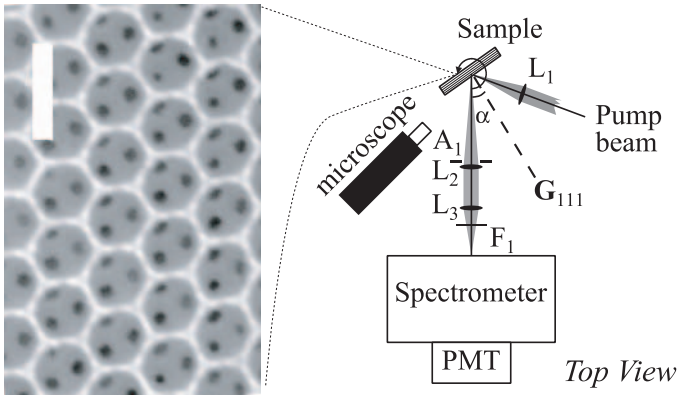

FIGURE 3.1: *(Left) Scanning electron micrograph of a 111 face of an inverse opal with a = 480 nm. Dark dots (three per sphere visible) correspond to cylindrical voids connecting this crystal layer to the next layer of air spheres. The scalebar represents 0.5 μm. (Right). Schematic overview of the setup. The pump beam is focused onto the sample face using lens L_1 (f=10 cm). Luminescence within a cone (apex angle set by aperture A_1) centered at a detection angle α relative to the sample surface normal is imaged onto the spectrometer entrance slit using L_1 and L_2 (f=12 cm). A Schott color filter F_1 prevents scattered laser light from entering the spectrometer. The detection angle α is varied by rotating the sample. A microscope was used to monitor the pump beam alignment, and the position of the pump spot on the sample.*

lattice parameter. Scanning electron microscopy (SEM) images show highly ordered spherical macropores that appear to be faithfully replicated from the opal template, despite an overall shrinkage of ~ 25%. Neighboring air holes are connected by round air channels ('windows') through the titania backbone, which appear as black spots in the SEM pictures, such as displayed in Fig. 3.1(a). These windows correspond to the contact points of latex spheres in the original template. The samples have overall dimensions of the order of millimeters and thicknesses of ~ 200 μm. They are composed of high-quality crystal domains with diameters of ~ 50 μm, as confirmed by small angle X-ray scattering [18]. Defects, displacements and polydispersity of the air spheres are inherited from the opal template. The internal titania-air interfaces have a roughness of $\lesssim$ 10 nm, limited by the grain size of titania crystallites. The high dielectric constant of anatase titania (ε = 6.25 to 6.5 for visible wavelengths [19]) makes these 'inverse opals' or 'air-sphere crystals' into some of the most strongly photonic crystals available for visible light, with a photonic strength $\Psi \approx 0.12$ [15].

In order to study spontaneous emission in these photonic crystals two different organic dyes were used, being Rhodamine 6G (R6G), and Nile Blue (NB) [20]. Crystals with lattice parameters ranging from a = 430, 480 nm, doped with R6G, to 480 and 510 nm (NB) were chosen for optimal overlap of the L-gaps with the emission spectra. To incorporate the dye, the air-sphere crystals were immersed in a dilute solution (~ 70 μmol/l for 24 h in the case of Nile Blue, and ~ 1 μmol/l for 1 h for R6G) of dye in ethanol, to promote the adsorption of dye molecules at the TiO_2-air interfaces

of the voids. Afterwards, the samples were rinsed and dried. It remains challenging to determine the density of dye molecules. From the molar adsorptivity [21] and a crude internal surface area estimate, we expect $\sim 10^2$ dye molecules per air sphere (of radius $\sim$ 200 nm). Such a concentration is far below the monolayer coverage density of $\sim 10^5$ chromophores per sphere. The estimate of 10^2 molecules per sphere may even be an upper bound, given the rinsing cycles after adsorption. The concentration of dye molecules is estimated to be low enough by more than 2 orders of magnitude to avoid reabsorption or energy transfer processes. An upper bound to the critical concentration for reabsorption is determined from the peak in absorption cross-section. Furthermore, our estimate takes due account of the extended path length photons traverse inside the samples due to random scattering.

To ensure that solely emission is recorded from internal sources, well within the bulk of the crystal, the dye adsorbed near the external sample surface was selectively bleached [9]. Bleaching of the dye was limited to the first few crystal layers by illuminating the photonic crystals with an intense laser beam (488 (R6G) or 514 nm (NB)) impinging at the Bragg angle. At this angle the pump intensity decreases exponentially with depth into the sample. Spectra were found to be independent of observation angle prior to bleaching. Bleaching caused angle-dependent modifications of the spectral lineshapes to occur. The crystal layers close to the external crystal-air interface were bleached until modification of the lineshapes stopped. Further bleaching only resulted in a decrease of the emission intensity.

A schematic overview of the optical setup used to measure emission spectra is shown in Fig. 3.1. Depending on the dye, the 488 nm (R6G) or 514 nm emission of an Ar-ion laser was used to excite the dye. The *p*-polarized pump beam was incident on the samples at angles away from the Bragg condition for the pump frequency. The pump beam was focused to a spot $\sim 30\ \mu$m in diameter on the sample surface using a 10 cm focal length lens. The samples were glued to needle-tips and mounted in a goniometer, to acquire emission spectra as a function of the detection angle α relative to the surface normal, which corresponds to the 111 reciprocal lattice vector. The angle of incidence of the pump beam also changed with the sample orientation, although the illuminated spot remained the same. At $\alpha = 0°$, the incident angle of the pump beam amounted to $\sim 30°$. For increasing α, the surface normal of the sample was rotated towards the pump beam. The alignment of the laser beam on the sample and the rotation axis of the goniometer was monitored through a long working distance microscope. Emission within a cone of 5° around the detection angle α was imaged onto the entrance slit of an Oriel MS-257 0.25 m, f/4 grating spectrometer (in the case of Nile Blue), resp. a Carl Leiss[1] prism spectrometer (R6G), which was calibrated using the emission lines of a neon lamp. The *p*-polarized component of the emission was selectively probed, either due to spectrometer grating efficiencies, or by using a polarizer in the case of the R6G measurements. In both instances, the resolution amounted to $\sim 100\ \text{cm}^{-1}$. A Hamamatsu R3809U Micro Channel Plate detector was used to record the fluorescence. The spectra have been corrected for detector dark

[1] Carl Leiss GmbH Berlin, as opposed to Carl Zeiss.

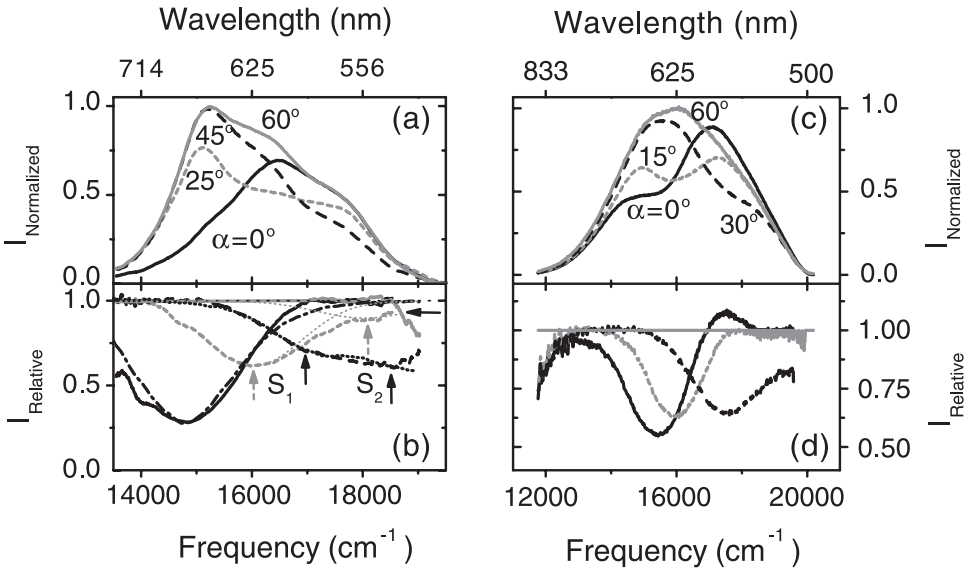

FIGURE 3.2: *Normalized emission spectra as a function of frequency for Nile Blue (a) resp. R6G (c) in titania inverse opal with lattice spacings* a = 510 *nm resp.* 480 *nm. Bottom panels (b) and (d) show the corresponding relative intensities obtained from the spectra in (a) and (c). Black curves are obtained at* $\alpha = 0°$*, grey dashed curves at* 25° *(a,b) resp.* 15° *(c,d), black dashed at* 45° *(a,b) resp* 30° *(c,d), and solid grey curves at* 60°*. Reflectivity data in (b) are shown for* $\alpha = 0°$ *(black dash-dotted) and* 30° *(black dotted curves). Double stop bands at* 25° *and* 45° *are indicated by arrows in (b). Fitted double Gaussians are indicated by thin grey dotted lines for* $\alpha = 25°$*.*

count, and the measured intensities of spectra at various angles have been adjusted to overlay their low- or high frequency ranges. In these frequency ranges no crystal effects are observed to modify the spectra.

3.3 Emission spectra and stop bands

Emission spectra at select detection angles of Nile Blue in a crystal with a = 510 nm, and of R6G in a crystal with a = 480 nm are presented in Fig. 3.2(a) resp. (c). For detection angles larger than 60°, the spectral line shapes of the emission remain unchanged, and the high frequency edge of the emission spectra has the same shape as observed at low detection angles, between $\alpha = 0°$ and 25°. This implies that at angles larger than 60° the stop band does not overlap the emission spectrum of the dye, both in the case of Nile Blue and R6G. In comparison, at $\alpha = 0°$ the photonic crystal with a = 510 nm greatly suppresses the emission of Nile Blue in the spectral range from 14000 to 16200 cm^{-1}. With increasing detection angle the low-frequency components of the emission recover, and the frequency range in which emission is suppressed shifts to higher frequencies, as expected from Bragg's law for a photonic crystal stop

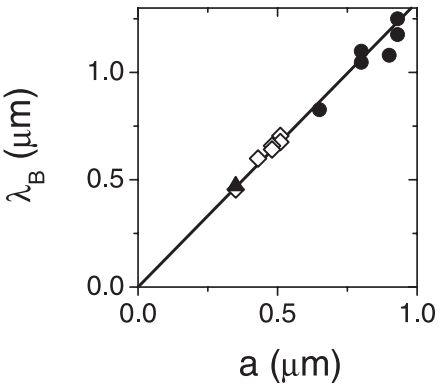

FIGURE 3.3: *Central wavelength λ_B (in air) versus lattice parameter a of the first order Bragg diffraction by 111 lattice planes of titania inverse opals. Open diamonds correspond to stop bands in emission (Chapters 3 and 4). Closed circles correspond to stop gaps in diffuse transmission (Chapter 7). The closed triangle (Chapter 6) and open diamond (Chapter 4) at $a = 350$ nm were determined from reflectivity. The solid line is Bragg's law, assuming an effective refractive index $n_e = 1.15$ (consistent with TiO_2 volume fractions between 6% (n_e^2 from averaged ε) and 10% (n_e from averaged n)). Lattice parameters were determined from SEM images. Symbol sizes are comparable to the error in a.*

gap from a single set of lattice planes. The same observations hold for the emission spectra of R6G in the sample with $a = 480$ nm, although the suppression bands are blue shifted. At $\alpha = 0°$ for instance, the suppression is shifted to the range from 15000 to 17000 cm^{-1}, in accordance with the reduced lattice parameter (see Figure 3.3). For both dyes we verified that the emitted intensity is proportional to the pump power, and that the line shapes are independent of the pump intensity. As expected based on the low dye doping concentration, these observations show that lasing and amplified spontaneous emission effects can be excluded. By traversing sample faces with the pump beam focus, we were able to map the angle-resolved spectral line shapes as a function of position on the sample, with a resolution of 50 μm. The spectral line shapes are well reproduced over sample areas up to 0.8 mm in diameter. In general, the angle-dependent modifications of the spectral line shapes as shown in Fig. 3.2(a) and (c) occur on those regions of photonic crystal samples which show bright opalescence. On the other hand, spectra from parts of photonic crystals which did not show clear opalescence, also did not show a clear angle-dependence. The angle-dependent modification was observed both in experiments with Nile Blue and with R6G. The blue shift of the stop band center frequencies at $\alpha = 0°$ with decreasing lattice parameter is demonstrated in Fig. 3.3. We find stop band center frequencies 14800 cm^{-1}, 15500 cm^{-1}, 15600 cm^{-1} and 17200 cm^{-1} respectively, for $a = 510, 480$ nm (NB) and $480, 430$ nm (R6G). Both the blueshift of the $\alpha = 0°$ stop band with decreasing lattice parameter, and the reproducibility of the experiment with different dyes indicate that the observed features are indeed a photonic crystal effect.

To determine the directionally dependent photonic stop band effect on the emission spectra, one would like to determine a 'transfer function' that depends solely on the photonic crystal, and not on the choice of dye. Such a transfer function can be found by dividing the angle-dependent fluorescence spectra by a suitable reference. *A priori*, the spectra are determined by *(i)* directional redistribution due to stop gaps (as observed), *(ii)* the (local) photonic density states sampled by the sources and *(iii)* the inhomogeneous broadening of the dye, which is partly determined by chemical interactions with the substrate. As dye molecules effectively act as four level systems, lineshapes in different photonic systems can be compared without taking into account the pump light distribution, as long as the pump wavelength is the same. To focus purely on the directionally dependent modifications, the reference spectrum should originate from a system with the same chemical and optical environment of the light sources. The reference of choice is therefore the angle-integrated emission spectrum of the dye in the specific sample under consideration. As quantitatively motivated both empirically and theoretically in Chapter 7, the spectrum observed for $\alpha \geq 60°$ is a good measure of the angle-integrated spectrum over most of the spectral range. This is due to the fact that no photonic stop gap overlaps the emission spectra for detection angles in excess of 60°. Dividing the $\alpha = 0°$ lineshape by the $\alpha = 60°$ spectrum, a stop band centered at 14800 cm^{-1} for $a = 510$ nm (Nile Blue) and 15600 cm^{-1} for $a = 480$ nm (R6G) is indeed obtained. The analysis may be slightly improved by noting that dividing a spectrum at angle α_1 by a spectrum at α_2 with negligible stop band overlap gives the stop band at α_1 if the ratio is less than unity. The stop band at α_2 is found from the inverse ratio. The analysis is more complicated if the transfer functions themselves exceed unity (Fig. 3.2(d), see Chapter 7), and if the ratio is taken of spectra with partially overlapping stop gaps. By careful analysis we were able to correct the $\alpha = 60°$ spectrum for a residual stop band at very high frequency (> 18500 cm^{-1} for $a = 510$ nm, resp. 19300 cm^{-1} for $a = 480$ nm). The line shape ratios for different samples and dyes are largely sample-independent, hence the stop bands are unambiguously determined.

Using the corrected $\alpha = 60°$ spectrum, we have extracted stop bands for all detection angles, a selection of which is shown in Fig. 3.2(b) for Nile Blue, and (d) for R6G. At emission angles close to $\alpha = 0°$, single broad stop bands appear. It is apparent that the relative width of the stop band $\Delta\omega/\omega = 10$ to 15% is so broad, that it is comparable to the broad spectral range of the organic dyes. The large stop band width is a signature of strong photonic interaction. At larger detection angles, a transition to a double stop band appears. The stop band edge frequencies will be discussed in Section 3.5. For frequencies within a stop band, the emission is reduced by $\sim$ 50 to 75%. Apart from stop bands, the $\alpha = 0°$ data in Fig. 3.2(d) show a slight enhancement compared to the 60° spectrum in a frequency window to the blue of the L-gap. This enhancement will be explained in Section 7.4. Figures 3.2(b) and (d) clearly demonstrate that photonic stop gaps impose a strong attenuation on the transfer of radiant energy to free space. We explain the magnitude of the attenuation in Section 3.4.

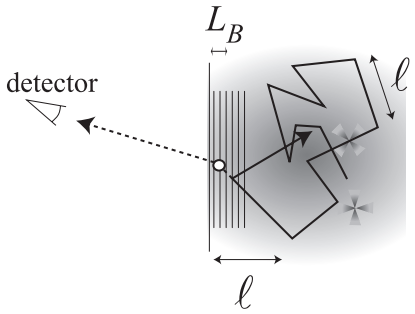

FIGURE 3.4: *(Sketch) Each individual source has a position dependent radiation pattern, determined by the Bloch modes available at the source position. Directional properties of each source are washed out by multiple scattering over length scales ℓ. Near the external interface the crystal planes internally diffract the diffuse luminescence, giving rise to stop bands in the spectra. The relevant length scale for internal diffraction is L_B.*

3.4 Diffuse transport and the stop band attenuation

For light sources embedded in a perfect crystal, one would expect that no emission into stop gap directions is possible. A perfect crystal should therefore give rise to a complete vanishing of the fluorescence intensity in stop gap directions. Instead, we observe an attenuation of 50% to 75% at $\alpha = 0°$ for all crystals studied. Limited attenuation of emission in stop band directions has previously been observed in the case of weakly photonic crystals [6–12]. For such near index-matched photonic crystals, the limited attenuation has been identified as being due to single scattering by intrinsic defects near the sample surface [9]. In the present case, the mechanism appears related, as it can also be attributed to random scattering. In weakly photonic samples the mean free path ℓ typical for random scattering exceeds the sample dimensions. In contrast, transport of light in the titania inverse opals is diffuse[2] on length scales $\ell \sim 15\ \mu$m smaller than the sample thickness $L \sim 200\ \mu$m. In brief, one should take into account that fluorescence emitted by a light source inside the bulk of the crystal does not reach the detector directly, but undergoes a series of scattering events, as sketched in Fig. 3.4. Even though different sources can have different radiation patterns, owing to their different local photonic environment, none of these directional properties of each source inside the photonic crystal reaches the observer. Instead, emission from all sources propagates diffusively to the crystal interface. Diffuse light emanating from a depth $z < \ell$ less than the mean free path from the surface propagates ballistically to the crystal-air interface, but may be redirected to the detector by some scattering event less than ℓ from the surface (see Fig. 3.4). The mean free path ℓ is larger than the exponential attenuation length L_B associated with Bragg diffraction

[2] An introduction to diffusion theory, and experiments to determine the transport mean free path ℓ as well as explanations of the source of random multiple scattering are the subject of Chapter 6. The interplay of internal Bragg diffraction and diffusion of light has been investigated in the experiments reported in Chapter 7.

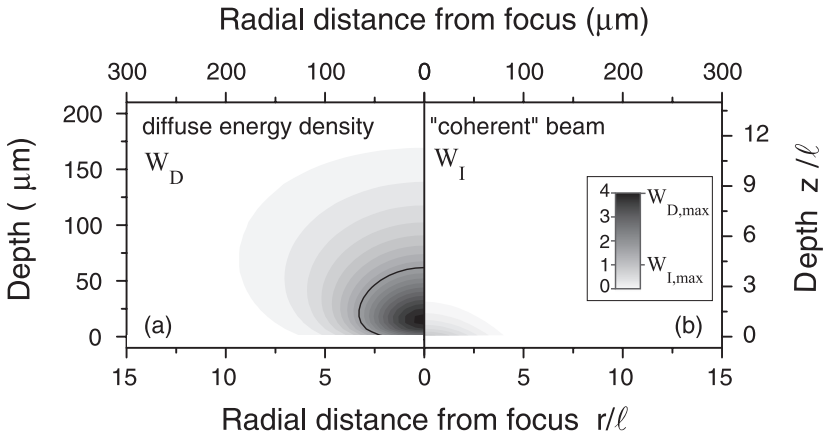

FIGURE 3.5: *(Left) Calculated energy density of the diffuse pump light for a sample of* 200 *μm thickness, a mean free path of* 15 *μm and a pump beam of waist* $w = 30$ *μm. Assumptions of the calculation are described in the text. Pump light is spread out over a large volume of* 65×40 *μm at a mean depth of* 50 *μm. Within this volume the diffuse energy density exceeds the energy density of the ballistic beam (right) by a factor* ~ 4.

(typically $L_B/\ell \sim 0.2$–0.5). Hence, intensity scattered at a distance $z < L_B$ less than the Bragg attenuation length from the interface is hardly Bragg diffracted. On the other hand the remaining fraction $1 - L_B/\ell$ for which the last scattering event occurs in the range $L_B < z < \ell$ propagates a sufficient distance to develop a stop band due to internal Bragg diffraction. This crude model predicts a total attenuation in the stop band equal to $1 - L_B/\ell = 50\%$ to 80%, in agreement with the experiment.

The pump light distribution is also affected by random multiple scattering. The diffusion approach therefore gives an adequate description of the spatial dependence of the pump light energy density within the sample, on length scales comparable to or bigger than the mean free path. In order to determine the size and depth of the sample volume in which dye molecules are excited by the pump light, we examine the solution of the stationary diffusion equation

$$D\nabla^2 W_D = \frac{I(\mathbf{r})}{\ell} \tag{3.1}$$

for the diffuse pump light energy density W_D, with diffusion coefficient $D = 1/3c\ell$ and boundary conditions as explained in Chapter 6. The source term in the diffusion equation is determined by the incident intensity distribution

$$I(r,z) = I_0 e^{-r^2/(2w^2)} e^{-z/\ell}, \tag{3.2}$$

where z denotes the depth into the sample, and r the distance from the axis of the incident beam. The Gaussian incident beam with peak intensity I_0 decays exponentially with depth into the sample due to extinction according to Lambert-Beer's law.

In correspondence with the experiment, we consider a slab of thickness $L = 200\ \mu$m that is infinite in the lateral directions, and a pump beam waist size $w = 30\ \mu$m. We take a mean free path $\ell = 15\ \mu$m, in accordance with the experiments presented in Chapter 6.

We find a diffuse pump light energy density W_D extending over a volume several mean free paths across, as displayed in Fig. 3.5(a). On the $r = 0$ axis collinear with the input beam, the mean depth $\langle z \rangle = \int z W_D(z) dz / \int W_D(z) dz$ at which dye molecules are excited amounts to $\sim 50\ \mu$m. The mean injection depth increases with increasing waist w to a maximum of order $\sim L/3$ (for $L \gg \ell$). As a measure of the spatial extent of the diffusely pumped volume, we propose $\sqrt{\langle r^2 \rangle}$ at mean injection depth, amounting to $\sim 65\ \mu$m in the radial direction, and $\sqrt{\langle z^2 \rangle - \langle z \rangle^2} \sim 40\ \mu$m along the sample normal. To obtain the total energy density within the sample, one should add the contribution of the exponentially attenuated incident beam (so-called 'coherent beam') to the diffuse energy density, which is plotted in the separate panel Fig. 3.5(b). Naturally, the contribution W_I of the coherent beam is confined to a much smaller volume, *i.e.*, one mean free path from the surface, with a lateral extent equal to the beam waist. More strikingly, the maximum energy density of the coherent beam (at the sample surface) is lower than the maximum energy density of the diffuse light (at $z \sim 2\ell$) by approximately a factor 4. This result indicates, as expected, that random multiple scattering increases the average path length that pump light traverses in the medium, thus enhancing the pump efficiency. In conclusion, diffuse transport of light is crucial in determining *(i)* the pump light distribution, and *(ii)* the attenuation of emission in stop band directions.

3.5 Stop bands beyond simple Bragg diffraction

At low emission angles close to normal to the 111 lattice planes, single broad stop bands appear in Fig. 3.2(b) and (d). Interestingly, at larger detection angles $\alpha \geq 25°$, a transition to a *double* stop band appears. As a typical example, we focus on Fig. 3.2(b). To clarify the double-stop band structure, which appears partly obscured due to the large width of the stop bands compared to the frequency separation, we have indicated the center frequencies of the stop bands with arrows. We denote the low-frequency stop bands by S_1, and the higher frequency stop band by S_2. With increasing angle, the higher frequency stop band S_2 becomes more apparent, while S_1 decreases in amplitude. The stop band spectrum at $\alpha = 45°$ shows evidence of a weak S_1 feature at 17000 cm^{-1} and a clear S_2 band at 18700 cm^{-1}. For $\alpha = 60°$, no more evidence of the S_1 band is found, and the low-frequency edge of the S_2 band has shifted beyond 18500 cm^{-1} (black horizontal arrow), leaving the emission spectrum essentially unsuppressed. Neither the occurrence of double stop bands, nor their frequency dependence can be explained as simple Bragg diffraction from a single set of lattice planes, but are likely due to a coupled wave phenomenon.

To confirm that the stop bands in emission of internal sources indeed correspond to the photonic band structure, additional reflectivity measurements were performed.

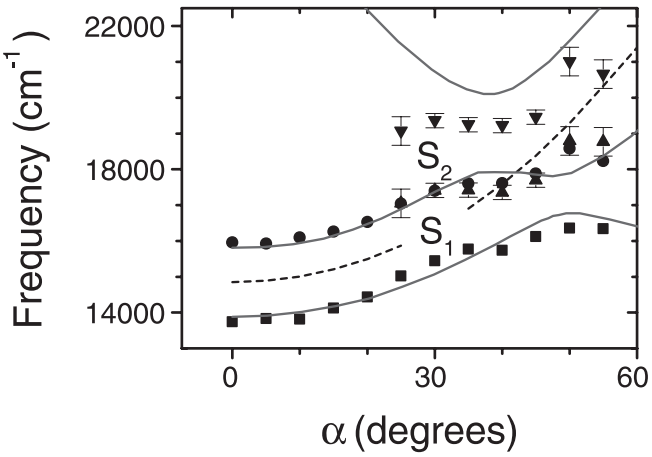

FIGURE 3.6: *Angular dependence of the stop band edges, determined from spectra as plotted in 3.2(b). Squares and circles are the lower resp. upper edges of the low frequency stop band S_1; triangles and inverted triangles correspond to the S_2 stop band edges. Solid lines are eigenfrequencies calculated using the plane wave method. The dotted curve is the stop band center frequency assuming single Bragg diffraction from 111 planes.*

The reflectivity was determined using externally incident plane waves from a white light source in conjunction with a Fourier-transform spectrometer, as described in Ref. [15, 22]. Reflectivity experiments readily reveal the center frequencies and widths of stop bands. To allow for a direct comparison of the reflectivity bands with stop bands in emission, reflectivity data $R(\omega)$ are scaled onto the emission stop bands as $1-\beta R(\omega)$. The scaling constant β accounts for the difference between peak reflectivity and attenuation at the center of the stop band. The peak reflectivity of $\sim$ 20% is limited by mosaic spread and grain boundaries occurring on a length scale of $\sim 50\,\mu$m, much smaller than the probe beam diameter $\sim 500\,\mu$m. Representative reflectivity results for $\alpha = 0°$ and 45° are shown in Fig. 3.2(b). As expected, a single stop band is revealed at a reflection angle $\alpha = 0°$, and a much broader double reflection band appears at $\alpha = 45°$, in agreement with the emission data. Although minor differences between reflectivity and emission data remain, there is good agreement between the single- and double stop bands in emission and in reflectivity. This confirms that the avoided crossing observed in the emission spectra is caused by the photonic band structure.

To quantify the dispersion of both stop bands S_1 and S_2, we have extracted the upper and lower frequency edges of the stop bands for all detection angles, as shown in Figure 3.6 for a typical example. Here, we have defined the stop band edges as the frequencies at half minimum of an attenuation band. An ideal diffraction peak would have a flat top with 100% reflectivity or attenuation, that abruptly falls off at the edges. Extinction causes a rounding of stop bands, and reduces the maximum reflectivity, or attenuation. In the absence of broadening mechanisms such as crystal

strain, the edges at half maximum (resp. minimum) of reflectivity or emission bands still represent a reliable though heuristic measure of the widths of stop gaps in the dispersion relation [23, 24]. Central frequencies and stop band edges were extracted by fitting double Gaussian peak shapes to the data in Figure 3.2(b). The number of adjustable parameters was limited by assuming both Gaussians to have equal frequency widths. An example of such a fit is indicated by the two thin grey dotted lines in Figure 3.2(b). The stop band edges of both stop gaps can be determined unambiguously from the two-Gaussian fit. For small angles $\alpha \leq 30°$, the center frequency of stop band S_1 closely follows the frequency dependence expected for simple Bragg diffraction, corresponding to the dotted line indicated in Fig. 3.6. Near $\alpha = 30°$, there is a marked departure from simple Bragg diffraction, characterized by *(i)* the appearance of the high frequency stop band S_2, and *(ii)* the fact that the S_1 center frequency remains at frequencies lower than Bragg's law predicts. The two bands display an avoided crossing centered at ~ 17000 cm^{-1} over a large angular range.

3.6 Geometry of the avoided crossing in the Brillouin zone

The avoided crossing phenomenon evident in stop gaps in emission has previously been observed in reflectivity experiments on similar samples [22]. Essentially, the internal Bragg diffraction phenomenon giving rise to the stop gap at larger diffraction angle is not solely determined by the 111 lattice planes, but also by the family of 200 lattice planes. It is important to note that the avoided crossing does not appear between just two dispersion branches, but that three reciprocal lattice vectors are involved. To illustrate the physics, we consider a cross-section of the first Brillouin zone through the Γ, U, L, K points, as sketched in Fig. 3.7. The stop gap associated with simple Bragg diffraction by the 111 crystal planes appears when the wave vector $\mathbf{k}$ touches the hexagonal facet of the first Brillouin zone. In this case $\mathbf{k}$ is strongly coupled to its Bragg diffracted counterpart $\mathbf{k}' = \mathbf{k} + \mathbf{G}_{111}$, on the opposite face of the Brillouin zone [3]. The L-gap corresponds to an *internal* propagation angle $\alpha' = 0$, with wave vector $\mathbf{k}$ pointing from Γ to $-L$. The stop gap associated with 111 diffraction for larger angle α' can be traced by scanning the tip of the wave vector $\mathbf{k}$ along the LU-line, away from the $(-)L$-point. At some point the wave vector passes the $-U$ point and moves into the second Brillouin zone. At the angles α' where $\mathbf{k}$ is close to the $-U$ point, the plane wave with wave vector $\mathbf{k}$ not only couples to $\mathbf{k}' = \mathbf{k} + \mathbf{G}_{111}$, but also to the 200 diffracted $\mathbf{k}'' = \mathbf{k}' + \mathbf{G}_{200}$. In a Bragg diffraction experiment this implies that, given the incident wave vector $\mathbf{k}_{\text{in}} = \mathbf{k}$, two diffracted wave vectors appear simultaneously inside the crystal, *e.g.*, $\mathbf{k}'$ and $\mathbf{k}''$. The dispersion relation, and diffraction efficiencies, are determined by the coupling between all three waves (or six, to account for polarization), and can not be described by the crossing of two separate stop gaps determined by simple Bragg diffractions. Instead, the electromagnetic waves organize into normal modes in which the $\mathbf{G} = 000, 111$ and 200 components

[3] The L-gap itself can be understood as an avoided crossing between two dispersion branches involving $G = 000$ and $G = 111$, as evident in the repeated zone scheme in Fig. 1.1.

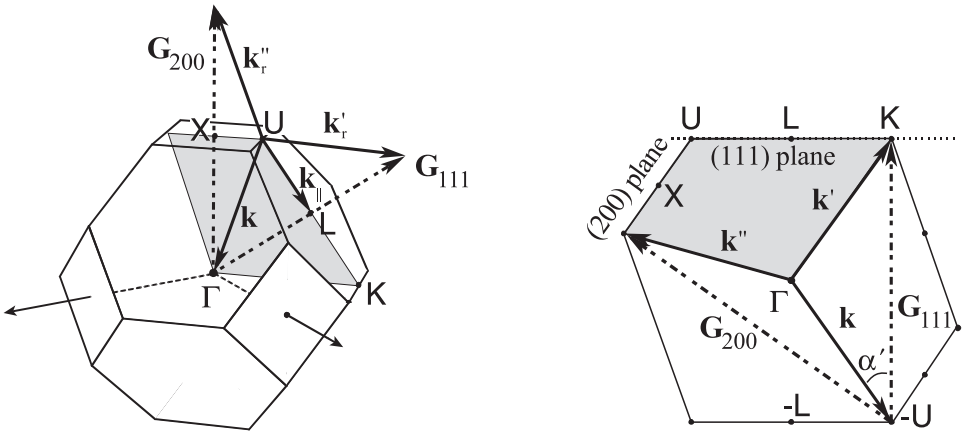

FIGURE 3.7: *The geometry of the avoided crossing displayed in a cut (right) through the Brillouin zone (left) through* Γ, K, L, U. *Reciprocal lattice vector* $\mathbf{G}_{111}$ *is the sample surface normal. As the internal propagation angle* α' *relative to* $\mathbf{G}_{111}$ *is increased (by increasing* $\mathbf{k}_{\|}$*), the wave vector* $\mathbf{k}$ *crosses the* $-U$ *point. Near this point* $\mathbf{k}$ *not only couples to* $\mathbf{k}'$ *through* $\mathbf{k}' - \mathbf{k} = \mathbf{G}_{111}$*, but simultaneously to* $\mathbf{k}''$ *via* $\mathbf{G}_{200}$.

are mixed, and which have anticrossing normal mode frequencies. It is important to note that the 200 diffracted beam with wave vector $\mathbf{k}''$ is not measured in this experiment. Instead, evidence for the 200 diffraction is found from the modified angle- and frequency dependence of the 111 diffracted beam alone. Due to the large index contrast, the modification of both 111 and 200 diffraction processes compared to simple Bragg diffraction extends over a large angular and frequency range.

3.7 Band structure

To investigate the angle-dependent features of the dispersion relation and to arrive at a quantitative comparison with the stop band edges in Fig. 3.6, we have calculated the plane-wave band structure. The position dependent dielectric function $\varepsilon(\mathbf{r})$ assumed here, is based on experimental observations of the structure of the crystals [16, 18]. For the model we assume close-packed air spheres (radius $r = a/\sqrt{8}$) covered by overlapping shells of solid material ($\varepsilon = 6.5$) of outer radius $1.09r$, and connected by cylindrical windows of radius $0.4r$ connecting neighboring air spheres. The shell thickness and window size are compatible with SEM observations, and correspond to a volume fraction of $\sim 10.7\%$ titania, consistent with available data [18]. The three anticrossing bands in the resulting band structure for the relevant polarization are shown in Fig. 3.6. The full band structure agrees with reflectivity features both in the regime of first order and second order Bragg diffraction [22, 25]. Internal wave vectors were converted to external propagation angle by applying parallel momentum conservation at the crystal-air interface. The two curves starting at $\alpha = 0°$ correspond to

eigenfrequencies of the mixed 000 and 111 modes, and delimit the 111 Bragg diffraction stop band edges. It is clear that the calculated mode frequencies agree well with the S_1 stop band edges derived from the emission spectra. The intermediate and high frequency modes agree well with the edges of the S_2 stop band. Though these dispersion curves were calculated using 725 plane waves, the same qualitative behavior is apparent in a model employing only the $G = 000, 111$ and 200 (and symmetry related) reciprocal lattice vectors [22]. This indicates that the observed avoided crossing is due to the 200 Bloch mode that couples with the 000 and 111 modes.

3.8 Conclusion

We have studied the angular distribution of spontaneous emission of dyes in strongly photonic inverse opals. We have found wide stop bands that strongly attenuate the transfer of radiant energy to free space. For the first time we find a double stop band in emission spectra. The angular dependence of the center frequencies of the two stop bands show an avoided crossing over a large angular and frequency range. The avoided crossing is determined by multiple Bragg wave coupling of 000, 111 and 200 modes, and is well understood in terms of the photonic band structure. In the range of the avoided crossing the modes become nearly dispersionless. Flattening of dispersion relations due to band repulsions is the hallmark of strong multiple wave coupling phenomena that will ultimately result in a photonic band gap. Depending on the range of solid angle over which the avoided crossing occurs, a significant modification of the density of states can be expected. Experiments to probe the density of states are the subject of Chapter 4. Furthermore, we conclude that random multiple scattering due to structural disorder plays a key role in the transport of luminescence and pump light.

References

[1] Y. P. Yang and S. Y. Zhu, *Spontaneous Emission from a Two-Level Atom in a Three-dimensional Photonic Crystal*, Phys. Rev. A **62**, 013805 (2000).

[2] N. Vats and S. John, *Non-Markovian Quantum Fluctuations and Superradiance Near a Photonic Band Edge*, Phys. Rev. A **58**, 4168 (1998).

[3] G. M. Nikolopoulos and P. Lambropoulos, *Beyond Single-Photon Localization at the Edge of a Photonic Band Gap*, Phys. Rev. A **61**, 053812 (2000).

[4] O. J. Painter, R. K. Lee, A. Scherer, A. Yariv, J. D. O'Brien, P. D. Dapkus, and I. Kim, *Two-Dimensional Photonic Band-Gap Defect Mode Laser*, Science **284**, 1819 (1999).

[5] C. J. M. Smith, H. Benisty, D. Labilloy, U. Oesterle, R. Houdré, T. F. Krauss, R. M. De La Rue, and C. Weisbuch, *Near-Infrared Microcavities Confined by Two-Dimensional Photonic Band Gap Crystals*, Electron. Lett. **35**, 228 (1999).

[6] V. N. Bogomolov, S. V. Gaponenko, I. N. Germanenko, A. M. Kapitonov, E. P. Petrov, N. V. Gaponenko, A. V. Prokofiev, A. N. Ponyavina, N. I. Silvanovich, and S. M. Samoilovich, *Photonic Band Gap Phenomenon and Optical Properties of Artificial Opals*, Phys. Rev. E **55**, 7619 (1997).

[7] T. Yamasaki and T. Tsutsui, *Spontaneous Emission from Fluorescent Molecules Embedded in Photonic Crystals Consisting of Polystyrene Microspheres*, Appl. Phys. Lett. **72**, 1957 (1998).
[8] K. Yoshino, S. B. Lee, S. Tatsuhara, Y. Kawagishi, M. Ozaki, and A. A. Zakhidov, *Observation of Inhibited Spontaneous Emission and Stimulated Emission of Rhodamine 6G in Polymer Replica of Synthetic Opal*, Appl. Phys. Lett. **73**, 3506 (1998).
[9] M. Megens, J. E. G. J. Wijnhoven, A. Lagendijk, and W. L. Vos, *Light Sources Inside Photonic Crystals*, J. Opt. Soc. Am. B **16**, 1403 (1999).
[10] S. G. Romanov, A. V. Fokin, V. Alperovich, N. P. Johnson, and R. M. De La Rue, *The Effect of the Photonic Stop-Band Upon the Photoluminescence of CdS in Opal*, Phys. Status Solidi A **164**, 169 (1997).
[11] S. V. Gaponenko, A. M. Kapitonov, V. N. Bogomolov, A. V. Prokofiev, A. Eychmüller, and A. L. Rogach, *Electrons and Photons in Mesoscopic Structures: Quantum Dots in a Photonic Crystal*, JETP Lett. **68**, 142 (1998).
[12] A. Blanco, C. López, R. Mayoral, H. Míguez, F. Meseguer, A. Mifsud, and J. Herrero, *CdS Photoluminescence Inhibition by a Photonic Structure*, Appl. Phys. Lett. **73**, 1781 (1998).
[13] Z.-Y. Li and Z. Q. Zhang, *Weak Photonic Band Gap Effect on the Fluorescence Lifetime in Three-Dimensional Colloidal Photonic Crystals*, Phys. Rev. B **63**, 125106 (2001).
[14] M. Megens, J. E. G. J. Wijnhoven, A. Lagendijk, and W. L. Vos, *Fluorescence Lifetimes and Linewidths of Dye in Photonic Crystals*, Phys. Rev. A **59**, 4727 (1999).
[15] M. S. Thijssen, R. Sprik, J. E. G. J. Wijnhoven, M. Megens, T. Narayanan, A. Lagendijk, and W. L. Vos, *Inhibited Light Propagation and Broadband Reflection in Photonic Air-Sphere Crystals*, Phys. Rev. Lett. **83**, 2730 (1999).
[16] J. E. G. J. Wijnhoven and W. L. Vos, *Preparation of Photonic Crystals Made of Air Spheres in Titania*, Science **281**, 802 (1998).
[17] D. J. Norris and Y. A. Vlasov, *Chemical Approaches to Three-Dimensional Semiconductor Photonic Crystals*, Adv. Mater. **13**, 371 (2001).
[18] J. E. G. J. Wijnhoven, L. Bechger, and W. L. Vos, *Fabrication and Characterization of Large Macroporous Photonic Crystals in Titania*, Chem. Mater. **13**, 4486 (2001).
[19] *Handbook of Optical Constants of Solids*, edited by E. D. Palik (Academic Press, New York, 1952).
[20] U. Brackmann, *Lambdachrome Laser Dyes* (Lambda Physik GmbH, Göttingen, 1997).
[21] C. Anderson and A. J. Bard, *An Improved Photocatalyst of TiO_2/SiO_2 Prepared by a Sol-Gel Synthesis*, J. Phys. Chem. **99**, 9882 (1995).
[22] H. M. van Driel and W. L. Vos, *Multiple Bragg Wave Coupling in Photonic Band-Gap Crystals*, Phys. Rev. B **62**, 9872 (2000).
[23] R. W. James, *The Optical Principles of the Diffraction of X-Rays* (G. Bell & Sons, London, 1954).
[24] W. L. Vos, H. M. van Driel, M. Megens, A. F. Koenderink, and A. Imhof, *Experimental Probes of the Optical Properties of Photonic Crystals*, (2001), in [26].
[25] W. L. Vos and H. M. van Driel, *Higher Order Bragg Diffraction by Strongly Photonic Fcc Crystals: Onset of a Photonic Bandgap*, Phys. Lett. A **272**, 101 (2000).
[26] *Photonic Crystals and Light Localization in the* 21st *Century*, edited by C. M. Soukoulis (Kluwer, Dordrecht, 2001).

Chapter 4

Broadband Fivefold Reduction of Vacuum Fluctuations Probed by Dyes

We have observed for the first time a strong angle-independent modification of spontaneous emission spectra from laser dyes in photonic crystals, made of inverse opals in titania. We show that both the fluorescence quantum efficiency and weak disorder play a key role in interpreting the experimental data. We compare the angle-independent emission spectra of dye in photonic crystals with spectra from such crystals with much smaller lattice spacings, for which emission is in the long wavelength limit. The data reveal inhibition of emission up to a factor ~ 5 *over a large bandwidth of* 13% *of the first order Bragg resonance frequency. The center frequency and bandwidth of the inhibition agree with the calculated total density of states, but the measured inhibition of the vacuum fluctuations is much larger. Due to the specific location of the dye molecules, we likely probe the strongly modulated local photonic density of states.*

4.1 Introduction

Within the framework of quantum electrodynamics (QED), it has long been recognized that the properties of the electromagnetic mode density may be used to tailor fundamental atom-radiation interactions [1]. Numerous cavity QED experiments have demonstrated the effects of manipulating vacuum fluctuations. Prime examples are reductions and enhancements of spontaneous emission rates and energy transfer processes, cavity induced energy level shifts, and Van der Waals and Casimir forces [1–5]. Cavity QED experiments are generally limited to narrow spectral bandwidths, and small spatial volumes, *i.e.*, near the center of the cavity. It is highly desirable to be able to manipulate vacuum fluctuations over large bandwidths and extended spatial volumes in solid state systems, as proposed for photonic band gap materials [6–8].

Complete suppression of vacuum fluctuations is expected in the case of a photonic band gap, a frequency range for which no electromagnetic modes exist. As explained in Chapter 2, a photonic band gap arises from strongly coupled Bragg diffrac-

tions in periodic dielectric structures with periodicity comparable to the wavelength of interest. Such a complete suppression of the density of states is hard to realize. In pioneering experiments on 3D photonic crystals, the inhibition was limited to a few percent by the small dielectric contrast [9–12]. Significant inhibition of spontaneous emission by strongly photonic crystals has not yet been reported, although several authors have (mis)interpreted stop gaps in emission as such [13–16]. A change of the spontaneous emission rate of a dipole is clearly an angle-integrated property, that can not be addressed by measuring the emission spectrum in one particular direction without further justification. Furthermore, a main complication is to find a proper reference system to which emission properties inside a photonic crystal can be compared, and to properly account for the role of luminescence quantum efficiency in the experiment. In this chapter, we examine the angle-independent spontaneous emission power from dyes in photonic crystals, compared to reference spectra obtained from chemically identical crystals with a much smaller lattice constant, for which the dye emission is in the long wavelength limit. We report broadband inhibition of spontaneous emission in strongly photonic titania air sphere crystals. This work opens up new research opportunities for studies of quantum optical phenomena in condensed matter environments.

4.2 Fermi's Golden Rule and quantum efficiency

The aim of the experiment presented in this chapter, is to verify the degree to which spontaneous emission is influenced by the photonic total or local radiative density of states (DOS, resp. LDOS) for frequencies in the pseudogap of titania inverse opals. The pseudo gap is the range of frequencies starting at and just above the L-gap, the stop gap associated with the lowest order Bragg diffraction (see Fig. 2.4). The local radiative density of states $N_{\rm rad}(\mathbf{r}, \hat{\mathbf{d}}, \omega)$ affects the radiative decay rate $\Gamma_{\rm rad}(\mathbf{r})$ of a dipole transition with transition frequency ω_0 at dipole position $\mathbf{r}$ through Fermi's Golden Rule according to

$$\Gamma_{\rm rad}(\mathbf{r}) = \frac{\pi\omega_0\mu^2}{3\hbar\varepsilon_0} N_{\rm rad}(\mathbf{r}, \hat{\mathbf{d}}, \omega_0), \tag{4.1}$$

where $\hat{\mathbf{d}}$ is the transition dipole orientation, and μ the transition dipole moment [17]. The most obvious experiment consists of taking a two level system, keeping the 'atom' part (ω_0 and μ) fixed, and comparing the decay rate Γ of a source at a well defined position in the crystal with the decay rate of the source in a reference system with a known local radiative density of states. For total DOS characterization, one would need to average the result over all source sites and orientations in the crystal unit cell. Such a measurement is based on having *(i)* a source with quantum efficiency near unity, *(ii)* a chemically identical reference system with controlled LDOS, and *(iii)* knowledge of or control over the location of the luminescent sources. In Sections 4.2 and 4.3, we explain the intricacies associated with the source quantum efficiency and discuss the optimal choice of reference satisfying these criteria.

In a time-resolved fluorescence measurement the recorded signal is proportional to the excited state population at time t, which decays with a decay rate Γ_{tot}. This total decay rate is determined by the sum of both the radiative and all nonradiative decay channels, and reads $\Gamma_{\text{tot}} = \Gamma_{\text{rad}} + \Gamma_{\text{NR}}$. Here the nonradiative decay rate Γ_{NR} results from all competing nonradiative decay channels. Evidently, changes in Γ_{rad} can only be determined from a dynamic measurement if the quantum efficiency $\eta = \Gamma_{\text{rad}}/\Gamma_{\text{tot}}$ is of order unity. At the risk of obscuring the discussion, we note that the quantum efficiency *depends on the source position* in the case of a spatially inhomogeneous local radiative DOS, unless nonradiative decay can be ruled out completely.

Naively, one might expect that the total emission power in a continuous wave (cw) experiment may also reflect the local radiative density of states, since a gap in the LDOS would obviously result in a total absence of emitted photons. However, closer examination shows that the total emission power is not indicative of the LDOS for sources with near unit quantum efficiency. We consider an effective two-level system that is pumped at a constant rate P. The excited state population is governed by

$$\frac{dN_2}{dt} = P - \Gamma_{\text{tot}} N_2 \tag{4.2}$$

and amounts to $N_2 = P/\Gamma_{\text{tot}}$ in the stationary case. The number of photons I emitted per unit time is the fraction η of decay instances $\Gamma_{\text{tot}} N_2$ in which a photon is actually emitted, *i.e.*, $I = \eta\Gamma_{\text{tot}} N_2 = \eta P = P\Gamma_{\text{rad}}/\Gamma_{\text{tot}}$. For unit quantum efficiency this relation simply states that every incident pump photon is converted into an emitted photon and implies that the emitted power at fixed pump rate is not related to the DOS. Still, this result apparently conflicts with the notion that the emitted power vanishes if the source frequency matches a gap in the DOS. This controversy is easily resolved by noting that a constant nonzero pump rate can not be achieved for identically zero decay rate, *i.e.*, in the case of a transition in the photonic band gap and unit quantum efficiency. Then, the pump rate drops to zero as soon as all light sources are excited. Generally, this saturation argument comes into play for pump energy densities W_D such that the absorption rate per emitter $\frac{W_D c}{\hbar\omega}\sigma_a$ (where σ_a is the absorption cross-section) is comparable to or larger than the decay rate Γ_{tot}. This regime is not met in the experiments reported in this thesis, but is automatically met if $\Gamma_{\text{tot}} = 0$. An alternative perspective originates from classical electromagnetic theory for a radiating dipole antenna [18]. In this picture, a constant pump rate corresponds to a dipole antenna in which a constant power is fed and which therefore radiates at a constant output power. As the local radiative density of states decreases, a larger dipole current is needed to input the same power. For a frequency in the gap an infinite current would be needed to drive the dipole at the specified power. The converse notion is at the heart of FDTD calculations [19], where the emitted power at given dipole current is used to determine the LDOS.

A most surprising result is obtained if one considers a system of low quantum efficiency. Then, the total decay rate $\Gamma_{\text{tot}} = \Gamma_{\text{NR}}(1 + \eta + O(\eta^2))$ is completely determined by the nonradiative decay channels. The emitted power $I = P\Gamma_{\text{rad}}/\Gamma_{\text{tot}} \cong P\Gamma_{\text{rad}}/\Gamma_{\text{NR}}$

is therefore an excellent signature of the radiative decay rate if it is referenced to a system with the same nonradiative decay channels. In conclusion, cw and time-resolved measurements can be used in complementary cases to probe the photonic density of states. For efficient sources the emission power only reflects the pump rate and the decay time reveals the LDOS. For inefficient sources on the other hand, the emission power reflects the LDOS, but the total decay time is not affected by the photonic environment.

4.3 Nonphotonic reference host

The choice of reference host in which to embed the chosen luminescent species is of prime importance for a comparison with the photonic system. It is essential that the reference system provides the same chemical environment as the photonic system to ensure an unchanged transition dipole moment, the same nonradiative decay rate and the same inhomogeneous broadening. Lifetime changes observed in several time-resolved experiments in which the refractive index mismatch in a photonic system was tuned by infilling with different solvents were rather due to changes in the transition dipole moment or chemical interactions [20], than to photonic effects [9, 10]. Indeed it is well known that, *e.g.*, the polarity of a solvent influences the emission properties of organic dyes. Furthermore it is clear from the discussion above, that especially in the case of a cw measurement, the reference material should provide the same nonradiative decay rate Γ_{NR} in order to make a comparison of emitted powers possible.

It is beneficial to choose a luminescence species with a large inhomogeneous linewidth if the emission power of inefficient sources is to be probed. Sources with a narrow *homogeneous* linewidth should be chosen to ensure that each emitter probes the local radiative DOS in a frequency window narrow compared to the spectral features of the LDOS. If an ensemble of sources is chosen with a large inhomogeneous linewidth, many frequencies can be probed independently but simultaneously. In addition, a large inhomogeneous linewidth facilitates comparison of the emitted power from photonic and reference systems, independent from differences in pump efficiency. Comparison of the emitted power for the photonic and reference system only reveals the variation of the LDOS unambiguously, if differences in the pump rate are accounted for. A priori, this necessitates quantifying the detection- and pump efficiency for both the photonic and reference experiment. For an inhomogeneously broadened lineshape, the ratio of the photonic to the reference spectrum of inefficient sources

$$\frac{I_{\text{photonic}}}{I_{\text{reference}}} = \frac{P_{\text{photonic}}}{P_{\text{reference}}} \frac{\Gamma_{\text{rad,photonic}}}{\Gamma_{\text{rad,reference}}} = A \frac{\langle N_{\text{rad,photonic}} \rangle(\omega)}{\langle N_{\text{rad,reference}} \rangle(\omega)} \tag{4.3}$$

reveals the frequency dependence of the *ratio* of the photonic and reference local radiative DOS (averaged over source positions $\mathbf{r}$ and orientations $\hat{\mathbf{d}}$, as $\langle\ \rangle$ indicates) over a large frequency range. The constant of proportionality A contains the differences in

pump- and detection efficiency, and can be eliminated if the ratio of $\langle N_{\mathrm{rad,photonic}}\rangle(\omega)$ to $\langle N_{\mathrm{rad,reference}}\rangle(\omega)$ is explicitly known at some specific frequency, particularly if the inhomogeneous spectrum of the photonic sample extends to frequencies below the window of photonic behavior.

Within the constraint of identical chemical composition, one may consider, *e.g.*, disordered titania composites, such as powders or pulverized samples as suitable references for experiments on titania inverse opals. However, such a material would be highly multiply scattering [21], possibly giving rise to a strongly modulated and position dependent local radiative DOS [22]. A titania inverse opal with a very small lattice constant on the other hand, is optimally suited as a reference environment. As outlined in Chapter 2, the band structure depends only on the normalized frequency $\omega a/2\pi c$. A crystal with small lattice parameter a will therefore only be photonic for large frequencies. For sufficiently small lattice constant, the spectrum of the emitter will probe the long wavelength regime of such chemically identical crystals. In this regime the crystals behave as weakly scattering effectively homogeneous media, and provide a DOS with a quadratic frequency dependence typical for a medium with the effective refractive index of the titania inverse opals.

4.4 Experiment

Analogous to the experiment documented in Chapter 3, we studied titania inverse opals with cubic lattice parameters $a = 430$ and 480 nm doped with the organic laser dye Rhodamine 6G (R6G), and with lattice parameter $a = 510$ nm doped with the organic laser dye Nile Blue [23]. These dyes feature emission spectra with a large inhomogeneous width of order 5000 cm^{-1}. The homogeneous linewidth is of order $\lesssim 170\ \mathrm{cm}^{-1}$, as borne out by photon echo experiments [24], and cavity enhanced emission of dye in microspheres [4, 25]. In addition to the aforementioned 'photonic' samples, titania inverse opals with lattice spacing $a = 350$ nm were prepared as reference hosts. The reference crystals, manufactured along the same preparation route as the 'photonic' samples, but starting from smaller template spheres, were doped with dye according to the same procedure used for the photonic samples. Explicitly, the R6G-doped samples were prepared by 30 min. immersion in a dilute ~ 1 μmol solution of R6G in ethanol, followed by rinsing and drying. Nile Blue samples were similarly immersed for 24 h., rinsed and dried, using a 70 μmol solution of Nile Blue in ethanol. To select emission from the bulk of the photonic crystals, the dye adsorbed near the external sample surface was irreversibly bleached by illuminating the crystals with an intense laser beam at the Bragg angle [26]. Bleaching was monitored by the saturation of the stop gap depth in the $\alpha = 0°$ emission spectrum, where α is the emission angle relative to the surface normal, which coincides with the 111 reciprocal lattice vector. For the reference samples, surface bleaching was attempted using the 457 nm line of an Argon laser at normal incidence. Bleaching of the reference samples caused an overall reduction of emission intensity at constant pump power, without introducing drastic changes of the angle-independent emission lineshapes. As the dye

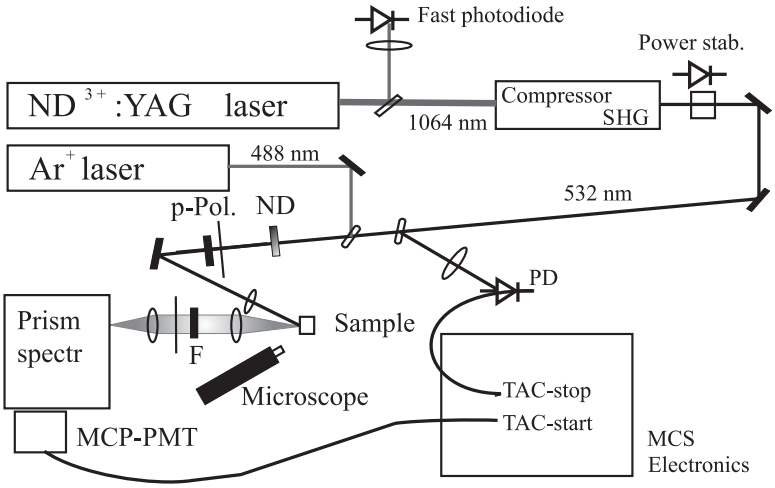

FIGURE 4.1: *Set up for time resolved and cw fluorescence experiments. Pulses from a mode-locked Nd^{3+}:YAG laser are pulse-compressed and frequency doubled. Mode locking is monitored by a fast photodiode, and the cw frequency-doubled power is actively stabilized. Part of the beam is split off onto a trigger diode (PD), while the remaining part is attenuated (ND filter), p-polarized, and focused onto the sample (see Fig. 3.1). Alignment of the sample is monitored using a long working distance microscope. Emission is focused onto the prims spectrometer entrance slit, filtered (F), detected by a microchannel plate photomultiplier tube (MCP-PMT), and recorded with a multichannel scaler (MCS). For cw measurements on R6G, the 488 nm line of an Argon laser was used.*

molecules are adsorbed onto the titania, our probe of the local radiative DOS is limited by the volume fraction of solid material, which comprises less than 12% of the unit cell volume.

The dye in the crystals was excited with a *p*-polarized laser beam emitted by cw Argon ion lasers[1] tuned to a wavelength of $\lambda = 488$ nm in the case of R6G-doped samples (see Fig. 4.1). For spectral measurements of emission from Nile-Blue doped samples, as well as for time-resolved fluorescence decay measurements, *p*-polarized emission from a mode-locked frequency-doubled Nd^{3+}:YAG laser was employed. The actively mode-locked Nd^{3+}:YAG laser (Spectra Physics 3800) generated 12 W average output power in TEM_{00} mode in 100-150 ps pulses (full width at half maximum) at a 80 MHz repetition rate. These pulses were shortened to 5–10 ps in a Spectra Physics 3595 fiber/grating pulse compressor to achieve a high power for second harmonic generation. The system was actively stabilized at a constant average power of $\sim$ 400 mW at 532 nm. In all experiments, the cw excitation power at the sample was below 10 μW focused to a spot 30 μm in diameter. Samples were mounted on a goniometer allowing to vary the detection angle α relative to the surface normal. Stop gaps in the emission spectra (see previous chapter) were used as a quality check

[1] In order of appearance: Spectra Physics 2016, Coherent Innova 90, Lexel 85

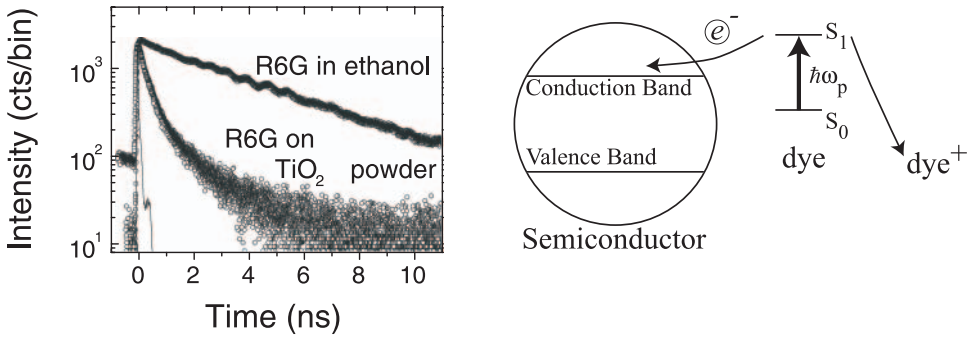

FIGURE 4.2: *(a) The decay of R6G adsorbed on titania powder is very fast compared to the single-exponential decay of R6G dissolved in ethanol (3.6 ns lifetime). The instrument response is shown for comparison (thin line). (b) Titania caused nonradiative decay of dye by electron transfer; the excited electron is transferred to the conduction band of the semiconductor, leaving the dye oxidized.*

of the crystals. The position of the pump spot on the sample, and the alignment of the sample and beam relative to the goniometer axis were monitored and controlled to within 20 μm using a small long working-distance microscope. Fluorescence was imaged onto the entrance slit of a Carl Leiss monochromator equipped with a flint prism. The slit width was set to accommodate the low count rates due to the limited dye concentrations, providing a resolution of $\sim$ 100 cm^{-1}. A Hamamatsu R3809U Micro Channel plate (MCP) detector was used to record the fluorescence. For time-resolved measurements, both the MCP signal and pulses from a trigger photodiode monitoring the pump beam were passed through constant fraction discriminators. The time lag between the MCP signal and trigger was fed to a multi-channel analyzer as a voltage generated by a time to amplitude converter (TAC). The MCP-pulses (average rate of $\lesssim 10^4$ s^{-1}) were used as TAC start pulses, while the trigger-diode output was connected to the TAC stop input. This time-correlated single-photon counting technique provides a resolution of 55 ps [27].

In order to verify the quantum efficiency of dye on titania, we measured the luminescence decay of dye on a powder of anatase titania particles (Aldrich). For R6G on titania (see Fig. 4.2) we find a very fast decay, characterized by a $\sim$ 500 ps decay time. After rapid decay over $\sim$ 1 decade, a slower time tail sets in. The luminescence decay of R6G dissolved in ethanol, on the other hand, is observed to be single-exponential with a decay time of 3.6 ns, as expected from literature [28]. Evidently, the quantum efficiency of R6G on titania is strongly reduced compared to the $\sim$ 95 % quantum efficiency in ethanol. We use the first moment of the data as a measure of the decay time. Comparison to the expected radiative decay rate (3.6 ns)$^{-1}$ yields an estimate of the quantum efficiency less than 10% [28, 29]. The relevant nonradiative decay mechanism for organic dyes on semiconductors is a well-documented electron-transfer process [30]. In this process the excited state of the dye has an energy above the con-

duction band of the TiO_2 to which it is adsorbed. After excitation the excited electron is transferred to the semiconductor, leaving the dye molecule oxidized. This efficient electron transfer process is the basis of the so-called 'organic solar cell' developed by O'Regan and Grätzel [31]. The oxazine dye Nile Blue has a low quantum efficiency $\lesssim 15\%$ both in solution [23] and on titania. Several schemes were considered to prevent the electron transfer in order to retain a high quantum efficiency. Any scheme in which the dye is incorporated in the crystal (for instance incorporated in small SiO_2 spheres) before the titania is formed is incompatible with the heating stage necessary to form and crystallize the titania, as dyes generally do not withstand temperatures in excess of 350°C. Coating of the TiO_2 surface with a $\sim$ 5 nm layer of SiO_2 prior to adsorbing the dye was demonstrated to prevent the electron transfer in the case of titania powders [32]. New methods are currently being developed to coat the inner surface of the titania air sphere crystals with such an insulating layer [33]. Given the low quantum efficiency of dyes on titania, we have designed a cw experiment to probe the photonic DOS.

As alternative luminescent species, quantum dots or lanthanide ions may be considered. Unfortunately, most colloidal quantum dots are not stable when exposed to air and water, do not usually have a quantum efficiency near unity, and may not be immune to electron transfer processes [34]. Still, quantum dots with inorganic coating (such as CdSe-ZnS/ZnSe/ZnS/CdS core-shell nanocrystals) to passivate the surface electronically and chemically appear to be among the most promising and flexible light sources for future experiments [35–38]. Rare earth ions on the other hand have the disadvantage of not providing an inhomogeneously broadened spectrum. Their narrow spectrum compared to the large bandwidth of the L-gap and pseudo gap, would necessitate a much larger set of lattice spacings a to map the LDOS over the normalized frequency ($\omega a/2\pi c$) range of interest. Furthermore, the efficiency of luminescence for rare earth ions strongly depends on the chemical environment, and is not well studied for titania hosts. Typically, efficient emission is obtained only after shielding the ions, using organic ligands for instance [39, 40].

4.5 Inhibition of emission and the DOS

Emission spectra at several detection angles for a R6G doped crystal with $a = 480$ nm are presented in Fig. 4.3. As described in Chapter 3, internal Bragg diffraction of the diffusely propagating luminescence causes clearly observable stop bands suppressing the spectra in angle-dependent frequency ranges, as apparent in Fig. 4.3(a). Before discussing the connection between angle-dependent, angle-integrated, and reference emission spectra, it is instructive to discuss the experimental signatures indicative of good or bad sample quality. Lineshapes reported on in this chapter (apart from Fig. 4.3(b)) are from samples with $a = 430$, 480 and 510 nm which showed clear stop gaps and well reproducing line shapes over extended sample areas. Of the many crystals with these lattice parameters examined in the experiment, a fraction $\approx 30\%$ was found for which emission spectra did not show any signature of photonic behavior.

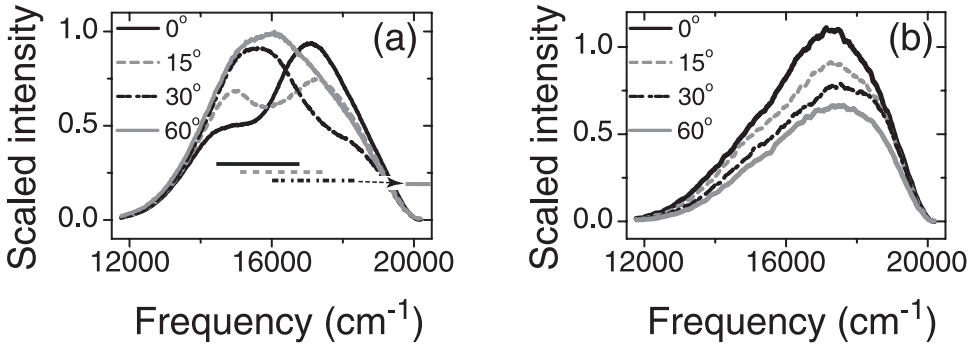

FIGURE 4.3: *(a) Internal Bragg diffraction causes strongly angle-dependent emission spectra (see Chapter 3) from well ordered photonic crystals (R6G, a = 480 nm). Horizontal bars indicate the stop bands that attenuate the spectra and shift to higher frequency with increasing angle (see Chapter 3). (b) Emission spectra of R6G on a apparently disordered sample made from a template with the same sphere size. No visible opalescence was discernible from the area coincident with the pump and detection focus.*

Several samples showed both areas resulting in clear stop gaps, and apparently disordered areas. In the latter cases, no stop gaps or gaps with depths less than 10% were found to affect the spectra, as apparent in Fig. 4.3(b) (a = 480 nm, R6G doped sample). Visual inspection of such samples or sample areas showed only faint or no opalescence, and SEM and optical microscopy indicated that large unstructured lumps of titania covered the sample surfaces. Such lumps may have been formed where the polystyrene template did not stick to the capillary walls during infiltration with the TiO_2 precursor. Emission lineshapes from these crystals, for which the fabrication was apparently not satisfactory, significantly differ from the emission lineshapes observed at any angle for the obviously photonic samples. Although lack of stop gaps, absence of opalescence, and the observation of solid titania chunks only provide information on surface quality, we regard these crystals as apparently disordered. Emission spectra from the apparently disordered samples resemble spectra from dye in the reference hosts, apart from a broadening. We note that crystals with bad surface quality can not be surface-selectively bleached by using a pump beam at the Bragg angle. Sets of spectra without stop gaps may therefore be mixtures of emission from dye near the surface, from dye in disordered, and from dye in ordered air sphere arrays. The 'photonic' spectra presented in this chapter were reproduced over sample areas at least $(\sim 0.5\ \mathrm{mm})^2$ in size, as probed by measuring lineshapes at many angles for a detection focus that was systematically scanned over grids with spacings 50 to 100 μm over the sample surfaces.

Figure 4.3(a) shows that the frequency range in which spectra are suppressed due to Bragg diffraction shifts to higher frequencies with increasing angle. Modification of the spectra ceased for angles α exceeding 60°. The line shapes were independent

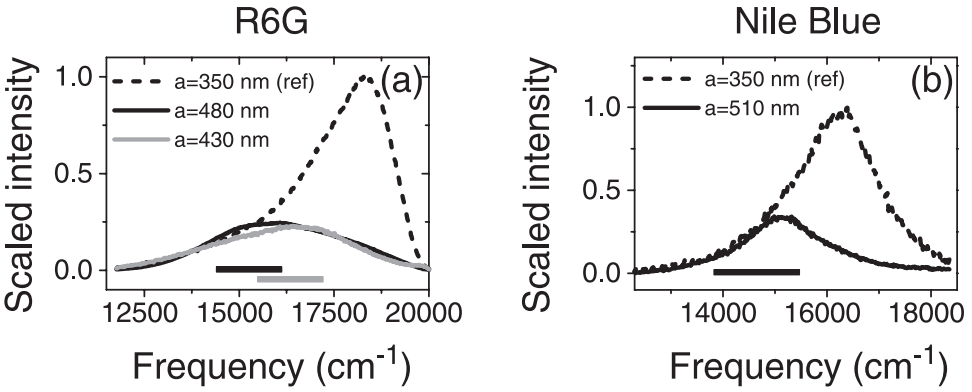

FIGURE 4.4: *(a) Emission spectra of R6G in TiO_2 inverse opals with a = 430, 480 nm (grey, resp. black) detected at $\alpha = 60°$ strongly differ from the angle-independent emission spectrum of R6G in a TiO_2 inverse opals with a = 350 nm (not photonic in the frequency range shown). (b) same for Nile Blue on a sample with a = 510 nm (black curve) and in the reference (a = 350 nm, dashed curve). Horizontal bars in both panels indicate the L-gaps of the relevant crystals (same color coding as the curves).*

of pump intensity, and the emission intensity was found to increase in proportion to the pump power. The $\alpha \geq 60°$ spectra are representative of the angle-averaged total emission power, as discussed below. The $\alpha = 60°$ spectra for R6G doped samples with a = 430, 480 nm differ significantly from spectra of R6G in reference samples with a = 350 nm, as shown in Fig. 4.4(a). A sizable reduction of emission power in the frequency window from ~ 15500 to 20000 cm^{-1} is apparent when the spectra are scaled to match on the low frequency side below any Bragg condition. The reduction, which occurs in a frequency window blue shifted relative to the L-gap, results in clear red shifts of the maximum emission frequencies. A similar spectral shift was observed when comparing $\alpha = 60°$ spectra of the Nile Blue sample (a = 510 nm) with its reference, see Fig. 4.4(b). The reference line shapes reproduced well on a multitude of reference samples, and were independent of angle, due to the fact that the lowest order Bragg diffraction occurs at 22000 cm^{-1}, far above the dye emission frequencies. The reduction is not due to differences in chemical interactions of the dye with its environment, since the reference samples are chemically identical to the photonic samples. Red shifts due to reabsorption are excluded, since the dye concentrations were sufficiently low by at least two orders of magnitude.

We extract the photonic LDOS effect on the total emission by dividing the $\alpha = 60°$ spectra by the emission spectrum of the same dye in the reference samples, as shown in Fig. 4.5 both for the R6G data sets with a = 480, 430 nm, and for the Nile Blue sample with a = 510 nm. Due to the low efficiency of these dyes on titania, the intensity ratios, which are scaled to unity on the low frequency shoulder, represent the LDOS probed by the dye, divided by the reference LDOS. The lowest order stop gap of the

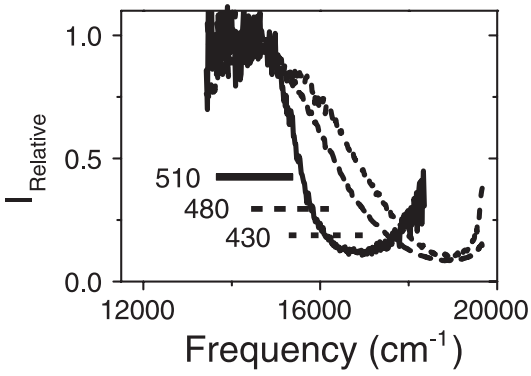

FIGURE 4.5: *Intensity ratios of spectra in Fig. 4.4 to the reference spectrum for R6G, with a = 480 nm (dashed) and a = 430 nm (dotted) and Nile Blue, for a = 510 nm to the Nile Blue reference spectrum. The inhibition shifts to the red with increasing lattice constant a. Horizontal bars indicate the L-gaps.*

reference samples at 22000 cm^{-1} is far above the dye spectrum. Hence, the reference LDOS has a well defined quadratic frequency dependence [41, 42]. The width of the inhibition range $\sim$ 2000 cm^{-1}, *i.e.*, 13% of the L-gap center frequency, attests to the strongly photonic character of the inverse opals. The inhibition range is blue shifted relative to the L-gap. Indeed, from a simple angle-dependent stop-gap consideration one expects that the blue edge of the L-gap corresponds to the frequency for which the largest fraction of solid angle is simultaneously contained in a stop gap [43]. The shift of the inhibition to higher frequency with smaller lattice parameter, confirms that the spectral changes are due to the photonic crystal properties.

A crucial observation is that the $\alpha = 60°$ spectra are representative of the spectral distribution of angle-averaged luminescence in the bulk. Due to the bleaching it is clear that all the luminescence is generated in the bulk of the photonic crystal, and the surface LDOS does not play a role. Still, the surface crystal layers affect the angle-dependent emission spectra through internal reflection. Here, we explain how the angle-averaged luminescence can be extracted from the angle-resolved spectra. Scattering by disorder plays a key role in the interpretation. Since the transport mean-free path $\sim$ 15 μm [44] is much smaller than the sample thickness $\sim$ 200 μm, the luminescence propagates diffusively through the bulk of the crystals. The spectral distribution $W(\omega)$ of the diffuse luminescence in the bulk is the 4π sr average of spectra of all dye molecules in the pump volume, and is thus determined only by the LDOS and the inhomogeneous line broadening of the dye. The diffuse luminescence acquires an angular dependence only when it exits the sample, as explained in Chapter 3. This angle and frequency-dependent modification of the diffuse luminescence spectrum is due to internal Bragg diffraction [45] and may be calculated from diffusion theory with internal reflection [46–48]. In Chapter 7 the applicability of this model will be discussed, based on theory and on experiments us-

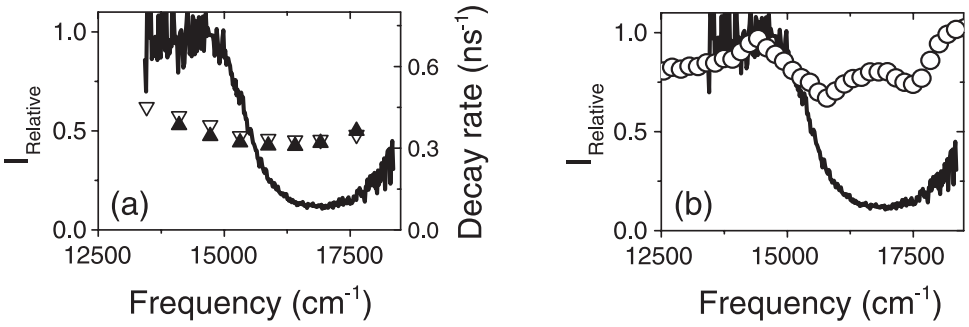

FIGURE 4.6: *(a) Black curve: intensity ratio for Nile Blue, a = 510 nm taken from Fig. 4.5 for comparison with the spectrally resolved fluorescence decay rates of Nile Blue in the reference (closed triangles) and photonic crystal (open triangles). No significant difference is observed, due to the low quantum efficiency. (b) Black curve as in (a). The open circles indicate the total DOS calculated for a titania inverse opal a = 510 nm, divided by ω^2 and scaled to match on the low frequency edge.*

ing diffuse light injected by externally incident plane waves. According to diffusion theory, the diffuse intensity escaping in an angular range from α to $\alpha + d\alpha$ equals $\frac{3}{2}W(\omega)\cos\alpha[\tau_e(\omega) + \cos\alpha][1 - R(\alpha,\omega)]\,d(\cos\alpha)$. For exit angles *outside* a stop gap (*i.e.*, $\alpha \geq 60°$), the internal reflection coefficient $R(\alpha,\omega)$ vanishes for all emission frequencies. Hence, the frequency dependence of the measured spectrum at $\alpha \geq 60°$ is only determined by the angle-integrated emission spectrum $I(\omega)$, and the so-called extrapolation length ratio $\tau_e(\omega)$. This frequency-dependent parameter is related to the angle and polarization averaged internal reflection coefficient [47, 48], and can be derived from $R(\alpha,\omega)$ according to Eqs. (7.1,7.17) (see Ref. [47, Eq. (2.22) and (3.5–3.9)]). We estimate the internal reflection coefficient $R(\alpha,\omega)$ to be less than 70% for directions within a stop gap [45], and 0% outside. For $\alpha = 60°$, we find that the extraction efficiency, $\tau_e(\omega) + \frac{1}{2}$, increases by less than 30% as the frequency increases from the red to the blue edge of the L-gap, and linearly decreases by less than 10% as the frequency is increased to the blue edge of the emission spectra. Consequently, the $\alpha = 60°$ emission spectra are representative of the spectral distribution of diffuse luminescence $W(\omega)$ in the bulk to within better than 30%. We conclude that the large difference of up to a factor 5 between the $\alpha = 60°$ emission spectra from the photonic crystals and reference spectra in Fig. 4.4 is due to a large change in the angle-integrated total emission power. Given the low efficiency of the emitters, such a reduced emission reflects the modulation of the photonic LDOS. Detailed analysis shows that the true inhibition of total emission may even exceed the lineshape ratio in Fig. 4.5, due to a slightly enhanced extraction efficiency for $\alpha = 60°$ for frequencies in the inhibition band.

For comparison with the cw experiment, we have performed time resolved measurements for the Nile Blue doped samples, shown in Fig. 4.6(a). No significant difference is apparent between total decay rates in the photonic crystal and the reference,

neither for frequencies below, or in the range of inhibited radiative decay evident from the spectra. It appears that the low quantum efficiency precludes determination of the radiative decay rate from a dynamic measurement, but allows to extract changes in radiative decay rate from the emitted power. A lengthening of the radiative lifetime according to the inhibition in Fig. 4.5, causes a variation $\lesssim 10\%$ of the total lifetime for a quantum efficiency of 10%. This variation is within the wavelength dependence of the lifetime on individual samples. Furthermore our limited dynamic range, set by the pump pulse repetition rate, does not allow unambiguous observation of lengthened lifetimes. Lacking efficient emitters on semiconductors such as TiO_2 [30], the complementary experiments in which a lengthening of the total lifetime is expected currently remain out of reach. In view of the large magnitude of the inhibition of emission on titania, recently developed silica, zirconia, and alumina air sphere crystals may prove to be sufficiently photonic for such experiments, despite the lower index contrast. These host materials do not cause quenching by electron transfer [33].

Remarkably, the magnitude of the reduction in emitted power, amounting to at least a factor 5 relative to the low frequency edge, exceeds the reduction in total solid angle for light propagation. The reduction in solid angle for light propagation amounts to a factor 2, which is a simple estimate of the reduction of the total DOS [43]. To investigate this further, we have calculated the total DOS using the H-field inverted matrix technique [42, 49], and the *fcc* Brillouin zone integration scheme [50] explained in Chapter 2. Eigenfrequencies were calculated on a coarse grid of 2480 k-points spanning the irreducible part of the Brillouin zone, using 725 plane waves. To describe the dielectric structure, we used the model presented in Chapter 3, in which close-packed air spheres are assumed, surrounded by shells of titania ($\varepsilon = 6.5$) with cylindrical windows between neighboring spheres. This model predicts reflectivity features in excellent agreement with prior experiments [51], both in the range of first and second order Bragg diffraction (*i.e.*, up to band 9), and is in agreement with structural data. As shown in Fig. 4.6(b), the total DOS, normalized by the quadratic DOS in the reference samples is indeed reduced in a frequency range coincident with the experimentally determined inhibition window. The modulation of the total DOS, however, amounts to even less than the factor of 2 estimated from the reduction in total solid angle of allowed propagation directions. Clearly, a complete understanding of the large reduction of the emitted power requires a full calculation of the *local* DOS, taking the spatial distribution and dipole orientation of the emitters into account. In the experiment presented here, the spatial distribution of emitters limits the probe volume to those $\sim 6-12\%$ of the unit cell occupied by titania. Future experiments using, *e.g.*, atomic vapors as emitters, may allow to probe the local DOS over the remaining unit cell volume. Calculating the local DOS averaged over *part of* the unit cell currently remains a formidable task beyond the scope of this thesis. As yet, the local DOS of realistic three-dimensional structures has only been calculated for a limited number of positions in the unit cell by less than a handful of authors [41, 42, 52]. We note that a time-resolved decay measurement for efficient

fluorescent sources would not show a simple single exponential decay, but would be composed of contributions from sources with different decay times depending on the LDOS at their positions. The first moment of the intensity distribution over time should correspond to the source-averaged reduction in emission power reported in this chapter. In view of the expected complexity of the fluorescence decay of ensembles of sources, it is of prime importance to develop combinations of light sources and photonic crystal materials for which the decay dynamics in absence of LDOS variations is completely understood, and which feature a high quantum efficiency.

4.6 Conclusion

We have observed for the first time inhibition of spontaneous emission in a photonic crystal. This is a first demonstration of the feasibility of creating novel solid state photonic environments that allow experiments shielded from vacuum fluctuations. We have demonstrated that inhibition occurs over a large frequency bandwidth, in accordance with theoretical predictions. The extraordinarily large inhibition compared to the expected variation of the total DOS shows that far reaching spontaneous emission control may even be realized without a full photonic band gap. Central issues to master such control, however, revolve around *(i)* quantitative knowledge of the local density of states throughout the unit cell, *(ii)* control over the locations of the emitters, and most importantly *(iii)* the luminescence quantum efficiency. Each photonic crystal backbone material, usually chosen on the merit of large real and small imaginary dielectric constant, will pose different challenges if efficient emitters are called for. The electron transfer processes occurring on semiconductors like titania simply present an illustrative example of such a specific constraint due to materials issues. Finally, we have shown the relevance of structural disorder in the interpretation of emission experiments.

References

[1] S. Haroche, in *Systèmes Fondamentaux en Optique Quantique / Fundamental Systems in Quantum Optics*, edited by J. Dalibard, J. M. Raimond, and J. Zinn-Justin (North-Holland, Amsterdam, 1992), Chap. 13, pp. 767–940.

[2] K. H. Drexhage, H. Kuhn, and F. P. Schäfer, *Variation of the Fluorescence Decay Time of a Molecule in Front of a Mirror*, Ber. Bunsenges. Phys. Chem. **72**, 329 (1968).

[3] D. J. Heinzen, J. J. Childs, J. E. Thomas, and M. S. Feld, *Enhanced and Inhibited Visible Spontaneous Emission by Atoms in a Confocal Resonator*, Phys. Rev. Lett. **58**, 1320 (1987).

[4] A. J. Campillo, J. D. Eversole, and H.-B. Lin, *Cavity Quantum Electrodynamic Enhancement of Stimulated Emission in Microdroplets*, Phys. Rev. Lett. **67**, 437 (1991).

[5] P. Andrew and W. L. Barnes, *Forster Energy Transfer in an Optical Microcavity*, Science **290**, 785 (2000).

[6] E. Yablonovitch, *Inhibited Spontaneous Emission in Solid-State Physics and Electronics*, Phys. Rev. Lett. **58**, 2059 (1987).

[7] *Photonic Band Gap Materials*, edited by C. M. Soukoulis (Kluwer, Dordrecht, 1996).

[8] *Photonic Crystals and Light Localization in the* 21st *Century*, edited by C. M. Soukoulis (Kluwer, Dordrecht, 2001).
[9] J. Martorell and N. M. Lawandy, *Observation of Inhibited Spontaneous Emission in a Periodic Dielectric Structure*, Phys. Rev. Lett. **65**, 1877 (1990).
[10] E. P. Petrov, V. N. Bogomolov, I. I. Kalosha, and S. V. Gaponenko, *Modification of the Spontaneous Emission of Dye Molecules in Photonic Crystals*, Acta Phys. Pol. A **94**, 761 (1998).
[11] M. Megens, J. E. G. J. Wijnhoven, A. Lagendijk, and W. L. Vos, *Fluorescence Lifetimes and Linewidths of Dye in Photonic Crystals*, Phys. Rev. A **59**, 4727 (1999).
[12] Z.-Y. Li and Z. Q. Zhang, *Weak Photonic Band Gap Effect on the Fluorescence Lifetime in Three-Dimensional Colloidal Photonic Crystals*, Phys. Rev. B **63**, 125106 (2001).
[13] S. V. Gaponenko, A. M. Kapitonov, V. N. Bogomolov, A. V. Prokofiev, A. Eychmüller, and A. L. Rogach, *Electrons and Photons in Mesoscopic Structures: Quantum Dots in a Photonic Crystal*, JETP Lett. **68**, 142 (1998).
[14] K. Yoshino, S. B. Lee, S. Tatsuhara, Y. Kawagishi, M. Ozaki, and A. A. Zakhidov, *Observation of Inhibited Spontaneous Emission and Stimulated Emission of Rhodamine 6G in Polymer Replica of Synthetic Opal*, Appl. Phys. Lett. **73**, 3506 (1998).
[15] A. Blanco, C. López, R. Mayoral, H. Míguez, F. Meseguer, A. Mifsud, and J. Herrero, *CdS Photoluminescence Inhibition by a Photonic Structure*, Appl. Phys. Lett. **73**, 1781 (1998).
[16] S. G. Romanov, T. Maka, C. M. Sotomayor-Torres, M. Müller, and R. Zentel, *Suppression of Spontaneous Emission in Incomplete Opaline Photonic Crystals*, J. Appl. Phys. **91**, 9426 (2002).
[17] E. Fermi, *Quantum Theory of Radiation*, Rev. Mod. Phys. **4**, 87 (1932).
[18] J. D. Jackson, *Classical Electrodynamics* (John Wiley & Sons, New York, 1975).
[19] Y. Xu, R. K. Lee, and A. Yariv, *Quantum Analysis and the Classical Analysis of Spontaneous Emission in a Microcavity*, Phys. Rev. A **61**, 033807 (2000).
[20] B. Y. Tong, P. K. John, Y. T. Zhu, Y. S. Liu, S. K. Wond, and W. R. Ware, *Fluorescence-Lifetime Measurements in Monodispersed Suspensions of Polystyrene Particles*, J. Opt. Soc. Am. B **10**, 356 (1993).
[21] R. H. J. Kop, P. de Vries, R. Sprik, and A. Lagendijk, *Observation of Anomalous Transport of Strongly Multiple Scattered Light in Thin Disordered Samples*, Phys. Rev. Lett. **79**, 4369 (1997).
[22] B. A. van Tiggelen and E. Kogan, *Analogies Between Light and Electrons-Density-of-States and Friedels Identity*, Phys. Rev. A **49**, 708 (1994).
[23] U. Brackmann, *Lambdachrome Laser Dyes* (Lambda Physik GmbH, Göttingen, 1997).
[24] P. C. Becker, H. L. Fragnito, J. Y. Bigot, C. H. Brito Cruz, R. L. Fork, and C. V. Shank, *Femtosecond Photon Echoes from Molecules in Solution*, Phys. Rev. Lett. **63**, 505 (1989).
[25] M. D. Barnes, W. B. Whitten, S. Arnold, and J. M. Ramsey, *Homogeneous Linewidths of Rhodamine 6G at Room Temperature from Cavity-Enhanced Spontaneous Emission Rates*, J. Chem. Phys. **97**, 7842 (1992).
[26] M. Megens, J. E. G. J. Wijnhoven, A. Lagendijk, and W. L. Vos, *Light Sources Inside Photonic Crystals*, J. Opt. Soc. Am. B **16**, 1403 (1999).
[27] D. Bebelaar, *Time Response of Various Types of Photomultipliers and its Wavelength Dependence in Time-Correlated Single-Photon Counting with an Ultimate Resolution of 47 Ps*, Rev. Sci. Instr. **57**, 1116 (1986).
[28] P. R. Hammond, *Self-Absorption of Molecular Fluorescence, the Design of Equipment for Measurement of Fluorescence Decay, and the Decay Times of some Laser Dyes*, J. Chem.

Phys. **70**, 3884 (1979).
[29] R. G. Kubin and A. N. Fletcher, *Fluorescence Quantum Yields of some Rhodamine Dyes*, J. Lumin. **27**, 455 (1982).
[30] P. V. Kamat, *Photochemistry on Nonreactive and Reactive (Semiconductor) Surfaces*, Chem. Rev. **93**, 267 (1993).
[31] B. O' Regan and M. Grätzel, *A Low-Cost, High-Efficiency Solar-Cell Based on Dye-Sensitized Colloidal TiO_2 Films*, Nature **353**, 737 (1991).
[32] L. Bechger, A. F. Koenderink, and W. L. Vos, *Emission Spectra and Lifetimes of R6G Dye on Silica-Coated Titania Powder*, Langmuir **18**, 2444 (2002).
[33] L. Bechger, *in preparation*, Ph.D. thesis, Universiteit Twente, 2003.
[34] E. P. A. M. Bakkers, E. Reitsma, J. J. Kelly, and D. Vanmaekelbergh, *Excited-State Dynamics in CdS Quantum Dots Adsorbed on a Metal Electrode*, J. Phys. Chem. B **103**, 2781 (1999).
[35] C. B. Murray, D. J. Norris, and M. G. Bawendi, *Synthesis and Characterization of Nearly Monodisperse CdE (E=S, Se, Te) Semiconductor Nanocrystallites*, J. Am. Chem. Soc. **115**, 8706 (1993).
[36] B. O. Dabbousi, J. Rodriguez-Viejo, F. V. Mikulec, J. R. Heine, H. Mattousi, R. Ober, K. F. Jensen, and M. G. Bawendi, *(CdSe)ZnS Core-Shell Quantum Dots: Synthesis and Characterization of a Size Series of Highly Luminescent Nanocrystallites*, J. Phys. Chem. B **101**, 9463 (1997).
[37] X. Peng, M. C. Schlamp, V. Kadavanich, and A. P. Alivisatos, *Epitaxial Growth of Highly Luminescent CdSe/CdS Core/Shell Nanocrystals with Photostability and Electronic Accessibility*, J. Am. Chem. Soc **119**, 7019 (1997).
[38] C. de Mello Donegá, S. G. Hickey, S. F. Wuister, D. Vanmaekelbergh, and A. Meijerink, *Single-Step Synthesis to Control the Photoluminescence Quantum Yield and Size Dispersion of CdSe Nanocrystals*, J. Phys. Chem. B **107**, 489 (2003).
[39] F. J. P. Schuurmans, *Light in Complex Dielectrics*, Ph.D. thesis, University of Amsterdam, 1999.
[40] A. Polman, *Erbium as a Probe of Everything ?*, Physica B **300**, 78 (2001).
[41] T. Suzuki and P. K. L. Yu, *Emission Power of an Electric-Dipole in the Photonic Band-Structure of the Fcc Lattice*, J. Opt. Soc. Am. B **12**, 570 (1995).
[42] K. Busch and S. John, *Photonic Band Gap Formation in Certain Self-Organizing Systems*, Phys. Rev. E **58**, 3896 (1998).
[43] M. S. Thijssen, R. Sprik, J. E. G. J. Wijnhoven, M. Megens, T. Narayanan, A. Lagendijk, and W. L. Vos, *Inhibited Light Propagation and Broadband Reflection in Photonic Air-Sphere Crystals*, Phys. Rev. Lett. **83**, 2730 (1999).
[44] A. F. Koenderink, M. Megens, G. van Soest, W. L. Vos, and A. Lagendijk, *Enhanced Backscattering from Photonic Crystals*, Phys. Lett. A **268**, 104 (2000).
[45] H. P. Schriemer, H. M. van Driel, A. F. Koenderink, and W. L. Vos, *Modified Spontaneous Emission Spectra of Laser Dye in Inverse Opal Photonic Crystals*, Phys. Rev. A **63**, 011801 (2001).
[46] A. Lagendijk, R. Vreeker, and P. de Vries, *Influence of Internal Reflection on Diffusive Transport in Strongly Scattering Media*, Phys. Lett. A **136**, 81 (1989).
[47] J. X. Zhu, D. J. Pine, and D. A. Weitz, *Internal Reflection of Diffusive Light in Random Media*, Phys. Rev. A **44**, 3948 (1991).
[48] D. J. Durian, *Influence of Boundary Reflection and Refraction on Diffusive Photon Transport*, Phys. Rev. E **50**, 857 (1994).
[49] H. S. Sözüer, J. W. Haus, and R. Inguva, *Photonic Bands: Convergence Problems with the*

Plane-Wave Method, Phys. Rev. B **45**, 13962 (1992).
[50] H. J. Monkhorst and J. D. Pack, *Special Points for Brillouin-Zone Integrations*, Phys. Rev. B **13**, 5188 (1976).
[51] H. M. van Driel and W. L. Vos, *Multiple Bragg Wave Coupling in Photonic Band-Gap Crystals*, Phys. Rev. B **62**, 9872 (2000).
[52] Z.-Y. Li, L. L. Lin, and Z. Q. Zhang, *Spontaneous Emission from Photonic Crystals: Full Vectorial Calculations*, Phys. Rev. Lett. **84**, 4341 (2000).

Chapter 5

Ultra-fast Switching of the Density of States and of Photonic Band Gaps

We demonstrate theoretically that the photonic density of states of three-dimensional semiconductor photonic crystals can be switched on a femtosecond time scale through two-photon excitation of free carriers. Density of states calculations for GaAs inverse opals show that realistic excitation pulses induce a large shift in frequency and a change in width of the photonic band gap. Depending on the frequency, several basic switching schemes are possible, such as switching the DOS from a high value to zero, from zero to a high value, and from high to zero to high on ~ 100 *fs timescales, independent of the relaxation time of the semiconductor. This switching method allows for ultrafast control of spontaneous emission and cavities on time scales comparable to spontaneous emission and cavity dynamics.*

5.1 Introduction

In recent years, many proposals have been put forward for the use of photonic crystals in studying novel quantum optics and for applications in modern opto-electronics [1, 2]. To date, such proposals as well as the experiments have focused on the properties of photonic crystals with a fixed dielectric constant and structure. Clearly the potential of photonic crystals can be strongly enhanced if the photonic band structure and band gap can somehow be controlled as a function of time. In this chapter we propose a method to switch the density of states (DOS) in photonic crystals. Contrary to several other suggestions to switch photonic crystals [3–8], we investigate a scheme that achieves extremely large modifications of the DOS on ultrafast time scales of $\sim$ 100 fs. The switching mechanism is based on refractive index changes in the photonic crystal backbone due to two-photon excitation of free carriers. It will be demonstrated that, for a given frequency window, the density of states can be swept from a high value to zero, from zero to a high value and even from high through zero back to a high value. Such switching schemes may be important for, *e.g.*, manipulating the emission of excited atoms with appropriately chosen transi-

tion frequencies [9, 10]. Such atoms could for instance first be 'frozen' in the excited state, until the DOS is switched from inhibiting spontaneous emission to a high value ($\sim$ 10 times above vacuum) resulting in a sudden accelerated decay. Also, the ability to quickly open and close the gap may allow photons to be encaged near defect cavities for a specified period of time. These examples underline both the fundamental interest, and the usefulness for applications involving, *e.g.*, lasers or optical information processing, of ultrafast switching of the density of states [11].

The switching technique presented here is also applicable to the switching of Bragg diffraction and concomitant stop gaps [3, 4, 6–8]. The same switching technique may therefore be applied to, *e.g.*, switchable Bragg reflectors, or for instance to the fast switching of beam steering devices, by manipulating the superprismatic properties due to the curvature of the photonic dispersion surfaces in time [12, 13]. In fact, switching of Bragg diffraction by two-photon excitation of free carriers has recently been demonstrated for two-dimensional silicon photonic crystals by Leonard and coworkers [14]. It is important to note that photonic band gap switching is distinct from the switching of Bragg diffraction conditions. The dispersive effects listed above may also be produced and switched in weakly photonic structures without a full band gap, or lower dimensional structures. At a given frequency in a stop gap, however, the change in DOS is usually small. Only switching of 3D structures allows complete control over the photonic density of states.

5.2 Switching mechanisms for photonic crystals

Control over the optical properties of photonic crystals can be achieved by either changing the complex index of refraction ($n' + in''$) of one or more of the constituent materials, or by changing the geometry of the unit cell or the lattice spacing in time. Tuning of the lattice spacing in time appears to be viable only for the tuning of Bragg diffraction, as it depends on mechanical properties of materials that can only be used for fabrication of weakly photonic crystals. Examples include tuning of lattice parameters of colloidal arrays embedded in polymeric hydrogel, which expands as a function of pH or temperature [3], and elastic deformation of polymer photonic crystals [15]. It does not appear possible to switch or tune the geometrical arrangement of composite structures of air and semiconductor backbone, the materials of choice to achieve a photonic band gap. Modulating the semiconductor backbone density by a compressive sound wave may give rise to small refractive index changes. The switching speed and uniformity would be limited by ultrasound absorption at high acoustic frequencies (GHz range).

Several methods to switch the complex index of refraction of one or more of the constituent materials of a photonic crystal have been put forward [4, 6–8]. Such a time-resolved technique can be judged by at least four factors: *(i)* the magnitude of the relative change in the real part of the refractive index n', which determines the degree to which a gap in the density of states can be modified, *(ii)* the degree to which induced optical absorption as gauged by n'' is minimized, *(iii)* the time scale over

which inducing and relaxation of the index change occurs, and *(iv)* the uniformity of the change in the 3D composite. In this chapter we propose optical pumping of free carriers in semiconductor photonic crystals via two-photon absorption as an excellent way of switching the properties of 3D photonic crystals. With a careful choice of material, pump frequency, pump intensity and pulse width, this switching technique is optimal with respect to the four criteria listed above.

To change the refractive index contrast, the solid semiconductor backbone with bulk dielectric constant ε_{BG} of a photonic crystal is excited with an optical pulse to create a free-carrier plasma through two-photon absorption. Recent results [16–18] indicate that the complex index of refraction of semiconductors in which moderately high densities of free carriers are excited is well described by the Drude model [19, 20]. According to the Drude model, the frequency dependent complex conductivity of free carriers

$$\sigma(\omega) = \frac{\sigma_0}{1 - i\omega\tau} \quad \text{with} \quad \sigma_0 = \frac{Ne^2\tau}{m}, \tag{5.1}$$

is determined by the carrier density N, charge e, effective mass m and the momentum relaxation time τ. Adding contributions of holes and electrons, which are created in equal amount, and incorporating the conductivity in the dielectric constant according to $\varepsilon(\omega) = \varepsilon_{BG}(\omega) + i\sigma/\varepsilon_0\omega$, the textbook results for the real part of ε at frequency ω

$$\varepsilon'(\omega) = \varepsilon'_{BG}(\omega) - \frac{Ne^2}{\varepsilon_0}\left(\frac{1}{m_e}\left(\frac{\tau_e^2}{1+\omega^2\tau_e^2}\right) + \frac{1}{m_h}\left(\frac{\tau_h^2}{1+\omega^2\tau_h^2}\right)\right) \tag{5.2}$$

and the imaginary part

$$\varepsilon''(\omega) = \varepsilon''_{BG}(\omega) + \frac{Ne^2}{\omega\varepsilon_0}\left(\frac{1}{m_e}\left(\frac{\tau_e}{1+\omega^2\tau_e^2}\right) + \frac{1}{m_h}\left(\frac{\tau_h}{1+\omega^2\tau_h^2}\right)\right) \tag{5.3}$$

are obtained [20]. For the purpose of demonstrating the switching potential, the backbone of the photonic crystal is assumed here to be a crystalline GaAs *fcc* inverse opal, a structure that may be realized in the near future. Free carrier excitation, however, is easily achieved in any semiconductor material. We take parameters relevant for GaAs from Ref. [21] (see Fig. 5.1). The optimum excitation for switching the photonic crystal properties maximizes the change in the real part of the refractive index, while keeping the increase in the imaginary part to a minimum to prevent photons from being absorbed. For the present proposal, the limit $\omega\tau_{e,h} \gg 1$ is relevant, and absorption is assumed not to occur in the unswitched semiconductor (*i.e.* $\varepsilon''_{BG} = 0$). In this case, the dielectric constant can be approximated by

$$\varepsilon(\omega) \approx \varepsilon_{BG} - \frac{\omega_p^2}{\omega^2}\left(1 - \frac{i}{\omega\tau}\right) \tag{5.4}$$

with $\tau \sim \tau_e \sim \tau_h$ and the plasma frequency defined as $\omega_p = Ne^2/\varepsilon_0 m$ (with $m^{-1} = m_e^{-1} + m_h^{-1}$). Consequently, the real and imaginary part of the refractive index can be

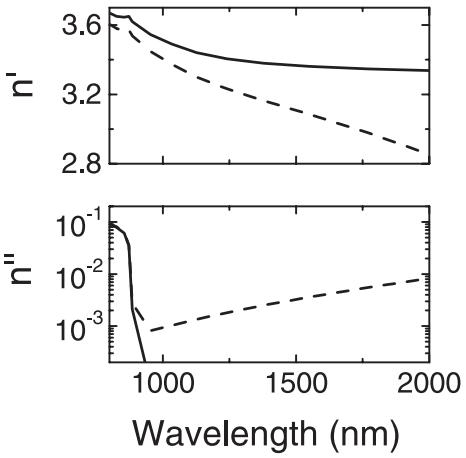

Room temperature parameters GaAs	
m_e	$0.065m_0$
m_h	$0.51m_0$
m_0	9.12×10^{-31} kg
τ_e	9.25×10^{-14} s
τ_h	2.18×10^{-14} s

FIGURE 5.1: *Real and imaginary part n' (top) resp. n'' (bottom) of the refractive index of crystalline GaAs before (solid) and after (dashed) excitation of a free carrier plasma. The excitation described here (corresponding to a free carrier density $N = 4.8 \times 10^{19}$ cm^{-3}) requires a 0.1 μJ pulse to excite a $(20\ \mu m)^3$ region. Values for the electron- and hole effective masses $m_{e,h}$ and the momentum relaxation times $\tau_{e,h}$ at high carrier densities and room temperature are tabulated on the right [21].*

approximated as

$$n' \approx \sqrt{\varepsilon_{\mathrm{BG}} - \frac{\omega_p^2}{\omega^2}} \quad \text{and} \quad n'' \approx \frac{1}{2n'} \frac{\omega_p^2}{\omega^2} \frac{1}{\omega\tau}, \tag{5.5}$$

where the ratio ω_p/ω of the plasma frequency to the probe frequency ω is assumed to remain smaller than $\varepsilon_{\mathrm{BG}}$. For refractive index switching by free carriers, the plasma frequency is the essential switching parameter. For probe frequencies of the order of the plasma frequency ($\omega_p/\omega \sim 1$) the change in the real part of the refractive index n' is large, while the damping can remain limited, given the estimates $\omega\tau_{e,h} \sim 10^2$. An optimal refractive index change can be achieved at a moderate free-carrier density of $N = 4.8 \times 10^{19}$ cm^{-3}, *i.e.*, $\omega_p = 1.6 \times 10^{15}$ Hz. The effect of such an optical free carrier excitation in GaAs, according to Eq. (5.2, 5.3) is shown in Figure 5.1, which reveals a change in n' from 3.36 to 3.08, for a probe wavelength $\lambda = 1500$ nm. This change is large compared to, *e.g.*, the effect of nonlinear switching techniques as discussed in Section 5.5. Sizable changes in n' on femtosecond time scales induced by ultrafast optical excitation have recently been observed in experiments on bulk GaAs [17].

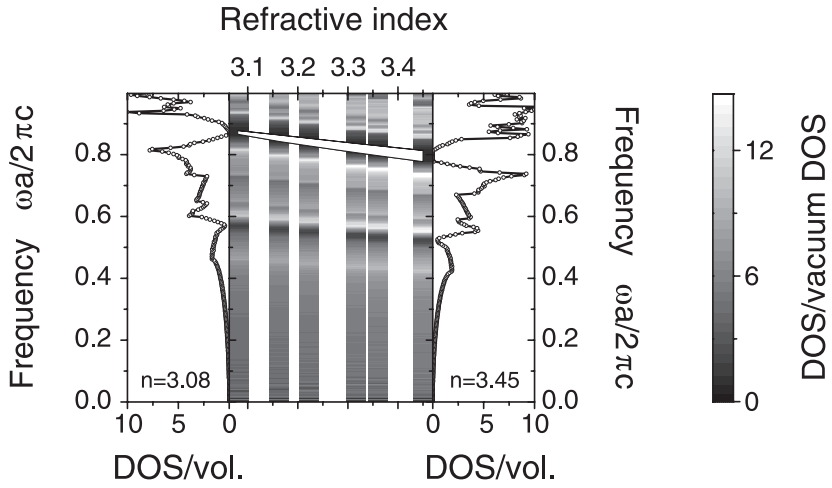

FIGURE 5.2: *Dependence of the density of states for an inverse opal of close packed air spheres on the refractive index of the semiconductor backbone n' in the range from* 3.06 *(excited GaAs) to* 3.45 *(unexcited Si). Leftmost- and rightmost panel show the DOS per unit volume for the two limiting index contrasts; contour plots of DOS per unit volume normalized to* $(\omega a/2\pi c)^2$ *show that the changes in the DOS are dominated by a shift in frequency of all spectral features, due to the change in effective refractive index. Furthermore the band gap (white bar) narrows with decreasing backbone refractive index n'.*

5.3 Effect on DOS: possible experiments

To quantitatively predict the effect of excitation of the semiconductor backbone on the properties of the photonic crystal, we have calculated the density of states for a nonabsorbing *fcc* close-packed inverted opal with refractive indices in the range $3.08 \leq n' \leq 3.45$. This range includes the experimentally achievable index range for GaAs ($3.08 \leq n' \leq 3.36$) or Si. The DOS, shown in Figure 5.2 and 5.3(a), has been calculated as a function of frequency for each value of the refractive index. Reducing the refractive index of the GaAs backbone by free carrier excitation has two effects on the photonic density of states. Firstly, the reduced index contrast between the constituents making up the photonic crystal causes a narrowing of the photonic band gap. Secondly, the change in the average refractive index of the photonic crystal causes a rescaling of the frequency axis of the density of states, resulting in a blueshift of the band gap with decreasing refractive index. As witnessed by Figure 5.2, the gross spectral features are similar, though shifted in frequency. In fact, rescaling the frequency axis by the square root of the volume averaged dielectric constant roughly aligns the spectral features of the density of states. It is important to note that the low frequency edge of the band gap of the excited crystal is swept all the way past the high frequency edge of the gap of the unexcited crystal, as is clearly seen in Figure 5.3(a).

Several qualitatively different switching schemes may be envisaged, depending on

the choice of probe frequency relative to the band gap of the unexcited crystal. Here, we discuss switching effects for three different key frequencies, marked by dotted lines in Figure 5.3. At these frequencies the density of states as a function of refractive index n' is linearly interpolated for $3.08 \leq n' \leq 3.36$, the relevant switching range for probe wavelengths $\lambda \sim 1500$ nm. The accuracy of the interpolation for intermediate n' values (obtained from the calculated density of states at $n' = 3.08, 3.22$ and 3.36) is expected to be better than 5%, as verified by comparison with additional DOS calculations. The index of refraction as a function of time $n'(t)$ is calculated assuming two-photon absorption in the GaAs backbone due to a Gaussian optical pump pulse at $\lambda = 1.06\,\mu$m. In this way, the DOS as a function of time is obtained theoretically assuming quasistatic conditions, for pump pulses of 200–300 fs, as shown in Figure 5.3.

For a probe frequency (labelled with (i) in both panels of Fig. 5.3) within the band gap before excitation, the DOS can be dramatically increased on an ultrafast time scale using an experimentally reasonable pulse energy. The pulse energy of $\sim 0.1\,\mu$J injected into a region of $(20\,\mu\text{m})^3$, remains below the damage threshold of bulk GaAs [17]. The DOS is increased from zero to a value beyond the density of states of a corresponding homogeneous dielectric, giving rise to a very large relative change. The relaxation time is set by the relaxation time of the semiconductor backbone, and may be even slower than a nanosecond timescale. A possible experiment would be to embed light sources such as excited atoms in the center of a block of photonic crystal large enough to show an appreciable gap in the local density of states. Efficient sources with transition frequency in the gap will be frozen in the excited states over timescales longer than their lifetime in vacuum, until the optical environment is suddenly switched from inhibiting spontaneous emission to enhancing it, allowing emission of photons to occur. As the absorption length (to be discussed below) is sufficiently long, emission can escape from the photonic crystal.

A complementary switching event can be achieved for a probe frequency above the high frequency edge of the band gap of the unexcited photonic crystal. As demonstrated by curve (ii) in Figure 5.3(b), the DOS is switched from a high value to zero, thereby inhibiting the emission of fluorescent species inside the crystal. A somewhat more elaborate sequence of events can be produced using two pulses, for probe frequencies just above the high frequency edge of the band gap of the unexcited state. Figure 5.3 curve (iii) shows that the photonic DOS can be switched from a high to near zero value using a first excitation pulse. A second excitation, say 1 ps later, to further decrease the semiconductor refractive index can then be applied to switch the DOS back to a high value. In this way the band gap can be opened and closed within a picosecond, at a rate that is independent of the relaxation time of the refractive index of the backbone. An interesting experiment would be to study a point defect, acting as a cavity inside the photonic crystal. Light can be sent into this cavity at frequencies for which the DOS is finite. The first excitation pulse then switches the DOS to a low value, causing photons to be localized in the cavity for a duration limited by the absorption time of the semiconducting material, or longer, considering that the cavity mode density can largely be confined

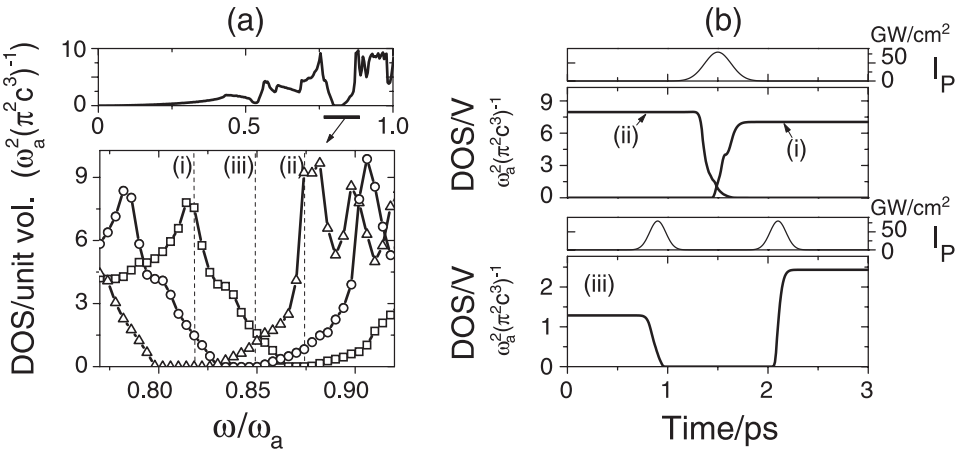

FIGURE 5.3: *(a). DOS per unit volume for an unexcited GaAs inverse opal (top panel) With* $n' = 3.36$. *The solid underscore marks the frequency range of interest around the band gap, in which the DOS per unit volume is displayed for* $n' = 3.36$ *(triangles) (unexcited),* 3.22 *(circles) (partly excited) and* 3.08 *(squares) (excited according to Fig. 5.1). Three frequencies of interest are highlighted by dashed lines,* $\omega a/2\pi c = 0.818$ *(i),* 0.873 *(ii) and* 0.850 *(iii). The DOS per unit volume versus time at these frequencies is plotted in panel (b) (larger plots), together with the incident optical excitation pulses (narrower plots). The pulse parameters are described in the text.*

in air if an air-filled cavity is used. The DOS can then be switched up by the second pump pulse, allowing photons to escape the cavity.

5.4 Absorption, extinction and finite size effect

The switching schemes proposed above have been derived assuming that infinite photonic crystals are uniformly pumped, neglecting for instance the role of induced absorption. Several of these open issues will be addressed in this section.

The effects of induced absorption or extinction can be treated as perturbations to our calculations, as discussed by Krokhin and Halevi [22]. The absorption induced by excited free carriers is gauged by the increase in n'' at the relevant probe wavelength. For a homogeneous medium the damping time ω''^{-1} of a mode with complex frequency $\omega' + i\omega''$ is set by $\omega'' = (n''/n')\omega'$. For optically excited GaAs with a free carrier density of $N = 4.8 \times 10^{19}$ cm^{-3}, as in Figure 5.1, this damping time corresponds to 1340 optical cycles for a probe frequency $\lambda = 1500$ nm, where $n'' = 0.0023$. In bulk GaAs this corresponds to an absorption length of 0.10 mm, or ~ 80 lattice spacings for the inverse opals discussed here. The damping *time* in a photonic crystal compares favorably to the damping time in bulk backbone material. As any mode of the photonic crystal is distributed over both the air and the semiconductor, the damping

time of any mode will be longer than the damping time $\omega''^{-1} = 1.1$ ps in bulk GaAs. Naturally the absorption *length* of a given mode of the photonic crystal need not be increased in correspondence with the absorption time, since the group velocity v_g can be very small, resulting in a short absorption length $L_a = v_g/\omega''$. Extinction due to random scattering can also be described in terms of an imaginary contribution to the refractive index. Experimentally, the contribution of random scattering to n'' has been found to be 2 to 3 orders of magnitude smaller than n' in titania inverse opals ($n' = 2.7 \pm 0.4$) [23]. In the case of absorption the DOS can not be defined anymore by the counting of eigenfrequencies of the wave equation. The local DOS can still be defined through the imaginary part of the Green's function however, and a generalized DOS may then be constructed as the unit cell average of the local DOS. In this framework, Krokhin and Halevi propose that the DOS for frequencies well inside the gap is increased by absorption or extinction to a value $(A\omega''/\omega_c)/\sqrt{|1-\omega'/\omega_c|}$. Here, A is some structure dependent factor of the order of the vacuum DOS at ω_c, and ω_c is the gap edge [22]. Inserting the upper bound on the absorption time ω'' determined by the absorption in GaAs, shows that the DOS in the gap remains lower than 0.01 times the vacuum density of states. Correspondingly a large switching contrast in DOS of $\sim 10^3$ remains feasible, due to the large decrease of n'.

Other issues that merit scrutiny, are the effect of finite size of the photonic crystal to be used, the volume of crystal that can be pumped by two-photon excitation, and the uniformity of the refractive index change. Recent calculations on the effect of finite size suggest that even 5 unit cell spacings suffice to create a deep pseudogap (local DOS less than 10^{-3} times the vacuum value) in the local density of states in the center of the photonic crystal [24], sufficient to cause substantial inhibition of emission. Calculations on defect cavities in finite size 3D crystals suggest that Q values better than 10^4 can be reached despite the finite size [25]. Apparently, substantial switching of spontaneous emission or microcavities can be achieved with blocks of photonic crystal $\sim$ 10 unit cells across, corresponding to $\sim$ (20 μm)^3. To uniformly excite free carriers, light must penetrate a substantial distance into the photonic crystal, with a penetration depth comparable to, or longer than the dimension $\sim$ 20 μm of the volume that needs to be pumped. Such long penetration depths can be achieved via two-photon absorption, in contrast to direct one photon absorption. In the absence of other processes, the penetration depth for a bulk material is given by $d_{\text{bulk}} = 1/(\beta I_{\text{peak}})$, where β is the nonlinear absorption coefficient and I_{peak} is the peak intensity of the pump beam. At a pump wavelength of $\lambda = 1.06\,\mu$m, $\beta = 26$ cm/GW for GaAs [26, 27]. As only 26% of the volume of the structured crystal consists of GaAs, the penetration depth d_{pc} in the crystal is expected to be $\sim$ 4 times longer than the bulk penetration depth. Naturally, the pump beam wavelength should be chosen such that it penetrates into the crystal, *i.e.*, away from a Bragg condition. In choosing the optimal pump pulse, two considerations are important in order to determine the peak intensity I_{peak} and the pulse duration δt, given a desired refractive index change. The peak intensity is fixed by the penetration-depth requirement $d_{\text{pc}} = 20\,\mu$m, resulting in $I_{\text{peak}} = 80$ GW/cm^2. Assuming a Gaussian pulse profile, the pulse duration should be

set to $\delta t = 330$ fs, to achieve an energy per pulse of $\sim 0.15\,\mu$J sufficient to excite a free carrier density of $N = 4.8 \times 10^{19}$ cm^{-3}, corresponding to the index change in Fig. 5.1. These parameters have been chosen with the goal of minimizing the pulse length, while retaining the minimum penetration depth and an index change large enough to support all three switching schemes in Fig. 5.3. In fact for the two-pulse switching scheme (iii) each pulse only needs to excite half of the total desired free carrier density, allowing to shorten the pump pulses, while retaining the same penetration depth. Conversely, if the pulse duration is kept fixed at 330 fs a longer penetration depth and thus more spatially uniform excitation can be achieved both in scheme (iii) (where lower peak intensities per pulse are needed) and in schemes (i), and (ii). The latter switching schemes only employ a large differential change of the DOS at one band edge, and can therefore be realized with a smaller free carrier density than assumed in the calculations presented in Section 5.3, by tuning the probe frequency closer to the relevant band gap edge. The uniformity and size of the excitation volume can be further enhanced by pumping from several sides [28], or at the cost of switching speed, *i.e.*, while increasing δt and decreasing I_{peak} at constant pulse energy.

5.5 Switching time scales and magnitudes

It is well known that two-photon absorption causes electrons in semiconductors to be excited on a femtosecond time scale [16–18]. The rise time of the refractive index change is therefore set by the duration of the pump pulse δt. Switching of the photon DOS may thus occur on ultrafast time scales $\sim$ 300 fs. On the other hand, the duration of the low index state after excitation is also an important figure of merit of the switching process. The duration of the low index state is determined by the relaxation time of the free carriers, which depends on the degree of disorder in the semiconductor, the nature of the semiconductor band gap, and the excited free carrier density. Relaxation times range from 10 ps in amorphous silicon [29], to $\sim 100\,\mu$s in crystalline Si [30], and are on the order of nanoseconds for GaAs [31]. We anticipate that relaxation times in macroporous composite structures such as photonic crystals may be relatively short, for instance because many surface recombination pathways are offered. The low-index state relaxation time has been assumed to be longer than the picosecond scale in Fig. 5.3. Relaxation times may be judged useful for switching, *e.g.*, spontaneous emission, if the relaxation time is of the order of or longer than the free-space emission lifetime of the fluorescent species involved (ranging from nanoseconds for organic fluorophores, to milliseconds for rare earth ions). Along the same lines, a relaxation rate comparable to the damping time of the microcavity (picosecond range) is optimal for cavity based experiments. Generally, short relaxation times have the advantage that the whole switching process can be repeated quickly.

Both the timescales for inducing and relaxation of the index change, and the magnitude of the relative index change compare favorably to other techniques for switching the optical properties of photonic crystals. Alternative proposals that have

been put forward either rely on different means to change the refractive index of the high index backbone, or on the infiltration of tunable birefringent materials in the voids in the photonic crystal. The ordering and alignment of liquid crystals, ferroelectric or ferromagnetic materials can be controlled by temperature, or by electric and magnetic fields to tune Bragg diffraction conditions, as proposed theoretically by Figotin and Godin [4]. Recently, several groups have tuned photonic Bragg conditions by tuning the alignment of liquid crystals infiltrated in opals thermally or with electric fields [6–8]. Large variations in the refractive index of the liquid crystals on the order of $\delta n'/n' = 0.1$ are possible, but the time scale is limited to the millisecond or microsecond scale. Even tuning of the gap in the density of states in an inverse opal by liquid crystal infiltration has been proposed [5]. Unfortunately, it is impossible for an experimentally realizable inverse opal with $n' \sim 3.5$ to retain a photonic band gap upon full infiltration of the air voids with a liquid crystal ($n' \sim 1.6$), as the refractive index contrast drops below threshold. Therefore, infiltration with only a thin layer of liquid crystal on the air sphere surfaces was suggested [5]. Surface anchoring effects of nematic molecules may strongly reduce the proposed switching effect. If all the infiltrated liquid crystal could be switched, the effect is characterized by a band gap narrowing, without causing a shift of the center frequency. It is useful to recall that the drastic shift of the band gap (Fig. 5.1) due to changes of the average refractive index allows for more versatile switching schemes, such as the two-pulse scheme indicated in Figure 5.3 (curve (iii)). The limitations of the millisecond time scale, too slow for many fluorescence or microcavity experiments, can be overcome either by ultrafast free carrier generation as proposed here, or by nonlinear techniques based on the optical Kerr effect. Unfortunately the achievable refractive index change by Kerr switching is an order of magnitude less than the change in n' achieved by free carrier excitation. Still, optical Kerr switching may allow ultrafast switching studies that employ the large differential density of states change at a band gap edge.

5.6 Outlook

In this chapter the effect of uniformly switching the index of refraction on the photonic density of states has been described in a quasistatic framework, *i.e.*, assuming that the electrodynamics at time t can be described by the density of states for the instantaneous refractive index $n'(t)$. The actual physics resulting from suddenly changing the refractive index contrast in photonic crystals appears to be much richer, depending on the time scales involved. Time scales that are relevant in a typical emission experiment, are for instance *(i)* the duration of the switching pulse, *(ii)* the inverse bandwidth of the gap, and *(iii)* the free-space spontaneous emission rate. These timescales always remain much longer than the inverse optical frequency itself. In the present proposal, the pulse duration remains longer than the inverse bandwidth of the gap ($1/\Delta f = 160$ fs). For much shorter pump pulses the bandwidth of the excitation would exceed the bandwidth of the photonic band gap, which may give rise to novel effects not captured in the quasistatic approximation.

For experiments involving defect cavities inside photonic crystals, the analysis is even more complicated. Switching of the semiconductor backbone will not only affect the cavity Q-factor, allowing the trapping or releasing of photons, but may also cause a shifting of the cavity resonance frequency. Here, an important difference between air-filled and dielectric cavities should be considered. Defect cavities have been theoretically studied as a function of their size in structures with fixed refractive index contrast for 3D and 2D structures [25, 32]. Generally, it is found that a defect created by removing dielectric material, sustains a single mode if the defect volume exceeds a certain threshold. The mode frequency of such an air-filled cavity splits off from the lower band edge, and shifts to the band gap center as the defect volume is increased. Dielectric-filled defects on the other hand, can sustain more modes. The mode eigenfrequencies split off from the upper band edge at a certain lower defect volume threshold, and shift into the lower band edge as an upper defect volume threshold is reached. In a switching experiment, the cavity volume is fixed, but the refractive index contrast of crystal constituents and possibly the defect is changed. In such an experiment, one can conceive of a dielectric-filled defect which is too large to support a bound mode in the unexcited state of the semiconductor. A first switching pulse would allow the defect to have a high Q cavity mode. The defect would be too small to support a cavity mode after two excitation pulses have been applied to reduce the refractive index, causing a release of the stored energy. An air-filled cavity on the other hand, is not expected to support this two-pulse switching scheme. We would expect the threshold defect volume of an air-filled cavity to decrease with increasing photonic crystal index contrast. According to this assumption, any air-filled defect cavity large enough to sustain a mode in the switched, lower index contrast crystal, also sustains a mode before switching. A first excitation pulse would sweep the cavity frequency from the middle of the gap towards the bottom edge, while the second excitation pulse could be used to release photons. Unfortunately, an air-filled cavity would be more favorable for storing photons than a dielectric cavity, due to the smaller damping time associated with the concentration of mode density in the non-absorbing material. The quasistatic analysis presented here, does not allow proper treatment of the relevant timescales for the electromagnetic field to adjust its frequency to the cavity, or the degree to which switching of multimode cavities causes redistribution of the electromagnetic field over different modes. Future FDTD calculations will in principle allow to investigate the relevant timescales. In a more general sense the physics of photonic crystals with a time-varying dielectric constant is largely unexplored. A rudimentary analysis [33] has shown the possibility of photons of frequency ω_1 to transfer into a mode of frequency ω_2 if the dielectric constant periodically varies with frequency $\omega_2 - \omega_1$. For photonic crystals in the optical regime, the frequency difference between bands is so large that it appears hard to find a suitable mechanism for such periodic modulation of the dielectric constant. Hence, interband transitions are unlikely, though intraband transitions involving small frequency shifts appear feasible. Such transitions should also involve a momentum conservation rule, which depends on the wave vector of the perturbation. In the present proposal, the whole

crystal backbone is switched, without breaking the crystal symmetry. This should be contrasted to experiments on electronic systems where tuning is often achieved with external fields, thus breaking the translational symmetry of the electronic potential [20]. A second important difference between switching of the photonic band structure and the physics of time-varying perturbations of electronic systems is imposed by the bosonic nature of photons. Whereas the occupation of levels up to the Fermi level needs to be considered for time dependent perturbations of electronic systems, a photon can in principle be launched in any Bloch wave [20].

References

[1] *Photonic Band Gap Materials*, edited by C. M. Soukoulis (Kluwer, Dordrecht, 1996).

[2] *Photonic Crystals and Light Localization in the* 21st *Century*, edited by C. M. Soukoulis (Kluwer, Dordrecht, 2001).

[3] J. M. Weissman, H. B. Sunkara, A. S. Tse, and S. A. Asher, *Thermally Switchable Periodicities and Diffraction from Mesoscopically Ordered Materials*, Science **274**, 959 (1996).

[4] A. Figotin and Y. A. Godin, *Two-Dimensional Tunable Photonic Crystals*, Phys. Rev. B **57**, 2841 (1998).

[5] K. Busch and S. John, *Liquid-Crystal Photonic-Band-Gap Materials: The Tunable Electromagnetic Vacuum*, Phys. Rev. Lett. **83**, 967 (1999).

[6] K. Yoshino, Y. Shimoda, Y. Kawagishi, K. Nakayama, and M. Ozaki, *Temperature Tuning of the Stop Band in Transmission Spectra of Liquid-Crystal Infiltrated Synthetic Opal as Tunable Photonic Crystal*, Appl. Phys. Lett. **75**, 932 (1999).

[7] D. Kang, J. E. Maclennan, N. A. Clark, A. A. Zakhidov, and R. H. Baughman, *Electro-Optic Behavior of Liquid-Crystal-Filled Silica Opal Photonic Crystals: Effect of Liquid-Crystal Alignment*, Phys. Rev. Lett. **86**, 4052 (2001).

[8] S. W. Leonard, J. P. Mondia, H. M. van Driel, O. Toader, S. John, K. Busch, A. Birner, U. Gösele, and V. Lehmann, *Tunable Two-Dimensional Photonic Crystals Using Liquid-Crystal Infiltration*, Phys. Rev. B **61**, R2389 (2000).

[9] E. Yablonovitch, *Inhibited Spontaneous Emission in Solid-State Physics and Electronics*, Phys. Rev. Lett. **58**, 2059 (1987).

[10] A. F. Koenderink, L. Bechger, H. P. Schriemer, A. Lagendijk, and W. L. Vos, *Broadband Fivefold Reduction of Vacuum Fluctuations Probed by Dyes in Photonic Crystals*, Phys. Rev. Lett. **88**, 143903 (2002).

[11] P. M. Johnson, A. F. Koenderink, and W. L. Vos, *Ultrafast Switching of Photonic Density of States in Photonic Crystals*, Phys. Rev. B **66**, 081102 (2002).

[12] M. Notomi, *Theory of Light Propagation in Strongly Modulated Photonic Crystals: Refractionlike Behavior in the Vicinity of the Photonic Band Gap*, Phys. Rev. B **62**, 10696 (2000).

[13] H. Kosaka, T. Kawashima, A. Tomita, M. Notomi, T. Tamamura, T. Sato, and S. Kawakami, *Superprism Phenomena in Photonic Crystals*, Phys. Rev. B **58**, R10096 (1998).

[14] S. W. Leonard, H. M. van Driel, J. Schilling, and R. B. Wehrspohn, *Ultrafast Band-Edge Tuning of Two-Dimensional Silicon Photonic Crystals Via Free-Carrier Injection*, Phys. Rev. B **66**, 161102 (2002).

[15] K. Yoshino, Y. Kawagishi, M. Ozaki, and A. Kose, *Mechanical Tuning of the Optical Properties of Plastic Opal as a Photonic Crystal*, Jpn. J. Appl. Phys **38**, L786 (1999).

[16] H. M. van Driel, *Kinetics of High-Density Plasmas Generated in Si by 1.06- and 0.53-μm Picosecond Laser Pulses*, Phys. Rev. B **35**, 8166 (1987).
[17] L. Huang, J. P. Callan, E. N. Glezer, and E. Mazur, *GaAs under Intense Ultrafast Excitation: Response of the Dielectric Function*, Phys. Rev. Lett. **80**, 185 (1998).
[18] K. Sokolowski-Tinten and D. von der Linde, *Generation of Dense Electron-Hole Plasmas in Silicon*, Phys. Rev. B **61**, 2643 (2000).
[19] P. Drude, *Zur Elektronen theorie. I*, Annalen der Physik **1**, 566 (1900).
[20] N. W. Ashcroft and N. D. Mermin, *Solid State Physics* (Holt, Rinehard and Winston, New York, 1976).
[21] A. Dargys and J. Kundrotas, *Handbook on Physical Properties of Ge, Si, GaAs and InP* (Science and Encyclopedia Publishers, Vilnius, 1994), and references therein.
[22] A. A. Krokhin and P. Halevi, *Influence of Weak Dissipation on the Photonic Band Structure of Periodic Composites*, Phys. Rev. B **53**, 1205 (1996).
[23] J. Galisteo Lòpez and W. L. Vos, *Angle Resolved Reflectivity of Single-Domain Photonic Crystals, Effects of Disorder*, Phys. Rev. E **66**, 036616 (2002).
[24] D. M. Whittaker, *Inhibited Emission in Photonic Woodpile Lattices*, Opt. Lett. **25**, 779 (2000).
[25] P. R. Villeneuve, S. H. Fan, and J. D. Joannopoulos, *Microcavities in Photonic Crystals: Mode Symmetry, Tunability, and Coupling Efficiency*, Phys. Rev. B **54**, 7837 (1996).
[26] G. C. Valley, T. F. Boggess, J. Dubard, and A. L. Smirl, *Picosecond Pump-Probe Technique to Measure Deep-Level, Free-Carrier and Two Photon Cross Sections in GaAs*, J. Appl. Phys. **66**, 2407 (1989).
[27] A. A. Said, M. Sheik-Bahae, D. J. Hagan, T. H. Wei, J. Wang, J. Young, and E. W. Van Stryland, *Determination of Bound-Electronic and Free-Carrier Nonlinearities in ZnSe, GaAs, CdTe and ZnTe*, J. Opt. Soc. Am. B **9**, 405 (1992).
[28] D. S. Wiersma and A. Lagendijk, *Light Diffusion with Gain and Random Lasers*, Phys. Rev. E **54**, 4256 (1996).
[29] A. Haché and M. Bourgeois, *Ultrafast All-Optical Switching in Silicon-Based Photonic Crystal*, Appl. Phys. Lett. **77**, 4089 (2000).
[30] Z. G. Ling, P. K. Ajmera, M. Anselment, and L. F. DiMauro, *Lifetime Measurements in Semiconductors by Infrared Absorption Due to Pulsed Optical Excitation*, Appl. Phys. Lett. **51**, 1445 (1987).
[31] M. C. Beard, G. M. Turner, and C. A. Schmuttenmaer, *Transient Photoconductivity in GaAs as Measured by Time-Resolved Terahertz Spectroscopy*, Phys. Rev. B **62**, 15764 (2000).
[32] K. Sakoda, *Optical Properties of Photonic Crystals* (Springer Verlag, Berlin, 2001).
[33] J. N. Winn, S. H. Fan, and J. D. Joannopoulos, *Interband Transitions in Photonic Crystals*, Phys. Rev. B **59**, 1551 (1999).

Chapter 6

Enhanced Backscattering from Opals and Inverse Opals

We have studied enhanced backscattering of both polystyrene opals and strongly photonic crystals of air spheres in TiO_2 in the wavelength range of first and higher order stop bands. The shape of the enhanced backscattering cones is well described by diffusion theory. We find transport mean free paths of the order of 15 μm both for opals and air-sphere crystals. Close to the stop band, the cone width is decreased due to internal reflections generated by the photonic band structure. Broadening may occur due to Bragg attenuation of the coherent beam by Bragg diffraction. We present a model that incorporates these effects and successfully explains the data. The dominant role of sphere polydispersity and displacements in determining the mean free path is discussed. A tractable, quantitative model demonstrates the grave consequences of polydispersity and displacements for scattering in all two and three-dimensional photonic crystals.

6.1 Introduction

In the last decade many efforts have been devoted to fabricate three-dimensional photonic crystals. Fundamental interest in these novel dielectric structures is spurred by the possibility of a photonic band gap, a frequency range for which no modes exist at all. Tailoring of the electromagnetic mode density by a photonic crystal allows to control fundamental atom-radiation interactions in solid state environments [1, 2]. In this context the hallmark of a photonic band gap is the eagerly awaited full inhibition of spontaneous emission [1]. As John first pointed out, disorder in otherwise perfectly periodic photonic crystals is of fundamental interest for the observation of Anderson localization of light [3]. Anderson localization [4] of light is a delicate interference effect in multiple scattering in disordered optical materials, such as semiconductor powders [5–7] and novel macroporous 'spongelike' GaP structures [8].

Despite advances in fabricating periodic structures with high refractive index contrast, all state of the art structures are still tainted by unintentional disorder. Two and three-dimensional photonic crystals alike suffer from fluctuations in position and size of the building blocks of 2–5%, both for lithographically prepared [9–11] and self-organized structures [12, 13]. Such fluctuations are dictated on a fundamental level by the finite temperature at which, *e.g.*, the unit cell building blocks form and assemble into a crystalline array. Disorder adversely affects the interference-induced photonic crystal properties, and causes reduced Bragg reflectivity [14], extinction of transmitted light [14, 15], and unexpected lossiness of incorporated waveguides [16]. Ultimately, disorder can destroy the photonic band gap [17].

While much research has focused on fabrication and optical characterization of stop gaps, little effort has been spent on understanding the cause or effect of random multiple scattering. The work presented in this chapter is the first to quantify the degree to which multiple scattering affects the optical properties of photonic crystals, apart from a study concerned with the effect of disorder on the optical transmission of near index-matched opals [15]. We present enhanced backscattering measurements from both opal photonic crystals and strongly photonic crystals consisting of air spheres in titania [12, 13, 18]. The effect of enhanced backscattering is especially suited to quantify the random scattering in photonic crystals since it inherently averages over the full sample volume. Backscattering cones were recorded for wavelengths in the range of the lowest order stop bands, to probe the interaction of the randomness inherently present in the samples with the photonic band structure. Surprisingly, the shape of the enhanced backscattering cones is well described by the diffusion theory for light transport in random media [19, 20]. The photonic crystals appear to be weakly scattering, since the transport mean free paths we observe are large compared to the wavelengths used. We have developed a model based on diffusion theory which shows that the width of the backscatter cone is increased in the stop band due to attenuation of the coherent beam, and decreased at the blue edge of the stop band due to Bragg-enhanced internal reflection. The model for the cone width is consistent with our data, and has been confirmed by a recent study [21]. The dominant scattering mechanism appears to be due to polydispersity and displacements of the spheres of which the crystals consist. Before presenting the enhanced backscattering experiment (Section 6.4, 6.5) and their consequences regarding disorder in photonic crystals (Section 6.6, 6.7), the necessary concepts from multiple scattering theory will first be introduced in Sections 6.2 and 6.3.

6.2 Multiple scattering and diffusion

In a homogeneous dielectric, light simply propagates in straight trajectories. Any inhomogeneity (compared to the microscopically averaged properties of the dielectric) causes scattering, meaning that the amplitude of an incident wave decreases, and is redistributed over different waves [22, 23]. Though scattering causes extinction of an incident beam, the energy is not removed from the wave field, as in an absorption

process. The strength with which a scatterer interacts with the wave field is measured by its scattering cross-section σ_s (units of area), which is the ratio of the power removed from the incident beam by scattering to the incident intensity. The scattering cross-section of a particle (or rather the scattering efficiency Q_s, the ratio of σ_s to the geometrical cross-section) is maximal in the so-called Mie regime, if the size of the particle matches the wavelength of light. Scattering is very inefficient for particles much smaller than the wavelength (Rayleigh limit), and limited by geometrical optics for particles much larger than the wavelength.

If a medium contains many inhomogeneities, light may be scattered many times. The average distance between scattering events is called the scattering mean free path ℓ_s [24]. Multiple scattering occurs if the sample thickness exceeds the scattering mean free path. To first approximation, the scattering mean free path ℓ_s is simply set by the density ρ and the cross-section of the scatterers according to

$$\ell_s = \frac{1}{\rho\sigma_s}. \tag{6.1}$$

This approximation, known as the independent-scattering approximation, is strictly valid only for uncorrelated low-density arrangements of scatterers. The optical properties of a medium with correlated scatterers can naturally be vastly different from the properties of a random arrangement of scatterers, as beautifully illustrated by photonic crystals. In photonic crystals, the scatterers collectively give rise to a photonic band structure and associated Bloch modes, which each have an infinitely long mean free path.

An exact solution for the propagation of light in a random multiple scattering medium requires solving Maxwell's equations given the shape and position of each scatterer. In general, the wave field for a given scatterer distribution can be very complicated, and interference plays an important role, as witnessed by, for example, speckle. The wave fields strongly depend on the specific realization of disorder, so it is more useful to study ensemble averaged quantities. In the weakly multiple scattering regime $\lambda \ll \ell_s \ll L$ (with λ the wavelength and L the sample size) the wave character can be discarded, and the multiple scattering can be described as a random walk for a photon density. More specifically, the ensemble averaged transport of light can be described by a diffusion equation for the electromagnetic energy density W. In the extreme regime $\ell_s \lesssim \lambda$ this approach breaks down, and interference strongly modifies the diffuse transport, or even halts the transport in the case of Anderson localization [4].

The transport of the diffuse intensity is quantified by the diffusion constant $D = \frac{1}{3} v_E \ell$. The diffusion constant D is determined by the energy velocity v_E and the mean free path ℓ over which the direction of propagation is randomized [20, 25]. This length scale is known as the transport mean free path. If scatterers scatter predominantly in the forward direction, many scattering events may be needed to randomize the direction of propagation. Hence the transport mean free path exceeds the scattering mean free path ℓ_s for anisotropic scatterers. The energy velocity is set by the group velocity of the medium, as well as resonant properties of the scatterers, which

may cause transport to be slowed down by long dwell times of the field in each scatterer [25, 26]. In photonic crystals the energy velocity may be small, both because the group velocity (averaged over the Bloch modes at the specified frequency) may be small, and because point defects may be highly resonant scatterers. The diffusion equation

$$\frac{\partial W}{\partial t} = D\nabla^2 W + S \tag{6.2}$$

does not fully specify the energy density W unless the source of diffuse light S, as well as boundary conditions are given. For an externally incident plane wave of intensity I_0, the 'coherent' beam, formed by the wave scattered in the forward direction, acts as the source for diffuse light. This gives rise to a source term $S(\mathbf{r}) = (I_0/\ell_s)\exp(-z/\ell_s)$ that decays exponentially with depth z due to extinction by scattering (Lambert-Beer's law).

The appropriate boundary conditions for the diffusion equation are a subtle matter, which remain subject of debate [27–33]. It is generally agreed upon that both von Neumann boundary conditions (no flux through the sample interface) and Dirichlet boundary conditions (no diffuse intensity at the interface) are wrong. Instead, extrapolative boundary conditions

$$W + z_e \nabla W \cdot \mathbf{n} = 0 \quad \text{at interface with outward normal} \quad \mathbf{n}, \tag{6.3}$$

are expected to be appropriate to calculate the diffuse intensity distribution inside a random medium. This boundary condition essentially requires that the diffuse intensity extrapolates to zero at a distance z_e from the boundary. The ratio $\tau_e = z_e/\ell$ is referred to as extrapolation length ratio. A value $\tau_e = \tau_0 = \frac{2}{3}$ is appropriate to calculate the energy density to within 1% for diffusive media without internal reflection [31], and is consistent with the Milne extrapolation length ($z_e = 0.7104\ell$) derived from the more complete radiative transfer theory [24].

Internal reflection of diffuse photons that arrive at the boundary acts as a source of diffuse flux reinjected into the sample. Internal reflection can therefore significantly modify the diffuse energy density distribution, as taken into account by modifying the extrapolation length appearing in the boundary condition. The extrapolation length increases with the average internal reflection coefficient. The detailed flux argument to derive the extrapolation length z_e, and the angle and polarization averaged internal reflection coefficient $\bar{R}$ will be reviewed in Chapter 7. Though lacking a clear physical basis, the result of Zhu, Pine and Weitz [29]

$$\tau_e = \frac{2}{3}\frac{1+\bar{R}}{1-\bar{R}} \tag{6.4}$$

is often used to account for internal reflection, since it is in reasonable agreement with experiments. Obviously, their result reduces to $\tau_e = 2/3$ for negligible internal reflection. For unit average internal reflection, the diffuse flux $\propto \nabla W \cdot \mathbf{n}$ transmitted by the interface must be 0, corresponding to an infinite extrapolation length.

It may not be obvious whether the diffusion framework holds at all for transport of light in photonic crystals with disorder, and if the photonic dispersion has any influence on the transport of multiply scattered light. It is a tremendous task to develop an exact multiple scattering theory for photonic crystals with disorder, analogous to, *e.g.*, the successful point scatterer model [34]. In such a theory one would consider scatterers embedded in a host which has the Green's function of the photonic crystal. This appears a formidable task, as a tractable model or a numerically efficient means to construct the Green's function are lacking. Numerical approaches have sofar been based on truncated eigenmode expansions of the Green's function [35, 36]. To ensure convergence, however, the frequency was either chosen within a photonic band gap (no propagating modes), or absorption was introduced into the model. As a completely different approach one might apply existing multiple scattering theory for nearly periodically arranged scatterers in a homogeneous background medium. It would appear hard to reproduce the photonic properties of the completely ordered limit however, since photonic crystal phenomena depend on delicate interference phenomena due to the periodicity.

6.3 Enhanced backscattering

Enhanced backscattering is an interference phenomenon in multiple scattering that survives the ensemble averaging over realizations of the disorder [19, 20, 37, 38]. Enhanced backscattering is therefore not contained in the diffusion equation, as all interference is neglected in the diffusion approximation. A constructive interference contribution always arises in the intensity scattered by a disordered medium in the exact backscatter direction, irrespective of the realization of the disorder. As illustrated in Fig. 6.1 the essential mechanism at work is constructive interference of counterpropagating light paths. Suppose a medium is illuminated by a plane wave with wave vector $\mathbf{k}_{\text{in}}$. We may trace some path along which the wave propagates, as indicated by the solid line in Fig. 6.1(a), which enters the medium and has a first scattering event at A, visits many scatterers, and leaves the random medium in direction $\mathbf{k}_{\text{out}}$ after a last scattering event at B. For every such path there is a counterpropagating counterpart, starting at B, visiting all scatterers in reverse order, and exiting from the sample after a last scattering event at point A. As the path lengths are exactly equal within the sample, the phase difference $d/\lambda \cos(\theta)$ between the wave emanating from A and the wave from B depends solely on the distance d between the first and last scattering event, and the angle θ between incident and scattered direction. Essentially, A and B act as two interfering coherent point sources at distance d from each other. Each individual source-separation d will give rise to an oscillatory interference pattern in the far field, with angular separation between fringes decreasing with increasing source separation (see Fig. 6.1(b)). As all interference contributions are constructive in the backscattering direction, an interference peak will remain after summing over contributions of all paths. In other directions however, the different contributions dephase, and the average intensity will be half the intensity in the exact backscatter direction.

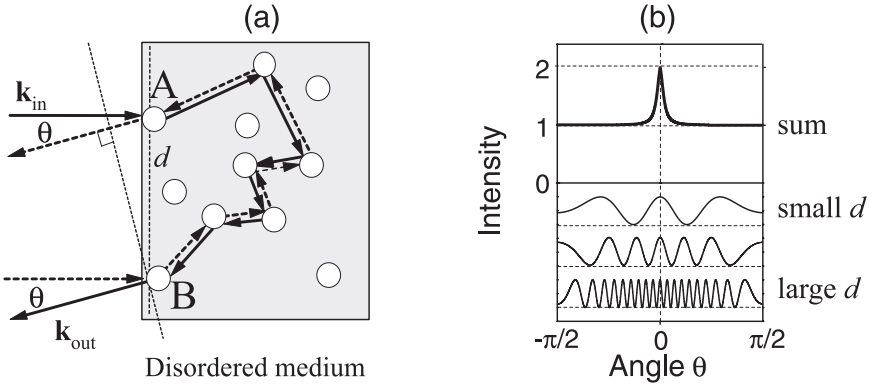

FIGURE 6.1: *(a) Schematic drawing to illustrate enhanced backscattering. A plane wave (horizontal arrows) is incident on a multiple scattering medium (grey slab). Each random path, visiting many scatterers, has a time reversed counterpart, that undergoes the scattering events in reverse order. The phase difference between the path starting at A and ending at B, and its reverse is built up outside the medium, since the path lengths are equal within the medium. The path length difference* $d\cos(\theta)$ *only depends on the end point separation* d *between A and B, and the angle* θ *relative to the backscatter direction. Each source separation produces a far field interference pattern* $I(d,\theta) \propto 1+\cos(2\pi d\cos(\theta)/\lambda)$*, as shown in (b). The larger the separation d, the faster the variation of I with* θ*. The backscatter cone is obtained by summing contributions over all paths. Constructive interference only survives averaging in the exact backscatter direction, as shown in (b) (top).*

The shape of the cone can be calculated in the diffusion approximation. In essence, the enhanced backscattering cone is obtained by summing the far field interference patterns $\{1+\cos[(\mathbf{k}_{in}+\mathbf{k}_{out})\cdot(\mathbf{r}_A-\mathbf{r}_B)]\}$, over the positions of the first and the last scattering event, $\mathbf{r}_A$ resp. $\mathbf{r}_B$. In the following, we separate the perpendicular and parallel components $\mathbf{r}_{\perp,A,B}$ resp. z_A, z_B of $\mathbf{r}_{A,B}$ relative to the slab normal. Each contribution needs to be weighted by the probability that a wave entering the medium at scatterer A exits the medium at scatterer B. As a function of the incident and observation angle, θ_{in} resp. θ_{out}, this leads to the following expression for the backscattered flux per solid angle, per unit area of observed sample, normalized to the incident intensity, for a slab of thickness L [19]

$$\gamma(\theta_{in},\theta_{out}) = \iint \mathrm{d}\mathbf{r}_{\perp,A}\mathrm{d}\mathbf{r}_{\perp,B}\int_0^L\int_0^L F(\mathbf{r}_A,\mathbf{r}_B)\{1+\cos[(\mathbf{k}_{in}+\mathbf{k}_{out})\cdot(\mathbf{r}_A-\mathbf{r}_B)]\}$$

$$\times\exp\left[-\frac{1}{2}\left(\frac{z_A}{\ell_X}+\frac{z_B}{\ell_X}\right)\left(\frac{1}{\cos\theta_{in}}+\frac{1}{\cos\theta_{out}}\right)\right]\frac{\mathrm{d}z_A\mathrm{d}z_B}{\ell_s^2}. \qquad (6.5)$$

The exponential terms $\exp[-z_{A,B}/(2\ell_X)(\cos^{-1}\theta_{in}+\cos^{-1}\theta_{out})]\mathrm{d}\mathbf{r}_\perp\mathrm{d}z/\ell_s$ quantify the fraction of intensity in the exponentially decaying incident beam that first scatters in the volume element $\mathbf{r}_{A,B}, \mathbf{r}_{A,B}+\mathrm{d}\mathbf{r}_{A,B}$ at depth z relative to the sample interface, and the fraction of intensity in the exiting beam that has its final scattering event in the volume

element $\mathbf{r}_{B,A}, \mathbf{r}_{B,A} + \mathrm{d}\mathbf{r}_{B,A}$. In anticipation of results presented later we do not assume the attenuation length ℓ_X of the exponentially decaying beams $I = I_0 \exp(-z/\ell_X)$ to equal ℓ_s, as would be appropriate for media in which scattering represents the only attenuation of the input beam.

In the integral (6.5) the kernel $F(\mathbf{r}_A, \mathbf{r}_B)$ is the central ingredient originating from diffusion theory. It quantifies how much diffuse intensity will arrive at point $\mathbf{r}_B$ starting from a disturbance at point $\mathbf{r}_A$. More precisely, $F(\mathbf{r}_A, \mathbf{r})$ is the solution of the diffusion equation Eq. (6.2) with source term equal to $S = \delta(\mathbf{r} - \mathbf{r}_A)$ and appropriate boundary conditions Eq. (6.3) applied to the front and end surface of the slab. This propagator can be solved for exactly in the case of a slab, as derived in a detailed manner by van der Mark, van Albada and Lagendijk [19]. Essentially, the propagator for a semi-infinite medium can be constructed from the infinite space propagator by adding a term corresponding to an imaginary image source (or rather a sink) of diffuse intensity outside the medium, similar to the image charge method known in electrostatics [39].

We quote the result of performing the integration (6.5), using the kernel $F(\mathbf{r}_A, \mathbf{r}_B)$ from Ref. [19] for an infinite slab without internal reflection (*i.e.* $\tau_e = \tau_0 = \frac{2}{3}$), and an incident beam close to the sample normal ($\cos\theta_{\mathrm{in}} = 1$). In Ref. [19], only the case $\ell_X = \ell_s = \ell$ was considered. Since the penetration depth ℓ_X will appear important later, we have evaluated Eq. (6.5) for the case $\ell_X \neq \ell_s = \ell$, and introduce the shorthand $\xi = \ell/\ell_X$. As expected, we find a bell-shaped diffuse background

$$\gamma_\ell(\theta_{\mathrm{out}}) = \frac{3\cos\theta_{\mathrm{out}}}{\ell^3\xi^3}\left[1 + \tau_0\xi - \frac{1}{1+\cos\theta_{\mathrm{out}}}\right] \tag{6.6}$$

on top of which a triangular peak is superimposed [19, 20, 37, 38]

$$\gamma_c(\theta_{\mathrm{out}}) = \frac{3}{2\ell^3}\frac{\alpha + v\{1 - \exp[-2\tau_0\alpha]\}}{\alpha v[(v+\alpha)^2 + u^2]} \quad \text{with} \tag{6.7}$$

$$\alpha = k_0\ell\,|\sin\theta_{\mathrm{out}}| \tag{6.8}$$

$$u = k_0\ell\,(1 - \cos\theta_{\mathrm{out}}) \tag{6.9}$$

$$v = \frac{1}{2}\xi\left(1 + \frac{1}{\cos\theta_{\mathrm{out}}}\right). \tag{6.10}$$

This result reduces to the familiar expressions in the literature [19] for $\xi \to 1$ and only differs in the definition of v. It is easy to verify that the backscattered intensity $\gamma_c(\theta_{\mathrm{out}}) + \gamma_\ell(\theta_{\mathrm{out}})$ is exactly doubled in the exact backscatter direction. The present calculation does not include single scattering events, which do not have a distinct time-reversed counterpart. Single scattering events can therefore reduce the enhancement factor by contributing a nearly angle-independent background γ_s. The enhancement factor $\mathcal{E}$ is defined as

$$\mathcal{E} = \frac{\gamma_\ell(0) + \gamma_c(0)}{\gamma_s + \gamma_\ell(0) + \gamma_c(0)}. \tag{6.11}$$

The top of the cone appearing at $\theta_{out} = 0$ is cusped. The cusp of the cone results from contributions due to very long light paths; the longer the distance between first and last scattering event, the narrower the resulting interference contribution. This is easily understood from Fig. 6.1(a), if one realizes that the distance d along the sample surface between first and last scattering event scales as $\sqrt{N}\ell$ for a light path of N scattering events, with total length $\sim N\ell$. Any cut-off of long light paths, such as absorption or finite sample thickness will therefore cause a rounding of the cone.

The 'intrinsic' full width at half maximum

$$W_\ell \sim \frac{0.7}{k\ell} \quad \text{for } \xi = 1 \text{ and } \bar{R} = 0 \tag{6.12}$$

of the cone is inversely proportional to the mean free path, in keeping with the notion that longer light paths on average produce a narrower interference contribution. The width of the cone is affected by any mechanism that changes the path length distribution. One such effect incorporated in Eq. (6.7) is due to the penetration depth $\ell_X = \ell/\xi$. The smaller the penetration depth of the incident light, the shallower the distribution of start and end points of the contributing light paths. On average light paths that originate closer to the interface return to the interface in fewer steps than light paths starting from scatterers deeper inside the sample. A short penetration depth of the incident beam is therefore expected to cause a broadening of the cone.

A well-known effect, first pointed out by Lagendijk, Vreeker and de Vries [27], that has the opposite result on the cone, *i.e.*, a narrowing, is due to internal reflections. As internal reflection causes a reinjection of photons into the random walk process, photons have a higher probability to traverse a longer light path, with the associated larger distance between first and last scattering event. Several theories have been put forward to deal with the effect of an angle- and polarization averaged reflection coefficient $\bar{R}$. Three approaches are quoted here, which give quantitatively different, though qualitatively similar results. It appears that the cone *shapes* do not change significantly under the influence of $\bar{R}$ and ξ; their effect can therefore be quantified through the change in width W from the intrinsic width $W_\ell = 0.7/(k\ell)$, or equivalently by the difference between the mean free path ℓ, and the *apparent* mean free path $\ell_W = 0.7/(kW)$.

The theory of Lagendijk, Vreeker, and de Vries [27] accounts for internal reflection by modifying the magnitude and sign of the image source contribution to the diffuse intensity propagator. The image source is adapted to match the reentrant photon flux. If both internal reflection and $\xi \neq 1$ are incorporated in this framework one finds an increase of the cone width by a scaling factor

$$\frac{W}{W_\ell} = \frac{\ell}{\ell_W} = \frac{(1+\tau_0)^2}{1+2\tau_0} \frac{\xi\,[1+2(\varepsilon+\tau_e)\,\xi]}{[1+(\varepsilon+\tau_e)\,\xi]^2} \quad \text{with} \quad \varepsilon = \frac{\bar{R}}{1-\bar{R}}. \tag{6.13}$$

In the original paper [27], the extrapolation length ratio τ_e in this equation was kept fixed at τ_0. This should be contrasted to the approach of Zhu, Pine and Weitz, who propose modifying the extrapolation length ratio τ_e according to Eq. (6.4), without

adapting the magnitude of the image source (*i.e.*, keeping $\varepsilon = 0$). It was later suggested in Ref. [40] that one should combine both approaches, keeping $\varepsilon = \bar{R}/(1-\bar{R})$ and using τ_e as defined in (6.4). It is straightforward to show for $\xi = 1$, that according to the latter suggestion the effect of internal reflection is very well approximated by [40]

$$W \approx W_\ell(1-\bar{R}). \tag{6.14}$$

This relation was derived independently in Ref. [29], and is generally agreed upon by workers in the field. In this thesis, we follow Ref. [40], as it is the only theory to yield Eq. (6.14). Obviously, an increase of the internal reflection causes a drastic narrowing of the cone, up to the point where the cone width vanishes for total reflection. In contrast, the widening of the cone saturates at a maximum value $25/7 \approx 3.5$, which is the width if all first and last scatterers would be confined to a plane at $z = 0$. This limit is already reached for penetration depths less than $\sim \frac{1}{3}\ell$, *i.e.*, $\xi \sim 3$. These features are present in all three models, though the predictions differ quantitatively by up to $\sim 30\%$ in predicted cone broadening in the parameter range $1 \le \xi \le 5$ and $0 \le \bar{R} \le 1$.

6.4 Experiment

We have studied opals consisting of polystyrene spheres (Duke Scientific, polydispersity $\sim 2\%$) of which opals were made by sedimentation in 0.3 mm thick, 3 mm wide flat glass capillaries (Vitro Dynamics). The opals were prepared by J.E.G.J. Wijnhoven. Those opals that consisted of spheres of radii 120, 180, 213, 241, 262 resp. 326 nm were grown from a suspension in water using a centrifuge. Crystals consisting of spheres of radius 403, 426 and 439 nm were formed by slow sedimentation under gravity and formed large domains ($\sim$ 1 mm). After crystallization the suspending liquid was slowly evaporated from the capillaries to obtain polycrystalline opals of 74 volume percent polystyrene in air, which are more than 10 mm in length. The refractive index contrast is 1.59, resulting in a photonic strength $\Psi = 7\%$. Small-angle X-ray diffraction experiments have confirmed that such crystals have an *fcc* structure [13, 41]. These crystals are stacked with (111) planes along the capillary faces.

We measured enhanced backscattering cones of the polystyrene opals with the off-centered rotation technique [42]. This technique provides a very high angular resolution of approximately 0.4 mrad, that is (Fourier) limited by the illumination area of 2.5 mm in diameter. A simplified overview of the setup is shown in Fig. 6.2. The incident beam is aligned through the rotation center R of a central rotation stage. A large beam splitter is mounted on the rotation stage, and directs part of the incident beam onto the mirror image R' of R. The mirror image R' is the rotation center for a secondary rotation stage. The remaining part of the beam is dumped. The sample is mounted on the rotation axis of the secondary rotation stage, which is fitted onto the central rotation stage. By mirror symmetry, the beam reflected off the beam splitter always hits the sample at the same spot R'. The secondary rotation stage needs to be turned in conjunction with the central rotation platform, in order to keep the angle

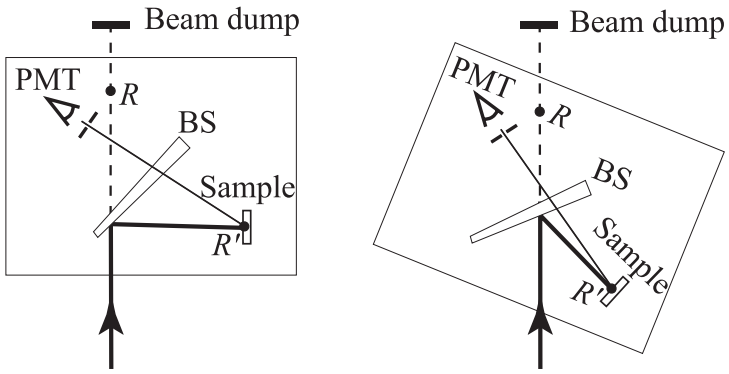

FIGURE 6.2: *Schematic representation of the off-centered rotation setup used to measure enhanced backscattering from opals. The incident beam is reflected off a beam splitter onto the sample at R′. Backscattered light is detected through the beam splitter. The detection angle around the backscatter direction is varied by rotating the central stage with the detector, the beamsplitter, and the sample stage at R′ around R, the mirror image of R′ in the beam splitter front plane. To keep the angle of incidence constant, the sample is rotated around R′ in unison with the central stage.*

of incidence of the laser beam onto the sample constant. The merit of this technique is due to the fact that the path of the backscattered light from the sample through the beam splitter to the detection optics on the central rotation stage, is independent of the rotation angle. Hence one does not need to correct for any angle-dependence in the optical transmission of components in the detection path, though it is necessary to calibrate the angle dependent reflectance of the beam splitter. Cones were recorded using three different lasers operating at wavelengths of 632 nm (HeNe), 685 nm, and 780 nm (laser diodes). The incident light was linearly polarized and detection was in the linear polarization-conserving channel. Furthermore, the detection optics consisted of a 1 m focal length lens behind the beam splitter which focused the backscattered light onto the tip of an optical fiber which transported the light to a photomultiplier tube. The beam splitter was wedged to avoid ghost reflections. Speckle averaging was performed by continuously varying the tilt angle of the samples, and by adding runs with the sample slightly shifted relative to the illumination spot. The illuminated spot was on the tilt axis, and the tilt amplitude was smaller than 6°. The tilt angle remained slightly off-normal at all times, to keep the specular reflection from opals and capillary walls from reaching the detector.

To investigate a more strongly photonic material we studied an *fcc* crystal of air spheres in titania (refractive index contrast ~ 2.5). The crystal was made by filling the voids of an opal of polystyrene spheres of 180 nm radius with a precursor of TiO_2 and subsequently removing the polystyrene by calcination [12]. Small angle X-ray diffraction showed that the lattice parameter is 360 ± 10 nm and that the periodic structure extends all the way throughout the sample [13]. The lattice parameter corresponds to a Bragg reflection at ~ 470 nm.

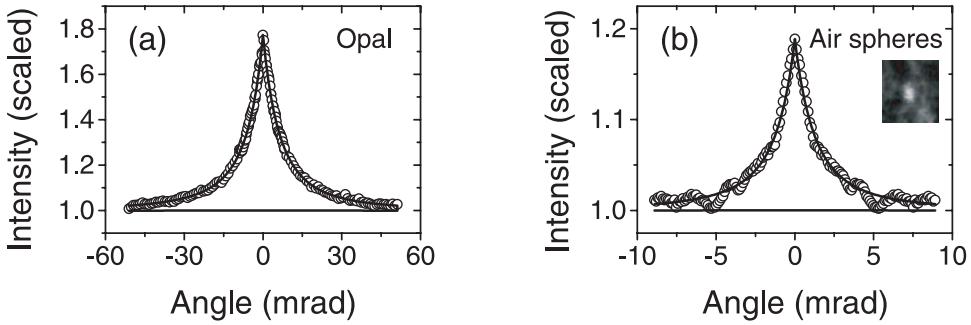

FIGURE 6.3: *The backscattered intensity normalized to the diffuse background as a function of angle* θ *for (a) an opal composed of spheres of radius 326 nm measured at a wavelength of 780 nm, and (b) the air-sphere crystal* ($\lambda = 460$ *nm). The curves are least-squares fits to the data of the cone shape predicted by diffusion theory for a disordered medium. For the air spheres we find the profile as a function of* $|\theta|$ *by integrating over circles concentric with the peak in the two-dimensional image (inset). The points* $\theta < 0$ *are duplicates of* $\theta > 0$.

We measured backscattering from the air-sphere crystals using a setup allowing continuous tuning of the wavelength. As a light source we used a parametric oscillator pumped by the third harmonic of a diode pumped Nd:YAG laser (Coherent Infinity 40-100 XPO). The wavelength of the parametric oscillator is fully tunable over the visible spectrum, and its short coherence length facilitates speckle averaging. The beam from the oscillator was collimated to a divergence of ~ 1 mrad; the beam diameter was ~ 0.5 mm at the position of the air-sphere crystal. The beam was incident on a (111) plane of the sample via a beam splitter which is wedged to avert ghost reflections. The backscattered intensity was collected on a Kappa CF 8/1 FMC 8-bit CCD camera positioned in the focal plane of a positive lens. The detection was in the polarization-conserving channel. The sample was slightly tilted to keep the specular reflection away from the backscattering direction . Speckle averaging was performed by spinning the sample, averaging over multiple camera exposures, and averaging concentric circles in the two dimensional images. This setup is optimal in the sense that the resolving power ~ 1 mrad is mainly determined by the Fourier limit set by the sample size, and convenient since it allows fast data acquisition.

6.5 Backscattering cones from photonic crystals

Figure 6.3(a) shows the backscattered intensity of a polystyrene opal composed of spheres of radius 326 nm measured at a wavelength of 780 nm. A triangular peak is observed in the backscatter direction $\theta = 0$, superimposed on the diffuse background, which is scaled to unity. The enhancement factors $\mathcal{E}$, defined in Eq. (6.11), range between 1.45 and 1.85 for the backscatter cones of opals. In the polarization-conserving detection channel single scattering is also detected. Since single scattering paths do

not have time reversed counterparts, single scattering contributes to the diffuse background only. Consequently, the cones are expected to have enhancement factors less than 2.

From the full width at half maximum W, typically 10 mrad for the opals, we estimate that the transport mean free path ℓ is of the order of 15 μm. Clearly ℓ is large compared to the wavelength $\lambda \sim 0.7$ μm. From a multiple scattering point of view, opals are therefore only weakly disordered. The transport mean free path is also much longer than the sphere radii $r \leq 0.5$ μm and exceeds 10 times the cubic lattice parameter a. We have found that backscatter cones of different opals composed of spheres of identical radius are of the same width within 10%. To study the effect of the capillary walls we have also measured enhanced backscattering from an opal which we removed from its capillary. No difference with the cone resulting from a duplicate opal still in its capillary was found. Visual inspection of the opals shows that the surface of the crystals is covered by colorful Bragg reflecting domains of various sizes, typically $\ll 1$ mm for the centrifuged samples ($r \leq 326$ nm), and ~ 1 mm for the remaining opals. We studied samples of which the surface was partly covered by small, and partly by large domains. No correlation between cone width and the size of the domains was found. Hence, the domain boundaries do not determine the degree of scattering. Enhanced backscattering inherently averages over the whole sample volume, while the Bragg reflections are determined by crystalline order close to the surface.

The backscatter cone of an air-sphere crystal ($\lambda = 460$ nm) is shown in Figure 6.3(b). These data were acquired by G. van Soest, M. Megens, and F. J. P. Schuurmans. The inset shows the two dimensional image obtained from averaging multiple camera exposures. The backscatter cone shows as a bright spot. The backscattered intensity as a function of $|\theta|$ is obtained by averaging circles concentric with the intensity peak. To facilitate visual inspection the data is plotted both for $\theta > 0$ and $\theta < 0$. The enhancement factor observed in case of the air-sphere crystals is typically 1.3. We attribute the low enhancement factor to experimental limitations related to the small sample size. The width of the backscatter cones of the air-spheres is typically 5 mrad.

The solid lines in Figures 6.3(a) and 6.3(b) are least-squares fits of the shape predicted by diffusion theory for the case of random, non-absorbing, semi-infinite slabs [20], without internal reflection ($\bar{R} = 0$), and taking $\xi = 1$ in Eq. (6.7). The only adjustable parameters are an overall scaling factor, the enhancement factor $\mathcal{E}$, and the width-determining parameter $\ell_W \approx 0.7 n_e (k_e W)^{-1}$ in terms of the full width at half maximum W of the cone. Here $k_e = \frac{2\pi}{\lambda} n_e$ is the wave vector of light in the medium of effective refractive index n_e. Diffusion theory describes the shape of the backscatter cones from our photonic crystals well, although the intensity scattered by the opal with $r = 120$ nm decreases more rapidly at large angles. It is remarkable that a theory developed to describe multiple scattering in random media fits the shape of backscatter cones originating from photonic crystals. This result indicates that the diffusion propagator is not strongly modified by the occurrence of stop gaps in the

dispersion. This may appear surprising, as stop gaps cover up to 50% of all directions in the case of photonic crystals.

We limit the discussion of the diffusion propagator to frequencies for which propagating modes exist in the perfect photonic crystal. In this case the macroscopic energy density balance considerations leading to the diffusion equation are still expected to hold on length scales ℓ, exceeding the wavelength λ and the size of the unit cell. One may analyze the influence of stop gaps on diffusion through the bulk of a photonic crystal within a random walk picture. Clearly, a photon can not be scattered into a stop gap direction, as propagation into stop gap directions is forbidden in photonic crystals. Stop gaps therefore result in a photon random walk for which the outgoing wave vector for each scattering event is chosen on the dispersion surfaces at the probe frequency. The inhomogeneous sampling of the sphere of exit directions may translate into the components D_{x_i,x_j} of the diffusion tensor, where $x_{i,j} = x, y$ or z. As a simple model, one may study a random walk with exponential step length distribution and nonuniform angular probability distribution determined by the stop gaps. It may appear surprising that light can diffuse equally well into stop gap directions, as in any other direction. In this respect, it is important to realize that for points A and B on a line coincident with a stop gap direction, diffuse transport is *not* governed by paths propagating along AB. One finds that the real, symmetric diffusion tensor[1] $D_{x_i,x_j} \propto \langle x_i x_j \rangle$ has a symmetry consistent with the symmetry of the crystal involved. For noncubic crystals the diffuse transport of light may be anisotropic, similar to the anisotropic diffuse transport in partially disordered nematics [43], or anisotropically etched strongly scattering GaP macroporous sponges [44]. For cubic crystals the diffusion is isotropic. The coneshape is therefore expected to agree with diffusion theory for isotropic random media, in agreement with the experiment.

Optical absorption is detrimental for photonic band gap effects, which rely on multiple scattering and interference. Because very long light paths are sampled near the top of enhanced backscatter cones, *i.e.*, many times the sample thickness, enhanced backscattering is well suited to investigate absorption. Similar to the definition of the scattering mean free path, the absorption mean free path ℓ_a can be defined as the distance over which a wave decays by $1/e$ due to absorption. The cone however, is sensitive to the diffuse absorption length L_a, which is the mean distance between starting and ending point of a photon random walk of length ℓ_a. This length $L_a = \sqrt{\ell \ell_a/3}$ is obviously much smaller than the absorption mean free path ℓ_a. Absorption, or finite sample thickness (L) causes cone rounding over an angular range $\theta \propto 1/kL_c$, where L_c is L or L_a, depending on which is shorter. From the sharpness of the cusp at 0° in Figure 6.4, we determine an upper bound to the absorption mean free path in polystyrene opal of at least 0.5 cm, that is $> 10^4 \times \lambda$, or $20 \times L$. As the observed cone rounding is comparable to the angular resolution, the absorption mean free path may even be longer. Enhanced backscattering is one of the few techniques in which the sample thickness does not set a limit on the magnitude of the absorp-

[1] Since we do not present dynamic measurements, we ignore the possibility of an anisotropic energy velocity.

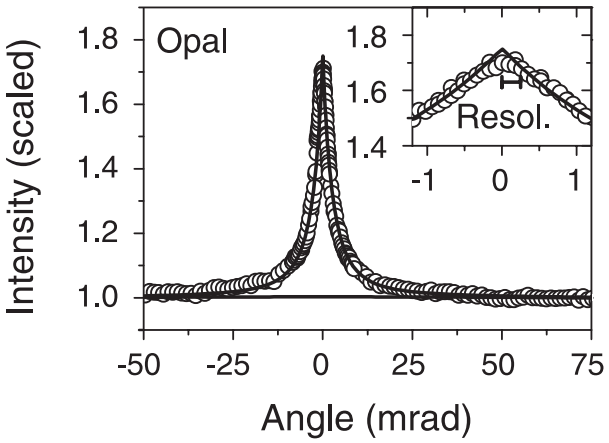

FIGURE 6.4: *The backscattered intensity normalized to the diffuse background as a function of angle* θ *for an opal composed of spheres of radius 180 nm measured at a wavelength of 685 nm. The inset shows the top of the cone, which is expected to be cusped for infinite nonabsorbing samples. The rounding, which appears limited by the angular resolution, provides an upper limit to the absorption length.*

tion mean free path that can be measured. Unfortunately, the large angular resolution needed to quantify weak absorption requires a large extent of the sample perpendicular to the beam. In this respect, the sample size of the air sphere crystals appears to be limiting.

6.6 Photonic effect on the cone width

For random media without diffuse internal reflection, ℓ_W is identical to the transport mean free path ℓ. For disordered media with an effective refractive index mismatch with the surroundings, the cone is narrowed as a result of internal reflections [27], as exemplified by Eq. (6.13). Here, we discuss the effect of stop bands on the value of ℓ_W. It is instructive to consider the fitted length scale ℓ_W as a function of the size parameter $x = k_0 r = (2\pi/\lambda)r$, which equals $\pi/\sqrt{2}\,[\omega a/(2\pi c)]$, of the polystyrene spheres (Figure 6.5(a)), or air spheres (Figure 6.5(b)): both the scattering properties of the spheres and air holes, and the stop band frequencies of the crystals scale with x [22]. The frequencies of the (111) Bragg reflections in the relevant size parameter range were measured in a normal-incidence reflectivity measurement as described in Ref. [18]. We have indicated the red and blue edges of the associated L-gaps by vertical lines in Figures 6.5(a) and 6.5(b). For the opals, higher order normal-incidence stop bands are indicated by vertical marks on the bottom axis.

For the opals the data are grouped by sample in Figure 6.5(a) since comparison between different samples is *a priori* difficult due to possible differences in defect

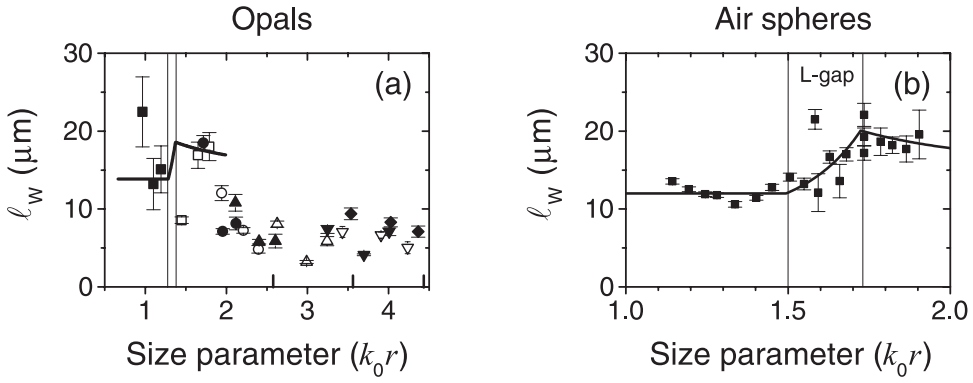

FIGURE 6.5: *The width determining parameter ℓ_W as a function of the size parameter $x = (2\pi/\lambda)r$ for (a) all polystyrene samples (sphere radii* 120 (■), 180 (□), 213 (●), 241 (○), 262 (▲), 326 (△), 403 (▼), 426 (▽), 439 *nm* (♦)*) and (b) the air-sphere crystal. The red and blue edge of the first order L-gap are indicated in (a) and (b) by vertical lines. In (a) higher order L-gap stop bands are indicated by vertical marks on the bottom axis. The center frequencies of the stop bands are inferred from reflectivity spectra. The solid curves result from the diffusion model incorporating photonic crystal effects, and are scaled to match the value of ℓ_W at the red edge of the stop band. Apart from the scaling factor there is no adjustable parameter.*

structure. The reproducibility of the cone width among sets of opals of identical spheres and the modest scatter suggest that a comparison over the whole size parameter range is allowed. A marked decrease of ℓ_W from 20 to 7 μm starting at the red side of the first order (111) stop band is observed, followed by an increase at the blue edge. After a maximum near $x = 1.7$ the value of ℓ_W remains close to 7 μm. The data from the air-sphere crystal (Figure 6.5(b)) were acquired as a function of wavelength over the whole visible spectrum. An increase of ℓ_W from $\ell_W \approx 14$ μm starting at the red edge of the (111) stop band to $\ell_W \approx 20$ μm at the blue edge is observed for the air-sphere crystal.

We expect the variation of ℓ_W close to the stop band to be caused by the photonic band structure. A Mie calculation [22] indeed shows that the scattering properties of the individual spheres in the opals and air-sphere crystal are nearly constant in the size parameter range of the stop band. The width of the cone is crucially influenced by the fact that the (111) planes are parallel to the sample surface, resulting in L-gaps which coincide with the incident and backscatter direction. Starting from the diffusion approach [19, 27], we observed in Section 6.3 that the cone width is affected by two different mechanisms, the first of which concerns internal reflection of the diffuse intensity, and the second the attenuation length of the coherent beam.

The external photonic crystal boundary can influence the cone width through both mechanisms. Two important cases are considered in Fig. 6.6, depending on the orientation of the reciprocal lattice vectors relative to the sample boundary. The experiments reported in this thesis are limited to the case where the sample normal

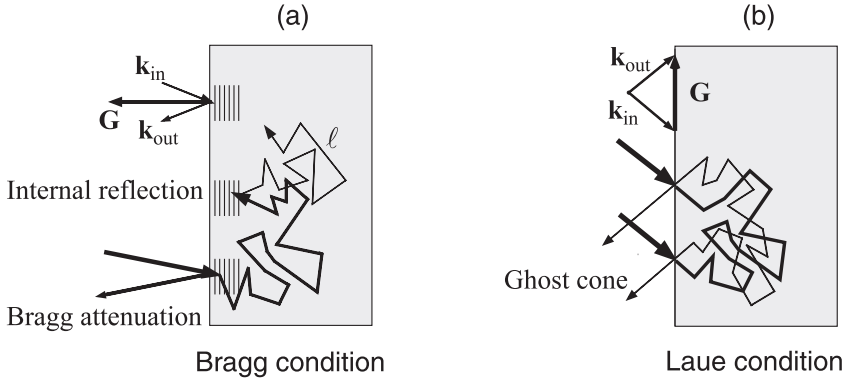

FIGURE 6.6: *(a)The backscatter cone is affected by two mechanisms if the frequency is in a stop band for a reciprocal lattice vector normal to the surface. The cone is broadened if the incident beam (lower left, bold arrow) is attenuated by Bragg diffraction,* i.e., *if it matches the Bragg condition* $\mathbf{k}_{out} - \mathbf{k}_{in} = \mathbf{G}$ *for the [111] reciprocal lattice vector* **G** *(upper left corner). Light paths in the medium are internally reflected if they arrive at the sample boundary at an orientation matching the Bragg condition. The internal reflections create longer light paths, hence the cone is narrowed. (b) Satellite or 'ghost' cones may appear if the incident wave vector matches a Laue condition. The enhanced backscattering cone of the Laue diffracted beam is found by taking the mirror image of the conventional cone in the crystal planes associated with* **G**.

coincides with the 111 reciprocal lattice vector, associated with the lowest order stop gap. As sketched in Fig. 6.6(a), the injection of diffuse light from incident beams into the samples may be strongly frequency dependent due to Bragg attenuation of the incident beam. The associated Bragg attenuation length L_B is expected to be of the order of a few lattice spacings. Since Bragg attenuation shortens the penetration depth of the incident beam, the cone width is expected to increase according to Eq. (6.13). On the other hand Bragg diffraction can enhance the internal reflection coefficient (Fig. 6.6(b)), causing narrowing of the cone due to reinjection of diffuse photons. It is important to note that the cone broadening due to Bragg attenuation of the coherent beam strongly depends on both the frequency and the angle of incidence of the probe beam around which the backscatter cone is recorded. On the other hand the cone narrowing due to internal reflection of diffuse intensity is a much more robust effect that only depends on the probe frequency through the frequency dependence of the angle-averaged internal reflection coefficient.

The alternative case, sketched in Fig. 6.6(b) was first considered by Gorodnichev and coworkers [45]. If the incident wave vector matches a Laue diffraction condition for some reciprocal lattice vector, the diffuse intensity may be enhanced both in the backscatter direction and in the Laue diffracted counterpart of the backscatter direction. This case is most easily analyzed if the relevant reciprocal lattice vector is parallel to the crystal surface. The secondary cone can be understood as the enhanced backscattering of the Laue diffracted beam that is set up by the incoming beam prior

to the first scattering event. According to Ref. [46], the intensity in the primary and secondary cone together adds up to an enhancement factor 2. Experimental observation in opals or inverse opals is hampered by the polycrystalline averaging around the 111 reciprocal lattice vector. Here, we are concerned with the cone width for incident and backscattered beam in a Bragg diffraction geometry.

Relevant parameters, such as the stop band width and the maximum solid angle of excluded directions, as well as the attenuation length for frequencies in the stop band are conveniently expressed in terms of the photonic strength parameter Ψ. In essence, the photonic strength parameter is the polarizability α per unit cell volume [47] of the scatterers that compose the photonic crystals, and it equals the relative frequency width of the L-gap (see Chapter 2, Eq. (2.11)). In a two-band approximation [48, 49], the maximum angular extent of the stop band is a cone of half apex angle approximately $\theta_{\max} = \arctan(\sqrt{2\Psi}) \approx \sqrt{2\Psi}$ [50], which is attained at the blue edge of the L-gap. We estimate the diffuse reflection coefficient by employing the procedure described in Ref. [29], replacing the directional reflection coefficient $R(\theta)$ by 1 for directions within a stop band, and 0 outside. This model predicts a maximum value $\bar{R} \approx 4\Psi$ for the angle-averaged diffuse reflection coefficient appearing in Eq. (6.4), which would imply a narrowing of the cone by a factor ~ 1.4 for opals ($\Psi = 0.07$) and ~ 2 ($\Psi = 0.12$) for the air-sphere crystal. The calculated diffuse reflection coefficient increases linearly with frequency from zero at the red edge to its maximum value at the blue edge. It decreases beyond the stop band, as the solid angle of excluded propagation directions diminishes. The effect of internal reflections due to the effective refractive index mismatch of the samples is negligible. Due to the complexity of the second and higher order Brillouin zones, we have not yet attempted to extend the model to the frequency range of higher order stop bands.

If the incident and backscatter direction coincide with a stop gap, the incident and backscattered beam are attenuated by Bragg diffraction in addition to the extinction by random scattering which also occurs for incident beams outside a stop gap (*cf.* Fig. 6.6(a)). The composite attenuation length is obtained by combining both attenuation length scales in $\ell_X^{-1} = \ell^{-1} + L_B^{-1}$, where L_B is the Bragg attenuation length. Since the L-gaps in the opals and air-sphere crystal extend over a cone of half apex angle $\gtrsim 0.2$ rad which is much larger than the typical width of the enhanced backscatter cones $\lesssim 20$ mrad, we assume an angle independent attenuation length. This assumption does not hold at frequencies close to the stop band edges. The two-band model [48, 49] predicts that the attenuation length $L_B = 2d_{111}/(\pi\Psi)$ scales with the 111 crystal plane spacing $d_{111} = a/\sqrt{(3)}$ and is inversely proportional to the photonic strength Ψ. We find $L_B \approx 6d_{111} = 1.5\,\mu$m at the center of the L-gap for the inverse opal with $a = 360$ nm, and $L_B \approx 10d_{111}$ for the polystyrene opals. However, experimental studies indicate that the attenuation length is at least a factor two [51] to five [15, 52] longer than predicted by the two-band model. The disagreement has been attributed to disorder in general [52] and planar stacking faults specifically [51]. If the magnitude of the attenuation length is a factor of five larger than predicted by the two-band model, it is of the order of or longer than the transport mean free path itself, so the

effect of attenuation on the cone width is insignificant, *i.e.*, $\xi \approx 1$. Apparently, it remains a challenge to interpret attenuation lengths in photonic gaps, especially in the limit of high refractive index.

The solid curve in Figure 6.5(a) results from the model presented in the previous section, limited to cone narrowing due to internal reflection only (*i.e.*, keeping $\xi = 1$). The photonic strength parameter $\Psi = 0.07$, determined by the relative full width at half maximum of the normal incidence reflection peak of the opals, was used to evaluate the diffuse reflection coefficient. We expect the cone to be unaffected by the photonic band structure for frequencies below the stop gap, for which a Bragg condition is never met. Consequently, we scale the solid curve in Figure 6.5(a), *i.e.*, ℓ_W/ℓ as defined in Eq. (6.13), to match ℓ_W at the red edge of the stop band where $\ell_W = \ell$. The model contains no other adjustable parameter. As the wavelength is tuned into the stop band the theory predicts an increase of ℓ_W at the blue edge of the stop band which is due to the internal reflections. The predicted ratio between ℓ_W at the red side and ℓ_W at the blue side of the gap depends only on the internal reflection correction. The predicted increase by a factor $1/(1-\bar{R}) \approx 1.4$ agrees with the data. For the more strongly photonic air-sphere crystals, the denser sampling of size parameters close to the L-gap allows a more detailed comparison of the model and the data. The model (solid curve in Figure 6.5(b)) successfully explains the narrowing of the backscatter cones at the blue side of the stopgap relative to the red side by a factor ≈ 2 which is consistent with $\bar{R} \approx 4\Psi \approx 0.5$.

No evidence for the cone broadening predicted in Eq. (6.13) is discerned in the frequency dependence of the apparent mean free path ℓ_W reported in Fig. 6.5. In part, this may be due to the fact that disorder in itself strongly increases the attenuation length by a factor two [51] to five [15, 52]. The expected effect on the apparent mean free path ℓ_W of both internal reflection and various magnitudes of the Bragg attenuation of the incident beam combined, is plotted in Fig. 6.7, for the case of the TiO_2 inverse opal. A cone broadening exceeding a factor 2 is expected for the frequency-dependent Bragg attenuation length predicted by the two-band scalar wave approximation (SWA). The broadest cone is expected at the minimum of the solid curve in Fig. 6.7, for a frequency just above the red edge of the L-gap.

Figure 6.7 demonstrates the effect of extending the attenuation length by a factor 2 to 10, as consistent with Ref. [15, 51, 52]. The expected cone broadening reduces to a 20% effect, comparable with the scatter and uncertainty in the data. It appears that a more careful experiment needs to be conducted to clarify the role of the attenuation length in inverse opals. Presently, the small sample size $\lesssim$ 1 mm dictates an angular resolution $\sim$ 1 mrad, which is 20% of the angular width of the cone for inverse opal. One would therefore need either a larger sample, or a smaller mean free path, to precisely determine $\xi = 1 + \ell/L_B$ from enhanced backscattering. For the opals, the probe wavelengths and lattice parameters did not allow careful study of the cone width as the normalized frequency a/λ did not sample the Bragg condition at near normal incidence.

The novel cone widening phenomenon due to Bragg attenuation predicted by

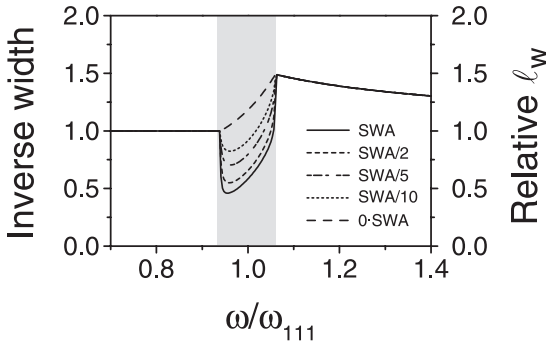

FIGURE 6.7: *The apparent mean free path ℓ_W inferred from the inverse cone width in units of the true mean free path ℓ according to the simple diffusion model with photonic internal reflection and Bragg attenuation Eq.(6.13). The frequency dependent angle-integrated internal reflection coefficient and the Bragg attenuation length are approximated by a two-band scalar wave approximation, and only depend on the photonic strength, $\Psi = 0.12$ for the inverse opal. Different curves were obtained with the same frequency dependent internal reflection, but with Bragg attenuation length reduced by factors $1, 2, 5, 10, \infty$ (lines as indicated in the graph) compared to the scalar wave approximation (SWA)*

Eq. (6.13) is not an artifact of our theory. In fact, an experiment confirming our theory was recently conducted [21] on more disordered ($\ell = 7\ \mu$m) silica opals with size parameter comparable to our $k_0 r = 1.5$ ($\lambda = 632$ nm, $r = 150$ nm). The smaller mean free path widens the cone, allowing a better resolution compared to the cone width. In contrast to our experiment, Huang *et al.* tuned the angle of incidence at fixed probe wavelength through the Bragg condition in a specific search of the cone widening. Despite the low enhancement factor ~ 1.2 and high noise level (20 % of the interference peak) in their enhanced backscattering cones, a widening of the cone by a factor ~ 2 appears for incidence angles matching the Bragg condition. Their measurements appear to be consistent with $L_B = 5.1\ \mu$m$= 22 d_{111}$, *i.e.*, $\xi = 2.4$, amounting to about twice the attenuation length predicted by the scalar wave approximation. Unfortunately, the cone widening does not appear to be easily usable as an accurate probe for the attenuation length, as the cone widening in Eq. (6.13) saturates with increasing ξ. At $\xi = 2.4$ for instance, a 25% variation in L_B causes only a 5% variation in the cone broadening factor.

6.7 Scattering by polydispersity and displacements

Finally, we discuss a scattering mechanism which accounts for the order of magnitude of the transport mean free paths measured in the opals. For a comparison of the data with a scattering model, we define the apparent scattering efficiency of each sphere in the opal as $Q_{\text{app}} = 1/(\rho \ell_W \pi r^2)$, where we neglect the cone widening correction on ℓ. Here, $\rho = \varphi/(\frac{4}{3}\pi r^3)$ is the sphere number density in the close-packed *fcc* opal

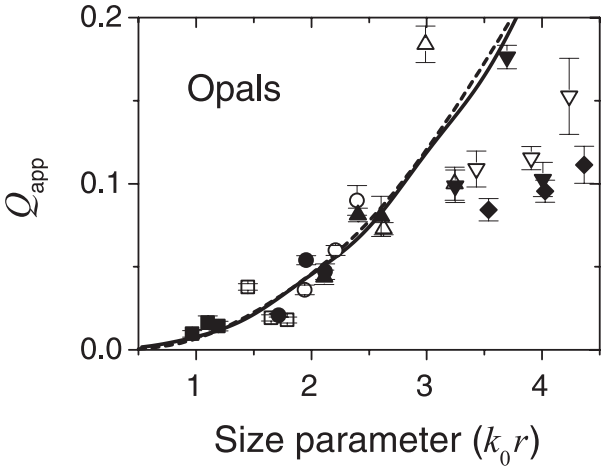

FIGURE 6.8: *The apparent scattering efficiency per sphere Q_{app} as a function of the size parameter, for radii* 120 *(■),* 180 *(□),* 213 *(●),* 241 *(○),* 262 *(▲),* 326 *(△),* 403 *(▼),* 426 *(▽),* 439 *nm (♦). The solid line is the Rayleigh-Gans scattering efficiency of a thin shell (thickness* 5% *of the radius) of refractive index 1 in an effective medium of refractive index* 1.45*. The dashed line is a quadratic approximation.*

(volume fraction $\varphi = 0.74$). As shown in Figure 6.8, we observe that the apparent cross-section increases quadratically with the size parameter (dashed line), and is at the level of $\sigma_{app} = Q_{app}\pi r^2 = 0.015\pi r^2$ for $k_0 r = 1$. The quadratic scaling $\ell \propto 1/\omega^2$ is distinct from the Rayleigh-like ω^{-4} reported in Ref. [15], and will be further confirmed for air sphere crystals in Chapter 7. For larger size parameters, the apparent scattering efficiency saturates, as is typical for the scattering efficiency of objects large or comparable in size relative to the wavelength. A Rayleigh-like ω^{-4} scaling behavior would indicate scattering by inhomogeneities with cross-section much smaller than the wavelength. A quadratic scaling on the other hand is typical for Rayleigh-Gans scattering [22], and suggests weak scatterers that are of the order of the wavelength in size.

Naively, one might assume that, *e.g.*, missing spheres and grain boundaries play a role in determining the degree of scattering. If the opal is treated as a homogeneous medium with effective refractive index $n_{eff} = 1.45$, the cross-section of a single missing sphere can be estimated from Mie theory. A point defect density worse than 1 missing sphere out of 30, *i.e.*, 0.13 per cubic unit cell, would be required to generate the degree of scattering reported here. As the experimentally estimated density of 10^{-2} missing spheres per cubic unit cell [15, 51, 53, 54] remains far below 0.1 per unit cell, point defects do not appear to be the dominant source of scattering.

Instead, we propose that the scattering in opals is mainly due to polydispersity of the spheres and small displacements from their lattice sites. As a simple model, we consider the *difference* in refractive index profile of the displaced, slightly poly-

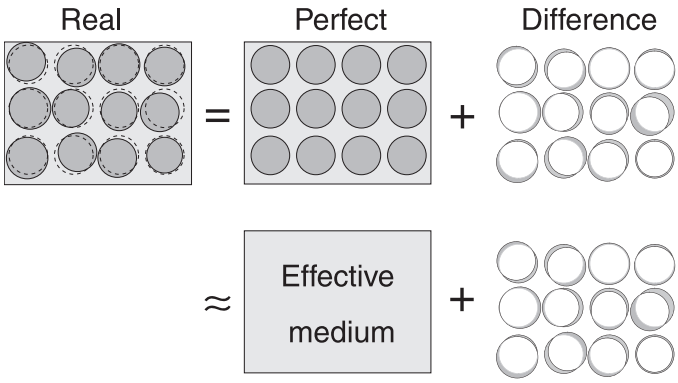

FIGURE 6.9: *Sketch of a real photonic crystal that is a stack of building blocks with a certain spread in size, slightly displaced from the ideal lattice sites. This structure can be thought of as the sum of the ideal structure, which does not scatter, and the difference between the real and ideal structure. This difference is a collection of thin shells that weakly scatter. For an order of magnitude estimate, we model the ideal 'background' structure as an effective medium.*

disperse Mie-spheres as compared to the ideally ordered structure. As schematically indicated in Fig. 6.9, this difference is a collection of thin shells of air and polystyrene, which we assume to be embedded in an effective medium of index $n_{\text{eff}} = 1.45$ relevant for the opals. We have calculated the Rayleigh-Gans scattering efficiency [22] of thin spherical shells of refractive index[2] 1 and radius r equal to the sphere radius embedded in an effective medium with index of refraction $n_{\text{eff}} = 1.45$. One should note that one cannot truly replace the geometrical disorder by a collection of spherical scatterers centered at the lattice sites. In fact, although the *average* difference shell is spherical and aligned with the lattice, such a model gives rise to a photonic band structure, as it involves a periodically varying index contrast. It remains unclear how to deal with the remnant positional correlations of the 'difference' shells that give rise to random scattering. In the comparison presented here, we ignore the correlation and assume independent scattering, *i.e.*, $\ell = (\rho\, Q_{\text{shell}} \pi r^2)^{-1}$ for shells with scattering efficiency Q_{shell} and density ρ equal to the sphere density in the crystal. Within the Rayleigh-Gans approximation the scattering efficiency of a thin shell reads

$$Q_{\text{shell}} = |m-1|^2 x_e^2 \left(\frac{\Delta r}{r}\right)^2 \int_0^\pi [1+\cos^2(\theta)] \sin(\theta) \frac{\sin^2[2x_e \sin(\theta/2)]}{[2x_e \sin(\theta/2)]^2}\, \mathrm{d}\theta, \quad (6.15)$$

in terms of the index contrast $m = n_{\text{shell}}/n_{\text{eff}}$, size parameter within the medium $x_e = n_{\text{eff}} k_0 r$, and relative shell thickness $\Delta r/r$. The integral runs over the scattering angle θ relative to the incident direction. As shown in Figure 6.8, this simple shell model (solid line) compares well to the data for shell thicknesses which are 4% of the nearest neighbor distance between spheres in the crystal. In the range $0.5 \leq k_0 r \leq 5$ the

[2] The 'air' shells have a larger index contrast (1/1.45) than the polystyrene shells (1.59/1.45) relative to the effective index.

scattering efficiency Q_{shell} is well approximated by a quadratic dependence $Q_{\text{shell}} \simeq 9(m-1)^2(\Delta r/r)^2(k_0 r)^2$. For smaller size parameters, far below the Bragg condition, the integral in Eq. (6.15) causes a $Q_{\text{shell}} \propto (k_0 r)^4$ dependence, in accordance with Rayleigh scattering. The value $\Delta r/r \sim 4\%$ is consistent with the small sphere polydispersity of ~2%, and with the estimated root mean square displacement u_{RMS}. In *fcc* crystals of polystyrene spheres in suspension at a volume fraction of 56% the displacement u_{RMS} was determined to be ~ 3.5% of the nearest neighbor distance [41]. In the more dense opals we estimate $u_{\text{RMS}} \lesssim 3.5\%$.

For titania inverse opals the increase of Q_{shell} due to the enhanced index contrast of the difference shells ($m = 2.5/1.18$) is partly compensated by the decrease in effective refractive index ~ 1.18 that reduces x. The mean free path in the inverse opal considered here is compatible with a difference shell thickness of 2.5% of the nearest neighbor distance. We expect two and three dimensional periodic structures prepared along alternative routes to suffer from at least the same degree of scattering. Authors quote size variations of ~ 5% for air-holes in lithographically prepared state of the art 2D crystal slabs [9, 10]. Layer-by-layer micromachined woodpile structures on the other hand, appear to suffer most from displacements of ~ 7% of the nearest neighbor distance. According to the scaling in Eq. (6.15), the fluctuations need to be reduced by at least an order of magnitude to allow for photonic crystals to operate over length scales up to a millimeter. Reducing fluctuations in position and size to the required subnanometer level appears to be a virtually impossible task.

6.8 Conclusion

We have reported the first observations of enhanced backscattering of light by photonic crystals. The results indicate that the opals and the strongly photonic air-sphere crystals are weakly randomly scattering since the observed transport mean free paths are much longer than optical wavelengths. The transport mean free path also exceeds the typical periodicity of the crystals, *i.e.*, the 111 plane separation, by an order of magnitude. It appears that the scattering is dominated by the polydispersity and random displacements of the building blocks of which the crystals are composed. We have demonstrated that the cone shape is affected by the photonic band structure through two mechanisms: the inverse cone width is increased as a consequence of diffuse internal reflections which result from Bragg scattering, while it may decrease due to attenuation of the coherent beam which acts as the source of the diffuse intensity. An extension of the diffusion model incorporating these effects successfully explains the narrowing of the cones which is observed as the frequency is tuned from the red to the blue edge of the L-gap. The lack of reported experimental studies of the attenuation length hampers the accurate description of the increase in cone width in the stop band itself. The Bragg attenuation length in photonic crystals and the influence of disorder thereon is certainly not well understood or experimentally determined. Further efforts to quantify the attenuation length in photonic crystals as a function of frequency, orientation and mean free path may benefit from the the-

oretically predicted cone widening effect, as it provides one of the few experimental probes for which the sample thickness is irrelevant. Unfortunately, the probe is only sensitive if ℓ/L_B is of the order 1 to 3. We have presented a first analytical model that successfully describes the degree of scattering by imperfections in photonic crystals. We conclude that formidable accuracy in fabrication is required if photonic crystals at optical frequencies are desired to operate as millimeter-sized platforms for manipulating photons.

References

[1] E. Yablonovitch, *Inhibited Spontaneous Emission in Solid-State Physics and Electronics*, Phys. Rev. Lett. **58**, 2059 (1987).

[2] A. F. Koenderink, L. Bechger, H. P. Schriemer, A. Lagendijk, and W. L. Vos, *Broadband Fivefold Reduction of Vacuum Fluctuations Probed by Dyes in Photonic Crystals*, Phys. Rev. Lett. **88**, 143903 (2002).

[3] S. John, *Strong Localization of Photons in Certain Disordered Dielectric Superlattices*, Phys. Rev. Lett. **58**, 2486 (1987).

[4] P. W. Anderson, *Absence of Diffusion in Certain Random Lattices*, Phys. Rev. **109**, 1492 (1958).

[5] D. S. Wiersma, P. Bartolini, A. Lagendijk, and R. Righini, *Anderson Localization of Light*, Nature **390**, 671 (1997).

[6] J. Gómez Rivas, R. Sprik, A. Lagendijk, L. D. Noordam, and C. W. Rella, *Mid-Infrared Scattering and Absorption in Ge Powder Close to the Anderson Localization Transition*, Phys. Rev. E **62**, R4540 (2000).

[7] J. Gómez Rivas, R. Sprik, A. Lagendijk, L. D. Noordam, and C. W. Rella, *Static and Dynamic Transport of Light Close to the Anderson Localization Transition*, Phys. Rev. E **63**, 046613 (2001).

[8] F. J. P. Schuurmans, M. Megens, D. Vanmaekelbergh, and A. Lagendijk, *Light Scattering Near the Localization Transition in Macroporous GaP Networks*, Phys. Rev. Lett. **83**, 2183 (1999).

[9] T. Baba and N. Fukaya, *Light Propagation Characteristics of Defect Waveguides in a Photonic Crystal Slab*, in [16] 105 (2000).

[10] M. Notomi, K. Yamada, A. Shinya, J. Takahashi, C. Takahashi, and I. Yokohama, *Extremely Large Group-Velocity Dispersion of Line Defect Waveguides in Photonic Crystal Slabs*, Phys. Rev. Lett. **87**, 253902 (2001).

[11] S. Ogawa, K. Tomoda, and S. Noda, *Effects of Structural Fluctuations on Three-Dimensional Photonic Crystals Operating at Near Infrared Wavelengths*, J. Appl. Phys. **91**, 513 (2002).

[12] J. E. G. J. Wijnhoven and W. L. Vos, *Preparation of Photonic Crystals Made of Air Spheres in Titania*, Science **281**, 802 (1998).

[13] J. E. G. J. Wijnhoven, L. Bechger, and W. L. Vos, *Fabrication and Characterization of Large Macroporous Photonic Crystals in Titania*, Chem. Mater. **13**, 4486 (2001).

[14] J. Galisteo Lòpez and W. L. Vos, *Angle Resolved Reflectivity of Single-Domain Photonic Crystals, Effects of Disorder*, Phys. Rev. E **66**, 036616 (2002).

[15] Y. A. Vlasov, M. A. Kaliteevski, and V. V. Nikolaev, *Different Regimes of Light Localization in a Disordered Photonic Crystal*, Phys. Rev. B **60**, 1555 (1999).

[16] *Photonic Crystals and Light Localization in the* 21st *Century*, edited by C. M. Soukoulis (Kluwer, Dordrecht, 2001).
[17] Z.-Y. Li and Z. Q. Zhang, *Fragility of Photonic Band Gaps in Inverse-Opal Photonic Crystals*, Phys. Rev. B **62**, 1516 (2000).
[18] M. S. Thijssen, R. Sprik, J. E. G. J. Wijnhoven, M. Megens, T. Narayanan, A. Lagendijk, and W. L. Vos, *Inhibited Light Propagation and Broadband Reflection in Photonic Air-Sphere Crystals*, Phys. Rev. Lett. **83**, 2730 (1999).
[19] M. B. van der Mark, M. P. van Albada, and A. Lagendijk, *Light Scattering in Strongly Scattering Media: Multiple Scattering and Weak Localization*, Phys. Rev. B **37**, 3575 (1988).
[20] M. B. van der Mark, *Propagation of Light in Disordered Media: A Search for Anderson Localization*, Ph.D. thesis, University of Amsterdam, 1990.
[21] J. Huang, N. Eradat, M. E. Raikh, Z. V. Vardeny, A. A. Zakhidov, and R. H. Baughman, *Anomalous Coherent Backscattering of Light from Opal Photonic Crystals*, Phys. Rev. Lett. **86**, 4815 (2001).
[22] H. C. van de Hulst, *Light Scattering by Small Particles* (Dover, New York, 1981).
[23] C. F. Bohren and D. R. Huffman, *Absorption and Scattering of Light by Small Particles* (John Wiley & Sons, New York, 1983).
[24] A. Ishimaru, *Wave Propagation and Scattering in Random Media* (Academic Press, New York, 1978).
[25] M. P. Albada, B. A. van Tiggelen, A. Lagendijk, and A. Tip, *Speed of Propagation of Classical Waves in Strongly Scattering Media*, Phys. Rev. Lett. **66**, 3132 (1991).
[26] A. Lagendijk and B. A. van Tiggelen, *Resonant multiple scattering of light*, Phys. Rep. **270**, 143 (1996).
[27] A. Lagendijk, R. Vreeker, and P. de Vries, *Influence of Internal Reflection on Diffusive Transport in Strongly Scattering Media*, Phys. Lett. A **136**, 81 (1989).
[28] I. Freund and R. Berkovits, *Surface Reflections and Optical Transport Through Random Media: Coherent Backscattering, Optical Memory Effect, Frequency, and Dynamical Correlations*, Phys. Rev. B **41**, 496 (1990).
[29] J. X. Zhu, D. J. Pine, and D. A. Weitz, *Internal Reflection of Diffusive Light in Random Media*, Phys. Rev. A **44**, 3948 (1991).
[30] T. M. Nieuwenhuizen and J. M. Luck, *Skin Layer of Diffusive Media*, Phys. Rev. E **48**, 569 (1993).
[31] D. J. Durian, *Influence of Boundary Reflection and Refraction on Diffusive Photon Transport*, Phys. Rev. E **50**, 857 (1994).
[32] M. U. Vera and D. J. Durian, *Angular Distribution of Diffusely Transmitted Light*, Phys. Rev. E **53**, 3215 (1996).
[33] M. U. Vera, P.-A. Lemieux, and D. J. Durian, *Angular Distribution of Diffusely Backscattered Light*, J. Opt. Soc. Am. A **14**, 2800 (1997).
[34] P. de Vries, D. V. van Coevorden, and A. Lagendijk, *Point Scatterers for Classical Waves*, Rev. Mod. Phys. **70**, 447 (1998).
[35] C. Caloz, A. K. Skrivervik, and F. E. Gardiol, *Comparison of Two Methods for the Computation of Green's Functions in Photonic Bandgap Materials: The Eigenmode Expansion Method and the Phased-Array Method*, Microw. Opt. Technol. Lett. **27**, 323 (2000).
[36] M. Doosje, B. Hoenders, and J. Knoester, *Scattering of Light on the Surfaces of Photonic Crystals*, Opt. Commun. **206**, 253 (2002).
[37] Y. Kuga and A. Ishimaru, *Retroreflectance from a Dense Distribution of Spherical Particles*, J. Opt. Soc. Am. A **8**, 831 (1984).

[38] E. Akkermans, P. E. Wolf, and R. Maynard, *Coherent Backscattering of Light by Disordered Media: Analysis of the Peak Line Shape*, Phys. Rev. Lett. **56**, 1471 (1986).
[39] J. D. Jackson, *Classical Electrodynamics* (John Wiley & Sons, New York, 1975).
[40] P. N. den Outer, *Multiple Light Scattering in Random Scattering Media*, Ph.D. thesis, University of Amsterdam, 1995.
[41] W. L. Vos, M. Megens, C. M. van Kats, and P. Bösecke, *X-Ray Diffraction of Photonic Colloidal Single Crystals*, Langmuir **13**, 6004 (1997).
[42] D. S. Wiersma, M. P. van Albada, and A. Lagendijk, *An Accurate Technique to Record the Angular Distribution of Backscattered Light*, Rev. Sci. Inst. **66**, 5473 (1995).
[43] D. S. Wiersma, A. Muzzi, M. Colocci, and R. Righini, *Time-Resolved Anisotropic Multiple Light Scattering in Nematic Liquid Crystals*, Phys. Rev. Lett. **83**, 4321 (1999).
[44] P. M. Johnson, B. P. J. Bret, J. Gómez Rivas, J. Kelly, and A. Lagendijk, *Anisotropic Diffusion of Light in a Strongly Scattering Material*, Phys. Rev. Lett. **89**, 243901 (2002).
[45] E. E. Gorodnichev, S. L. Dudarev, D. B. Rogozkin, and M. I. Ryazanov, *Weak Localization of Waves in Incoherent Scattering in Crystals*, Sov. Phys.–JETP **69**, 1017 (1989).
[46] A. Y. Sivachenko, M. E. Raikh, and Z. V. Vardeny, *Coherent Umklapp Scattering of Light from Disordered Photonic Crystals*, Phys. Rev. B **245103**, 63 (2001).
[47] W. L. Vos, R. Sprik, A. van Blaaderen, A. Imhof, A. Lagendijk, and G. H. Wegdam, *Strong Effects of Photonic Band Structures on the Diffraction of Colloidal Crystals*, Phys. Rev. B **53**, 16231 (1996).
[48] K. W. K. Shung and Y. C. Tsai, *Surface Effects and Band Measurements in Photonic Crystals*, Phys. Rev. B **48**, 11265 (1993).
[49] R. J. Spry and D. J. Kosan, *Theoretical Analysis of the Crystalline Colloidal Array Filter*, Appl. Spectroscopy **40**, 782 (1986).
[50] M. Megens, J. E. G. J. Wijnhoven, A. Lagendijk, and W. L. Vos, *Fluorescence Lifetimes and Linewidths of Dye in Photonic Crystals*, Phys. Rev. A **59**, 4727 (1999).
[51] J. F. Bertone, P. Jiang, K. S. Hwang, D. M. Mittleman, and V. L. Colvin, *Thickness Dependence of the Optical Properties of Ordered Silica-Air and Air-Polymer Photonic Crystals*, Phys. Rev. Lett. **83**, 300 (1999).
[52] Y. A. Vlasov, V. N. Astratov, O. Z. Karimov, A. A. Kaplyanskii, V. N. Bogomolov, and A. V. Prokofiev, *Existence of a Photonic Pseudogap for Visible Light in Synthetic Opals*, Phys. Rev. B **55**, R133356 (1997).
[53] Y. A. Vlasov, N. Yao, and D. J. Norris, *Synthesis of Photonic Crystals for Optical Wavelengths from Semiconductor Quantum Dots*, Adv. Mater. **11**, 165 (1999).
[54] Y. A. Vlasov, X. Z. Bo, J. C. Sturm, and D. J. Norris, *On-Chip Natural Assembly of Silicon Photonic Bandgap Crystals*, Nature **414**, 289 (2001).

Chapter 7

Angular Redistribution of Diffuse Light

Unavoidable structural disorder in photonic crystals causes weak multiple scattering of light. The consequences are extinction of incident and diffracted beams and the generation of diffuse light. We have studied the spectral and angular properties of the diffuse intensity transmitted by photonic crystals. The diffuse transmitted intensity is distributed over exit directions in a strikingly non-Lambertian manner, depending strongly on frequency. The remarkable frequency and angle dependence is quantitatively explained by a model incorporating diffusion theory and band structure on equal footing. The diffuse transmission reveals both the photonic band structure and the frequency-dependent extrapolation length. The model also describes the angle-dependent modification observed in emission spectra of internal sources in photonic crystals (Chapter 3). Total transmission corrected for the internal reflections shows a decrease of the transport mean free path slower than the characteristic Rayleigh law for frequencies in the range of first order Bragg diffraction. Hence the effect of structural disorder on the prospective higher order photonic band gap may be less severe than expected from previous reports.

7.1 Introduction

As interference is at the basis of photonic crystal properties, any mechanism that destroys the coherence of the composite structure may be detrimental to the advances promised in recent literature [1, 2]. Calculations have recently shown the effects of fluctuations in size and position of the unit cell building blocks on the photonic band gap. A fluctuation of order $\sim$ 5% of the unit cell size was found to be critical [3–5] in closing the band gap for inverse opals. Real two and three-dimensional structures inevitably suffer from disorder due to size-polydispersity, roughness and misarrangements of the building blocks. Fluctuations in size and position in current state of the art structures range from $\sim$ 3.5% of the nearest neighbor distance for air spheres in inverse opals [6], to 4–7% for 2D semiconductor photonic crystal slabs [7, 8] and layer-by-layer woodpile crystals [9]. In experiments these faults result in, *e.g.*, reduced Bragg reflection efficiency [10], apparent broadening of pho-

tonic stop gaps [11], and large transmission losses through crystals and incorporated wave guides [2]. It remains unclear how to quantify structural disorder of fabricated structures. No satisfactory theoretical framework exists to relate structural disorder to its optical effect, which is gauged by the mean free path ℓ over which light becomes diffuse. Furthermore, the fate of randomly scattered photons is unknown after they leave the incoming Bloch wave, both from a theoretical and experimental point of view. Since absorption ideally does not occur, the diffuse energy density is expected to exceed the energy density of the incoming beam over most or all of the bulk of any three-dimensional photonic crystal that is larger in size than ℓ in all three dimensions. Hence, it is of prime importance to know where scattered photons go after a mean free path, and how they leave a photonic crystal.

Small angle X-ray scattering [6] and electron microscopy have provided a quantitative measure of structural disorder in terms of polydispersity and misarrangements of the components that build up the titania inverse opals. These parameters determine the transport mean free path ℓ, which was recently determined experimentally for opals [12–14, see also Chapter 6] and inverse opals [13]. In this chapter we quantitatively account for the angle and frequency resolved characteristics of diffuse light transmitted by inverse opals. We show that the diffuse light is strongly affected by internal Bragg reflection, causing a drastic frequency-dependent redistribution of diffuse light over exit angles. This redistribution may be quantitatively explained by combining diffusion theory with internal reflections resulting from stop gaps in the photonic band structure. Our experiment also reveals the frequency dependence of the transport mean free path in the frequency range of the first order pseudo-gap. We find an increase of the scattering strength slower than Rayleigh's ω^4 law with frequency. This observation is similar to the results for opals reported in Chapter 6. The scaling points at the dominance of polydispersity, small displacements and roughness as sources of random scattering [13], as opposed to missing spheres or grain boundaries [12].

7.2 Diffusion theory of angle-resolved transmission

When a light beam with an intensity spectrum I_ω^{in} is incident on a photonic crystal surface, some fraction $R_{\omega,\gamma}^{\text{front}} I_\omega^{\text{in}}$ is (Bragg) reflected. The dependence on frequency ω and incidence angle γ (see Fig. 7.1) is indicated by subscripts, since these parameters are essential in the experiment, but not important in developing diffusion theory. The remaining light that is not Bragg reflected propagates into the sample where it suffers from extinction due to scattering by defects. The light removed from the incident beam is multiply scattered on length scales [15] equal to the transport mean free path ℓ, which we have determined to be of the order of $\ell \approx 15\,\mu$m for our opals and inverse opals, as obtained from enhanced backscattering measurements presented in Chapter 6. Since the thickness L of our crystals typically exceeds the mean free path, these crystals are opaque due to multiple scattering. In random media, the transport of multiply scattered light is usually well accounted for by the diffusion equation [15, 16]

introduced in Section 6.2. In this section, we review aspects of diffusion theory that are relevant for the angle-resolved transmission experiment presented in this chapter.

The success of diffusion theory depends on the use of appropriate boundary conditions, obtained by considering the diffuse fluxes at the sample walls. These conditions require that the diffuse intensity extrapolates to 0 at a distance $z_{e,\omega}$ from the sample walls, where the extrapolation length

$$z_{e,\omega} = \frac{2}{3}\left(\frac{1+\bar{R}^D_\omega)}{1-\bar{R}^D_\omega)}\right)\ell_\omega, \tag{7.1}$$

is determined by the polarization and angle-averaged internal reflectivity $\bar{R}^D_\omega$ of the sample boundaries [17–19]. The extrapolation length is crucial in correctly determining ℓ from enhanced backscattering or total transmission measurements, in which transmitted light integrated over all angles is collected. For example, it is well known that the total transmitted intensity $I^T_{\omega,\gamma}$ depends on the sample thickness according to

$$\begin{aligned} I^T_{\omega,\gamma} &:= I^{\text{in}}_\omega T_{\omega,\gamma} \\ &= I^{\text{in}}_\omega [1 - R^{\text{front}}_{\omega,\gamma}] \frac{\ell_\omega + z_{e,\omega}}{L + 2z_{e,\omega}}. \end{aligned} \tag{7.2}$$

Unless $z_{e,\omega}$ is accurately known, ℓ_ω can only be determined from the total diffuse transmission $T_{\omega,\gamma}$ if a series of measurements with fixed $R^{\text{front}}_{\omega,\gamma}$ is performed as a function of sample thickness L. For photonic crystals, varying L is a challenge, hence the extrapolation length should be known for a total transmission measurement to be useful in determining ℓ_ω.

The extrapolation length ratio $\tau_{e,\omega} := z_{e,\omega}/\ell_\omega$ can be determined from angle-resolved diffuse transmission (see Fig. 7.1(a)), which is determined by refraction and reflection of the diffuse flux at the sample interface. The relation between the angle-dependent and the angle-averaged internal-reflection coefficient, and the use of diffuse transmission to study both, was first discussed by Zhu, Pine and Weitz [18]. Their argument is based on a simple flux consideration. Following their approach, we consider a semi-infinite diffusively scattering sample bounded by a plane interface. We assume the sample to be limited to $z > 0$, where the z-axis is the sample surface normal. One may consider the flux through a small surface ds at the origin that is due to the diffuse energy density $W_{\omega,\gamma}(r,\phi,\alpha)$ in a volume element $\mathrm{d}V = r^2 \sin\alpha\, \mathrm{d}r\mathrm{d}\phi\mathrm{d}\alpha$ centered around a point (r,ϕ,α), in spherical coordinates (see Fig. 7.1(b)). This flux $\mathrm{d}J_{\omega,\gamma}\,\mathrm{d}s$ is set by the energy $W_{\omega,\gamma}(r,\phi,\alpha)\mathrm{d}V$ contained in the volume element dV, the subtended fractional solid angle $\cos\alpha\,\mathrm{d}s/4\pi r^2$, and the loss $\exp(-r/\ell_\omega)$ due to scattering *en route* to ds:

$$\mathrm{d}J_{\omega,\gamma}\mathrm{d}s = \frac{v_E}{\ell_\omega} \times W_{\omega,\gamma}(r,\phi,\alpha)\mathrm{d}V \times \frac{\cos\alpha\,\mathrm{d}s}{4\pi r^2} \times \exp(-r/\ell_\omega). \tag{7.3}$$

The ratio of energy velocity v_E and ℓ_ω is the inverse transport mean free time associated with the diffusion. The total flux from inside the sample onto the surface per

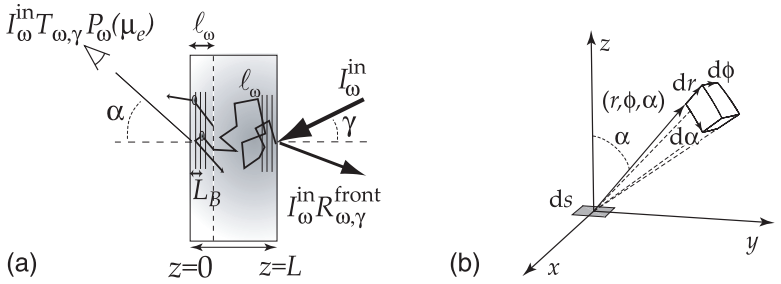

FIGURE 7.1: *(a) We consider a light beam I_ω^{in} incident on a photonic crystal sample. Generally, a fraction $R_{\omega,\gamma}^{front} I_\omega^{in}$ of the intensity is reflected, which depends on the frequency ω and the angle of incidence γ. In the sample the light diffuses with typical step length ℓ_ω. The diffuse glow on the transmission side is measured as a function of* $\cos\alpha = \mu_e$. *The depth of stop bands in the escape function is determined by ℓ and the Bragg attenuation length L_B (see Section 7.5). (b) Coordinates used to calculate the contribution of a differential scattering volume* $\mathrm{d}V = r^2 \sin(\alpha)\mathrm{d}r\mathrm{d}\phi\mathrm{d}\alpha$ *inside a scattering sample to the diffuse flux through a surface* ds. *The z-axis is the inward normal to the sample interface.*

unit area may be found by integrating $\mathrm{d}J_{\omega,\gamma}$ over the upper half space

$$\mathcal{J}_{\omega,\gamma}^{\text{interior}} = \frac{v_E}{4\pi\ell_\omega} \int_0^\infty \mathrm{d}r \int_0^{2\pi} \mathrm{d}\phi \int_0^{\pi/2} \mathrm{d}\alpha \; W_{\omega,\gamma}(r,\phi,\alpha) \exp(-r/\ell_\omega) \sin\alpha\cos\alpha. \tag{7.4}$$

It is important to note that the dominant contribution to the integral comes from the first mean free path ($z \lesssim \ell$) due to the exponential term. Secondly, as W satisfies the diffusion equation it varies only slowly on length scales comparable to ℓ. One may therefore replace $W_{\omega,\gamma}$ by a first-order Taylor expansion, to find the angle-dependent incident flux

$$J_{\omega,\gamma}^{\text{interior}}(\alpha) = \frac{v_E}{2} W_{\omega,\gamma}(z)\cos\alpha\sin\alpha + \frac{v_E\ell_\omega}{2}\frac{\partial W_{\omega,\gamma}(z)}{\partial z}\cos^2\alpha\sin\alpha \qquad \text{at } z = 0 \tag{7.5}$$

after integration over r and ϕ only. The total flux $\mathcal{J}_{\omega,\gamma}^{\text{interior}}$ is obtained by integrating $J_{\omega,\gamma}^{\text{interior}}(\alpha)$ over α,

$$\mathcal{J}_{\omega,\gamma}^{\text{interior}} = \frac{v_E}{4} W_{\omega,\gamma}(z) + \frac{v_E\ell_\omega}{6}\frac{\partial W_{\omega,\gamma}(z)}{\partial z} \qquad \text{at } z = 0. \tag{7.6}$$

According to the same reasoning, the total flux $\mathcal{J}_{\omega,\gamma}^{\text{exterior}}$ due to the (virtual) diffuse intensity outside the sample reads

$$\mathcal{J}_{\omega,\gamma}^{\text{exterior}} = \frac{v_E}{4} W_{\omega,\gamma}(z) - \frac{v_E\ell_\omega}{6}\frac{\partial W_{\omega,\gamma}(z)}{\partial z} \qquad \text{at } z = 0. \tag{7.7}$$

This flux of photons entering the random medium from outside is expected to be identically zero, unless photons originating from inside the sample are reinjected due to internal reflection. Accordingly, one is led to define the angle-averaged reflection coefficient $\bar{R}^D_\omega$

$$\mathcal{J}^{\text{exterior}}_{\omega,\gamma} = \bar{R}^D_\omega \mathcal{J}^{\text{interior}}_{\omega,\gamma}, \tag{7.8}$$

which sets the extrapolative boundary condition

$$W_{\omega,\gamma}(z) - \frac{2}{3}\ell_\omega \frac{1+\bar{R}^D_\omega}{1-\bar{R}^D_\omega} \frac{\partial W_{\omega,\gamma}}{\partial z} = 0 \qquad \text{at } z = 0 \tag{7.9}$$

in agreement with the extrapolation length defined in Eq. (7.1). On the other hand, it stands to reason that the total flux $\mathcal{J}^{\text{exterior}}_{\omega,\gamma}$ reinjected into the sample, is obtained by summing the angle-dependent reflected flux $R^D_\omega(\alpha) J^{\text{interior}}_{\omega,\gamma}(\alpha)$ over all angles α. This allows us to relate the angle-averaged diffuse-reflection coefficient $\bar{R}^D_\omega$ to the angle-dependent internal-reflection coefficient $R^D_\omega(\alpha)$. Summing over α one finds

$$\begin{aligned} \mathcal{J}^{\text{exterior}}_{\omega,\gamma} &= \int_0^{\pi/2} R^D_\omega(\alpha) J^{\text{interior}}_{\omega,\gamma}(\alpha) \mathrm{d}\alpha \qquad (7.10) \\ &= \frac{v_E}{2} C_{1,\omega} W_{\omega,\gamma}(z) + \frac{v_E \ell_\omega}{2} C_{2,\omega} \frac{\partial W_{\omega,\gamma}}{\partial z} \qquad \text{at } z = 0, \\ \text{with} \quad C_{n,\omega} &= \int_0^{\pi/2} R^D_\omega(\alpha)\, \cos^n(\alpha) \sin\alpha \, \mathrm{d}\alpha. \qquad (7.11) \end{aligned}$$

Identifying $\mathcal{J}^{\text{exterior}}_{\omega,\gamma}$ in Eq. (7.10) with $\bar{R}^D_\omega \mathcal{J}^{\text{interior}}_{\omega,\gamma}$ according to (7.8), one may solve for $\bar{R}^D_\omega$ to obtain

$$\bar{R}^D_\omega = \frac{3C_{2,\omega} + 2C_{1,\omega}}{3C_{2,\omega} - 2C_{1,\omega} + 2}. \tag{7.12}$$

This appears to be the key expression to relate the angle-dependent internal-reflection coefficient $R^D_\omega(\alpha)$ to the angle-averaged reflection coefficient $\bar{R}^D_\omega$, and to the extrapolation length ratio $\tau_{e,\omega}$ through Eq. (7.1).

Angle-resolved diffuse transmission experiments are very useful to determine the extrapolation length, as well as obtain information about the angle-dependent internal-reflection coefficient $R^D_\omega(\alpha)$. Only the fraction $J^{\text{interior}}_{\omega,\gamma}(\alpha)[1 - R^D_\omega(\alpha)]$ of the flux incident from inside the sample onto the sample boundary is transmitted, as the remaining fraction $J^{\text{interior}}_{\omega,\gamma}(\alpha) R^D_\omega(\alpha)$ contributes to the reentrant flux. Using the expression (7.5) for $J^{\text{interior}}_{\omega,\gamma}(\alpha)$, and the boundary condition $W_{\omega,\gamma}(z) = z_{e,\omega} \partial_z W_{\omega,\gamma}(z)$, one finds that the intensity transmitted between angles α and $\alpha + \mathrm{d}\alpha$ equals

$$I_{\omega,\gamma}(\alpha)\mathrm{d}\alpha = \frac{v_E}{2} \frac{\partial W_{\omega,\gamma}}{\partial z} \cos\alpha \, [z_{e,\omega} + \ell_\omega \cos\alpha] \cdot [1 - R^D_\omega(\alpha)] \sin\alpha \, \mathrm{d}\alpha \quad \text{at } z = 0. \tag{7.13}$$

The angle-resolved diffuse transmitted intensity can be factorized

$$I_{\omega,\gamma}(\mu_e)\mathrm{d}\mu_e = I_\omega^{\mathrm{in}} T_{\omega,\gamma} P_\omega(\mu_e)\mathrm{d}\mu_e \tag{7.14}$$

into the total transmission $T_{\omega,\gamma}$ and the probability $P_\omega(\mu_e)\mathrm{d}\mu_e$ for a diffuse photon in the sample to be transmitted at an angle between $\alpha = \cos^{-1}\mu_e$ and $\cos^{-1}(\mu_e + \mathrm{d}\mu_e)$. The total transmitted intensity

$$I_{\omega,\gamma}^T = I_\omega^{\mathrm{in}} T_{\omega,\gamma} = \frac{1}{3} v_E \ell \frac{\partial W_{\omega,\gamma}(z)}{\partial z} = D\frac{\partial W_{\omega,\gamma}(z)}{\partial z} \quad \text{at the exit interface} \tag{7.15}$$

equals the flux through the sample interface given by Fick's law. The normalized probability distribution $P_\omega(\mu_e)$ is given by

$$P_\omega(\mu_e) = \frac{3}{2}\mu_e[\tau_{e,\omega} + \mu_i] \cdot [1 - R_\omega^D(\mu_i)]. \tag{7.16}$$

As $P_\omega(\mu_e)$ describes the distribution of photons over the available escape angles, it will be referred to as 'escape function'. One should be aware that we have slipped in a distinction between internal angle $\cos^{-1}\mu_i$, and external angle $\cos^{-1}\mu_e$ relative to the z-axis into Eq. (7.16), which accounts for refraction effects at the interface.

The angular dependence of the escape function $P_\omega(\mu_e)$ has been found to agree with experiments on random media if an effective refractive index is used to model $R_\omega^D(\mu_i)$ according to Fresnel's law, and to convert internal to external propagation angles $\cos^{-1}\mu_i$ resp. $\cos^{-1}\mu_e$ using Snell's law [18, 19]. As the refractive indices of constituents of usual random media such as powders or macroporous sponges are barely frequency dependent [20–22], only a weak frequency dependence of T, P and ℓ would be expected. For highly dispersive photonic crystals, however, the Fresnel model is not expected to describe the internal-reflection coefficient well at all. In contrast, light emanating from a depth $z < \ell$ from the crystal surface is expected to be Bragg attenuated (*i.e.*, internally reflected) for angles and frequencies matching the Bragg condition [23, 24]. Hence the photonic band structure is expected to give rise to a strongly angle and frequency-dependent internal-reflection coefficient $R_\omega^D(\mu_i)$, resulting in stop bands in the diffuse transmission. Furthermore, these stop bands cause a frequency-dependent extrapolation length [13], as witnessed by the experiment presented in Chapter 6.

It is clear that the mean free path ℓ in photonic crystals can only be quantitatively obtained from enhanced backscattering or total transmission if the frequency-dependence of the extrapolation length is taken into account. A reduction of the enhanced backscattering cone width due to enhanced internal reflection has indeed been observed for frequencies matching the first Bragg diffraction order of an inverse opal photonic crystal [13, see Chapter 6]. Furthermore, we note that the refraction law to convert μ_i to μ_e is highly complex in photonic crystals [25]. In comparing external reflectivity measurements with band structure calculations, reasonable agreement has been obtained for the lowest order stop bands using Snell's law with a geometrically averaged refractive index [26, 27].

In this chapter we report experimentally determined escape functions $P_\omega(\mu_e)$ of inverse opals. We discuss the measured frequency-dependence of the escape function at chosen detector angles (Section 7.4.1) in terms of photonic stop gaps. In Section 7.4.2 a different perspective is offered by considering the angular redistribution of diffuse light, *i.e.*, the angle-dependence of the escape function for several chosen frequencies. We combine the diffusion theory with a simple model for the angle and frequency dependence of the internal-reflection coefficient $R^D_\omega(\mu_i)$ in Section 7.5. Subsequently, we discuss the agreement between the model and the experimental data over the full angular and frequency range, and address the magnitude of the internal-reflection coefficient. In Section 7.7, we present the total transmission measurements, and we use the extrapolation length ratio determined from Section 7.5 to interpret the total transmission measurements in terms of the transport mean free path.

7.3 Experiment

We have studied *fcc* photonic crystals consisting of air spheres in anatase TiO_2 (refractive index 2.7 ± 0.4) with lattice parameters $a = 800, 900, 930 \pm 20$ nm. Details of fabrication and characterization are reported in Ref. [6]. The surfaces of the samples are parallel to the 111 crystal planes. These photonic crystals are strongly photonic, as they have a relative frequency width of the lowest order Bragg diffraction, or L-gap, equal to $\Psi = 0.12$. The crystals studied in this chapter have larger lattice spacing than the crystals discussed in Chapters 3, 4 and 6 (see Fig. 3.3), but are otherwise similar. The colorful opalescence, corresponding to higher diffraction orders, indicates good sample quality. Most of the structural disorder is inherited from the opal templates. As probed by small angle X-ray scattering [6], the polydispersity and rms displacements of the air spheres from the lattice sites are less than 3% of the nearest neighbor distance throughout the bulk of the crystals. Together with the roughness of the titania shells (≤ 10 nm [6]) this constitutes the main source of scattering determining the transport mean free path of $\ell \sim 15$ μm [13, Chapter 6]. As the thickness $L \sim 200$ μm of the samples exceeds the mean free path, diffuse transport of light is indeed expected. Samples were mounted on a rotation stage to allow control over the orientation of the surface normal (parallel to the 111 reciprocal lattice vector) relative to the incident beam. As shown in Figure 7.2 the detector was mounted on a separate concentric rotation stage, allowing the detector angle α relative to the sample surface normal to be varied from 0 to 90 degrees, independently of the incidence angle γ.

Diffuse-transmission spectra were recorded in the range $0° \leq \alpha \leq 90°$ every 5°. For spectrally resolved measurements, light from an incandescent lamp (tungsten-halogen) was passed through a Fourier-Transform spectrometer (Biorad FTS-6000) operated at a resolution of 32 cm^{-1}. The beam emanating from the spectrometer was focused onto a pinhole, acting as a point source. This point source was imaged with a camera objective (f=50 mm) onto a spot of 0.40 mm radius encompassing many domains on the sample surface. The apex angle of the incident beam (10°) was chosen to optimize the incident power. The angular resolution for diffuse transmission is set by

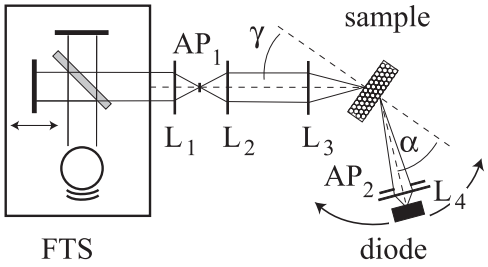

FIGURE 7.2: *Overview of the diffuse-transmission setup. The output of a tungsten-halogen source is passed through a Fourier-Transform Spectrometer (FTS). The beam is focused onto a pinhole AP_1 using lens L_1. The pinhole acts as a point source which is imaged on the front sample surface using lens L_2 and camera objective L_3. The angle of incidence γ is controlled by rotating the sample. The detector angle α is changed independently by rotating the diode together with aperture AP_2 and lens L_4 which determine the angular acceptance.*

the aperture of the detector of 5°, and is independent of the apex angle of the incident beam. Angle-resolved measurements of the diffuse transmitted intensity were obtained in the frequency range from 5500 to 14000 cm^{-1} by using both Si and InGaAs photodiodes. Higher frequencies can only be probed by replacing the light source. The diode signal yields an interferogram which is Fourier transformed to determine the diffuse transmitted intensity $I_{\omega,\gamma}(\mu_e = \cos\alpha)$ defined in Eq. (7.14). The total transmitted intensity spectra $I^T_{\omega,\gamma}$ are determined by summing the angle-resolved spectra of diffuse transmitted intensity weighted by $2\pi \sin\alpha\, d\alpha$ to approximate the integration over 2π solid angle. The total transmission $T_{\omega,\gamma}$ (Eq. (7.2)) is obtained by normalizing the total transmitted intensity spectrum $I^T_{\omega,\gamma}$ to the lamp spectrum I^{in}_{ω}, measured by removing the sample from the setup. The escape functions $P_\omega(\mu_e = \cos\alpha)$ are determined by dividing the angle-resolved spectra $I_{\omega,\gamma}(\mu_e)$ of diffuse transmitted intensity by the total transmitted intensity spectrum $I^T_{\omega,\gamma}$, as expressed by Eq. (7.14). Thus, the escape functions are independent of the lamp spectrum.

Alternatively, a HeNe (λ = 632 nm) or Nd:YVO_4 (λ = 1064 nm) laser beam could be used as single-frequency probes of the diffuse transmission, using a chopper and lock-in amplifier. The laser beam, not shown in Figure 7.2, overlapped with the white light beam starting from lens L_1. The greater sensitivity allowed the use of cross-polarized detection, contrary to the white light experiments. Cross-polarized detection avoids contributions of the unscattered beam to the detected signal.

7.4 Escape functions

Several raw spectra $I_{\omega,\gamma}(\mu_e)$ are shown in Figure 7.3 that demonstrate the diffuse transmitted intensity at chosen angles $\alpha = \cos^{-1}\mu_e$ = 15°, 30°, 50°, 75°, recorded for incidence angle γ = 0°. These data were obtained from a sample with lattice spacing a = 930 nm and recorded using an InGaAs detector. Comparison with the lamp

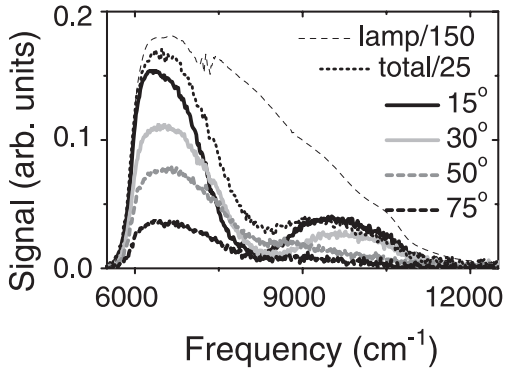

FIGURE 7.3: *Raw spectra of diffuse light transmitted by a titania inverse opal with a = 930 nm, for detection angles $\alpha = 15, 30, 50$ and 75°, and incidence angle $\gamma = 0°$. The spectrum of the lamp as recorded by the same InGaAs diode, as well as the total transmitted intensity spectrum are also shown (scaled as indicated). The detector acceptance angle, which affects the scaling factor between raw spectra and total transmission spectrum, was* 5°.

spectrum reveals several striking features. Firstly, for low frequencies $\sim$ 6000 cm^{-1} we observe a steady decrease in intensity with increasing angle, as would be expected from the dominant $\cos\alpha$ proportionality in Eq. (7.16). For higher frequencies, the lineshapes appear to depend on the detection angle α. Compared to the lamp spectrum, a wide stop band appears, centered at 8100 cm^{-1} for $\alpha = 15°$. To a large degree this attenuation band remains at the same frequency when the detector angle is increased. The total transmitted intensity spectrum $I^T_{\omega,\gamma}$ (dotted curve) indeed shows a wide attenuation band at 8000 cm^{-1}. The total transmission $T_{\omega,\gamma}$ will be discussed in Section 7.7. Closer examination of the angle resolved spectra shows that spectra at increased detection angle are further attenuated in a band shifting to larger frequency with increasing detector angle α, compared to the $\alpha = 15°$ spectrum. This dependence of α is best studied by examining the escape function.

7.4.1 Escape function versus frequency at selected angles

Escape functions $P_\omega(\mu_e)$ at detector angles $\alpha = \cos^{-1}\mu_e = 15°, 25°, 35°, 45°, 55°, 65°, 75°$ for an inverse opal with lattice parameter a = 930 nm are shown as a function of frequency ω in Figure 7.4. These data belong to the same set as the raw spectra in Fig. 7.3, and were obtained by dividing by the total transmitted intensity spectrum and correcting for the angular aperture d$(\cos\alpha)$. The frequency range was extended by combining the dataset represented in Fig. 7.3 with complementary data obtained by replacing the InGaAs diode with a Si detector (used for $\omega \geq 10500$ cm^{-1}) . In the common frequency window from 9000 to 11500 cm^{-1} in which both detectors are sensitive, the escape functions matched seamlessly within the noise for all detector angles α. It should be noted that no scaling constants are involved in Figure 7.4.

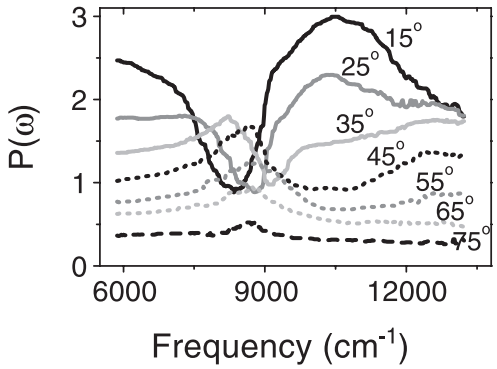

FIGURE 7.4: *Photon escape function as a function of frequency for an inverse opal with lattice parameter a = 930 nm for exit angles $\alpha = 15°, 25°, 35°, 45°, 55°, 65°, 75°$. The incidence angle is $\gamma = 0°$. The top axis shows normalized frequency units a/λ where λ is the wavelength in vacuum. No relative scaling or offset was applied to the curves.*

We do not find a dependence of the escape function on the incidence angle γ for $0° \leq \gamma \leq 30°$. This result validates the factorization in Eq. (7.14), as it confirms that $P_\omega(\mu_e) = I_{\omega,\gamma}(\mu_e)/I^T_{\omega,\gamma}$ is independent of γ. The factorization may be understood from the diffusive nature of the samples; as the direction of propagation is fully randomized, the probability for a photon to leave the sample at a specific exit angle α is not dependent on the incidence geometry. The only effect of the incidence angle γ is expected to be due to the reflectivity of the front surface ($R^{\text{front}}_\gamma(\omega)$ in Eq. (7.2)), which reduces the *total* transmission $T_{\omega,\gamma}$ for frequencies and incident angles matching the Bragg condition.

At low frequencies $\lesssim 6700$ cm^{-1} the escape function is unaffected by internal reflection and typical for a random medium with $z_e \approx \frac{2}{3}\ell$. As is evident in Fig. 7.4, the escape function at an exit angle of $\alpha = 15°$ is significantly reduced by $\gtrsim 70\%$ in a stop band centered at ~ 8200 cm^{-1} with full width at half maximum (FWHM) ~ 1300 cm^{-1}. This stop band in the escape function occurs due to internal Bragg reflections, as captured in the term $[1 - R^D_\omega(\mu)]$ in Eq. (7.16), and moves to higher frequencies with increasing exit angle α. At angles α exceeding $\sim 40°$, a much wider gap from 9000 to 12000 cm^{-1} is evident in Figure 7.4. Similar broadening, and the occurrence of a double-peak structure has been observed in reflectivity experiments [27, 28] and luminescence experiments (Chapter 3), and has been explained in terms of a multiple-Bragg wave coupling involving both 111 and 200 reciprocal lattice vectors [27]. Figure 7.4 shows that the stop gap at these larger angles is preceded by a frequency range characterized by an *increase* of the escape function relative to the low frequency value. This frequency range is coincident with the stop band at small detector angles. The increase has the same origin as the enhanced escape probability in the frequency range 9000 – 12000 cm^{-1} evident in the escape function spectrum at small detector angles. As escape directions within a stop gap are blocked by internal Bragg

reflection, photons are more likely to escape in the remaining directions, giving rise to an *enhanced* escape probability in directions *not coincident* with a stop gap. Equivalently, this enhanced escape probability is accounted for in the model (7.16) for $P_\omega(\mu)$ as an increase of the extrapolation length due to a larger average internal-reflection coefficient.

Similar results were obtained for a multitude of samples with different lattice parameters ($a = 800, 900, 930$ nm). The shift along the frequency-axis of the escape functions with lattice parameter confirms the photonic origin of the redistribution of the diffuse intensity (see Fig. 3.3). In conclusion, these observations clearly show that the diffuse intensity possesses a pronounced angle and frequency-dependent structure due to the strongly photonic crystal. This point is particularly important in the interpretation of common experiments, such as reflectivity or transmissivity measurements. The diffuse contribution to the signal may clearly not be corrected for by assuming a frequency independent background. In this respect a transmission measurement can be particularly misleading. Even if scattering by disorder precludes any coherent transmission (*i.e.*, for thick samples $L/\ell \gtrsim 5$), a detector along the incoming direction will still register a diffuse spectrum with an attenuation band coincident with the photonic stop gap. Evidently, a stop gap in transmission may only be trusted if the transmission for frequencies just *outside* the stop gap is close to 100%, indicative of low scattering. This requires an absolute calibration of the transmission. In the frequency range of higher order diffraction and the prospective photonic band gap, no strongly photonic crystals with thickness less than ℓ but larger than two unit cells appear to have been reported to date.

7.4.2 Strongly non-Lambertian redistribution

The redistribution of diffuse intensity over exit angles may be more fully appreciated by considering the escape function as a function of angle for selected constant frequencies, *cf.* Figure 7.5. The horizontal scale in terms of μ represents the large contribution of large exit angles in the distribution of intensity over the available hemisphere of exit directions. For clarity, the exit angle range from 0° to 45° covering half of the available polar exit angle range is indicated in gray. For reference we studied a calibration sample consisting of a vial with a dilute suspension of polystyrene spheres in water (dashed curve in Figure 7.5). In accordance with Ref. [19, 29], we find nearly Lambertian behavior corresponding to $P_L(\mu_e) = \frac{3}{2}\mu_e(\frac{2}{3} + \mu_e)$. Detailed analysis shows that the escape function of the calibration sample is accurately modelled by Eq. (7.16). A Fresnel-type model for the internal-reflection coefficient was used, assuming an effective index of 1.33 relevant for water, and taking multiple reflections in the vial walls into account [19].

For frequencies below the L-gap ($\omega = 6270$ cm^{-1}) the escape function of an inverse opal with $a = 930$ nm closely resembles the escape function measured for the random calibration sample, as witnessed by Fig. 7.5. From a fit of diffusion theory with a Fresnel model for the internal-reflection coefficient, we estimate an effective refractive index of $n_{\text{eff}} = 1.27 \pm 0.15$. This effective index is consistent with a 10 to

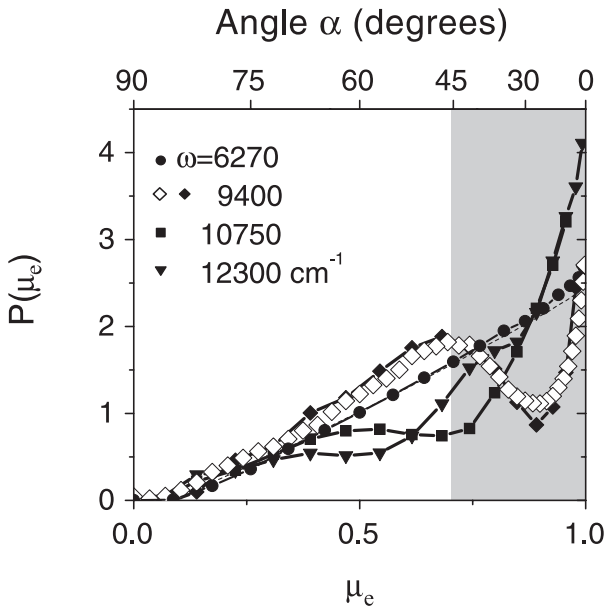

FIGURE 7.5: *Photon escape function as a function of the cosine μ_e of the escape angle α for an inverse opal with lattice parameter $a = 930$ nm for frequencies $\omega = 6270, 9400, 10750, 12300\ cm^{-1}$ (solid circles, diamonds, squares, resp. triangles) as extracted from a white light data set. These frequencies correspond to $a/\lambda = 0.58, 0.87, 1.0$ and 1.14. Open diamonds show a measurement obtained from the same sample using a Nd:YVO laser beam ($\omega = 9400\ cm^{-1}$). For an angular scale, refer to the top axis. The shaded region corresponds to half the available range for the exit angle α relative to the surface normal. The dashed line partially obscured by closed circles corresponds to a calibration measurement on a dilute colloidal suspension.*

20% volume fraction of solid material, depending on whether the effective index is assumed to correspond to the volume averaged index or volume averaged dielectric constant. The nearly Lambertian distributions for low frequencies should be contrasted to the strongly non-Lambertian distributions observed for higher frequencies. As an example we discuss the angular distribution of emitted photons at a frequency of 9400 cm^{-1}, to the blue of the L-gap, shown in Figure 7.5. The escape function at this frequency is clearly reduced in the range from $\alpha = 10°$ to 40°, and enhanced both for near-normal exit angles and for exit angles exceeding 40°. These features, as extracted from the white-light experiment, are excellently reproduced in an additional single-frequency measurement using a Nd:YVO_4 laser beam ($\lambda = 1.064\ \mu$m), also shown in Fig. 7.5. For increasing frequency ($\omega = 10750$, and 12300 cm^{-1}) the angular range of suppression relative to the Lambertian distribution shifts to larger α, leaving a central cone around the surface normal within which the escape probability is strongly enhanced by a factor up to ~ 2.

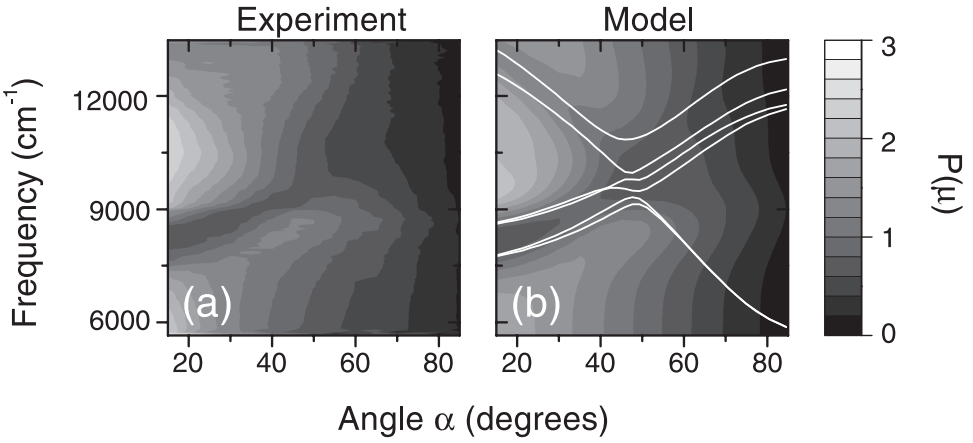

FIGURE 7.6: *(a) Contour plot of the measured photon escape function as a function of exit angle α and optical frequency corresponding to an inverse opal with a = 930 nm. (b) Contour plot of the fitted escape function, according to the diffusion model Eq. (7.16) combined with an internal-reflection coefficient derived from the band structure Eq. (7.17). The lowest 6 bands along the LU direction are plotted in white, using the effective index to transform internal propagation angles into external propagation angles. The band structure alone can not fully explain the frequency and angle dependence of the escape function. Features not expected from the band structure are, for instance, the enhanced escape probability for* $\alpha < 30°$ *and* $9000 \lesssim \omega \lesssim 12000\ cm^{-1}$*, and for* $\alpha > 30°$ *and* $7500 \lesssim \omega \lesssim 9000\ cm^{-1}$*. The common gray scale is displayed on the far right.*

7.5 Diffuse internal-reflection model

The full dataset to which Figure 7.4 corresponds is presented as a contour plot in Figure 7.6(a). For angles below $\sim 40°$ the shift of the stop gap to higher frequency with increasing exit angle is clearly discerned, as well as the widening of the stop gap for larger exit angles due to multiple Bragg wave coupling [27]. The concomitant enhancement of the escape function is evident in the range 9000–12000 cm^{-1} for small angles $\alpha < 30°$ and in the range 7500–9000 cm^{-1} for large exit angles $30° < \alpha < 60°$. In this section we proceed with a quantitative description of the data in terms of a semi-empirical model that combines diffusion theory with a model derived from a band structure calculation for the internal-reflection coefficient $R^D_\omega(\mu)$.

7.5.1 Internal-reflection coefficient

The internal-reflection coefficient of the inverse opals is modelled as the sum of two Gaussian reflection peaks

$$R^D_\omega(\mu_i) = R_1(\mu_i) \exp\left[-\frac{(\omega - \omega_1(\mu_i))^2}{2\Delta\omega_1(\mu_i)^2}\right] + R_2(\mu_i) \exp\left[-\frac{(\omega - \omega_2(\mu_i))^2}{2\Delta\omega_2(\mu_i)^2}\right], \qquad (7.17)$$

with angle-dependent peak reflectivities $R_{1,2}(\mu)$ and widths $\Delta\omega_{1,2}$. We expect such a model to capture the essential frequency dependence of the multiple Bragg wave coupling [24, 27] if the center frequencies $\omega_{1,2}(\mu)$ are chosen consistent with the photonic band structure.

We use the band structure for a model consisting of close-packed air spheres (radius $r = \frac{1}{4}\sqrt{2}a$) on an *fcc* lattice surrounded by high-index ($\varepsilon = 6.5$) spherical shells with outer radius $1.09r$, connected by cylindrical windows of radius $0.4r$ (see Chapter 3). The window size and the volume fraction of solid material are in agreement with structural data [6], and the resulting band structure has been found to agree with reflectivity bands in both the frequency range of first and second Bragg diffraction order [27, 30]. Previously, it has been observed that the band structure along the LU-line in reciprocal space (extended outside the first Brillouin zone) describes the angle-dependent reflectivity of polycrystalline samples satisfactorily [27]. Therefore we have calculated the dispersion relation along the LU-line, and determined $\omega_1(\mu)$ and $\omega_2(\mu)$ from the calculated stop band edges. To convert internal to external propagation angle we have used Snell's law[1]. An average refractive index $n = 1.28$ was chosen, consistent with the volume averaged dielectric constant for a titania volume fraction of 11%.

Contrary to the fixed reflection band center frequencies $\omega_{1,2}(\mu)$, we have adjusted the reflection peak widths $\Delta\omega_{1,2}(\mu)$, and the reflection peak heights $R_{1,2}(\mu)$ to obtain an optimal fit of the diffusion model Eq. (7.16) with internal reflection Eq. (7.17) to the data. We expect the parameter functions $R_{1,2}(\mu)$ and $\Delta\omega_{1,2}$ to vary smoothly with angle, and approximate them using cubic polynomials in μ. The polynomial coefficients are determined using a nonlinear least-squares minimization algorithm to optimally fit Eq. (7.16) to the data. In Section 7.5.2, we will discuss the agreement between the data and the simple model outlined above, and the angle dependence of the fitted lowest order peak reflectivity. In Section 7.7 we will review the frequency dependence of the extrapolation length ratio specified by the fitted $R_\omega^D(\mu)$ through Eq. (7.1).

7.5.2 Escape functions and band structure

In Figure 7.6(b) both the fit to the data in Fig. 7.6(a) and the lowest six calculated bands are displayed. The average difference between measured and calculated escape function is between 5 and 10%. The excellent correspondence of the model to the experimental data is more clearly displayed for two key frequencies in Figures 7.8(a) and (c). The agreement between the data and the model Eqs. (7.16, 7.17) is striking, given the simplicity of the model for the internal-reflection coefficient, the empirical nature of the escape function theory, and the limitations on the validity of diffusion theory imposed by the modest optical sample thickness ($2 < L/\ell < 10$).

[1] Refraction may be more accurately taken into account by using parallel momentum conservation at the interface. Within the theory of diffusion with internal reflections, the effective index will always remain a source of inconsistency, since it is unclear how to deal with the associated Fresnel reflections.

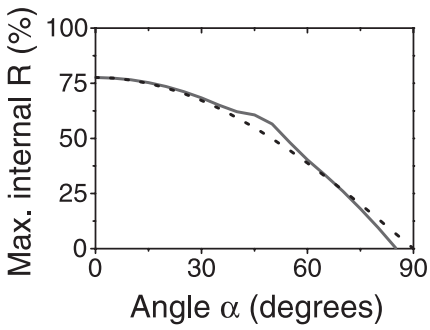

FIGURE 7.7: *Solid line: the fitted peak internal-reflection coefficient* R^D_ω *versus exit angle* α *for frequency* ω *coincident with the lowest order stop band center frequency* $\omega_1(\cos\alpha)$. *This curve corresponds to the fit (see Fig. 7.6(b)) to the experimental data shown in Fig. 7.4, 7.5 and 7.6(a). The peak internal-reflection coefficient decreases as* $\cos(\alpha)$ *(dashed line).*

Figure 7.6(b) clearly demonstrates that for quantitative understanding of the angle-resolved diffuse transmission, the band structure is useful but *not sufficient*. Although the lowest diffraction order at near-normal incidence in the band structure evidently corresponds to the attenuation band in the diffuse transmission, the enhanced transmission probability for wave vectors outside a stop band can not be explained from the dispersion relation alone. The extrapolation length ratio τ_e is the essential parameter determining the redistribution of intensity over exit directions. The frequency dependence of the extrapolation length ratio will be discussed in Section 7.7.

It is interesting to monitor the magnitude of the fitted internal-reflection coefficient of the lowest stop gap as a function of the photon escape angle α. As shown in Figure 7.7 for the fit to the experimental data in Fig. 7.6(a), we find a decrease of the reflection coefficient of the lowest gap with increasing angle which follows a cosine behavior over a large angular range. This supports our earlier report [24] in Chapter 3, stating that the stop gap depth for $\alpha = 0°$ in luminescence spectra (*i.e.*, using an internal source of diffuse light) is determined by the ratio of Bragg attenuation length and the transport mean free path ℓ. Briefly, diffuse photons emanating from a depth $z < \ell$ from the crystal-air interface propagate ballistically to the interface. Photons may be redirected into Bragg directions by scattering off defects in the surface layer $z < \ell$. Since ℓ is larger than the Bragg attenuation length $L_B \approx 0.2\ell$, light scattered at $z < L_B$ is hardly Bragg attenuated, while light scattered in $L_B < z < \ell$ results in a stop band (*cf.* Fig. 7.1). The stop band depth for $\alpha = 0°$ is therefore estimated as $1-R^D_{\omega_c}(\alpha = 0) \sim 1-L_B/\ell$, where ω_c is the stop band center frequency. This geometrical argument may be generalized by noting that for larger exit angles α, the path length to the crystal air interface increases with $\cos\alpha$. This increases the probability of being scattered at $z < L_B$, and reduces the internal-reflection coefficient to $\sim L_B \cos\alpha/\ell$, in agreement with Fig. 7.7. We conclude that the mechanism of diffusion and internal

reflection proposed for the angular redistribution of fluorescence from sources inside strongly photonic crystals [24] is confirmed by the present results and analysis.

7.6 Diffusion in case of a band gap: beyond Kossel lines

The exemplary agreement between the diffusion model and the experimental data is more clearly shown for two key frequencies in Figure 7.8(a) and (c). For a frequency in the L-gap, $\omega = 8200\ \mathrm{cm}^{-1}$, both the data and the diffusion model of the escape function are strongly reduced relative to the Lambertian distribution P_L in the range from $\alpha = 0$ to 35° (Fig. 7.8(a)). This range is shifted to larger angle in Fig. 7.8(c), corresponding to a frequency of $9300\ \mathrm{cm}^{-1}$. If the diffuse intensity corresponding to the escape function profile for $\omega = 8200\ \mathrm{cm}^{-1}$ would be projected on a screen, one would find a dark disk concentric with the sample normal, with radius corresponding to $\alpha = 35°$. For α beyond 35° the intensity would be slightly in excess of P_L. For the frequency $\omega = 9300\ \mathrm{cm}^{-1}$ above the L-gap, one would rather find a dark ring, surrounding a bright disk. We illustrate these concepts, by considering stereographic plots of the photon excess distribution

$$\Delta P_\omega(\mu_e) = P_\omega(\mu_e) - P_L(\mu_e) \tag{7.18}$$

versus exit angle in Figure 7.8(b),(d). In the stereographic plots, a polar coordinate (r, ϕ) corresponds to an azimuthal exit angle ϕ and polar exit angle α such that $r(\alpha) = \sin\alpha/(\cos\alpha + 1)$. A measurement on single crystal samples would show an azimuthal dependence of the escape function, since the 200 family of reciprocal lattice vectors oblique to the sample surface is involved in the Bragg diffraction. This dependence is lost in our experiment due to polycrystalline averaging. Azimuthally independent grey scales in Fig. 7.8(b),(d) have been generated from the model function plotted in (a) and (c). The dark disk in Fig. 7.8(b), and the forbidden ring with inner radius $\alpha = 34°$ and outer radius $\alpha = 50°$ in (d) are reminiscent of Kossel lines. Dark Kossel lines in diffuse transmission have been reported for weakly photonic crystals [31, 32]. These lines should in fact be called Seemann lines, as they are solely due to internal Bragg diffraction of diffuse light, and do not involve the subtle intensity features occurring in the X-ray fluorescence lines discovered by Kossel [33, 34]. Despite the distinction, we will use the term Kossel lines to remain consistent with current practice in the field of photonic crystals. Weakly photonic colloidal single crystals cause narrow Kossel lines in diffuse transmission. In such cases, the nearly free-photon approximation can be used to determine the crystal symmetry and orientation based on the geometry of the dark circles and hyperbolas. For strongly photonic inverse opals, the dark areas are not necessarily circles or hyperbolas, and the width of the internal reflection lines is extraordinarily large. The dark rings evident in Figure 7.5 and 7.8 can extend over $\gtrsim 30\%$ of the 2π sr solid angle, and the geometry of the internal reflection is strongly affected by multiple Bragg wave coupling. A geometrical analysis [31, 32] of dark lines in diffuse transmission to obtain the crystal symmetry is therefore not viable, but the full band structure should be used for

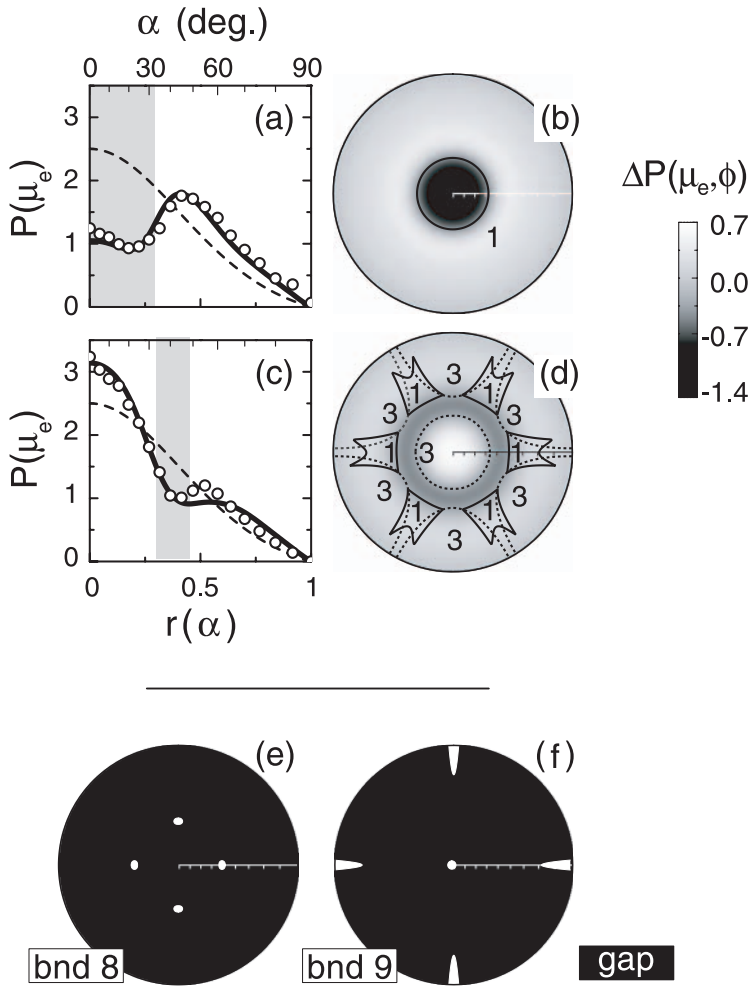

FIGURE 7.8: *Photon exit distribution $P(\mu_e)$ for frequencies $\omega = 8200\ cm^{-1}$ (a), resp. $9300\ cm^{-1}$ (c) measured for an inverse opal with $a = 930\ nm$. Both the data (dots) and the adapted diffusion model (solid curves in (a) and (c)) strongly differ from the Lambertian distribution P_L (dashed curves). Grey areas indicate forbidden exit angles according to the dispersion surface analysis. (b) and (d): stereographic plots of the photon excess distribution $\Delta P(\mu_e) = P(\mu_e) - P_L(\mu_e)$, corresponding to the model in (a) resp. (c). Solid curves in (b) and (d) indicate boundaries of regions in exit angle space, numbered with the band index, for which coupling to a photonic single crystal is possible. Bands 2 and 4 are nearly polarization degenerate with bands 1 resp. 3, and similar to within the line thickness. In panels (e) and (f) predictions are shown for the photon exit distribution for an inverse opal $\varepsilon = 11.9$ cut along a 100 plane (instead of a 111 plane, as in panels (b,d)). The only allowed exit angles are in the white pockets, belonging to band 8 ($\omega a/2\pi c = 0.776$) for frequencies below the full band gap, panel (e), resp. band 9 ($\omega a/2\pi c = 0.816$ above the band gap, panel (f)).*

interpretation. In addition, the large angular extent of the internal reflection lines of strongly photonic crystals and the associated large enhancements cause a strongly non-Lambertian distribution of diffuse intensity over exit directions. In contrast, the angular distribution of photons for weakly photonic crystals is practically equal to the Lambertian distribution P_L for angles outside the narrow internal reflection lines, since the extrapolation length is barely affected by internal reflection.

In a general analysis of the range of suppressed diffuse transmission at a specific frequency, it is necessary to determine the set of exit directions for which photons are blocked by internal reflection, *i.e.*, directions that do not couple to any Bloch mode. Such an analysis is outlined in Chapter 2.8, and is based on *(i)* photon dispersion surfaces in the photonic crystal, *(ii)* parallel momentum conservation at the interface, and *(iii)* causality requirements on the direction of the group velocity. We have determined dispersion surfaces and group velocities by interpolating from eigenfrequencies calculated on a dense **k**-grid within the volume of the irreducible wedge of the first Brillouin zone, and on the facets of the Brillouin zone[2]. In Figure 7.8(b),(d) the solid lines show results of solving the refraction problem for the two frequencies corresponding to the data. For clarity, only the *boundaries* of the forbidden regions in exit-angle space are indicated. For the frequency in the L-gap ($\omega = 8200$ cm^{-1}, Fig. 7.8(b)) coupling is only allowed to band 1 and the nearly polarization degenerate band 2, and is limited to $\alpha > 33°$, in perfect agreement with the data. For a higher frequency[3] above the L-gap ($\omega = 9300$ cm^{-1}, Fig. 7.8(d)) coupling to bands 1 and 2 is only allowed in 6 small lobes in exit angle space. For angles $\alpha < 34.5°$ coupling occurs to bands 3 and 4. For larger angles $\alpha > 51°$, 6 parabolas delimit angular ranges in which coupling from band 3 and 4 to air is allowed. The only angles to which diffuse light inside the samples can not couple are contained in a ring concentric with the origin, and 6 patches with $80° < \alpha < 90°$ and azimuthal width $\lesssim 6°$, too small to affect the experimental azimuthal average. The boundaries of the ring are sixfold symmetric, but not circular. Overall, the agreement of the central forbidden ring with the experimental data is gratifying.

Interesting possibilities are offered at frequencies near photonic band gap edges. For frequencies near the edge of any photonic band gap that closes away from the center of the Brillouin zone, all modes have wave vectors in pockets away from the **k**-space origin. In such cases, diffuse light may exit the photonic crystal only along isolated directions. As the shape of dispersion surfaces for frequencies near a band gap is nearly ellipsoidal, an effective mass approximation is well suited to predict the directionality of diffuse transmission. As an example which may soon be realized, we consider an inverse opal with a full photonic band gap, assuming a $\varepsilon = 11.9$ backbone containing *fcc* close-packed air spheres. In Figure 7.8(e) the solution of the refraction problem for a 100 cleaved crystal [35] is shown for a frequency $\hat{\omega} = \omega a/2\pi c$ just below the band gap. In the frequency range from $\hat{\omega} = 0.748$ up to the band gap edge $\hat{\omega} = 0.778$, the only allowed modes are in band 8, and the dispersion surfaces are ellipsoids

[2]We used 2992 equidistant k-points within the irreducible part of the Brillouin zone, 1816 points on the 111 facet and 1255 on the 200 facet of the Brillouin zone.

[3]Deeper analysis of the refraction problem is contained in Section 2.8 and Fig. 2.8.

around the W point. Diffuse light inside the crystal can only couple into a symmetric quadruplet of beams, with exit angles α relative to the sample normal around 40°. For frequencies *above* the band gap (limited by band 9 at the X-point) emission is directed into a central beam along the surface normal, with a width proportional to the square root of the detuning from the gap edge. Internal reflection causes the four beams at grazing exit angle (Fig. 7.8(f)) not to appear in a small frequency range just above the gap edge. In this frequency range, all light inside the crystal, be it multiply scattered from an external source or emission from inside the crystal, may only leave the crystal in one single narrow beam of diffuse light. Directional diffuse beams will occur for all band gap crystals for which the gap closes away from the **k**-space origin, including diamond, *fcc*, *hcp* and *bcc* structures.

7.7 Extrapolation length and total transmission

In this section we return to the experimental data of diffuse transmission of titania inverse opals. We use the extrapolation length ratio that results from the fit to the measured escape function to interpret the total transmission $T_{\omega,\gamma}$ of the titania inverse opals in terms of their transport mean free path. First, we present total diffuse-transmission measurements in Subsection 7.7.1. In Subsection 7.7.2 we analyze the frequency dependence of the extrapolation length ratio, and discuss total transmission corrected for internal reflections.

7.7.1 Total transmission

The total transmission of a sample with $a = 930$ nm as a function of frequency is shown in Figure 7.9(a) for incidence angles $\gamma = 0°$, 15° and 30°. The most apparent features are *(i)* a decrease of the total transmission with increasing frequency visible in all three traces and *(ii)* the occurrence of a band of reduced total transmission which shifts from 8100 cm^{-1} to higher frequencies with increasing angle of incidence γ. The center frequency of the angle-dependent band of reduced total transmission coincides with the photonic stop band measured in a reflectivity measurement and with the stop band in the escape function. The center frequency of the stop band is inversely proportional to the lattice parameter, as demonstrated by the blue shifted spectrum for a sample with $a = 800$ nm in Fig. 7.9(a). As less light enters the sample for wave vectors matching the Bragg reflection condition, the diffuse intensity injected into the sample is reduced in a frequency region matching the stop band for the incident direction. This reduction of the total transmission is caused by the reflectivity of the front surface, the factor $[1 - R^{\text{front}}_{\omega,\gamma}]$ in Eq. (7.2). The stop band width in the total transmission measurement is larger than the photonic width due to the large angular width $\Delta\gamma \sim 10°$ of the incident beam. The stop band depth in total transmission is limited by the external reflectivity R^{front}, which amounts to 50 to 70% for a wide beam spanning many domains. The stop gap minimum of 0.09 at $\gamma = 0°$ in the total transmission is indeed only 2 to 3 times less than the value just outside the stop gap

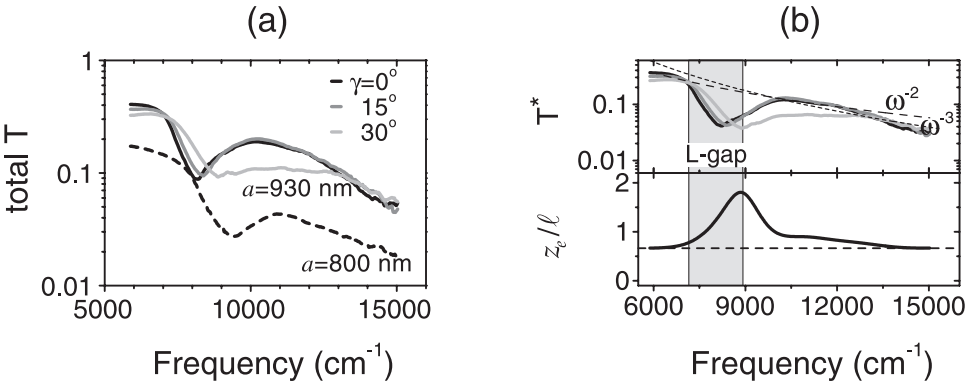

FIGURE 7.9: *(a) Measured total diffuse transmission as a function of optical frequency for a sample with lattice parameter a = 930 nm for incidence angles γ = 0°, 15°, 30° (solid lines, black, gray, light gray). For a sample with a = 800 nm the stop band at γ = 0° (L-gap) is shifted to higher frequency (data indicated by the dashed line). Lower panel in (b): extrapolation length ratio* $\tau_e = z_e/\ell$ *pertaining to the fit to the data in Fig. 7.6. Upper panel in (b):* $T^* = T/(1 + \tau_e[1 - 2T])$ *versus* ω, i.e., *total transmission data T in (a) corrected for the frequency-dependent extrapolation length (model, lower panel) for incidence angles γ = 0°, 15°, 30° (black, dark gray and light gray curves). Dashed lines represent the power laws* ω^{-3} *(short dashes), and* ω^{-2} *(long dashes).*

of roughly 0.3. This should be contrasted to the typical attenuation of several decades for stop gaps in characteristic 'coherent transmission' measurements, in which the intensity transmitted along the direction of the incident beam is monitored. As the coherent transmission decays exponentially with ℓ_ω/L such measurements are only feasible in thin (*i.e.*, small L [36]) or near-index matched (*i.e.*, large ℓ [12]) photonic crystals. The stop gap in coherent transmission is determined by diffraction from all the differently oriented crystallites encountered along the trajectory of the forward beam. The cumulative effect of all crystallites in the bulk causes a stop gap with high attenuation, and a width larger than the intrinsic photonic width [23]. This broadening of the stop gap in coherent transmission is not only limited by the angular spread of the incident beam, however, but mainly caused by misaligned and strained crystallites [11].

The decrease of the total transmission with increasing frequency is caused by a decrease of the mean free path ℓ_ω due to increasing scattering strength of defects at larger frequencies. We recognize two regimes in the total transmission, depending on the magnitude of the mean free path. Below $\omega = 7200$ cm^{-1} the total transmission of $T \sim 0.3$ indicates that the sample thickness $L \sim 200$ μm is at most a few transport mean free paths ($\ell_\omega \approx 60$ μm). In this regime the sample is not truly multiple scattering, causing deviations from the diffusion law Eq. (7.2) which relates ℓ_ω to the total transmission. For higher frequencies, we find a steeper decrease of the total transmission to ~ 0.05 at $\omega = 15000$ cm^{-1}, typical of $\ell_\omega \approx 10$ μm. As the thickness L of

the samples is not well known, accurate values for the mean free path ℓ can not be extracted. Though the values $\ell = 10$ to 60 μm agree with enhanced backscattering experiments on other samples, we focus only on the scaling of T with frequency. In the frequency range $\omega \geq 7200$ cm^{-1}, the mean free path is sufficiently small compared to the sample thickness to expect the Ohmic diffuse-transmission law Eq. (7.2) to hold. As the lowest Bragg diffraction overlaps with this frequency range, the analysis of total transmission in terms of the mean free path is complicated by the frequency dependence of the extrapolation length ratio.

7.7.2 Extrapolation length ratio and scattering strength

In Figure 7.9(b) the extrapolation length ratio $\tau_{e,\omega} = z_{e,\omega}/\ell_\omega$ pertaining to the fit to the data in Fig. 7.6 is presented as a function of frequency. In the small frequency limit, the extrapolation length ratio equals 2/3, as there are no internal reflections[4]. As the optical frequency reaches the L-gap, the extrapolation length ratio grows to a maximum of nearly 1.8, corresponding to a maximum average internal-reflection coefficient $\bar{R}^D_\omega \sim 45\%$. This maximum is reached at the blue edge of the L-gap, where the largest fraction of solid angle is covered by stop gaps [26]. The avoided crossing of two stop bands at $\alpha \geq 30^\circ$ enlarges the angle-averaged internal reflection in the same frequency window. For higher frequencies $\omega > 9500$ cm^{-1}, the extrapolation length ratio diminishes, as the range of internally reflected angles decreases. Though the qualitative behavior of the extrapolation length ratio may be explained by the band structure, the numerical value of the maximum, and details of the functional dependence are determined by, *e.g.*, the depth of the stop gaps involved.

From Eq. (7.2) it is clear that for frequencies *outside* a stop gap for the incident direction γ, for which $R^{\text{front}}_{\omega,\gamma} = 0$, the inverse optical thickness ℓ_ω/L may be expressed in terms of T_ω and $\tau_{e,\omega}$ as

$$\frac{\ell_\omega}{L} = T^*_\omega := \frac{T_\omega}{1 + \tau_{e,\omega} - 2\tau_{e,\omega} T_\omega}. \tag{7.19}$$

Using the extrapolation length ratio $\tau_{e,\omega}$ plotted in Fig. 7.9(b), we extract T^*_ω from the total transmission spectra presented in Fig. 7.9(a). We proceed to discuss the scaling behavior of the decrease of T^*_ω with increasing frequency. As T^*_ω equals ℓ_ω/L for frequencies outside a stop gap in total transmission, one might expect a ω^{-4} law typical for the scattering strength of particles much smaller than the wavelength, as reported for opals by Vlasov and coworkers [12]. Enhanced backscattering experiments on opals presented in Chapter 6, however, point at a scattering mechanism dominated by polydispersity and displacements. As scattering essentially occurs off thin 'difference' shells with size comparable to the wavelength, the associated scaling of the mean free path reaches into the quadratic Rayleigh-Gans regime for frequencies of the order of and above the lowest order Bragg diffraction. In this experiment, we find a decrease of ℓ_ω/L which appears faster than ω^{-2} and slower than ω^{-3} (dashed lines in

[4] The Fresnel reflection due to the effective refractive index is neglected in this analysis.

Fig. 7.9(b)). This observation holds for all the samples with a = 930, 900 and 800 nm, and was reproduced on samples with much smaller lattice parameters a = 690 and 500 nm. The latter samples are optically thicker, and the probe frequencies in the range of the experiment remain below the L-gap, *i.e.*, in the long wavelength regime. Though the frequency dependence of ℓ remains partly obscured due to the stop gaps in total transmission, the scattering does not increase as fast as Rayleigh's ω^4 law predicts. This is consistent with the scattering mechanism proposed in Chapter 6. One should bear in mind that the frequencies below and in the L-gap may belong to the cross-over regime from Rayleigh's ω^{-4} to Rayleigh-Gans's ω^{-2} scaling, in contrast to the higher frequencies used in Chapter 6. This may explain why ℓ decreases with frequency faster than ω^{-2} and slower than ω^{-3}. The fabrication of periodic structures with template-assisted self-assembly [6, 35, 37–39]), lithographic [7, 8] and layer-by-layer microfabrication methods [9] all involve displacements, roughness and polydispersity of the same magnitude. Hence we expect the random scattering in all the current state of the art photonic structures to be comparable.

7.8 Conclusion

We have presented frequency-resolved measurements of the angular distribution of diffuse transmitted light from strongly photonic crystals. We find a drastic frequency-dependent angular redistribution of diffuse transmitted light due to internal Bragg reflection. Though the ranges of strong internal reflection are governed by gaps in the dispersion relation, it is imperative for accurate modelling to take the redistribution into angles not contained in a stop gap into account. The relevant parameter, *i.e.*, the extrapolation length ratio, can not be derived from the band structure, but requires a diffusion model. We have presented the first model combining diffusion and the photonic internal reflection due to the band structure. The extrapolation length ratio which we calculate has a broader relevance in interpreting standard experiments such as enhanced backscattering or total transmission aimed at determining the transport mean free path in the frequency range of photonic stop gaps. Application to the total transmission of strongly photonic crystals reveals a mean free path decreasing from $\sim$ 60 to $\sim$ 10 μm as the frequency increases from below the first stop gap to just below the second order Bragg reflection. This decrease is surprisingly slower than ω^{-4}, indicating that polydispersity, roughness and site displacements of photonic building blocks form the dominant scattering mechanism.

The data and model presented here are especially relevant for the interpretation of emission measurements (see Chapters 3 and 4). The mechanism causing the angular dependence in emission spectra is the same diffuse internal reflection quantified here. Inspection of the stop bands in emission (Figure 3.2) show similar stop gap width, dispersion and depth as revealed by the escape function. Enhancement due to the extrapolation length may even be discerned in Figure 3.2(b). The internal reflectivity of the samples studied in this chapter (maximum $\sim$ 80% for $\alpha = 0°$) is somewhat higher than the stop gap depth $\sim$ 50 to 70% quoted in Chapter 3. We therefore

expect the extrapolation length ratio to be $\sim 1.35\ell$ (*i.e.* $\bar{R}^D_\omega = 34\%$) in the emission experiments. This is consistent with the estimate in Chapter 4. In Chapters 3 and 4 the angular dependence was separated from the angle integrated emission power spectra based on prior knowledge of external reflectivity experiments. Especially the fact that exit angles occur for which no stop gap overlaps the emission spectrum was instrumental in the analysis. Furthermore the spontaneous emission inhibition could only be estimated from the data to within the limits set by the magnitude of the extrapolation length ratio. Escape function measurements using externally injected light are useful to separate the angular dependence of emission spectra from the angle-integrated emission without prior knowledge of the dispersion. We expect that spectrally resolved emission measurements in the range of second order Bragg diffraction will require such complementary escape function measurements. In this frequency range (near bands 8 and 9), a multitude of reflectivity bands that barely shift with angle occur [30], causing a concomitant complicated frequency dependence of the extrapolation length ratio.

Finally, we would like to point out the similarity between the general analysis of the angle-resolved diffuse intensity distribution in Section 7.6 and high-resolution angle-resolved photoemission spectroscopy. This powerful technique is instrumental in the study of surface and projected bulk electronic band structures and Fermi surfaces in, *e.g.*, metals or high T_c superconductors [40, 41]. With this technique, the electron 'dispersion' surface (isoenergy surface) at the Fermi level translates into a structured angular distribution of photoelectrons. The analogy holds if the optical probe frequency is identified with the Fermi energy of the electron. Moreover, the optical experiment should be considered a zero temperature analogon of the electronic case. Experimentally, the probe depth in the photonic crystals, $\ell \lesssim 10$ unit cells, appears less restricted to the surface than in photoemission. Angle-resolved diffuse transmission on single crystal photonic crystals may prove to be a powerful technique for studying photonic dispersion. Theoretical analysis beyond the refraction construction (Fig. 7.8) may certainly benefit from electron theory developed for photoemission spectroscopy.

References

[1] *Photonic Band Gap Materials*, edited by C. M. Soukoulis (Kluwer, Dordrecht, 1996).

[2] *Photonic Crystals and Light Localization in the* 21st *Century*, edited by C. M. Soukoulis (Kluwer, Dordrecht, 2001).

[3] Z.-Y. Li and Z. Q. Zhang, *Fragility of Photonic Band Gaps in Inverse-Opal Photonic Crystals*, Phys. Rev. B **62**, 1516 (2000).

[4] Z.-Y. Li, X. D. Zhang, and Z. Q. Zhang, *Disordered Photonic Crystals Understood by a Perturbation Formalism*, Phys. Rev. B **61**, 15738 (2000).

[5] J. S. Kole, *New Methods for the Numerical Solution of Maxwell's Equations*, Ph.D. thesis, Rijksuniversiteit Groningen, 2003.

[6] J. E. G. J. Wijnhoven, L. Bechger, and W. L. Vos, *Fabrication and Characterization of Large Macroporous Photonic Crystals in Titania*, Chem. Mater. **13**, 4486 (2001).

[7] T. Baba and N. Fukaya, *Light Propagation Characteristics of Defect Waveguides in a Photonic Crystal Slab*, in [2] 105 (2000).
[8] M. Notomi, K. Yamada, A. Shinya, J. Takahashi, C. Takahashi, and I. Yokohama, *Extremely Large Group-Velocity Dispersion of Line Defect Waveguides in Photonic Crystal Slabs*, Phys. Rev. Lett. **87**, 253902 (2001).
[9] S. Ogawa, K. Tomoda, and S. Noda, *Effects of Structural Fluctuations on Three-Dimensional Photonic Crystals Operating at Near Infrared Wavelengths*, J. Appl. Phys. **91**, 513 (2002).
[10] J. Galisteo Lòpez and W. L. Vos, *Angle Resolved Reflectivity of Single-Domain Photonic Crystals, Effects of Disorder*, Phys. Rev. E **66**, 036616 (2002).
[11] W. L. Vos, M. Megens, C. M. van Kats, and P. Bösecke, *Transmission and Diffraction by Photonic Colloidal Crystals*, J. Phys.-Condens. Matter **8**, 9503 (1996).
[12] Y. A. Vlasov, M. A. Kaliteevski, and V. V. Nikolaev, *Different Regimes of Light Localization in a Disordered Photonic Crystal*, Phys. Rev. B **60**, 1555 (1999).
[13] A. F. Koenderink, M. Megens, G. van Soest, W. L. Vos, and A. Lagendijk, *Enhanced Backscattering from Photonic Crystals*, Phys. Lett. A **268**, 104 (2000).
[14] J. Huang, N. Eradat, M. E. Raikh, Z. V. Vardeny, A. A. Zakhidov, and R. H. Baughman, *Anomalous Coherent Backscattering of Light from Opal Photonic Crystals*, Phys. Rev. Lett. **86**, 4815 (2001).
[15] A. Ishimaru, *Wave Propagation and Scattering in Random Media* (Academic Press, New York, 1978).
[16] P. Sheng, *Introduction to Wave Scattering, Localization, and Mesoscopic Phenomena* (Academic Press, New York, 1995).
[17] A. Lagendijk, R. Vreeker, and P. de Vries, *Influence of Internal Reflection on Diffusive Transport in Strongly Scattering Media*, Phys. Lett. A **136**, 81 (1989).
[18] J. X. Zhu, D. J. Pine, and D. A. Weitz, *Internal Reflection of Diffusive Light in Random Media*, Phys. Rev. A **44**, 3948 (1991).
[19] M. U. Vera and D. J. Durian, *Angular Distribution of Diffusely Transmitted Light*, Phys. Rev. E **53**, 3215 (1996).
[20] J. Gómez Rivas, R. Sprik, A. Lagendijk, L. D. Noordam, and C. W. Rella, *Mid-Infrared Scattering and Absorption in Ge Powder Close to the Anderson Localization Transition*, Phys. Rev. E **62**, R4540 (2000).
[21] J. Gómez Rivas, R. Sprik, A. Lagendijk, L. D. Noordam, and C. W. Rella, *Static and Dynamic Transport of Light Close to the Anderson Localization Transition*, Phys. Rev. E **63**, 046613 (2001).
[22] F. J. P. Schuurmans, D. Vanmaekelbergh, J. van de Lagemaat, and A. Lagendijk, *Strongly Photonic Macroporous Gallium Phosphide Networks*, Science **284**, 141 (1999).
[23] M. Megens, J. E. G. J. Wijnhoven, A. Lagendijk, and W. L. Vos, *Light Sources Inside Photonic Crystals*, J. Opt. Soc. Am. B **16**, 1403 (1999).
[24] H. P. Schriemer, H. M. van Driel, A. F. Koenderink, and W. L. Vos, *Modified Spontaneous Emission Spectra of Laser Dye in Inverse Opal Photonic Crystals*, Phys. Rev. A **63**, 011801 (2001).
[25] M. Notomi, *Theory of Light Propagation in Strongly Modulated Photonic Crystals: Refractionlike Behavior in the Vicinity of the Photonic Band Gap*, Phys. Rev. B **62**, 10696 (2000).
[26] M. S. Thijssen, R. Sprik, J. E. G. J. Wijnhoven, M. Megens, T. Narayanan, A. Lagendijk, and W. L. Vos, *Inhibited Light Propagation and Broadband Reflection in Photonic Air-Sphere Crystals*, Phys. Rev. Lett. **83**, 2730 (1999).

[27] H. M. van Driel and W. L. Vos, *Multiple Bragg Wave Coupling in Photonic Band-Gap Crystals*, Phys. Rev. B **62**, 9872 (2000).
[28] S. G. Romanov, T. Maka, C. M. S. Torres, M. Müller, R. Zentel, D. Cassagne, J. Manzanares-Martinez, and C. Jouanin, *Diffraction of Light from Thin-Film Polymethylmethacrylate Opaline Photonic Crystals*, Phys. Rev. E **63**, 056603 (2001).
[29] D. J. Durian, *Influence of Boundary Reflection and Refraction on Diffusive Photon Transport*, Phys. Rev. E **50**, 857 (1994).
[30] W. L. Vos and H. M. van Driel, *Higher Order Bragg Diffraction by Strongly Photonic Fcc Crystals: Onset of a Photonic Bandgap*, Phys. Lett. A **272**, 101 (2000).
[31] T. Yoshiyama and I. Sogami, *Kossel Line Analysis on Colloidal Crystals in Semidilute Aqueous Solutions*, Phys. Rev. Lett. **53**, 2153 (1984).
[32] Ì. Ì. Tarhan and G. H. Watson, *Photonic Band Structure of Fcc Colloidal Crystals*, Phys. Rev. Lett. **76**, 315 (1996).
[33] W. Kossel, V. Loeck, and H. Voges, *Die Richtigungsverteilung der in einem Kristall enstandenen charakteristischen Röntgenstrahlung*, Z. f. Physik **94**, 139 (1935).
[34] R. W. James, *The Optical Principles of the Diffraction of X-Rays* (G. Bell & Sons, London, 1954).
[35] Y. A. Vlasov, X. Z. Bo, J. C. Sturm, and D. J. Norris, *On-Chip Natural Assembly of Silicon Photonic Bandgap Crystals*, Nature **414**, 289 (2001).
[36] J. F. Bertone, P. Jiang, K. S. Hwang, D. M. Mittleman, and V. L. Colvin, *Thickness Dependence of the Optical Properties of Ordered Silica-Air and Air-Polymer Photonic Crystals*, Phys. Rev. Lett. **83**, 300 (1999).
[37] J. E. G. J. Wijnhoven and W. L. Vos, *Preparation of Photonic Crystals Made of Air Spheres in Titania*, Science **281**, 802 (1998).
[38] A. Blanco, E. Chomski, S. Grabtchak, M. Ibisate, S. John, S. W. Leonard, C. López, F. Meseguer, H. Míguez, J. P. Mondia, G. A. Ozin, O. Toader, and H. M. van Driel, *Large-Scale Synthesis of a Silicon Photonic Crystal with a Complete Three-Dimensional Bandgap Near 1. 5 Micrometres*, Nature **405**, 437 (2000).
[39] O. D. Velev and E. W. Kaler, *Structured Porous Materials Via Colloidal Crystal Templating: From Inorganic Oxides to Metals*, Adv. Mater. **12**, 531 (2000).
[40] S. Hüfner, *Photoelectron Spectroscopy: Principles and Applications* (Springer Verlag, Berlin, 1995), and references therein.
[41] S. V. Borisenko, M. S. Golden, S. Legner, T. Pichler, C. Durr, M. Knupfer, J. Fink, G. Yang, S. Abell, and H. Berger, *Joys and Pitfalls of Fermi Surface Mapping in* $Bi_2Sr_2CaCu_2O_{8+\delta}$ *Using Angle Resolved Photoemission*, Phys. Rev. Lett. **84**, 4453 (2000).

Index

Summary

This thesis describes experimental studies of emission, diffusion and diffraction of light in strongly photonic crystals. Photonic crystals are three-dimensionally periodic dielectric composites with periodicities comparable to optical wavelengths. Bragg diffraction by sets of lattice planes causes the dispersion relation to organize into bands, separated by stop gaps. A stop gap is a frequency window for which propagation of light in a certain direction is forbidden. The dispersion bands for photons bear strong similarity to the energy bands of electrons in crystalline solids. Certain crystal symmetries, proper choice of refractive index contrast and suitable arrangement of the dielectric constituents can give rise to a *photonic band gap*. A photonic band gap is a frequency window for which no propagating modes exist in any direction. If an exited atom with transition frequency in the band gap is placed inside such a band gap crystal, it can not decay to the ground state, since no states are available for the photon that needs to be radiated. Indeed, a photonic band gap crystal was first proposed as a means to control radiative properties of atoms, for instance causing inhibition or enhancement of spontaneous emission. In analogy with semiconductors, photonic band gap crystals can be doped with defects; such dopants can create localized electromagnetic states for frequencies in the band gap. These defect cavities may form the basis for efficient miniature light sources, and for novel solid-state quantum-electrodynamical experiments. On a more applied level, photonic crystals are pursued to manipulate the propagation of light in optoelectronic components. Chapter 1 elaborates on several of the basic concepts underlying the interest in photonic band gap materials, and aims at providing a survey of recent progress in realizing and characterizing photonic crystals.

Recently, photonic crystals have been realized that consist of ordered arrays of air spheres in a solid backbone of titania. The refractive index contrast between air and titania is among the highest that can be achieved for visible light, and causes these samples to be strongly photonic. The photonic strength quantifies the degree to which propagation of light in a photonic crystal differs from propagation in a homogeneous medium. The titania inverse opals, for instance, are sufficiently photonic to exclude half of all directions of propagation for a specific frequency range. Accordingly, one would expect a significant reduction of the spontaneous emission rate of internal light sources.

The spontaneous emission rate of an emitter depends on the density of available photon modes at the emission frequency ('density of states', or 'DOS'). The properties of spontaneous emission from sources in photonic crystals are not solely determined by the DOS, however. In addition, the transport of radiant energy to the far field and out of the crystal is affected by dispersion and diffraction of emitted light by the photonic crystal. To unravel the different mechanisms that modify spontaneous

emission, a quantitative understanding of the properties of photonic crystals is vital. Chapter 2 provides an overview of optical properties of photonic crystals, regarding dispersion, DOS and refraction. Furthermore, Chapter 2 explains the plane-wave method that underlies the theoretical results used for interpreting observations in subsequent chapters.

In Chapters 3 and 4 different aspects are described of experiments that probe spontaneous emission from sources inside photonic crystals. In general, spontaneous emission is affected by two phenomena: *(i)* redistribution of spontaneous emission over emission angle due to stop gaps in the dispersion relation, and *(ii)* angle-independent changes that reflect the photonic DOS. The first phenomenon causes significant changes of spontaneous emission spectra for all photonic crystals, also for weakly photonic crystals in which neither the DOS, nor emission lifetimes are modified . The data discussed in Chapter 3 reveal angular redistribution of emission of organic dyes in titania inverse opals, caused by internal Bragg diffraction. A double attenuation band is observed, in contrast to the single band predicted by Bragg's law for diffraction by a single set of lattice planes. The angle-dependent center-frequencies of the gaps display an avoided crossing over a large angular range. The observations underline the relevance of coupling of simultaneous Bragg diffractions by different sets of lattice planes. Strong coupling of Bragg diffractions is a prerequisite for photonic band gap formation.

Chapter 4 shows evidence for unexpectedly large angle-independent changes in spontaneous emission power of dyes in inverse opals. Over a wide frequency range, the angle-independent spontaneous emission power is inhibited by a factor ~ 5. A careful analysis of the role of fluorescence quantum efficiency and the choice of non-photonic reference host is crucial in assessing the photonic origin of the observed inhibition. Although the frequency range over which suppression occurs agrees with the calculated reduction of the total density of states, the magnitude of the inhibition is much larger. We propose that the large inhibition is due to the local DOS, which accounts for the local coupling efficiency of spontaneous emission to the available modes at the position of the light source. This experiment is the first to demonstrate the effect of the local DOS on spontaneous emission in photonic crystals. This exciting result calls for theoretical calculations of the local DOS; a formidable task beyond the scope of this thesis. Ultimately, spontaneous emission properties can be manipulated to a larger degree than expected from the total DOS by optimizing the location of the emitters in the unit cell.

Motivated by the spontaneous emission control described in Chapter 4, Chapter 5 describes a method to modify the density of states on timescales of ~ 100 fs. The physics of propagation or emission of light in photonic crystals that are switched in time, is an unexplored field. In Chapter 5 the possibility of photonic band gap switching by two-photon excitation of free carriers in semiconductor-air photonic crystals is considered. Using realistic material parameters for GaAs, we find that femtosecond control of spontaneous emission and microcavities in inverse opals is feasible. Several switching schemes are possible, such as switching the DOS at fixed frequency from

zero to a high value, from a high value to zero or from high to zero to a high value. We discuss the catching and releasing of photons in point-defect cavities. This process depends on the time scale of the switching process. Particularly, the degree to which a probe photon changes color as a consequence of fast switching is a matter of great interest.

In practice, fabricated photonic crystals are never ideally ordered. The carefully prepared inverse opals studied in our group, for instance, are known to suffer from fluctuations in size and position of the air spheres of about 1% of the size of the unit cell. Similar numbers have recently been quoted for various state of the art structures made by different methods. On the one hand, this high degree of order gives rise to striking diffraction and dispersion, and is sufficient to strongly modify spontaneous emission (Chapters 3 and 4). On the other hand, the structural variations cause the direction of propagation of photons to randomize due to scattering over a length scale $\ell \sim 40$ lattice spacings. Chapter 6 describes a pioneering experimental study of enhanced backscattering in opals and inverse opals. Enhanced backscattering is an interference phenomenon in multiple scattering that allows to quantify the mean free path ℓ. Apart from finding ℓ, we uncover several novel effects that modify enhanced backscattering due to the photonic crystal backbone. Furthermore, we explain the magnitude of the mean free path in terms of a simple model based on scattering by small displacements and polydispersity of the unit cell building blocks. It appears that a formidable subnanometer fabrication accuracy is required to achieve photonic crystals that can operate as millimeter sized platforms for manipulating photons at optical frequencies.

As all photons are removed from incident and diffracted beams after a mean free path, it is highly relevant to study where the scattered photons go. Over length scales larger than a mean free path, photons are transported in a diffuse manner. In Chapter 7, we present an experiment that quantifies the angular distribution of diffuse photons transmitted by inverse opals. Angular distributions are observed that depend strongly on frequency, and differ markedly from expectations based on diffuse transport in random media. The frequency and angle-dependence can be quantitatively explained by diffusion theory combined with internal reflections due to gaps in the dispersion. The model also applies to the angular dependence of emission spectra reported on in Chapter 7. A surprising result is that the angular distribution of diffuse light allows reconstruction of the photonic dispersion relation in a manner analogous to angle-resolved photoemission spectroscopy in solid state physics.

Many researchers in the field of photonic crystals are focusing on fabricating structures and measuring reflection or transmission of these crystals. These aspects are not the subject of this thesis, and this thesis is not aimed at making more strongly photonic crystals. In contrast, this work delves deeper into the optics hidden beneath the opalescent surface of strongly photonic crystals. This subject is complicated even without a photonic band gap. I believe some of the novel insights presented in this work will ultimately be vital to understand the properties of photonic crystals that do form a leakproof cage for light.

Samenvatting voor iedereen

Fotonische kristallen zijn materialen die bijzondere verschijnselen vertonen wanneer men er met licht van buitenaf naar kijkt. In feite zijn fotonische kristallen zelfs ontworpen om nog onalledaagsere verschijnselen te veroorzaken wanneer de lichtbron binnen in het kristal wordt geplaatst. In het eerste deel van deze samenvatting wordt uitgelegd wat fotonische kristallen zijn en hoe ze werken. Aansluitend wordt de bijdrage van dit proefschrift aan het fysische begrip van fotonische kristallen toegelicht.

Interferentie

Zo op het oog vertonen fotonische kristallen eenzelfde kleurenspel als bijvoorbeeld opalen, parelmoer, pauwenveren of de onderkant van een compact-disc. Onder bepaalde belichtingen zijn fel gekleurde weerkaatsingen te zien die bij kleine verandering van belichting van kleur wisselen. Deze verschijning is heel anders dan die van de meeste gekleurde voorwerpen en materialen. De meeste materialen ontlenen hun kleur aan absorptie van licht; bepaalde kleuren uit het invallende licht worden opgenomen en verdwijnen. Het overgebleven licht bepaalt de kleur die we waarnemen. Zo is bladgroen groen omdat het alleen rood zonlicht absorbeert.

Fotonische kristallen ontlenen hun kleuren juist niet aan absorptie; het is zelfs van het allergrootste belang dat er geen licht 'kwijt raakt'. In plaats daarvan zijn de kleuren van fotonische kristallen 'interferentie'-kleuren. Voor interferentie is het essentieel dat licht een golfverschijnsel is (figuur S.1). Verschillende golven kunnen elkaar versterken als hun toppen samenvallen, of elkaar juist uitdoven als de toppen van de ene golf samenvallen met de dalen van de andere golf. Bij een dun zeepvlies, bijvoorbeeld, ziet men heldere kleuren in het gereflecteerde licht. Deze kleuren zijn het gevolg van versterkende interferentie van lichtgolven gereflecteerd aan de voorkant van het zeepvlies met golven gereflecteerd door de achterkant van het vlies. De golf gereflecteerd aan het achterste grensvlak legt een langere weg af dan de golf weerkaatst door het voorste grensvlak. Als dit weglengteverschil precies gelijk aan een golflengte is, lopen de beide weerkaatste golven precies in de pas (figuur S.1). Voor een vliesdikte d van 0.00025 mm levert dit een groenblauwe reflectie (golflengte $\lambda = 2d = 0.0005$ mm) als je loodrecht op het vlies kijkt. Omdat het weglengteverschil afhangt van de hoek, verandert de kleur afhankelijk van de kijkrichting. De sterkte van de interferentie kan vergroot worden door vele opeenvolgende lagen te gebruiken die regelmatig achter elkaar zijn geplaatst (zie figuur S.1). Zo'n reflectie aan een gelaagde structuur heet 'Bragg reflectie'[1].

[1] De Nobel-prijswinnaars (1915) William Bragg en Lawrence Bragg bestudeerden Bragg-reflecties van Röntgen-stralen aan atomaire kristallen.

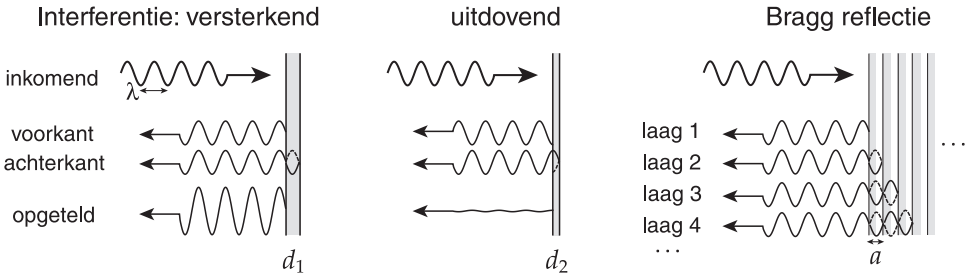

FIGUUR S.1: *Interferentie bepaalt de mate van weerkaatsing van licht door een dunne laag materiaal (grijs). De golf die gereflecteerd wordt aan de achterzijde legt de dikte d van de laag tweemaal af, zowel heen als terug. Als dit weglengteverschil 2d ten opzichte van de golf gereflecteerd aan de voorzijde een golflengte λ bedraagt (links) lopen toppen en dalen van de twee reflecties gelijk. Opgeteld (onder) geeft dit een heldere weerkaatsing. Als het weglengteverschil een halve golflengte is (midden), lopen beide reflecties ongelijk. De twee golven doven elkaar uit; er wordt netto geen licht gereflecteerd en alles wordt doorgelaten. Bragg reflectie treedt op voor een regelmatige oneindig herhalende stapeling van materialen (rechts). Omdat de reflecties van alle grensvlakken (roosterafstand a) allen in de pas lopen, geeft constructieve interferentie een zeer sterke reflectie.*

Een fotonisch kristal is een in *alle* drie dimensies (hoogte, breedte en diepte) regelmatig opgebouwd samenstelsel van materialen. Zo is een opaal bijvoorbeeld een dichte stapeling van kleine glasbolletjes die alle dezelfde straal hebben (ca. 0.0002 mm). Hoewel dit erg klein lijkt, is de afstand tussen de bouwstenen zo'n 1000 maal groter dan die tussen atomen in een normaal kristal, zoals bijvoorbeeld keukenzout. Waar de regelmaat van een normaal kristal past bij elektronen, is een fotonisch kristal gemaakt voor de lengteschaal die past bij fotonen: de golflengte van licht. Omdat een fotonisch kristal langs verscheidene richtingen dezelfde regelmaat ('roosterafstand') heeft, reflecteert het ook langs meerdere richtingen dezelfde kleuren. Door de materialen goed te kiezen en te rangschikken kan theoretisch zelfs een kristal gemaakt worden met een 'fotonische bandkloof'. Zo'n kristal weerkaatst een bepaalde kleur licht en houdt deze kleur buiten, ongeacht de richting waarin het licht invalt. Een bandkloof-kristal is dus een drie-dimensionale reflector, ook wel 'omnidirectionele spiegel' genoemd.

Fotonische bandkloof en de uitstraling van licht

Op zichzelf is een object dat een bepaalde kleur ongeacht de invalsrichting weerkaatst niet zo interessant. Een metalen doos is bijvoorbeeld ook zo'n omnidirectionele spiegel. Er is echter een belangrijk verschil tussen een metalen doos en een kristal met een bandkloof. Binnen in een metalen doos kan wel degelijk licht zijn; als men er een lichtbron in plaatst, straalt deze gewoon. Dat het licht van binnen aan de buitenkant niet zichtbaar is (en licht van buiten binnenin ook niet) heeft alleen te maken met het feit dat licht niet door het oppervlak van de doos heen kan. Een fotonisch kristal met

een bandkloof sluit daarentegen alle kleuren die het omnidirectioneel reflecteert echt uit. Licht van die kleuren kan in zo'n kristal dus niet zijn; *men kan de lichtbron wel proberen aan te zetten, maar hij zal geen licht uitzenden!* Het verrassende van deze situatie wordt duidelijk wanneer men denkt aan een atoom of molecuul als lichtbron. De kleuren die een atoom uitzendt kunnen heel precies voorspeld worden; deze hangen alleen af van de massa van de kern, en het aantal elektronen van het atoom. Een voorbeeld is het natrium atoom, bekend van de oranje verlichting langs snelwegen. Dit oranje licht wordt uitgezonden als het atoom terugvalt van een aangeslagen toestand naar de grondtoestand (figuur S.2(a)). Het uitzenden van het licht (emissie) gebeurt spontaan en in een willekeurige richting, en het moment van uitzenden berust op toeval. De kleur en de *gemiddelde* tijd tussen aanslaan en spontane emissie zijn karakteristieken van het atoom. Toch kan de levensduur beïnvloed worden. We stellen ons bijvoorbeeld voor dat het aangeslagen natrium atoom in een bandkloof kristal voor oranje licht wordt geplaatst. Omdat het kristal geen oranje licht toelaat kan het atoom niet stralen en moet het oneindig lang aangeslagen blijven (zie figuur S.2(c)). De levensduur van het atoom kan dus beïnvloed worden door zijn optische omgeving aan te passen. Kleine veranderingen in levensduur (meest versnellingen) zijn inderdaad waargenomen voor atomen tussen twee dicht op elkaar staande spiegels. Fotonische bandkloof materialen bieden een unieke mogelijkheid om spontane emissie te vertragen of echt te verbieden.

Nog vreemder wordt het als het atoom ingebouwd wordt bij een kleine verstoring in het regelmatige rooster van een fotonisch kristal met bandkloof. Er is voorspeld dat zo'n roosterfout er voor kan zorgen dat er in plaats van geen, precies één toestand voor het uit te zenden foton is. Omdat het defect van alle kanten omgeven is door perfect reflecterend kristal fungeert het als een kooi voor licht. Het licht wordt opgesloten in een volume λ^3 ter grootte van zijn eigen golflengte λ in alle drie dimensies. Als een aangeslagen atoom in zo'n kooi is geplaatst, kan het atoom wel een foton uitzenden,

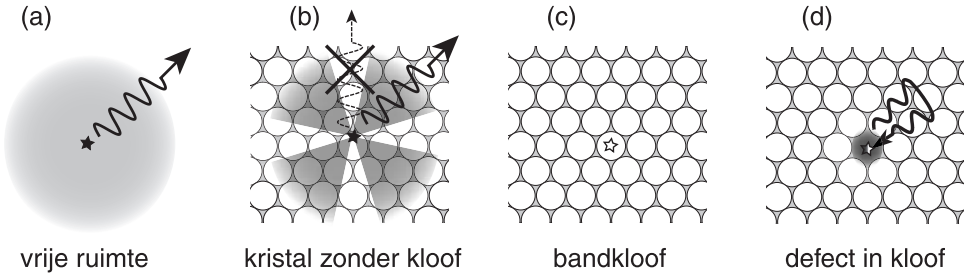

FIGUUR S.2: *(a) Een atoom of molecuul (symbool ⋆) in de vrije ruimte kan in alle richtingen stralen. (b) In een kristal zonder bandkloof zijn bepaalde stralingsrichtingen uitgesloten (×), maar blijven andere richtingen (grijze 'taartpunten') beschikbaar. (c) Als de uitstralingsgolflengte in een bandkloof valt straalt het atoom helemaal niet, en moet aangeslagen (☆) blijven. (d) bij een defect (missende bol) in een bandkloofmateriaal kan het atoom steeds weer een foton uitwisselen met het defect; het foton kan niet weg.*

maar het foton kan door de interferentie helemaal niet weg. Het foton kan steeds weer uitgezonden en opgenomen worden, terwijl het atoom wisselt tussen de grond- en de aangeslagen toestand (figuur S.2(d)). Samenvattend, kan gesteld worden dat fotonische kristallen het manipuleren van allerlei stralende processen van atomen en moleculen mogelijk maken. Ook is door verschillende onderzoeksgroepen voorgesteld dat fotonische kristallen gebruikt kunnen worden om de voortplanting van licht naar believen te beheersen. Deze vooruitzichten hebben ertoe geleid dat fotonische bandkloof kristallen door veel groepen nagestreefd worden. Enerzijds is er het doel om atomen in bandkloof-materialen te bestuderen en anderzijds de motivatie om ultrakleine optische schakelingen ('optische chips') en efficiënte miniatuur lichtbronnen te realiseren.

Kristallen maken

Helaas is het is erg moeilijk om een fotonische bandkloof te maken. Ten eerste is het een probleem dat de regelmaat van de structuur zo'n 0.0005 mm moet zijn om te passen bij de golflengte van zichtbaar licht. Deze lengte is zo klein dat alledaagse mechanische werktuigen om een structuur in elkaar te zetten geen uitkomst bieden. Het tweede, voornaamste, probleem is dat het materiaal moet bestaan uit een samenstelsel van componenten waartussen een zo groot mogelijk verschil in brekingsindex bestaat. De brekingsindex van een materiaal bepaalt hoeveel langzamer licht zich voortplant in dat materiaal dan in vacuum, en ontleent zijn naam aan het feit dat hij bepalend is voor hoe sterk een lichtstraal van richting verandert ('breekt') wanneer hij het betreffende materiaal binnen treedt. Veel materialen in de natuur hebben een brekingsindex van ongeveer 1.5. Zelfs als lucht (met de laagst mogelijke brekingsindex van 1.0) als één component voor het kristal gekozen wordt, moet de andere component een index van tenminste 2 á 3 hebben. Er is slechts een handvol materialen die in aanmerking komen.

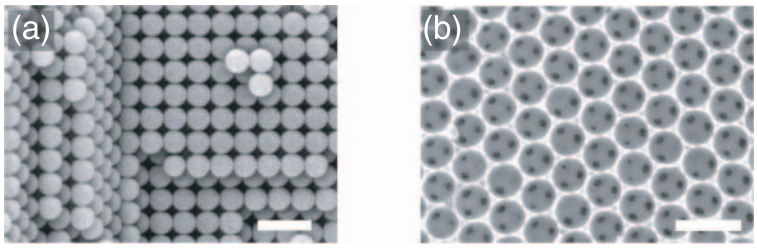

Figuur S.3: *Elektronen-microscopiebeelden van een kristal van (a) polystyreenbolletjes in lucht (synthetisch opaal) en (b) luchtbollen in titaandioxide. Regelmatige stapeling in alle drie dimensies is duidelijk zichtbaar in (a). Schaalbalken zijn in beide figuren 0.002 millimeter. In (b) getuigen de zwarte gaatjes (drie per luchtbol) van een driedimensionale structuur: zij bieden een doorkijk naar de onderliggende laag bollen. Elke luchtbol rust op drie onderliggende bollen. Plaatjes met dank aan Lydia Bechger.*

Vlak voor het begin van het hier beschreven onderzoek zijn in onze groep kristallen ontwikkeld van regelmatig gestapelde bollen gevuld met lucht en omhuld door titaandioxide (zie figuur S.3(b)). Titaandioxide is een doorzichtige stof met een brekingsindex van 2.7; poeders van dit materiaal verstrooien het licht zo sterk dat ze vaak gebruikt worden als wit pigment (titaanwit) in bijvoorbeeld verf, tandpasta of papier. Met behulp van reflectiemetingen weten we dat voor sommige kleuren meer dan de helft van alle voortplantingsrichtingen door Bragg reflectie 'verboden' is in de luchtbolkristallen. De kooi is dus nog niet gesloten, maar lijkt wel half dicht.

Spontane emissie in luchtbolkristallen

Om de invloed van de luchtbolkristallen op spontane emissie te meten, hebben we fluorescerende kleurstofmoleculen binnenin de luchtbollen van de kristallen ingebouwd. Anders dan atomen, zenden verschillende moleculen verschillende kleuren uit. Zo kun je het effect van een fotonisch kristal op de spontane emissie tegelijkertijd voor een scala aan kleuren meten. Metingen in hoofdstuk 3 laten zien dat het fotonisch kristal ervoor zorgt dat de verschillende kleuren die de moleculen uitstralen elk in heel verschillende richtingen naar buiten komen. Door interne weerkaatsing zijn bepaalde kleuren sterk onderdrukt voor sommige richtingen; deze richtingen komen precies overeen met die waarlangs dezelfde kleuren van buitenaf het best Bragg gereflecteerd worden door de roostervlakken. Een fotonisch kristal kan dus gebruikt worden om uitgestraald licht over hoeken te herverdelen, zoals weergegeven in figuur S.2(b). Opvallend aan de metingen is dat we aanwijzingen vinden voor het samenwerken van reflecties aan verschillende families roostervlakken, met verschillende oriëntaties. Samenwerking van weerkaatsing aan roostervlakken met veel verschillende richtingen in alle drie dimensies is uiteindelijk essentieel om de kooi voor licht aan alle kanten te sluiten.

Dit hoekafhankelijke effect heeft echter nog niets met spontane emissie levensduren te maken en kan ook gemeten worden voor lichtbronnen in fotonische kristallen waarin het brekingsindexverschil heel klein is. Omdat de kooi voor licht in onze luchtbolkristallen half dicht is, verwacht men dat een aangeslagen atoom of molecuul in zo'n kristal een twee keer zo lange levensduur heeft. Dit zou logisch zijn omdat er twee keer minder elektromagnetische toestanden beschikbaar zijn voor het uit te stralen licht. Door een zorgvuldige analyse van het hoekafhankelijke effect zijn we erin geslaagd om het over alle uitstralings-richtingen gemiddelde spectrum te meten (hoofdstuk 4). Dit spectrum is het door de moleculen in het fotonisch kristal uitgestraalde vermogen als functie van de golflengte. In vergelijking met dezelfde kleurstof in referentie-monsters blijkt dat de moleculen in fotonische kristallen tot wel vijf keer minder licht uitzenden in een bepaalde band van kleuren. Bij deze kleuren treedt over een heel groot hoekbereik Bragg diffractie op en zijn er dus vele voortplantingsrichtingen tegelijk verboden. Dit beeld wordt bevestigd door proeven met verschillende soorten kleurstoffen, en met kristallen met net iets andere roosterafstand. In een kristal met een kortere roosterafstand zijn zowel de reflectiepiek als de band van onder-

drukking naar kortere golflengten geschoven. In een tijdsopgelost experiment zou de onderdrukking van het uitgestraalde vermogen gelijk staan aan een vertraging van de spontane emissie. De gemeten onderdrukking is veel groter dan de verwachte tweevoudige onderdrukking. Dit komt doordat onderdrukking voor sommige plaatsen van de lichtbron ten opzichte van de luchtbollen beter werkt, dan op andere plaatsen.

Schakelen van de fotonische bandkloof

Hoofdstuk 5 loopt vooruit op het moment dat we spontane emissie daadwerkelijk geheel kunnen stoppen of juist versnellen met een fotonische bandkloof. Het ligt voor de hand dat de potentiële mogelijkheden van zo'n (nog door niemand bereikte) bandkloof veel groter zijn, als de bandkloof in de tijd gecontroleerd veranderd kan worden. De bandkloof van een kristal kan geschakeld worden door bijvoorbeeld de brekingsindex van één van de componenten te wijzigen. Voor de halfgeleidermaterialen die voldoende hoge brekingsindex hebben om een fotonische bandkloof te realiseren, blijkt dat de brekingsindex tijdelijk en ultrasnel verminderd kan worden door met een lichtpuls elektronen in de halfgeleider aan te slaan. Met praktisch beschikbare korte en intense laserpulsen kan de brekingsindex voldoende veranderd worden om de bandkloof sterk van kleur te laten verschuiven. Men zou daarmee bijvoorbeeld een aangeslagen natrium atoom in een kristal met een bandkloof voor oranje licht opeens met de schakelpuls tot spontane emissie kunnen laten overgaan. Hierbij zorgt de schakelpuls ervoor dat de bandkloof ineens niet meer oranje licht verbiedt, maar blauwere kleuren. Essentiëel is dat de kleur van de schakelpuls niet gelijk hoeft te zijn aan die van de emissiebron; anders zou de schakelpuls het kristal niet eens in kunnen! Dit hoofdstuk roept veel nieuwe theoretische vragen op; de eerste experimenten worden momenteel opgebouwd.

Veelvuldige verstrooiing

Bijna de helft van dit proefschrift behandelt experimenten aan het optische effect van het kleine beetje wanorde in de bijna perfect geordende kristallen. Natuurlijk zou het ideaal zijn als de kristallen perfect regelmatig zouden zijn; dit is echter onmogelijk te realiseren. In de titaandioxide luchtbolkristallen bijvoorbeeld, zijn er kleine variaties in straal en positie van de bollen van gemiddeld 2% van hun diameter. Ook voor kristallen gemaakt met andere technieken worden variaties van 3 – 7% gevonden. Een variatie van 2% in elke bouwsteen is zeer klein; klein genoeg om heldere reflecties te veroorzaken en de spontane uitstraling van licht sterk te onderdrukken, zoals gemeten in hoofdstuk 4. Desalniettemin zorgt het ervoor dat elke straal licht die het kristal binnenkomt na een bepaalde afstand ℓ willekeurig van richting verandert.

Willekeurige veelvuldige verstrooiing van licht treedt op in veel bekende ongeordende materialen, zoals poeders, verf, melk, wolken, enzovoorts. Wanneer een lichtstraal een deeltje tegenkomt, zoals een druppeltje in de wolk, verdeelt het licht zich over vele richtingen. Als het licht vaak verstrooid wordt, is aan het uitkomende licht

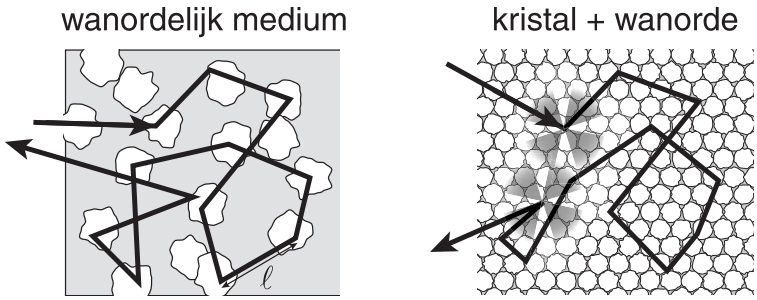

FIGUUR S.4: *(Links) In een wanordelijk mengsel van bijvoorbeeld kleine deeltjes (wit) in oplossing (grijs) wordt licht veelvuldig willekeurig verstrooid. Licht-paden veranderen steeds van richting; de gemiddelde afstand tussen verstrooiingen is de vrije weglengte ℓ. (Rechts) In fotonische kristallen met een klein beetje wanorde (zwaar overdreven in de figuur) is ℓ veel groter dan de roosterafstand. Bovendien vervolgt een lichtpad zijn weg na een verstrooiing nooit in een richting die door Bragg reflectie verboden is (alleen aangegeven voor de eerste en de laatste verstrooiing).*

niet te zien, hoe en waar het licht het materiaal ingekomen is. Zo'n materiaal ziet er (als het niet absorbeert) wit uit, in plaats van doorzichtig. Veelvuldige verstrooiing is van belang zodra het materiaal dikker is dan de *vrije weglengte* ℓ (Figuur S.4). In melk bijvoorbeeld, is de vrije weglengte zo'n $\ell = 0.1$ mm. Alleen als een glas melk dunner is dan 0.1 mm kan men er doorheen kijken.

De hoofdstukken 6 en 7 omvatten de eerste in de literatuur gerapporteerde metingen aan veelvuldig verstrooid ('diffuus') licht in fotonische kristallen. Metingen in hoofdstuk 6 beantwoorden de belangrijke vraag hoe groot de vrije weglengte van licht in fotonische kristallen is. De verstrooiing in de kristallen werd gemeten met behulp van de 'terugstrooikegel'. Door interferentie is de intensiteit van meervoudig verstrooid licht dat een monster verlaat verhoogd in een kleine kegel van hoeken rond de inkomende bundel. Uit metingen aan deze kegel blijkt dat het 'zicht' zo'n 40 roosterafstanden is. Het heeft dus niet veel zin om een fotonisch kristal groter te maken dan 40 roostervlakken in alle drie dimensies. Defecten die op elektronenmicroscopieplaatjes juist opvallen, zoals missende bollen, blijken de gemeten vrije weglengte niet te verklaren. Hiervoor zijn er veel te weinig van deze defecten. Een simpel model laat zien dat de kleine variaties in straal en positie van de bollen in het rooster bepalend zijn voor de mate van verstrooiing. Per bol is het effect van de variaties heel klein, maar door het grote aantal van deze verstoringen is het gezamenlijke effect overheersend. Met de huidige fabricage-technieken lijkt het een haast onmogelijke opgave om de variaties in positie en grootte van de bouwstenen zodanig te beperken, dat de vrije weglengte van de orde $\ell = 1$ mm wordt. Dit maakt 'optische chips' met verschillende functies achter elkaar vooralsnog schier onmogelijk.

In hoofdstuk 7 leggen metingen bloot hoe veelvuldig verstrooid licht uiteindelijk een fotonisch kristal verlaat. Dit is van belang omdat voor bijna alle drie-dimensionale fotonische kristallen geldt dat nagenoeg al het licht dat de kristallen binnenkomt pas na veelvuldige verstrooiing uittreedt. Omdat fotonische kristallen geen licht absor-

beren, is de intensiteit van het diffuse licht voor een kristal dikker dan ℓ uiteindelijk altijd groter dan die van de bundels die de experimentator wil manipuleren of bestuderen. Om in een experiment de diffuse bijdrage in de verdeling van het licht te scheiden van andere effecten, is het nodig de diffuse bijdrage goed te begrijpen. Voor een wanordelijk materiaal, zoals een glas melk, is precies bekend hoe diffuus licht zich verdeelt over de uittreehoeken, en geldt dat dit niet afhangt van de kleur van het licht. Hierdoor ziet melk er van alle kanten wit uit. Voor fotonische kristallen vinden we echter verdelingen die heel sterk afhangen van de kleur van het licht, en sterk verschillen van de verdeling bekend van wanordelijke media. Net als in hoofdstuk 3 speelt interne weerkaatsing een belangrijke rol. Interne weerkaatsing van het diffuse licht door roostervlakken voordat het licht het kristal verlaat, zorgt ervoor dat bepaalde kleuren sterk onderdrukt zijn voor sommige richtingen. Omdat het licht uiteindelijk toch ergens het materiaal moet verlaten, betekent dit dat je voor andere hoeken juist weer veel meer licht aantreft dan verwacht. Het is met name verrassend dat het door de wanorde verdwaalde licht uiteindelijk veel informatie geeft over het optische effect van de orde van het kristal. Ook levert dit experiment een spectaculaire voorspelling voor kristallen die zo sterk fotonisch zijn dat ze een bandkloof hebben. Voor kleuren licht die bijna in de bandkloof passen is de kooi voor licht bijna dicht, op een paar geïsoleerde richtingen na. Omdat alle andere uittreehoeken door interne weerkaatsing geblokkeerd zijn, betekent dit dat al het diffuse licht van deze kleuren het kristal in één bepaalde richting moet verlaten. Het is erg tegen-intuïtief dat een materiaal waarin licht meervoudig willekeurig verstrooid wordt, dit licht afgeeft in een gerichte bundel.

Dit proefschrift laat ten eerste experimenteel zien dat fotonische kristallen inderdaad spontane emissie van ingebouwde lichtbronnen beïnvloeden. Ten tweede legt het proefschrift een belangrijk knelpunt bloot waaraan het vakgebied het hoofd moet bieden: wanordelijke verstrooiing. In de race om een succesvolle bandkloof-structuur te maken, dient het belang van wanordelijke verstrooiing niet onderschat te worden. Alleen fenomenale nauwkeurigheid in preparaat-fabricage kan meervoudige verstrooiing minimaliseren. Anderzijds is de studie van meervoudige verstrooiing in fotonische kristallen interessant, omdat het nieuwe facetten toevoegt aan het vakgebied van licht-transport in ongeordende media.

Dankwoord

Traditioneel wordt een proefschrift altijd afgesloten met een dankwoord. Dit is een goed gebruik. Een vaak gehoorde verklaring is dat het dankwoord waarborgt dat delen van het voorliggende boekje daadwerkelijk gelezen worden door meer dan die tien mensen, die dit uit hoofde van hun werk doen. Zo'n verklaring is onzinnig, en doet afbreuk aan de bijdrage die velen aan mijn werk in de afgelopen vier jaar hebben geleverd. Zoals de meeste lezers bekend is, is mijn eigen promotieperiode door onvoorziene omstandigheden niet geheel volgens het boekje gelopen. Het moge dan ook duidelijk zijn dat ik bij veel mensen in het krijt sta die promotie in vier jaar toch mogelijk gemaakt hebben, zowel in Enschede als in Amsterdam.

Willem 'Zorro' Vos is wel het dichtst betrokken geweest bij mijn onderzoek, op de voet gevolgd door mijn andere promotor, Ad Lagendijk, die met name verantwoordelijk is voor lessen wetenschapssociologie en wetenschapspolitiek. Na samenwerken en veel discussies met Willem hoop ik in ieder geval veel geleerd te hebben over kritisch kijken naar het werk van anderen, het ontmaskeren van tweedehands auto's in artikelen van tsaristische makelij, en het zelf als Rolls Royce aan de man brengen van eigen werk. Succes van dit laatste vereist de gave om elk resultaat gedegen tot aan het gaatje door te interpreteren, om er vervolgens op Amerikaanse wijze mensen mee om de oren te slaan. Ad wil ik met name bedanken voor het creëren van een groep met een discussiesfeer waarin iedereen iedereens resultaten kan bekritiseren en bespreken.

Ik zal direct maar toegeven dat ik voor de kristallen die ik gebruikt heb in de afgelopen vier jaar, volledig afhankelijk was van Lydia Bechger en werk van haar voorganger Judith Wijnhoven. Ik wil Lydia echter niet alleen bedanken voor samples en SEM plaatjes en andere praktische zaken. Met name vond ik het erg prettig om iemand te hebben om wederzijdse persoonlijke ongenoegens te bespreken, zowel voor, tijdens als na de Amsterdamse stillegging van ons onderzoek en de verhuizing naar Twente. Het feit dat we gelijk begonnen in de groep, heeft (mij in ieder geval) zeker geholpen om de frustraties van het eerste jaar en de persoonlijke gevolgen van de verhuizing te overwinnen. Wat die laatste loodjes betreft wil ik ook Martijn voor het voetlicht brengen; het was erg gezellig om bijna tegelijkertijd vanuit Enschede de verschillende stadia van het Amsterdamse promotiereglement door te worstelen.

In de groep Complex Photonic Systems is veel veranderd in de afgelopen jaren; de naam van de groep, de locatie van de groep, de samenstelling en grootte van de groep en ook de sfeer. Toen ik kwam pikte ik een staartje mee van de aanwezigheid van Mischa en Frank. Hen wil ik met name bedanken voor de open-armen ontvangst (niet dat ik inhoudelijk veel begreep van Mischa's inzichten in fotonische kristallen), en met name de peptalks met Frank en Arnout in de trein naar Utrecht. Jaime en Gijs leerde ik juist meer kennen toen de arbodienst hangsloten ging uitdelen aan het Van der Waals-Zeeman instituut. Aan Gijs komt dan ook alle eer voor mijn enige foto met

eigen asbestlint- en slot! Poldercharro Jaime aan de andere kant wil ik bedanken voor mijn bijnaam 'electrontransfemius', opgedaan in tijden dat het onderzoek wat minder vlotte. Dit was het onderzoek met het infrarode 3800 beest; Rudolf was als groepslid altijd bereikbaar voor adviezen als de 3800 het weer 'ns niet deed, en natuurlijk voor numerieke adviezen. Met Peter, Boris, Cock, Henry S., en Juan heb ik gezellige kamergenootschappen gehad, although I still didn't quite recover from Juanito's biohazardous coffee-experiments and keep being amazed by Boris' French-Mediterranean love-life. Ook de gezellige lunches onder het toeziend oog van Jannie met luidruchtige Denis, Manu (hoe is het met je belastingformulier ?), Dirk, Yuri, Frank P., Dau, cynische Tom en Bert wil ik niet onvermeld laten. Henry 'Henk' van Driel wil ik niet alleen bedanken voor z'n inspirerende aanwezigheid tijdens zijn sabbatical, maar ook voor hulp bij de reflectiemetingen toen ik net in de groep was. Patrick wil ik met name noemen, vanwege de leuke tijden met het schakelpatent en de roemruchte lunch in het Amstelhotel. Toevallig kon ik de berekening doen die nodig was om het schakelvoorstel van Willem en Patrick verder uit te werken. Inmiddels zijn er weer vele gezellige mensen in de groep bijgekomen: Bas natuurlijk die er voor zorgde dat we na de verhuizing binnen een mum van tijd weer internet hadden, Karen om ons te administreren, zodat FOM ook wist waar we na verhuizing gebleven waren, en Léon om onze groepspraatjes in het gareel te houden. Inmiddels is onze groep ook eindelijk rijk aan afstudeerders. Jammer dat ik zelf geen student heb kunnen begeleiden; maar het was gezellig espresso tappen met Ivo, Arie en Karin. Vrijmibo's zijn hier in Enschede wel min of meer verleden tijd; Tijmen, Allard, Peter, Raymond en Willem wil ik echter bedanken voor al die gezellige keren dat we "krokodil[1]" aten in het lokale campusrestaurant.

Veel heb ik te danken aan mensen die nu nog in Amsterdam werken. Ten eerste Wim Koops; altijd klaar om weer een nieuwe Argon laser te installeren als de vorige opgebrand was. De hele groep heeft ook veel aan je te danken wat betreft je strijdlustige aanpak van de Amsterdamse kant van onze verhuizing. En dan ook nog eens de Begonia vaarwel moeten zeggen…Gerard Wegdam wil ik niet alleen bedanken voor het kortstondig uitlenen van zijn Coherent Innova 90, maar met name voor zijn sleutelrol in het op gang helpen houden van m'n emissieonderzoek nadat B54 wegens overmatige stoffigheid verzegeld was. De navolgende maanden met zuurstofsensor op zak in de kelder hebben geleid tot hoofdstuk 7 van dit boekje, en tenminste twee publicaties. Niemand werkt in het WZI zonder van een hele papierwinkel naadloos afgeschermd te worden door Mariet, Ineke, Roos en Ina; aan hen alle eer. Tegen de onmisbare technici kan ik alleen zeggen: dank voor de gezellige humor in barre tijden. Het zal jullie goed doen te weten dat de roemruchte begonia nu dagelijks rondjes snort onder leiding van Ivan. Tot slot wil ik Marc en Derk bedanken voor de computer-support (ook netwerk in je lab als de hubs achter slot-en grendel zitten), en alle AIO's van het WZI voor de sfeer van onze militantere overleggen. Hierbij wil ik speciaal Dennis de Lang even noemen, wegens onze gezamenlijke brievenschrijverij.

Daniël Vanmaekelbergh, John Kelly en Floris wil ik bedanken voor de stimule-

[1] Gallus Gallus Domesticus

rende werkbesprekingen in Utrecht, Amsterdam, Enschede en de stationsrestauratie op Apeldoorn CS over quantum dots, GaP en titania. Voorts wil ik Hans De Raedt en Kristel, Thilo en Sebas roemen om de geweldige discussiesfeer bij de diepgravende cluster-overleggen.

In Enschede zijn we zeer vriendelijk en voortvarend ontvangen en het is verwonderlijk dat we al na enkele maanden weer metingen deden. Hiervoor zijn bergen werk verzet; niet alleen door Ad, Willem en de andere groepsleden. Ook van vitaal belang zijn de inspanningen geweest van Cock en van Raymond, onze manager met vlotte babbel en platte bak; humor die precies past in de 'No Mercy' sfeer van Amsterdamse cowboys. Erg gezellig. Eigenlijk moet ik de hele TN faculteit en MESA+ bedanken voor het welkome en gezwind aangelegde onderdak. Speciaal wil ik onze ganggenoten van de werkplaats op vloer 2 en de mensen van Optische Technieken, speciaal Kobus, Niek, Eliane, Henk-Jan, Herman (in de trein) en hun collega's bedanken voor de hartelijke ontvangst. Niet alleen gezellig leuten met OT-ers op Veldhoven of Lunteren, maar ook gezamenlijke Advanced Photonic Systems bijeenkomsten waren aangenaam. Kobus Kuipers was in hoge mate verantwoordelijk voor het aanzwengelen van de Twents fotonische scene, en voor de interessante Ameland bijeenkomst; initiatieven die ik erg waardeerde. Voorts wil ik FOM niet onvermeld laten; ik ben het FOM-bureau zeer erkentelijk voor de financiële steun die zij boden om het voeren van een tweede huishouden in Twente te bolwerken.

Tot slot wil ik hier mijn vriendenkring buiten COPS om in Utrecht en omgeving en Brabant bedanken voor het in leven houden van iemand die anders waarschijnlijk in een natuurkundezombie veranderd zou zijn, en voor het af en toe bezoekjes afleggen nabij de Duitse grens. Met name wil ik mijn ouders bedanken voor de gezellige inspanning voor m'n omslagfoto en de carrière-adviezen op omslagpunten bij m'n COPS verblijf. Ans komt specifiek de eer toe nog een groot aantal tekstuele onvolkomenheden in dit boekje aangewezen te hebben; dank voor de vele moeite. Arie en Mia wil ik bedanken voor hun altijd-open-deur en voor hun inspanningen bij het inrichten van m'n Enschedese stulp. Bij Nicole tenslotte wil ik me verontschuldigen voor die weekenden dat ik in gedachten meer bij Maxwellvergelijkingen was, die vele avonden dat ik laat of knorrig was zoals het een OIO betaamt en natuurlijk voor het feit dat ik er even tussen uit moest verhuizen. Dank dus voor de vele kilometers naar de Westerstraat in je blauwe bolide, ondanks je eigen drukke baan en besognes.

List of Publications

Publications related to this thesis

1. A. F. Koenderink, M. Megens, G. van Soest, W. L. Vos, and A. Lagendijk, *Enhanced Backscattering from Photonic Crystals*, Phys. Lett. A **268**, 104–111 (2000).
2. H. P. Schriemer, H. M. van Driel, A. F. Koenderink, and W. L. Vos, *Modified Spontaneous Emission Spectra of Laser Dye in Inverse Opal Photonic Crystals*, Phys. Rev. A **63**, R011801:1–4 (2001).
3. W. L. Vos, H. M. van Driel, M. Megens, A. F. Koenderink, and A. Imhof, *Experimental Probes of the Optical Properties of Photonic Crystals*, in *Photonic Crystals and Light Localization in the 21st Century*, edited by C. M. Soukoulis (Kluwer, Dordrecht, 2001), pp. 191–218.
4. A. F. Koenderink, P. M. Johnson, J. F. Galisteo Lopez, and W. L. Vos, *Three-Dimensional Photonic Crystals as a Cage for Light*, C. R. Physique **3**, 65–77 (2002).
5. L. Bechger, A. F. Koenderink, and W. L. Vos, *Emission Spectra and Lifetimes of R6G Dye on Silica-Coated Titania Powder*, Langmuir **18**, 2444–2447 (2002).
6. A. F. Koenderink, L. Bechger, H. P. Schriemer, A. Lagendijk, and W. L. Vos, *Broadband Fivefold Reduction of Vacuum Fluctuations Probed by Dyes in Photonic Crystals*, Phys. Rev. Lett. **88**, 143903:1–4 (2002).
7. P. M. Johnson, A. F. Koenderink, and W. L. Vos, *Ultrafast switching of photonic density of states in photonic crystals*, Phys. Rev. B **66**, R081102:1–4 (2002).
8. A. F. Koenderink, L. Bechger, A. Lagendijk, and W. L. Vos, *An Experimental Study of Strongly Modified Emission in Inverse Opal Photonic Crystals*, Phys. Stat. Sol. (2003), (in press) Proceedings of the Heraeus Summerschool on Photonic Crystals in Wittenberg, Germany (July 2002).
9. A. F. Koenderink and W. L. Vos, *Light Exiting from Photonic Band Gap Crystals is Diffuse and Strongly Directional*, (2002), submitted to Phys. Rev. Lett.
10. A. F. Koenderink and W. L. Vos, *Anomalous Diffuse Transmission of Photonic Crystals*, (2002), submitted to Phys. Rev. E.

Publications not related to this thesis

11. D. J. Dieleman, A. F. Koenderink, M. G. A. van Veghel, M. A. de Vries, A. F. M. Arts, and H. W. de Wijn, *Physical and Geometrical Optics of Phonons*, Physica B **263–264**, 564–566 (1999).

12. D. J. Dieleman, A. F. Koenderink, A. F. M. Arts, and H. W. de Wijn, *Diffraction of Coherent Phonons Emitted by a Grating*, Phys. Rev. B **60**, 14719–14723 (1999).
13. D. J. Dieleman, A. F. Koenderink, M. G. A. van Veghel, A. F. M. Arts, and H. W. de Wijn, *Transmission of Coherent Phonons through a Metallic Multilayer*, Phys. Rev. B **64**, 174304:1–4 (2001).
14. A. Doelman, A. F. Koenderink, and L. R. M. Maas, *Quasi-periodically Forced Nonlinear Helmholtz Oscillators*, Physica D **164**, 1–27 (2002).

Miscellaneous

1. W. L. Vos, P. M. Johnson, and A. F. Koenderink, *Photonic Crystal Switch*, patent application no. WO. NL1018985 (2001).
2. A. F. Koenderink, L. Bechger, and W. L. Vos, *Fotonische kristallen: oases van stilte in het ruisend vacuum*, NTvN **68**, 188–192 (2002).

If you are not a nanotechnician:
try a larger (photo)copy .... see the PDF of
this thesis, available at
`www.photonicbandgaps.com`